

**MATERIALS FOR ADAPTIVE STRUCTURAL
ACOUSTIC CONTROL**

Period February 1, 1995 to January 31, 1996

Annual Report

VOLUME I

OFFICE OF NAVAL RESEARCH
Contract No.: N00014-92-J-1510

APPROVED FOR PUBLIC RELEASE — DISTRIBUTION UNLIMITED

Reproduction in whole or in part is permitted
for any purpose of the United States Government

L. Eric Cross

PENNSTATE

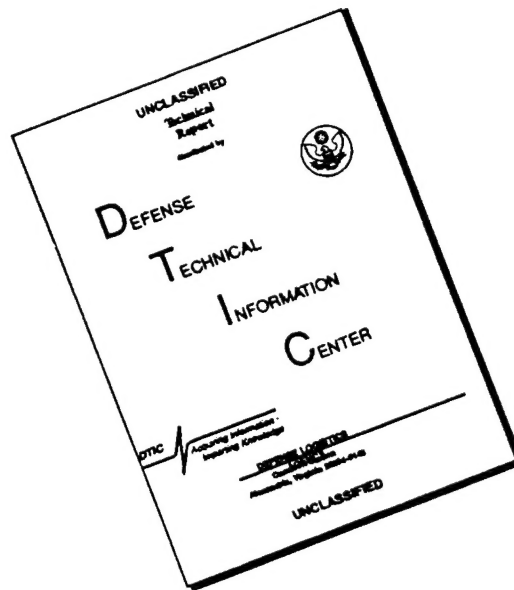


19960422 145

THE MATERIALS RESEARCH LABORATORY
UNIVERSITY PARK, PA

DTIC QUALITY INSPECTED 1

DISCLAIMER NOTICE



THIS DOCUMENT IS BEST QUALITY AVAILABLE. THE COPY FURNISHED TO DTIC CONTAINED A SIGNIFICANT NUMBER OF PAGES WHICH DO NOT REPRODUCE LEGIBLY.

REPORT DOCUMENTATION PAGE			Form Approved OMB No. 0704-0188	
<small>Public reporting burden for this collection of information is estimated to average 1 hour per response, including the time for reviewing instructions, searching existing data sources, gathering and maintaining the data needed, and completing and reviewing the collection of information. Send comments regarding this burden estimate or any other aspect of this collection of information, including suggestions for reducing this burden, to Washington Headquarters Services, Directorate for Information Operations and Reports, 1215 Jefferson Davis Highway, Suite 1204, Arlington, VA 22202-4302, and to the Office of Management and Budget, Paperwork Reduction Project (0704-0188), Washington, DC 20503</small>				
1. AGENCY USE ONLY (Leave blank)	2. REPORT DATE 3/13/96	3. REPORT TYPE AND DATES COVERED ANNUAL REPORT 02/01/95 TO 01/31/96		
4. TITLE AND SUBTITLE MATERIALS FOR ADAPTIVE STRUCTURAL ACOUSTIC CONTROL			5. FUNDING NUMBERS	
6. AUTHOR(S) L. ERIC CROSS				
7. PERFORMING ORGANIZATION NAME(S) AND ADDRESS(ES) MATERIALS RESEARCH LABORATORY THE PENNSYLVANIA STATE UNIVERSITY UNIVERSITY PARK, PA 16802			8. PERFORMING ORGANIZATION REPORT NUMBER	
9. SPONSORING/MONITORING AGENCY NAME(S) AND ADDRESS(ES) OFFICE OF NAVAL RESEARCH GERALD T. SMITH CODE 1513:NRJ OFFICE OF NAVAL RESEARCH RES. 800 NORTH QUINCY STREET 536 SOUTH CLARK STREET, RM 286 ARLINGTON, VA 22217-5660 CHICAGO, ILLINOIS 60606-1588			10. SPONSORING/MONITORING AGENCY REPORT NUMBER	
11. SUPPLEMENTARY NOTES				
12a. DISTRIBUTION / AVAILABILITY STATEMENT			12b. DISTRIBUTION CODE	
13. ABSTRACT (Maximum 200 words) SEE FOLLOWING THREE PAGES				
14. SUBJECT TERMS			15. NUMBER OF PAGES	
			16. PRICE CODE	
17. SECURITY CLASSIFICATION OF REPORT	18. SECURITY CLASSIFICATION OF THIS PAGE	19. SECURITY CLASSIFICATION OF ABSTRACT	20. LIMITATION OF ABSTRACT	

GENERAL INSTRUCTIONS FOR COMPLETING SF 298

The Report Documentation Page (RDP) is used in announcing and cataloging reports. It is important that this information be consistent with the rest of the report, particularly the cover and title page. Instructions for filling in each block of the form follow. It is important to *stay within the lines* to meet *optical scanning requirements*.

Block 1. Agency Use Only. (Leave blank).

Block 2. Report Date. Full publication date including day, month, and year, if available (e.g. 1 Jan 88). Must cite at least the year.

Block 3. Type of Report and Dates Covered. State whether report is interim, final, etc. If applicable, enter inclusive report dates (e.g. 10 Jun 87 - 30 Jun 88).

Block 4. Title and Subtitle. A title is taken from the part of the report that provides the most meaningful and complete information. When a report is prepared in more than one volume, repeat the primary title, add volume number, and include subtitle for the specific volume. On classified documents enter the title classification in parentheses.

Block 5. Funding Numbers. To include contract and grant numbers; may include program element number(s), project number(s), task number(s), and work unit number(s). Use the following labels:

C - Contract	PR - Project
G - Grant	TA - Task
PE - Program Element	WU - Work Unit Accession No.

Block 6. Author(s). Name(s) of person(s) responsible for writing the report, performing the research, or credited with the content of the report. If editor or compiler, this should follow the name(s).

Block 7. Performing Organization Name(s) and Address(es). Self-explanatory.

Block 8. Performing Organization Report Number. Enter the unique alphanumeric report number(s) assigned by the organization performing the report.

Block 9. Sponsoring/Monitoring Agency Name(s) and Address(es). Self-explanatory.

Block 10. Sponsoring/Monitoring Agency Report Number. (If known)

Block 11. Supplementary Notes. Enter information not included elsewhere such as: Prepared in cooperation with...; Trans. of...; To be published in... When a report is revised, include a statement whether the new report supersedes or supplements the older report.

Block 12a. Distribution/Availability Statement. Denotes public availability or limitations. Cite any availability to the public. Enter additional limitations or special markings in all capitals (e.g. NOFORN, REL, ITAR).

DOD - See DoDD 5230.24, "Distribution Statements on Technical Documents."

DOE - See authorities.

NASA - See Handbook NHB 2200.2.

NTIS - Leave blank.

Block 12b. Distribution Code.

DOD - Leave blank.

DOE - Enter DOE distribution categories from the Standard Distribution for Unclassified Scientific and Technical Reports.

NASA - Leave blank.

NTIS - Leave blank.

Block 13. Abstract. Include a brief (*Maximum 200 words*) factual summary of the most significant information contained in the report.

Block 14. Subject Terms. Keywords or phrases identifying major subjects in the report.

Block 15. Number of Pages. Enter the total number of pages.

Block 16. Price Code. Enter appropriate price code (*NTIS only*).

Blocks 17. - 19. Security Classifications. Self-explanatory. Enter U.S. Security Classification in accordance with U.S. Security Regulations (i.e., UNCLASSIFIED). If form contains classified information, stamp classification on the top and bottom of the page.

Block 20. Limitation of Abstract. This block must be completed to assign a limitation to the abstract. Enter either UL (unlimited) or SAR (same as report). An entry in this block is necessary if the abstract is to be limited. If blank, the abstract is assumed to be unlimited.

ABSTRACT

This report documents work carried forward over the fourth year of a five year ONR sponsored University Research Initiative (URI) entitled "Materials for Adaptive Structural Acoustic Control." The program has continued to underpin the development of new electro-ceramic, single crystal and composite materials combinations for both the sensing and actuation functions in adaptive structures.

For the lead based perovskite structure relaxor ferroelectric electrostrictors, new experimental and theoretical studies have underscored the critical role of nano-scale heterogeneity on either A or B sites of the ABO_3 in promoting dispersive dielectric response and the very strong opposing role of elastic stress and electrostrictive coupling in suppressing polarization fluctuations. Most important for practical application is the regimen where, under high electric field nano-polar regions begin to amalgamate into ferroelectric macro-domains with very mobile walls lead to unusually large extrinsic piezoelectric coefficients.

The program has explored a range of new relaxor:ferroelectric solid solutions which exhibit morphotropic phase boundaries between rhombohedral and tetragonal ferroelectric phases. Some of these compositions are much more tractable than PZT to grow in single crystal form. A major surprise is the very strong enhancement of the piezoelectric d_{33} and d_{31} in the crystal over that in the corresponding ceramic, and the massive anisotropy for different orientations and directions of poling. Optical studies suggest that the unusual effects reside largely in the extrinsic (domain controlled) response and we speculate about the mobility of walls in metastable phases, however further studies are required.

Antiferroelectric:ferroelectric phase switching studies in a wide range of compositions in the lead lanthanum zirconate stannate titanate system show that the first abrupt switchover to the rhombohedral ferroelectric phase only produces volume strain $\sim 0.2\%$ as checked both by dilatometry and by X-ray. There is a large enhancement under higher field to $\sim 0.6\%$ volume strain although the polarization does not change markedly. From thin film and single crystals studies there is mounting evidence of higher field ferroelectric:ferroelectric phase change, but again additional work is needed.

Size effect studies in perovskite ferroelectrics are continuing on this program and on the NSF/MRG in MRL. Scaling of the 90° stripe domains in thinned TEM samples of tetragonal composition begin to show departure from the accepted $1/2$ power law at sub micron sizes. The structure of domains under the three dimensional constraints of grains inside the ceramic is still however almost completely unknown. Computer modeling appear to show promise and codes are being explored which permit the mutual interactions to be varied and the corresponding two dimensional structures visualized.

In composite sensors, the focus has continued upon the flextensional configurations with the new inexpensive cymbal shaped amplifier proving superior in every respect to the original "moonie." The flat section on the cymbal end cap permits very easy stacking of elements and work is now in progress to develop large area panels for low frequency testing at the Penn State ARL.

Work has continued on the thin sheet 2:2 piezoceramic polymer composites, where the transverse poling and low density lead to a desirable combination of low electrical and low acoustic impedance. An alternative fabrication procedure using extruded PZT honeycomb appears most attractive.

Two problems of major importance in actuation have been topics for study. First what are the "intrinsic" material limitations for high strain electrically driven actuation in polarization controlled systems, and secondly what are the practical limitations in multilayer actuators as they are currently fabricated and how may they be alleviated. Work on the first topic is now largely completed, showing that strains $\sim 0.4\%$ could be switched more than 10^9 cycles in suitable PLZT compositions. Such reliability however requires near theoretical density, homogeneity, grain size control, critical attention to electrodes and electric field uniformity, none of which are adequately controlled in current actuator systems.

For practical actuators fabricated by inexpensive tape casting and co-firing techniques electrode termination is a major problem. In the simple MLC like designs, cracks initiate at field concentrations associated with the tip of the buried conductor layer. A new floating electrode design has been found to reduce this problem. For cracking near the end surfaces, poling of the termination layers reduces their stiffness and markedly improves performance. In the conventional structures it is also found that the floating electrode may be used directly as an acoustic emission pickup, giving early warning of cracking problems.

Under resonant driving conditions, the problems in actuators are markedly different. Heat build up and temperature run-away are significant problems traceable to dielectric loss, and new hard compositions and anti-resonant driving methods have been explored to reduce these problems.

In integration work on the high activity 0-3 composites is nearing completion. A new type of zig-zag actuator is being explored for the capability to combine both longitudinal and transverse actuation. Under a new ONR sponsored program with Virginia Polytechnic Institute and University new double amplifiers combining bimorph and flextensional concepts are being examined.

Processing studies permit the fabrication of the wide range of compositions and forms required in these material researches. Rate controlled sintering is proving to be highly advantageous, particularly for reducing delamination in integrated structures. Electrophoretic and

dielectrophoretic forming are showing promise in green assembly of thick film components where high green density is critical.

Thin film papers have been selected from the very broad range of work in MRL because of their relevance to transduction in piezoelectric and in phase switching systems.

TABLE OF CONTENTS

ABSTRACT	8
INTRODUCTION	10
1.0 GENERAL SUMMARY PAPERS	11
2.0 MATERIALS STUDIES	12
3.0 COMPOSITE SENSORS	12
4.0 ACTUATORS STUDIES	13
5.0 INTEGRATION ISSUES	14
6.0 PROCESSING STUDIES	14
7.0 THIN FILM FERROELECTRICS	15
8.0 GRADUATE STUDENTS IN THE PROGRAM	16
9.0 HONORS AND AWARDS	16
10.0 APPRENTICE PROGRAM	16
11.0 PAPERS PUBLISHED IN REFEREED JOURNALS	17
12.0 INVITED PAPERS PRESENTATIONS AT NATIONAL AND INTERNATIONAL MEETINGS	21
13.0 INVITED PAPERS PRESENTED AT UNIVERSITY, INDUSTRY AND GOVERNMENT LABORATORIES	23
14.0 CONTRIBUTED PAPERS AT NATIONAL AND INTERNATIONAL MEETINGS	24
15.0 BOOKS (AND SECTIONS THEREOF)	27

APPENDICES

VOLUME I

General Summary Papers

1. Cross, L.E., "Ferroelectric Materials for Electromechanical Transducer Applications," *Jpn. J. Appl. Phys.* **34**, 2525-2532 (1995).
2. Fernandez, J.F., A. Dogan, Q.M. Zhang, J.F. Tressler, and R.E. Newnham, "Hollow Piezoelectric Composites," submitted to *Sensors and Actuators: A. Physical* (1995).
3. Uchino, K., "Recent Developments in Ceramic Actuators—Comparison among USA, Japan and Europe," Workshop on Microsystem Technologies in the USA and Canada, Dusseldorf (1995).
4. Trolier-McKinstry, S., J. Chen, K. Vedam, and R.E. Newnham, "In Situ Annealing Studies of Sol-Gel Ferroelectric Thin Films by Spectroscopic Ellipsometry," *J. Am. Ceram. Soc.* **78** [7], 1907-1913 (1995).
5. Nair, N., A. Bhalla, and R. Roy, "Inorganic Lead Compounds in Electroceramics and Glasses," *Am. Cer. Soc. Bull.* **75** [1], 77-82 (1996).
6. Gentile, A. and F.W. Ainger, "Single Crystals," Chapter 9, Materials Science and Technology, A Comprehensive Treatment, **17A** Processing of Ceramics, Part 1 (R.J. Brook, editor), VCH Verlagsgesellschaft mbH, Weinheim, Fed. Repl. of Germany (1996).

Materials Studies

7. Choi, S.W., J.M. Jung, and A.S. Bhalla, "Dielectric, Pyroelectric and Piezoelectric Properties of Calcium-Modified Lead Magnesium Tantalate-Lead Titanate Ceramics."
8. Kim, Y.J., S.W. Choi, and A.S. Bhalla, "Dielectric, Pyroelectric Properties, and Morphotropic Phase Boundary in La-Doped $(1-x)\text{Pb}(\text{Mg}_{1/3}\text{Ta}_{2/3})-x\text{PbTiO}_3$ Solid Solution Ceramics", *Ferroelectrics* **173**, 87-96 (1995).
9. Alberta, E. and A.S. Bhalla, "A Processing and Electrical Property Investigation of the Solid Solution: $(x)\text{Pb}(\text{In}_{1/2}\text{Nb}_{1/2})\text{O}_3-(1-x)\text{Pb}(\text{Sc}_{1/2}\text{Ta}_{1/2})\text{O}_3$," submitted to *Ferroelectrics* (1995).
10. Zhang, Q.M., H. You, M.L. Mulvihill, and S.J. Jang, "An X-ray Diffraction Study of Superlattice Ordering in Lead Magnesium Niobate," *Solid State Comm.* **97** [8], 693-698 (1996).
11. Zhang, Q.M., J. Zhao, and L.E. Cross, "Aging of the Dielectric and Piezoelectric Properties of Relaxor Ferroelectric Lead Magnesium Niobate-Lead Titanate in the Electric Field Biased State," *J. Appl. Phys.* **79** (6), 1-7 (1996).

VOLUME II

Materials Studies (continued)

12. Zhang, Q.M., J. Zhao, T.R. Shrout, and L.E. Cross, "The Effect of Ferroelastic Coupling in Controlling the Abnormal Aging Behavior in Lead Magnesium Niobate-Lead Titanate Relaxor Ferroelectrics," submitted *J. Mat. Res.*
13. Mulvihill, M.L., L.E. Cross, and K. Uchino, "Low-Temperature Observation of Relaxor Ferroelectric Domains in Lead Zinc Niobate," *J. Am. Ceram Soc.* **78** (12) 3345-3351 (1995).
14. Mulvihill, M.L., L.E. Cross, and K. Uchino, "Dynamic Motion of the Domain Configuration in Relaxor Ferroelectric Single Crystals as a Function of Temperature and Electric Field," 8th Euro. Mtg. Ferroelectricity, Nijmegen (1995).
15. Mulvihill, M.L., K. Uchino, Z. Li, and Wenwu Cao, "In-Situ Observation of the Domain Configurations During the Phase Transitions in Barium Titanate," accepted *Phil. Mag. B* (1995).
16. Oh, K.Y., K. Uchino, and L.E. Cross, "Electric Properties and Domain Structures in Ba(Ti,Sn)O₃ Ceramics."
17. Cao, W., "Elastic and Electric Constraints in the Formation of Ferroelectric Domains," *Ferroelectrics*, **172**, 31-37 (1995).
18. Cao, W. and C.A. Randall, "The Grain Size and Domain Size Relations in Bulk Ceramic Ferroelectric Materials," accepted *J. Phys. Chem. Solids* (1995).
19. Cao, W., "Defect Stabilized Periodic Amplitude Modulations in Ferroelectrics," accepted *Phase Transitions* (1995).
20. Sopko, J., A. Bhalla, and L.E. Cross, "An Improved Quantitative Method for Determining Dynamic Current Response of Ppyroelectric Materials," *Ferroelectrics*, **173**, 139-152 (1995)

VOLUME III

Composite Sensors

21. Tressler, J.F., A. Dogan, J.F. Fernandez, J.T. Fielding, Jr., K. Uchino, and R.E. Newnham, "Capped Ceramic Hydrophones," submitted to Proc. IEEE Int'l Ultrasonics Symp., Seattle (1995).
22. Koc, B., A. Dogan, J.F. Fernandez, R.E. Newnham, and K. Uchino, "Accelerometer Application of the Modified Moonie (Cymbal) Transducer," submitted *Jpn. J. Appl. Phys.* (1995).
23. Zhao, J., Q.M. Zhang, and W. Cao, "Effects of Face Plates and Edge Strips on Hydrostatic Piezoelectric Response of 1-3 Composites," *Ferroelectrics* **173**, 243-256 (1995).
24. Wu, S.J., W. Qi, and W. Cao, "Numerical Study of Ultrasonic Beam Pattern of a 1-3 Piezocomposite Transducer," accepted *Proc. IEEE Trans. Ultrasonics, Ferroelectrics and Frequency Control*. (1995).

Composite Sensors (continued)–Volume III

25. Wang, H., Q.M. Zhang, and L.E. Cross, "Tailoring Material Properties by Structure Design--Radially Poled Piezoelectric Cylindrical Tube," *Ferroelectrics Lett.* (in press).
26. Zhang, Q.M. and X. Geng, "Electric Field Forced Vibration of a Periodic Piezocomposite Plate with Laminated Structure and Reflection and Transmission of a Plane Wave at the Fluid-Composite Interface," submitted to *IEEE Transactions on Ultrasonics, Ferroelectrics, and Frequency Control* (1995).
27. Geng, X., and Q.M. Zhang, "Dynamic Behavior of Periodic Piezoceramic-Polymer Composite Plates," *Appl. Phys. Lett.* **67** (21) (1995).
28. Zhang, Q.M., "Transverse Piezoelectric Mode Piezoceramic Polymer Composites with High Hydrostatic Piezoelectric Responses," *Proc. Int. Conf. on Electronic Components and Materials Sensors and Actuators*, Xi'an, China, 159-162 (1995)
29. Zhang, Q.M., H. Wang, J. Zhao, J.T. Fielding, Jr., R.E. Newnham, and L.E. Cross, "A High Sensitivity Hydrostatic Piezoelectric Transducer Based on Transverse Piezoelectric Mode Honeycomb Ceramic Composites," *IEEE Transactions on Ultrasonics, Ferroelectrics and Frequency Control* **43** (1), 26-42 (1996).
30. Zhang, Q.M., J. Chen, H. Wang, J. Zhao, L.E. Cross, and M.C. Trottier, "A New Transverse Piezoelectric Mode 2-2 Piezocomposite for Underwater Transducer Applications," *IEEE Transactions on Ultrasonics, Ferroelectrics, and Frequency Control* **42** (4), 774-780 (1995).
31. Cao, W., Q.M. Zhang, J.Z. Zhao, and L.E. Cross, "Effects of Face Plates on Surface Displacement Profile in 2-2 Piezoelectric Composites," *IEEE Transactions on Ultrasonics, Ferroelectrics, and Frequency Control* **42** (1), 37-41 (1995).
32. Cao, W. and W. Qi, "Plane Wave Propagation in Finite 2-2 Composites," *J. Appl. Phys.* **78** (7), 4627-4632 (1995).
33. Qi, W. and W. Cao, "Finite Element Analysis and Experimental Studies on the Thickness Resonance of Piezocomposite Transducers," accepted *Ultrasonic Imaging* (1995).
34. Cao, W. and W. Qi, "Multisource Excitations in a Stratified Biphase Structure," *J. Appl. Phys.* **78** (7), 4640-4646 (1995).

VOLUME IV

Actuator Studies

35. Uchino, K., "Materials Update: Advances in ceramic actuator materials," *Materials Lett.* **22**, 1-4 (1995).
36. Uchino, K., "Novel Ceramic Actuator Materials."
37. Aburatani, H., K. Uchino, and F. Yoshiaki, "Destruction Mechanism and Destruction Detection Technique for Multilayer Ceramic Actuators," *Proc. of the 9th Annual International Symposium on the Applications of Ferroelectrics*, 750-752 (1995).

Actuator Studies (continued)—Volume IV

38. Uchino, K. "Manufacturing Technology of Multilayered Transducers," *Proc. Amer. Ceram. Soc.*, Manufacture of Ceramic Components, 81-93 (1995).
39. Uchino, K. "Piezoelectric Actuators/Ultrasonic Motors--Their Development and Markets," *Proc. 9th ISAF*, 319-324 (1995).
40. Dogan, A., J.F. Fernandez, K. Uchino, and R.E. Newnham, "New Piezoelectric Composite Actuator Designs for Displacement Amplification," in press *Proc. Euroceram 95* (1995).
41. Onitsuka, O., A. Dogan, J.F. Tressler, Q.Su, S. Yoshikawa, and R.E. Newnham, "Metal-Ceramic Composite Transducer, The 'Moonie' ," *J. Intelligent Materials Systems and Structures* **6**, 447-455 (1995).
42. Fernandez, J.F., A. Dogan, J.T. Fielding, K. Uchino, and R.E. Newnham, "Tailoring High Displacement Performance of Ceramic-Metal Piezocomposite Actuators 'Cymbals'," submitted to *IEEE Transactions on Ultrasonics, Ferroelectrics, and Frequency Control* (1995).
43. Hirose, S., S. Takahashi, K. Uchino, M. Aoyagi, and Y. Tomikawa, "Measuring Methods for High-Power Characteristics of Piezoelectric Materials," *Mat. Res. Soc. Symp. Proc.* **360**, 15-20 (1995).
44. Takahashi, S., S. Hirose, K. Uchino, and K.Y. Oh, "Electro-Mechanical Characteristics of Lead-Zirconate-Titanate Ceramics Under Vibration-Level Change," *Proc. 9th ISAF*, 377-382 (1995).
45. Takahashi, Sadayuki, Yasuhiro Sasaki, Seiji Hirose, and Kenji Uchino, "Electro-Mechanical Properties of PbZrO_3 - PbTiO_3 - $\text{Pb}(\text{Mn}_{1/3}\text{Sb}_{2/3})\text{O}_3$ Ceramics Under Vibration-Level Change," *Mat. Res. Soc. Symp. Proc.* **360**, 305-310 (1995).

VOLUME V

46. Zheng, Jiehui, Sadayuki Takahashi, Shoko Yoshikawa, Kenji Uchino, and J.W.C. de Vries, "Heat Generation in Multilayer Piezoelectric Actuators," submitted to *J. Am. Ceram. Soc.* (1995).
47. Uchino, Kenji, "Review: Photostriction and its Applications," in press *J. Innovations in Mater. Res.* (1995).
48. Chu, Sheng-Yuan, and Kenji Uchino, "Photo-Acoustic Devices Using $(\text{Pb},\text{La})(\text{Zr},\text{Ti})\text{O}_3$ Ceramics," *Proc. 9th ISAF*, 743-745 (1995).

Integration Issues

49. Matsko, M.G., Q.C. Xu, and R.E. Newnham, "Zig-Zag Piezoelectric Actuators: Geometrical Control of Displacement and Resonance," *J. Intell. Mat. Syst. and Struct.* **6** (6), 783-786 (1995).
50. Xu, Baomin, Qiming Zhang, V.D. Kugel, and L.E. Cross, "Piezoelectric Air Transducer for Active Noise Control," submitted *Proc. SPIE* (1996).

Integration Issues (continued)–Volume V

51. Kumar, S., A.S. Bhalla, and L.E. Cross, "Underwater Acoustic Absorption by Collocated Smart Materials," accepted *Ferroelectric Letters* (1995).
52. Elissalde, Catherine and Leslie Eric Cross, "Dynamic Characteristics of Rainbow Ceramics," *J. Am. Ceram. Soc.* **78** [8], 2233-2236 (1995).

Processing Studies

53. Bowen, Christopher P., Thomas R. ShROUT, Robert E. Newnham, and Clive A. Randall, "Tunable Electric Field Processing of Composite Materials," *J. of Intelligent Material Systems and Structures* **6** (2), 159-168 (1995).
54. Zhang, Q.M., J. Zhao, T. ShROUT, N. Kim, and L.E. Cross, "Characteristics of the Electromechanical Response and Polarization of Electric Field Biased Ferroelectrics," *J. Appl. Phys.* **77** (5), 2549-2555 (1995).
55. Zhao, J., Q.M. Zhang, N. Kim, and T. ShROUT, "Electromechanical Properties of Relaxor Ferroelectric Lead Magnesium Niobate-Lead Titanate Ceramics," *Jpn. J. Appl. Phys.* **34**, 5658-5663 (1995).
56. Zipparo, M.J., K.K. Shung, and T.R. ShROUT, "Piezoelectric Properties of Fine Grain PZT Materials," *Proc. IEEE Int'l Ultrasonics Symposium* (1995).
57. Yoshikawa, Shoko, Ulagaraj Selvaraj, Paul Moses, John Witham, Richard Meyer, and Thomas ShROUT, "Pb(Zr,Ti)O₃[PZT] Fibers–Fabrication and Measurement Methods," *J. Intell. Mat. Syst. and Struct.* **6** (2), 152-158 (1995).
58. Hackenberger, W.S., T.R. ShROUT, A. Nakano, and R.F. Speyer, "Rate Controlled Sintering of Low Temperature Cofired Ceramic Multilayers Used for Electronic Packaging."
59. Randall, C.A., N. Kim, W. Cao, and T.R. ShROUT, "Domain-Grain Size Relation in Morphotropic Phase Boundary, Pb(Zr_{0.52}Ti_{0.48})O₃," 7th US:Japan Mtg. on Dielectric and Piezoelectric Ceramics, Tsukuba, 145-149 (1995).
60. Cann, David P., Clive A. Randall, and Thomas R. ShROUT, "Investigation of the Dielectric Properties of Bismuth Pyrochlores," accepted *Solid State Communication* (1995).

VOLUME VI

61. Mulvihill, Maureen L., Seung Eek Park, George Risch, Zhuang Li, Kenji Uchino, and Thomas R. ShROUT, "The Role of Processing Variables in the Flux Growth of PZN-PT Relaxor Ferroelectric Single Crystals."

Thin Films Ferroelectrics

62. Chen, H.D., K.R. Udayakumar, L.E. Cross, J.J. Bernstein, and L.C. Niles, "Dielectric, Ferroelectric, and Piezoelectric Properties of Lead Zirconate Titanate Thick Films on Silicon Substrates," *J. Appl. Phys.* **77** (7), 3349-3353 (1995).

Thin Films Ferroelectrics (continued)—Volume VI

63. Udayakumar, K.R., P.J. Schuele, J. Chen, S.B. Krupanidhi, and L.E. Cross, "Thickness-Dependent Electrical Characteristics of Lead Zirconate Titanate Thin Films," *J. Appl. Phys.* **77** (8), 3981-3986 (1995).
64. Chen, H.D., K.R. Udayakumar, C.J. Gaskey, and L.E. Cross, "Electrical Properties' Maxima in Thin Films of the Lead Zirconate-Lead Titanate Solid Solution System," *Appl. Phys. Lett.* **67** (23), 3411-3413 (1995).
65. Gaskey, C.J., K.R. Udayakumar, H.D. Chen, and L.E. Cross, "'Square' Hysteresis Loops in Phase-Switching Nb-Doped Lead Zirconate Stannate Titanate Thin Films," *J. Mater. Res.* **10** (11), 2764-2769 (1995).
66. Yamakawa, K., S. Trolier-McKinstry, J.P. Dougherty, and S. Krupanidhi, "Reactive Magnetron Co-Sputtered Antiferroelectric Lead Zirconate Thin Films," *Appl. Phys. Lett.* **67** (14), 2014-2016 (1995).
67. Ravichandran, D., K. Yamakawa, A.S. Bhalla, and R. Roy, "Alkoxide Derived $\text{SrBi}_2\text{Ta}_2\text{O}_9$ Phase Pure Powder and Thin Films."
68. Thakoor, Sarita, A.P. Thakoor, and L. Eric Cross, "Optical Non-Invasive Evaluation of Ferroelectric Films/Memory Capacitors," *Mat. Res. Soc. Symp. Proc.* **360**, 157-167 (1995).

ABSTRACT

This report documents work carried forward over the fourth year of a five year ONR sponsored University Research Initiative (URI) entitled "Materials for Adaptive Structural Acoustic Control." The program has continued to underpin the development of new electro-ceramic, single crystal and composite materials combinations for both the sensing and actuation functions in adaptive structures.

For the lead based perovskite structure relaxor ferroelectric electrostrictors, new experimental and theoretical studies have underscored the critical role of nano-scale heterogeneity on either A or B sites of the ABO_3 in promoting dispersive dielectric response and the very strong opposing role of elastic stress and electrostrictive coupling in suppressing polarization fluctuations. Most important for practical application is the regimen where, under high electric field nano-polar regions begin to amalgamate into ferroelectric macro-domains with very mobile walls which lead to unusually large extrinsic piezoelectric coefficients.

The program has explored a range of new relaxor:ferroelectric solid solutions which exhibit morphotropic phase boundaries between rhombohedral and tetragonal ferroelectric phases. Some of these compositions are much more tractable than PZT to grow in single crystal form. A major surprise is the very strong enhancement of the piezoelectric d_{33} and d_{31} in the crystal over that in the corresponding ceramic, and the massive anisotropy for different orientations and directions of poling. Optical studies suggest that the unusual effects reside largely in the extrinsic (domain controlled) response and we speculate about the mobility of walls in metastable phases, however further studies are required.

Antiferroelectric:ferroelectric phase switching studies in a wide range of compositions in the lead lanthanum zirconate stannate titanate system show that the first abrupt switchover to the rhombohedral ferroelectric phase only produces volume strain $\sim 0.2\%$ as checked both by dilatometry and by X-ray. There is a large enhancement under higher field to $\sim 0.6\%$ volume strain although the polarization does not change markedly. From thin film and single crystals studies there is mounting evidence of higher field ferroelectric:ferroelectric phase change, but again additional work is needed.

Size effect studies in perovskite ferroelectrics are continuing on this program and on the NSF/MRG in MRL. Scaling of the 90° stripe domains in thinned TEM samples of tetragonal composition begin to show departure from the accepted $1/2$ power law at sub micron sizes. The structure of domains under the three dimensional constraints of grains inside the ceramic is still however almost completely unknown. Computer modeling appears to show promise and codes are being explored which permit the mutual interactions to be varied and the corresponding two dimensional structures visualized.

In composite sensors, the focus has continued upon the flextensional configurations with the new inexpensive cymbal shaped amplifier proving superior in every respect to the original "moonie." The flat section on the cymbal end cap permits very easy stacking of elements and work is now in progress to develop large area panels for low frequency testing at the Penn State ARL.

Work has continued on the thin sheet 2:2 piezoceramic polymer composites, where the transverse poling and low density lead to a desirable combination of low electrical and low acoustic impedance. An alternative fabrication procedure using extruded PZT honeycomb appears most attractive.

Two problems of major importance in actuation have been topics for study. First what are the "intrinsic" material limitations for high strain electrically driven actuation in polarization controlled systems, and secondly what are the practical limitations in multilayer actuators as they are currently fabricated and how may they be alleviated. Work on the first topic is now largely completed, showing that strains $\sim 0.4\%$ could be switched more than 10^9 cycles in suitable PLZT compositions. Such reliability however requires near theoretical density, homogeneity, grain size control, critical attention to electrodes and electric field uniformity, none of which are adequately controlled in current actuator systems.

For practical actuators fabricated by inexpensive tape casting and co-firing techniques electrode termination is a major problem. In the simple MLC like designs, cracks initiate at field concentrations associated with the tip of the buried conductor layer. A new floating electrode design has been found to reduce this problem. For cracking near the end surfaces, poling of the termination layers reduces their stiffness and markedly improves performance. In the conventional structures it is also found that the floating electrode may be used directly as an acoustic emission pickup, giving early warning of cracking problems.

Under resonant driving conditions, the problems in actuators are markedly different. Heat build up and temperature run-away are significant problems traceable to dielectric loss, and new hard compositions and anti-resonant driving methods have been explored to reduce these problems.

In integration work on the high activity 0-3 composites is nearing completion. A new type of zig-zag actuator is being explored for the capability to combine both longitudinal and transverse actuation. Under a new ONR sponsored program with Virginia Polytechnic Institute and University new double amplifiers combining bimorph and flextensional concepts are being examined.

Processing studies permit the fabrication of the wide range of compositions and forms required in these material researches. Rate controlled sintering is proving to be highly advantageous, particularly for reducing delamination in integrated structures. Electrophoretic and

dielectrophoretic forming are showing promise in green assembly of thick film components where high green density is critical.

Thin film papers have been selected from the very broad range of work in MRL because of their relevance to transduction in piezoelectric and in phase switching systems.

INTRODUCTION

This report summarizes work carried out in the Materials Research Laboratory of The Pennsylvania State University during the fourth year of a five year ONR sponsored University Research Initiative (URI) entitled "Materials for Adaptive Structural Acoustic Control." The work is carried out largely in five sections each reporting to a senior faculty member.

These sections are:

Materials Studies	A.S. Bhalla
Composite Sensors	R.E. Newnham
Actuator Studies	K. Uchino
Integration Issues	J. Dougherty
Processing Studies	T.R. Shrout

In view of the reciprocity in the direct and converse piezoelectric effects it is no surprise that there is necessary and highly desirable overlap between sections. The best composite approaches require detailed consideration of integration issues and all materials necessarily depend on proper fabrication and the understanding generated in process studies.

Following long precedent, the document presents only a very brief narrative summary of the work accomplished which makes reference to the published studies from the group which form the technical appendices that are the bulk of this report.

For convenience as in earlier years the papers are grouped under the topic headings:

1. General Summary Papers
2. Materials Studies
3. Composite Sensors
4. Actuator Studies
5. Integration Issues
6. Processing Studies
7. Thin Film Ferroelectrics.

The General Summary Papers continue the educational role of the senior faculty comparing progress in United States, Europe, and Japan extolling the merits of composites particularly those with air as a second phase and debunking the 'myth' of lead ceramics. To react to the strong reawakening interest in single crystal systems an excellent summary on single crystal growth is included.

Relaxor systems continue to dominate the interest in materials and new morphotropic phase boundaries between rhombohedral relaxor and tetragonal ferroelectric phases promise major improvement in piezoelectric and coupling coefficients, with new challenges to understand the highly mobile domain walls in these systems. It is encouraging to see the theoretical modeling coming along to the extent that parameter manipulation can give "designer" domain structures in two dimensional systems.

In the competition for the best simple flextensional composite, the cymbal shaped cap design appears superior to the original moonie in all aspects. With kovar caps giving close thermal expansion match, actuation strain can be made independent of temperature over a wide range.

Progress on the transversely poled 2:2 composites has achieved outstanding d_{hg} figures of merit combined with excellent low acoustic and electrical impedance.

Reliability studies have focused more upon conventional co-fired multilayers and techniques to improve their performance. For resonant drive, heating is a major problem at high drive levels and new ceramics and driving methods are being examined. Interest is also continuing in photostriction and photo acoustic device structures.

Work on the high coupling 0:3 composite for integrated systems is being completed and new initiatives on two dimensional actuation and on double amplifier systems are being explored.

The control of grain size and its influence on electro-mechanical properties is of major interest, new rate controlled sintering promises significant improvement in consolidation and control. A new effort is being mounted on the flux growth of single crystals in the new relaxor:ferroelectric morphotropic phase boundary systems.

The laboratory has a very extensive program on the development of ferroelectric, relaxor ferroelectric, and antiferroelectric thin films. Only those papers which are directly relevant to transducer application of film structures has been included in this report.

1.0 GENERAL SUMMARY PAPERS

In discussing ferroelectric materials for transducer applications (Appendix 1) Cross contrasts the simplicity of the single crystal piezoelectrics and the complexity of the poled piezoceramic with its panoply of intrinsic and extrinsic contributions to response. He outlines the advantages of composite systems for controlling and enhancing wanted tensor coefficients and suppressing unwanted responses. The message is further taken up by Fernandez, et.al (Appendix 2) where the benefits of air as a second phase of very low acoustic impedance are further underscored. Recent developments in Ceramic Actuators are the topic for Uchino (Appendix 3) which compares and constrasts the recent progress in Europe, Japan, and the Unites States. For thin ferroelectric films, the importance of spectroscopic ellipsometry as a nondestructive characterization tool is underscored by Trolrier-McKinstry, et.al. (Appendix 4),

highlighting the far from ideal microstructure which can occur with inattention to detail in annealing ferroelectric films. It is to be hoped that environmental lobbies do not panic the country into inappropriate controls on the use of lead compounds in ceramics, as the industrial use in glass and ceramics (Nair, et. al., Appendix 5) can be quite safe. To reflect the increasing interest in single crystals relaxor:ferroelectric MPB compositions an interest chapter by Gentile and Ainger on single crystal growth techniques is included as Appendix 6.

2.0 MATERIAL STUDIES

Exciting new progress has been made in exploring the MPB composition regions in Ca modified $\text{PbMg}_{1/3}\text{Ta}_{2/3}\text{O}_3\text{:PbTiO}_3$ (Appendix 7) La modified $\text{PbMg}_{1/3}\text{Ta}_{2/3}\text{O}_3\text{:PbTiO}_3$ (Appendix 8) and the $\text{Pb}(\text{In}_{1/2}\text{Nb}_{1/2})\text{O}_3\text{:Pb}(\text{Sc}_{1/2}\text{Ta}_{1/2})\text{O}_3$ (Appendix 9) systems by A.S. Bhalla and co-workers.

Excellent ceramic piezoelectric properties are evident and the possibility of outstanding performance in single crystals is implied. More refined x-ray analysis (Zhang, Appendix 10) on $\text{PbMg}_{1/3}\text{Nb}_{2/3}\text{O}_3$ reveals the present of superlattice ordering on a nanometer scale as evidenced in TEM studies. The very important role of elastic interactions is evidenced in PMN:PT by aging studies of Zhang, et.al. (Appendix 11 and 12). The most important phase of the build up of nano-polar regions into domains under electric bias has been explored by optical studies of single crystals of lead zinc niobate (Mulvihill, et.al., Appendix 13) and the dynamics of the behavior as a function of temperature and field examined (Mulvihill, et.al., Appendix 14). The whole question of domain behavior in metastable phases is becoming of increasing interest as evidenced from optical studies of the phase changes in single crystal BaTiO_3 (Mulvihill, et.al., Appendix 15). The role of elastic constraint in modifying domain behavior in core shell type ceramics is exemplified by the domain behavior in $\text{Ba}(\text{TiSn})\text{O}_3$ ceramics (Oh, et.al., Appendix 16).

The role of elastic constraint on domain formation is further elucidated by the modeling studies of Cao (Appendix 17). Grain size:domain size inter-relations are further examined in experimental studies by Cao and Randall (Appendix 18) where the data show a clear departure from the accepted 1/2 power law in thinned sheet fine grain samples at grain sizes below 1 μm . Following the work of Rossetti and Cao (Appendix 19) develops a theoretical approach to explain the defect stabilization of a periodic modulation of the domain polarization. For the evaluation of pyroelectric response, Sopko, et.al. (Appendix 20) have developed an improved dynamic current mode method.

3.0 COMPOSITE SENSORS

Evidence of the versatility of the simple flextensional cymbal type transducer is presented in the very high hydrophone hydrostatic sensitivity (Tressler, et.al., Appendix 21), the use of a very similar design as a high sensitivity accelerometer (Koc, et.al., Appendix 22) and the three papers

which appear in the next actuator section dealing with the excellent actuation characteristic of the same simple inexpensive structure. A problem of major importance for the practical use of the 1:3 composite panels which are now becoming available through injection molding is the effects of face plates and edge strips on the hydrostatic response (Zhao, et.al., Appendix 23). The beam pattern to be expected from an uncapped 1:3 piezoceramic:polymer composite has been calculated using finite element methods for both pulse and continuous wave excitation (Wu, et.al., Appendix 24). An exciting modification to the simple 1:3 design is the 1:3 made up from radially poled piezoceramic tubes (Wang, et.al., Appendix 25). It is shown that in this system by suitable choice of design parameters d_{33} and d_{31} can be made to have the same sign. The next eight publications Appendices 26 through 32 deal with different aspects of the interesting behavior of transversely poled 2:2 piezoceramic polymer composites. The electric field forced vibrations of a plate with laminated structure and the reflection and transmission of plane waves are dealt with in Appendix 26, dynamic behavior is further considered in Appendix 27. Transverse mode systems with high hydrostatic sensitivity are covered in Appendix 28. A simple modification using an extruded ceramic honeycomb structure is discussed in Appendix 29 and shown again to have very high hydrostatic sensitivity. More general considerations in the design and fabrication of the classic 2:2 piezoceramic:polymer composite are covered in Appendix 30. Again the effects of capping face plates on surface displacement profiles are dealt with for the 2:2 composite in Appendix 31. Plane wave propagation in a finite 2:2 composite is discussed in Appendix 32. The extensive 2:2 composite studies are rounded off by finite element analysis and experimental studies of the thickness modes (Qi, et.al., Appendix 33) and by exploration of multisource excitations in Appendix 34 (Cao, et.al.)

4.0 ACTUATOR STUDIES

A good general introduction to ceramic actuator materials is given by Uchino (Appendix 35) covering recent advances in piezoelectric, electrostrictive and phase change systems. The more unusual materials which combine (super impose) more than one effect like the photostrictors, monomorphs, and shape memory ceramics are reviewed in Appendix 36. Lifetime limitations are discussed for conventional tape cast co-fired multilayer actuators in Appendix 37 and a new floating electrode concept suggested to control cracking due to field concentration.

Some of the issues related to manufacturing of multilayers are covered in Appendix 38 where it is suggested that grain size control and electrode material issues will be the focus for future development. The more specialized actuation needs for piezoelectric motors are discussed in Appendix 39 and the trends in development over the last twenty years traced by an analysis of the emphasis in patent disclosures. Flexensional amplification for transduction is discussed in Appendices 40 through 42. Topics covered are the evolution of design from the original moonie

with its machined moon shaped electrode cavity, towards the simpler less expensive cymbal design which has proven more effective in both sensor and actuator applications. Designs for high displacement actuation using the cymbal shape are discussed in Appendix 42, together with the need to match thermal expansion of cap and ceramic so as to avoid competing thermal actuation.

The topic of high vibration level driving and associated problems is taken up in the next three publications. Hirose, et.al. in Appendix 43 discuss measuring methods for characterizing the non linearity under high drive under both resonant and antiresonant conditions. It is demonstrated that lower loss levels and consequently less heating occur at antiresonance. The importance of the effective vibration velocity as a parameter for the study of high drive levels is underscored in Appendix 44. Materials design considerations for high drive levels are discussed in Appendix 45 where it is shown that optimum ternary compositions may be quite different to those which optimize low drive level performance. A very simple empirical rule for evaluating the temperature rise under strong driving in multilayer structures is presented in Appendix 46.

The interesting coupling of photo voltaic and piezoelectric effects in poled ceramics is discussed in Appendix 47. The resulting photostriction has been applied to simple relays, and to photo walking devices. The first evidence for optical stimulation of resonant response is also presented. The photostrictive effect in B site donor doped PLZTs is discussed in more detail in Appendix 48.

5.0 INTEGRATION ISSUES

A most interesting new type of zig-zag piezoelectric actuator is discussed in Appendix 49, the design is a hybrid between multilayer and bimorph characteristics and integrates the possibility for controlled two dimensional motion for motor or positioning applications. To couple to air loads at low frequency very large surface displacement are required. In Appendix 50 a new concept combining bimorph amplifiers with a type of flexensional amplification is discussed. This activity stems from a parallel ONR sponsored URI program and is included here for interest. Earlier studies of co-located actuator sensor combinations are reported in Appendix 51. The rainbow is a most interesting ceramic:cer integrated monomorph which may have wide application in adaptive control. Appendix 52 discusses the dynamical characteristics of monomorph actuators cut from the rainbow disk.

6.0 PROCESSING STUDIES

Dielectrophoretic control in the assembly of polymer ceramic composites is discussed in Appendix 53. Electric field control of the chaining phenomenon permits the assemblage of pseudo 1:3 ceramic polymer composites which can be monitored continuously during formation by dielectric measurement. The very large values of induced piezoelectric response in systems which

undergo ferroelectric:paraelectric and relaxor ferroelectric diffuse phase transitions are the subject of study in Appendices 54 and 55. For sharp transition systems very large nondispersive d_{33} values can be induced in an exceedingly limited temperature range. Both theory and experiment are covered in the papers. Fine grain PZT ceramics were prepared and properties measured in the frequency range up to 100 MHz (Appendix 56). Contrary to earlier "lore" the piezoelectric properties do not decrease markedly down to grain sizes $\sim 0.7 \mu\text{m}$ and the high frequency response is significantly improved. Fine fibers of PZT have been prepared by a sol gel "spinning" method to yield fired fibers of order 30μ in diameter (Yoshikawa, et.al., Appendix 57). New techniques were used to pole and to measure the fibers yielding property values similar to those of the bulk ceramic. Rate controlled sintering is discussed in the paper by Hackenberger, et.al. (Appendix 58) and some of the advantages of shrinkage control emphasized for multilayer co-fired systems. Processing capability permitted the development of compositions at the MPB composition ($\text{PbZr}_{0.52}\text{Ti}_{0.48}\text{O}_3$) with finely controlled grain size for a detailed study of effects on dielectric and piezoelectric properties (Randall, et.al., Appendix 59). Associated TEM studies show that the accepted relation domain size vs (grain size)^{1/2} breaks down at sizes below $1 \mu\text{m}$ and revealed interesting transgranular domain coupling. Glass like dielectric behavior similar to that in the lead magnesium niobate was observed in bismuth pyrochlore compositions at temperatures in the range 100 to 150°K (Appendix 60).

With the development of exciting morphotropic phase boundary compositions in alternative systems to PZT the challenge of growing high quality single crystals is now being taken up worldwide. For the lead zinc niobate:lead titanate system the variables in flux growth are being explored (Mulvihill, et.al., Appendix 61). Crystals up to 1.5 cm on edge have been grown and very high dielectric permittivities measured for both $\langle 001 \rangle$ and $\langle 111 \rangle$ orientations.

7.0 THIN FILM FERROELECTRICS

The laboratory has major programs related to thin film ferroelectrics only the papers which are relevant to the application of films to transduction are reproduced here.

For many transducing applications it is desirable to increase the force which can be generated by moving to thicker film dimensions. Chen, et.al. (Appendix 62) in joint work with Draper Labs report the generation of screen printed films up to $12 \mu\text{m}$ in thickness with g_{33} values $\sim 36 \cdot 10^{-3} \text{ Vm/N}$. Thickness dependence of properties in thin films for the size range below 6000 \AA is reported in Appendix 63. Excellent room temperature values were obtained but the Curie maxima were significantly 'smeared.' Electrical properties as a function of Zr/Ti ratio in PZTs are explored in Appendix 64. The maximum associated with the 52/48 morphotropic phase boundary composition is clearly evident in the thin films. In an important study Gaskey, et.al. (Appendix 65) show that "square loop" switching can be retained in thin film lead niobium

zirconate titanate stannate antiferroelectric films. Forward switching occurs at 175 kV/cm inducing a ferroelectric polarization level of 40 $\mu\text{C}/\text{cm}^2$ and elastic strain of 0.33%. Using magnetron co-sputtering Yamakawa, et.al. (Appendix 66) again demonstrate sharp switchover in films down to significantly lower thickness. Ferroelectric $\text{SrBi}_2\text{Ti}_2\text{O}_9$ layer structure composition has been prepared in phase pure form (Appendix 67). Crack free films up to 2.0 μm in thickness have been prepared. The photo response, photo current, photo voltage, reflectance and transmittance are shown to offer an excellent "tool" for the characterization of ferroelectric thin films (Appendix 68).

8.0 GRADUATE STUDENTS IN THE PROGRAM

<i>Student</i>	<i>Section</i>	<i>Supervisor</i>
Edward Alberta	Materials Studies	A.S. Bhalla
James Tressler	Composite Sensors	R.E. Newnham
Hideaki Aburatani	Actuator Studies	K. Uchino
Amod Joshi	Actuator Studies	K. Uchino
Burhanettin Koc	Actuator Studies	K. Uchino
Yan Chen	Integration Issues	J. Dougherty
George Risch	Processing Studies	T.R. Shrout

9.0 HONORS AND AWARDS

<u>Name of Person Receiving Award</u>	<u>Recipient's Institution</u>	<u>Name, Sponsor and Purpose of Award</u>
R.E. Newnham	Penn State University	American Ceramic Society's (Pittsburgh) 1995 Albert Victor Bleining Memorial Award Recipient, "for distinguished achievement in the field of ceramics."
Christopher Bowen (Advisors: C. Randall & R.E. Newnham)	Penn State University	Corning Foundation 1995-96 Science Fellowship Program
Aydin Dogan (Advisor: R.E. Newnham)	Penn State University	19th Annual Xerox Awards in Materials Research Award Winner

10.0 APPRENTICE PROGRAM

The objective of the ONR Apprentice Program was to provide the opportunity for minority graduating seniors to spend time in a major University Laboratory over their summer break. It was hoped that experiencing the excitement of the Research Program, the expertise of the faculty and interactions with a group of internationally respected visiting faculties in Intercollege Materials

Research Laboratory (IMRL) would motivate these young people to take up careers in Science and Engineering. The program has now been in place for sixteen years and has helped in the education of 42 graduating seniors. Because of the diverse backgrounds it is difficult to maintain continuing contact, but we know of at least two who have completed graduate school (PhD), one who is highly successful in business for himself, and several now in industrial research laboratories.

This summer we had two graduating high school seniors complete the program — Jamé Shields and Eureka Armstrong.

Jamé Shields is from Washington, DC and was referred to us by the Penn State University Upward Bound Math and Science Program. Ms. Shields participated in Upward Bound Math and Science the past three summers and was delighted to have an opportunity to work in a research facility this summer. Ms. Shields worked on several ONR projects gaining laboratory skills that she perceived to be relevant to her future plans. She will be attending The Tuskegee Institute, Tuskegee, Alabama, majoring in veterinary science.

Eureka Armstrong is from Philadelphia, Pennsylvania and joined IMRL as part of the Pre-Freshman Engineering and Science Program offered through the Eberly College of Science. Ms. Armstrong performed a number of lab duties in addition to conducting library literature searches. She realized that learning to do library searches this summer would benefit her not only in her freshman year at college but throughout her life. Ms. Armstrong is attending The Pennsylvania State University, University Park, Pennsylvania, majoring in biology. She plans to become a pediatrician.

Both young women indicated they had a positive experience and could relate the research conducted at IMRL to their career paths. Ms. Shields response to her summer employment was, "It is an experience I won't soon forget." Ms. Armstrong assessment was, "I feel IMRL and its staff have given me a great learning experience I shall truly cherish."

11.0 PAPERS PUBLISHED IN REFEREED JOURNALS

1. Cross, L.E., "Ferroelectric Materials for Electromechanical Transducer Applications," *Jpn. J. Appl. Phys.* **34**, 2525-2532 (1995).
2. Trolier-McKinstry, S., J. Chen, K. Vedam and R.E. Newnham, "In Situ Annealing Studies of Sol-Gel Ferroelectric Thin Films by Spectroscopic Ellipsometry," *J. Am. Ceram. Soc.* **78** [7], 1907-1913 (1995).
3. Gentile, A., F.W. Ainger, "Single Crystals," Chapter 9, *Materials Science and Technology, A Comprehensive Treatment*, **17A** Processing of Ceramics, Part 1 (R.J. Brook, editor), VCH Verlagsgesellschaft mbH, Weinheim, Fed. Repl. of Germany (1996).

11.0 PAPERS PUBLISHED IN REFEREED JOURNALS (continued)

4. Kim, Y.J., S.W. Choi and A.S. Bhalla, "Dielectric, Pyroelectric Properties, and Morphotropic Phase Boundary in La-doped $(1-x)\text{Pb}(\text{Mg}_{1/3}\text{Ta}_{2/3})_x\text{PbTiO}_3$ Solid Solution Ceramics," *Ferroelectrics* **173**, 87-96 (1995).
5. Zhang, Q.M., H. You, M.L. Mulvihill and S.J. Jang, "An X-ray Diffraction Study of Superlattice Ordering in Lead Magnesium Niobate," *Solid State Comm.* **97** [8], 693-698 (1996).
6. Zhang, Q.M., J. Zhao and L.E. Cross, "Aging of the Dielectric and Piezoelectric Properties of Relaxor Ferroelectric Lead Magnesium Niobate-Lead Titanate in the Electric Field Biased State," *J. Appl. Phys.* **79** (6), 1-7 (1996).
7. Zhang, Q.M., J. Zhao, T.R. Shrout, and L.E. Cross, "The Effect of Ferroelastic Coupling in Controlling the Abnormal Aging Behavior in Lead Magnesium Niobate-Lead Titanate Relaxor Ferroelectrics," submitted *J. Mat. Res.* (1995).
8. Mulvihill, M.L., L.E. Cross and K. Uchino, "Low-Temperature Observation of Relaxor Ferroelectric Domains in Lead Zinc Niobate," *J. Am. Ceram Soc.* **78** (12) 3345-3351 (1995).
9. Mulvihill, M.L., K. Uchino, Z. Li, and Wenwu Cao, "In-Situ Observation of the Domain Configurations During the Phase Transitions in Barium Titanate," accepted *Phil. Mag. B* (1995).
10. Cao, W., "Elastic and Electric Constraints in the Formation of Ferroelectric Comains," *Ferroelectrics*, **172**, 31-37 (1995).
11. Cao, W. and C.A. Randall, "The Grain Size and Domain Size Relations in Bulk Ceramic Ferroelectric Materials," accepted *J. Phys. Chem. Solids* (1995).
12. Cao, W., "Defect Stabilized Periodic Amplitude Modulations in Ferroelectrics," accepted *Phase Transitions* (1995).
13. Sopko, J., A. Bhalla, and L.E. Cross, "An Improved Quantitative Method for Determining Dynamic Current Response of Pyroelectric Materials," *Ferroelectrics*, **173**, 139-152 (1995).
14. Koc, B., A. Dogan, J.F. Fernandez, R.E. Newnham, and K. Uchino, "Accelerometer Application of the Modified Moonie (Cymbal) Transducer," submitted *Jpn. J. Appl. Phys.* (1995).
15. Zhao, J., Q.M. Zhang, and W. Cao, "Effects of Face Plates and Edge Strips on Hydrostatic Piezoelectric Response of 1-3 Composites," *Ferroelectrics*, **173**, 243-256 (1995).
16. Wang, H., Q.M. Zhang, and L.E. Cross, "Tailoring Material Properties by Structure Design--Radially Poled Piezoelectric Cylindrical Tube," *Ferroelectrics Lett.* (in press).
17. Geng, X. and Q.M. Zhang, "Dynamic Behavior of Periodic Piezoceramic-Polymer Composite Plates," *Appl. Phys. Lett.* **67** (21) (1995).

11.0 PAPERS PUBLISHED IN REFEREED JOURNALS (*continued*)

18. Zhang, Q.M., H. Wang, J. Zhao, J.T. Fielding, Jr., R.E. Newnham, and L.E. Cross, "A High Sensitivity Hydrostatic Piezoelectric Transducer Based on Transverse Piezoelectric Mode Honeycomb Ceramic Composites," *IEEE Transactions on Ultrasonics, Ferroelectrics and Frequency Control*, **43** (1), 26-42 (1996).
19. Zhang, Q.M., J. Chen, H. Wang, J. Zhao, L.E. Cross and M.C. Trottier, "A New Transverse Piezoelectric Mode 2-2 Piezocomposite for Underwater Transducer Applications," *IEEE Transactions on Ultrasonics, Ferroelectrics, and Frequency Control*, **42** (4), 774-780 (1995).
20. Cao, W., Q.M. Zhang, J.Z. Zhao, and L.E. Cross, "Effects of Face Plates on Surface Displacement Profile in 2-2 Piezoelectric Composites," *IEEE Transactions on Ultrasonics, Ferroelectrics, and Frequency Control*, **42** (1), 37-41 (1995).
21. Cao, W. and W. Qi, "Plane Wave Propagation in Finite 2-2 Composites," *J. Appl. Phys.* **78** (7), 4627-4632 (1995).
22. Qi, W. and W. Cao, "Finite Element Analysis and Experimental Studies on the Thickness Resonance of Piezocomposite Transducers", accepted *Ultrasonic Imaging* (1995).
23. Cao, W. and W. Qi, "Multisource Excitations in a Stratified Biphase Structure," *J. Appl. Phys.* **78** (7), 4640-4646 (1995).
24. Uchino, K., "Materials Update: Advances in Ceramic Actuator Materials," *Materials Lett.* **22**, 1-4 (1995).
25. Uchino, K. "Manufacturing Technology of Multilayered Transducers," *Manufacture of Ceramic Components, Proc. Amer. Ceram. Soc.*, Manufacture of Ceramic Components, 81-93 (1995).
26. Dogan, A., J.F. Fernandez, K. Uchino, and R.E. Newnham, "New Piezoelectric Composite Actuator Designs for Displacement Amplification," in press, *Proc. Euroceram 95* (1995).
27. Onitsuka, O., A. Dogan, J.F. Tressler, Q.Su S. Yoshikawa, and R.E. Newnham, "Metal-Ceramic Composite Transducer, The "Moonie" ", *J. Intelligent Materials Systems and Structures* **6**, 447-455 (1995).
28. Hirose, S., S. Takahashi, K. Uchino, M. Aoyagi, and Y. Tomikawa, "Measuring Methods for High-Power Characteristics of Piezoelectric Materials," *Mat. Res. Soc. Symp. Proc.*, **360**, 15-20 (1995).
29. Zheng, Jiehui, Sadayuki Takahashi, Shoko Yoshikawa, Kenji Uchino, and J.W.C. de Vries, "Heat Generation in Multilayer Piezoelectric Actuators," submitted to *J. Am. Ceram. Soc.* (1995).
30. Uchino, Kenji, "Review: Photostriction and its Applications," in press, *J. Innovations in Mater. Res.* (1995).

11.0 PAPERS PUBLISHED IN REFEREED JOURNALS (continued)

31. Matsko, M.G., Q.C. Xu and R.E. Newnham, "Zig-Zag Piezoelectric Actuators: Geometrical Control of Displacement and Resonance," *J. Intell. Mat. Syst. and Struct.* **6** (6), 783-786 (1995).
32. Elissalde, Catherine and Leslie Eric Cross, "Dynamic Characteristics of Rainbow Ceramics," *J. Am. Ceram. Soc.* **78** [8], 2233-2236 (1995).
33. Bowen, Christopher P., Thomas R. Shrout, Robert E. Newnham and Clive A. Randall, "Tunable Electric Field Processing of Composite Materials," *J. of Intelligent Material Systems and Structures* **6** (2), 159-168 (1995).
34. Zhang, Q.M., J. Zhao, T. Shrout, N. Kim, and L.E. Cross, "Characteristics of the Electromechanical Response and Polarization of Electric Field Biased Ferroelectrics", *J. Appl. Phys.* **77** (5), 2549-2555 (1995).
35. Zhao, J., Q.M. Zhang, N. Kim and T. Shrout, "Electromechanical Properties of Relaxor Ferroelectric Lead Magnesium Niobate-Lead Titanate Ceramics," *Jpn. J. Appl. Phys.* **34**, 5658-5663 (1995).
36. Yoshikawa, Shoko, Ulagaraj Selvaraj, Paul Moses, John Witham, Richard Meyer and Thomas Shrout, "Pb(Zr,Ti)O₃[PZT] Fibers—Fabrication and Measurement Methods", *J. Intell. Mat. Syst. and Struct.* **6** (2), 152-158 (1995).
37. Cann, David P., Clive A. Randall, and Thomas R. Shrout, "Investigation of the Dielectric Properties of Bismuth Pyrochlores," accepted *Solid State Communication* (1995).
38. Chen, H.D., K.R. Udayakumar, L.E. Cross, J.J. Bernstein, and L.C. Niles, "Dielectric, Ferroelectric, and Piezoelectric Properties of Lead Zirconate Titanate Thick Films on Silicon Substrates", *J. Appl. Phys.* **77** (7), 3349-3353 (1995).
39. Udayakumar, K.R., P.J. Schuele, J. Chen, S.B. Krupanidhi, and L.E. Cross, "Thickness-Dependent Electrical Characteristics of Lead Zirconate Titanate Thin Films," *J. Appl. Phys.* **77** (8), 3981-3986 (1995).
40. Chen, H.D., K.R. Udayakumar, C.J. Gaskey, and L.E. Cross, "Electrical Properties' Maxima in Thin Films of the Lead Zirconate-Lead Titanate Solid Solution System", *Appl. Phys. Lett.* **67** (23), 3411-3413 (1995).
41. Gaskey, C.J., K.R. Udayakumar, H.D. Chen, and L.E. Cross, " 'Square' Hysteresis Loops in Phase-Switching Nb-Doped Lead Zirconate Stannate Titanate Thin Films," *J. Mater. Res.* **10** (11), 2764-2769 (1995).
42. Yamakawa, K., S. Trolier-McKinstry, J.P. Dougherty, and S. Krupanidhi, "Reactive Magnetron Co-Sputtered Antiferroelectric Lead Zirconate Thin Films," *Appl. Phys. Lett.* **67** (14), 2014-2016 (1995).
43. Guo, R., S.A. Markgraf, Y. Furukawa, M. Sato, and A.S. Bhalla, "Pyroelectric Dielectric and Piezoelectric Properties of LiB₃O₅", *J. Appl. Phys.* **78** (12), 7234-7239 (1995).

12.0 INVITED PAPERS PRESENTATIONS AT NATIONAL AND INTERNATIONAL MEETINGS

1. Newnham, R.E., "Ceramic Engineering in the 21st Century: Scaling Up and Scaling Down," Danish Ceramic Society Meeting, Danish Technical University, Copenhagen, Denmark (February 20, 1995).
2. Newnham, R.E., "Smart Ceramics," Berzelius Memorial Lecture, Swedish Chemical Society Meeting, Stockholm, Sweden (February 24, 1995)
3. Randall, C.A., C.P. Bowen, T.R. Shrout, and R.E. Newnham, "Electric Field Processing of Electroceramic Composite Materials," Symposium M-Electromechanical Phenomena in Complex Fluids, Materials Research Society Meeting, San Francisco, CA (April 18, 1995).
4. Newnham, R.E., "Piezoelectric Composites with Open Spaces," IV European Ceramic Society Conference, Madrid, Spain (June 22-23, 1995).
5. Newnham, R.E., "Structure-Property Relationships in Sensors and Actuators," American Crystallographic Association Annual Meeting, Montreal, Quebec (July 23-28, 1995).
6. Newnham, R.E., "Composite Electroceramics: Sensors, Actuators, and Transducers," 50th Annual Ceramic Forum of the Pennsylvania Ceramics Association, Penn State University, PA (September 29, 1995)
7. Newnham, R.E., "Composite Electroceramic Sensors and Actuators," 47th Pacific Coast Regional Meeting of the American Ceramic Society, Seattle, WA (November 1-3, 1995).
8. Newnham, R.E., J. Fielding, M. McNeal, and V. Sundar, "Size Effects in Ferroic Materials," 47th Pacific Coast Regional Meeting of the American Ceramic Society, Seattle, WA (November 1-3, 1995).
9. Tressler, J.F., A. Dogan, J.F. Fernandez, J.T. Fielding, Jr., K. Uchino, and R.E. Newnham, "Capped Ceramic Hydrophones," 1995 IEEE International Ultrasonics Symposium, Seattle, WA (November 7-10, 1995).
10. Newnham, R.E., "Composites, Sensors, Actuators and Transducers," Symposium on Mathematical Methods in Materials Science, Minneapolis, MN (November 13-17, 1995).
11. Newnham, R.E., "Ferroic Sensors and Actuators," Committee on Advanced Materials and Fabrication Methods for Microelectromechanical Systems, National Academy of Sciences, Washington, DC (December 11-12, 1995).
12. Uchino, K., "New Piezoelectric Devices for Smart Actuator/Sensor Systems," The 4th ASEAN Sci. & Tech. Week, Bangkok, Thailand (August 21-September 1, 1995).
13. Uchino, K., "Piezoelectric Sensors and Actuators: Overview," Sensors Expo '95, Chicago, IL (September 12-14, 1995).
14. Takahashi, S., S. Hirose, and K. Uchino, "Materials for Piezoelectric Actuators," Mtg. Ferroelectric Mater. and Appl. (1995).
15. Uchino, K., "Ceramic Materials," Sponsored by National Metal and Materials Technology Center, Thailand (March 6-7, 1995).

12.0 INVITED PAPERS PRESENTATIONS AT NATIONAL AND INTERNATIONAL MEETINGS *(continued)*

16. Uchino, K., "Introduction of Ceramic Actuators," Sponsored by National Metal and Materials Technology Center, National Science and Technology Development Agency, Thailand (August 31-September 2, 1995).
17. Cao, Wenwu and Clive Randall, "Theoretical and Transmission Electron Microscopy Studies on Domain Structures in Ferroelectrics," The Third Williamsburg Workshop on Fundamental Experiments in Ferroelectrics (MIT/ONR), Williamsburg, Virginia (Feb. 1995).
18. Cao, Wenwu, "Computer Simulation on Domain Structures and Their Formation Kinetics in Ferroelectrics," 1995 ONR Transducer Materials and Transducer Workshop, The Pennsylvania State University (April 4-6, 1995).
19. Cao, Wenwu, "Modeling Methods in Ultrasonic Transducer Design," Ultrasonic Transducer Engineering Workshop, The Pennsylvania State University (August 16-18, 1995).
20. Bhalla, A.S., "Ferroelectric Single Crystal Fibers," American Ceramic Society Meeting, Cincinnati, Ohio (April 1995).
21. Bhalla, A.S., "Ferroelectric-Electrooptic Materials," Air Force/Army Workshop on Photorefractive Materials," Dayton, Ohio (August 1995).
22. Bhalla, A.S., "Relaxor Ferroelectrics," 1st Asian Ferroelectric Society Meeting, Xian, China (October 1995).
23. Bhalla, A.S., "PIN:PST System," Toyama University, Toyama, Japan (November 1995).
24. Cross, L.E., "Transducer Studies in IMRL: Overview," ONR Transducer and Transducer Materials Workshop, Penn State University, PA (April 4-6, 1995).
25. Cross, L.E., "Sensors and MEMS," DOD Senior Technologists Meeting, Washington, DC (May 23-24, 1995).
26. Cross, L.E., "Low Acoustic: Low Electrical Impedance High Strain Composite Actuators," ICCE2, New Orleans (August 21-24, 1995).
27. Cross, L.E., "New Questions Concerning Phase Switching Actuators," 3rd UK Transducer Workshop, Malvern, United Kingdom (August 31-September 1, 1995).
28. Cross, L.E., "Problems and Opportunities in Actuator Material Systems," ASME Design Engineering Technical Conference, Boston, MA (September 17-21, 1995).
29. Cross, L.E., "Materials Issues in Underwater Acoustics," ASME Design Engineering Technical Conference, Boston, MA (September 17-21, 1995).
30. Cross, L.E., "Materials for Adaptive Structural Control," ONR Workshop on Adaptive Quiet Structures," Naval Research Laboratory, Washington, DC (September 27-29, 1995).
31. Cross, L.E., "Active Control of Radiated Sound with Integrated Piezoelectric Composite Structure," Naval Research Laboratory, Washington, DC (September 27-29, 1995).

12.0 INVITED PAPERS PRESENTATIONS AT NATIONAL AND INTERNATIONAL MEETINGS *(continued)*

32. Cross, L.E., "Current Status on Transducer Material Studies in USA," First Asian Meeting on Ferroelectrics (AMF I), Xian, China (October 5-8, 1995).
33. Cross, L.E., "Amplified Piezoelectric Actuation for Air Acoustic Applications," Seventh US:Japan Seminar on Dielectric and Piezoelectric Ceramics, Tsukuba, Japan (November 15-17, 1995).

13.0 INVITED PAPERS PRESENTED AT UNIVERSITY, INDUSTRY AND GOVERNMENT LABORATORIES

1. Newnham, R.E., "Ceramic Engineering in the 21st Century: Scaling Up and Scaling Down," Center for Dielectric Studies Meeting (April 11-12, 1995).
2. Newnham, R.E., "Size Effects in Ferroics," International Center for Transducers and Actuators 13th Actuator Symposium, Penn State University, PA (April 18, 1995).
3. Newnham, R.E., "Smart Electroceramics," Inorganic Chemistry Dept., University of Uppsala, Sweden (February 22, 1995).
4. Newnham, R.E., "Piezoelectric Sensors and Actuators," Arrhenius Laboratory Seminar, University of Stockholm, Sweden (February 23, 1995).
5. Newnham, R.E., "Structure-Property Relationships in Sensors and Actuators," Acoustics Seminar, Applied Research Laboratory, Penn State University, PA (March 14, 1995).
6. Newnham, R.E., "Size Effects in Ferroic Solids," Office of Naval Research Meeting, Penn State University, PA (April 6, 1995).
7. Newnham, R.E., "Ceramic Engineering in the 21st Century," Center for Dielectric Studies Annual Meeting, Penn State University, PA (April 11, 1995).
8. Newnham, R.E., "Smart Ceramics," Spring Quarter Colloquium speech, Materials Science and Engineering Department, The Ohio State University, Columbus, Ohio (April 21, 1995).
9. Newnham, R.E., "Smart Composites," Robert B. Pond, Sr. Distinguished Materials Science Lecture at The John Hopkins University, Baltimore, Maryland (April 25, 1995).
10. Newnham, R.E., "Ceramic Engineering in the Twenty-First Century," Seminar at the Westinghouse Science and Technology Center (STC), Pittsburgh, PA (May 18, 1995).
11. Newnham, R.E., "Ceramic Engineering in the 21st Century," Award recipient of the Albert Victor Bleining Award Ceremony, American Ceramic Society, Pittsburgh, PA (May 19, 1995).
12. Newnham, R.E., "Ceramic Engineering in the 21st Century," Seminar at Middle East Technical University, Ankara, Turkey (May 25-26, 1995).
13. Newnham, R.E., "Smart Ceramics," Seminar at Middle East Technical University, Ankara, Turkey (May 25-26, 1995).

13.0 INVITED PAPERS PRESENTED AT UNIVERSITY, INDUSTRY AND GOVERNMENT LABORATORIES *(continued)*

14. Newnham, R.E., "Integrated Ceramics," Seminar at Middle East Technical University, Ankara, Turkey (May 25-26, 1995).
15. Newnham, R.E., "Structure-Property Relations in Ceramic Sensors and Actuator," Seminar at Middle East Technical University, Ankara, Turkey (May 25-26, 1995).
16. Newnham, R.E., "Smart Ceramics," Seminar at Daimler-Benz Aerospace (Dornier) Laboratory, Friedrichshafen, Germany (June 21, 1995).
17. Newnham, R.E., "Ceramic Sensors and Actuators," Fraunhofer Institute for Ceramics, Dresden, Germany (June 26, 1995).
18. Newnham, R.E., "Structure-Property Relations in Electroceramics," Seminar at Daimler-Benz Ceramic Research Laboratory, Ulm, Germany (June 30, 1995).
19. Newnham, R.E., "The Crystal Chemistry of Smart Materials," "Chemistry Colloquium, Davey Laboratory, Penn State University, PA (September 12, 1995).
20. Newnham, R.E., "Materials for Adaptive Structural Control-Sensor Development-URI," ONR Workshop on Adaptive Quiet Structures with Active Materials, Naval Research Laboratory, Washington, DC (September 27-29, 1995).
21. Newnham, R.E., "Smart Materials," Aerospace Engineering Department Seminar, Penn State University, PA (October 13, 1995).
22. Newnham, R.E., "Electroceramic Structure-Property Relationships," Philips Components, Roermond, The Netherlands (January 20-27, 1996).
23. Cross, L.E., "Piezoelectric Sensors and Actuators," Allied Signal Laboratories (October 24, 1995).
24. Uchino, K., "Recent Development of Piezoelectric Actuators," Omron Corp., Sakura, Japan (September 1995).
25. Uchino, K., "Reliability of Ceramic Actuators," Chichibu-Onoda Cement, Tsukuba, Japan (November 1995).
26. Uchino, K., "Piezoelectric Actuators," Gillet, Boston, MA (November 1995).
27. Uchino, K., "Ultrasonic Motors," Delphi-E, Rochester, NY (January 1996).

14.0 CONTRIBUTED PAPERS AT NATIONAL AND INTERNATIONAL MEETINGS

1. Newnham, R.E., A. Dogan, J. Fielding, J.F. Fernandez, D. Smith, J. Tressler, J. Wallis, K. Uchino, and W. Zhu, "Moonies, Cymbals and Bbs," Office of Naval Research Workshop, Penn State University, PA (April 4-6, 1995).

14.0 CONTRIBUTED PAPERS AT NATIONAL AND INTERNATIONAL MEETINGS *(continued)*

2. Zhang, Q.M., H. Wang, J. Fielding, R.E. Newnham, and L.E. Cross, "Piezoelectric Mode Piezoceramic Polymer Composites with High Hydrostatic Piezoelectric Responses," Office of Naval Research Workshop, Penn State University, PA (April 4-6, 1995).
3. Tressler, J.F., K. Uchino, and R.E. Newnham, "Ceramic-Metal Composite Transducers for Hydrophone Applications," Office of Naval Research Workshop, Penn State University, PA (April 4-6, 1995).
4. Dogan, A., J. Fernandez, K. Uchino, and R.E. Newnham, "The Effect of Design on the Characteristics of the 'Moonie and Cymbal' Actuators," Office of Naval Research Workshop, Penn State University, PA (April 4-6, 1995).
5. Fernandez, J., A. Dogan, J.T. Fielding, K. Uchino, and R.E. Newnham, "The Effect of Materials on the Performance of 'Cymbal' Actuators," Office of Naval Research Workshop, Penn State University, PA (April 4-6, 1995).
6. Sundar, V. and R.E. Newnham, "Nonlinear Electromechanical Coupling in Perovskite Glass Ceramics and Ferroic Materials with Diffuse Phase Transitions," American Ceramic Society Meeting, Cincinnati, OH (April 30-May 3, 1995).
7. Fielding, J.T., Jr, M.P. McNeal, S.J. Jang, and R.E. Newnham, "High Frequency Dielectric Properties in $\text{Pb}(\text{Sc}_{1/2}\text{Ta}_{1/2})$ and $\text{Pb}(\text{Sc}_{1/2}\text{Nb}_{1/2})\text{O}_3$ Relaxor Ferroelectrics," American Ceramic Society Meeting, Cincinnati, OH (April 30-May 3, 1995).
8. Gaskey, C.J., K.R. Udayakumar, H.D. Chen, L.E. Cross, and R.E. Newnham, "Effects of Size and Composition on Transport Properties and Breakdown Strength in Antiferroelectric Thin Films," American Ceramic Society Meeting, Cincinnati, OH (April 30-May 3, 1995).
9. Fernandez, J.F., A. Dogan, J. Tressler, J.T. Fielding, K. Uchino, and R.E. Newnham, "Temperature Dependence of High Displacement Ceramic-Metal Composite Actuators," American Ceramic Society Meeting, Cincinnati, OH (April 30-May 3, 1995).
10. Fernandez, J.F., A. Dogan, and R.E. Newnham, "Piezoelectric Composites with Open Spaces," IV European Ceramic Society Conference, Italy (June 22-23, 1995).
11. Fernandez, J.F., A. Dogan, and R.E. Newnham, "Temperature Dependence of New Design Ceramic-Metal Composite," IV European Ceramic Society Conference, Italy (June 22-23, 1995).
12. Dogan, A., J.F. Fernandez, K. Uchino, and R.E. Newnham, "Flexensional Ceramic-Metal Composite Transducers 'Moonie and Cymbal'," IV European Ceramic Society Conference, Italy (June 22-23, 1995).
13. Fielding, J.T., Jr., J.F. Fernandez, A. Dogan, K. Uchino, and R.E. Newnham, "Characterization of Ceramic-Metal Composite Transducer with Multilayer Piezoceramic Element," Amer. Ceram. Soc. 97th Annual Mtg., E-8, Cincinnati, Ohio (April 30-May 3, 1995).

14.0 CONTRIBUTED PAPERS AT NATIONAL AND INTERNATIONAL MEETINGS (continued)

14. Zheng, J., S. Takashishi, S. Yoshikawa, K. Uchino, and J.W.C. de Vries, "Heat Generation in Multilayer Piezoelectric Actuators," Amer. Ceram. Soc. 97th Annual Mtg., E-14, Cincinnati, Ohio (April 30-May 3, 1995).
15. Aburatani, H. and K. Uchino, "New Internal Electrode Designs for Multilayer Ceramic Actuators," Amer. Ceram. Soc. 97th Annual Mtg., EP-46, Cincinnati, Ohio (April 30-May 3, 1995).
16. Joshi, A., S. Hirose, S. Takahashi, and K. Uchino, "High Power Characteristics of Piezoelectric Materials," Amer. Ceram. Soc. 97th Annual Mtg., EP-47, Cincinnati, Ohio, (April 30-May 3, 1995).
17. Tressler, J.F., K. Uchino, and R.E. Newnham, "Ceramic-Metal Composite Transducers for Hydrophone Applications," Amer. Ceram. Soc. 97th Annual Mtg., EP-49, Cincinnati, Ohio (April 30-May 3, 1995).
18. Song, S.R. and K. Uchino, "Semiconductive Behavior in the $(1-x)\text{Pb}(\text{Zr}_{0.9}\text{Ti}_{0.1}\text{O}_3-x(\text{K}_{0.5}\text{Bi}_{0.5})\text{ZrO}_3$ Monomorph Materials," Amer. Ceram. Soc. 97th Annual Mtg., E-65, Cincinnati, Ohio (April 30-May 3, 1995).
19. Mulvihill, M., L.E. Cross, and K. Uchino, "Dynamic Motion of the Domain Configuration in Relaxor Ferroelectric Single Crystals as a Function of Temperature and Electric Field," The 8th European Mtg. Ferroelectricity, P16-08, Nijmegen (July 1995).
20. Hirose, S., M. Aoyagi, Y. Tomikawa, S. Takashi, and K. Uchino, "High-Power Characteristics at Antiresonance Frequency of Piezoelectric Transducers," Ultrasonic Int'l, Edinburgh (July 4-7, 1995).
21. Uchino, K., "Remaining Theoretical Problems in Ceramic Actuators," ONR Workshop on Fundamental Ferroelectrics, Williamsburg, VA (February 5-8, 1995).
22. Mulvihill, M.L., L.E. Cross, and K. Uchino, "Domain Motion in Normal and Relaxor Ferroelectric Single Crystals Under Applied Temperature and Electric Field," 13th Smart Actuator Symp., State College, PA (April 1995).
23. Uchino, K., "Photostrictive Actuators and their Applications," 4th Japan Int'l SAMPE Symp. & Exhibition, Tokyo, Japan (September 25-28, 1995).
24. Mulvihill, M.L., L.E. Cross, and K. Uchino, "Dynamic Motion of the Domain Configuration in Relaxor Ferroelectric Single Crystals as a Function of Temperature and Electric Field," 7th US-Japan Seminar on Dielectric and Piezoelectric Ceramics, V-18, Tsukuba, Japan (November 14-17, 1995).
25. Dogan, A., K. Uchino, and R.E. Newnham, "Unique Flexensional Composite Transducer Designs for Both Sensor and Actuator Applications," 1st US-Japan Workshop on Smart Materials and Structures, Seattle, Washington (December 4-5, 1995).
26. Tressler, J.F., A. Dogan, J.F. Fernandez, J.T. Fielding, Jr., K. Uchino, and R.E. Newnham, "Capped Ceramic Hydrophones," IEEE Int'l Ultrasonics Symp., Seattle, Washington (1995).

14.0 CONTRIBUTED PAPERS AT NATIONAL AND INTERNATIONAL MEETINGS (continued)

27. Jin, B.M., R. Guo, and A.S. Bhalla, "Piezoelectric Properties and Equivalent Circuits of Ferroelectric Relaxor Single Crystals," American Ceramic Society Annual Meeting, Cincinnati, Ohio (May 1-3, 1995).
28. Guo, R., B.M. Jin, and A.S. Bhalla, "Temperature Dependent Electro-optic Properties of Ferroelectric Tungsten Bronze $Pb_xBa_{1-x}Nb_2O_6$ Single Crystals," American Ceramic Society Annual Meeting, Cincinnati, Ohio (May 1-3, 1995).
29. Guo, R., "Polarization Fluctuation Phenomena in Tungsten Bronze Ferroelectric Materials," American Ceramic Society Annual Meeting, Cincinnati, Ohio (May 1-3, 1995).
30. Guo, R., S.A. Markgraf, Y. Furukawa, M. Sato, and A.S. Bhalla, "Dielectric, Piezoelectric and Related Tensor Properties of LiB_3O_5 Crystals," First Asian Meeting on Ferroelectrics, Xi'an, China (October 4-8, 1995).
31. Jin, B.M., R. Guo, and A.S. Bhalla, "Piezoelectric Properties and Equivalent Circuits of Ferroelectric Relaxor Single Crystals," First Asian Meeting on Ferroelectric, Xi'an, China (October 4-8, 1995).
32. Jin, B.M., I.W. Kim, R. Guo, and A.S. Bhalla, "UV-VIS and IR Optical Absorption Properties Changes Caused by MgO Incorporation in $LiNbO_3$ Crystals," First Asian Meeting on Ferroelectrics, Xi'an, China (October 4-8, 1995).

15.0 BOOKS (AND SECTIONS THEREOF)

1. Uchino, K., *Encyclopedia of Advanced Materials*, Edit. D. Bloor et al. (Partial Charge: Ceramic Actuators), Pergamon, UK (1994).
2. Uchino, K., *New Actuator Handbook for Precision Control*, Editor in Chief and Partial Author (Introduction, Piezoelectric and Electrostrictive Effects, Shape Memory Ceramics, Photostrictive Actuators, etc.), Fuji Techosystem, Tokyo (1994).
3. Troiler-McKinstry, S., K. Vedam, N. Chindaudom, and R.E. Newnham, Characterization of Ferroelectric Thin Films by Spectroscopic Ellipsometry, Chapter in *Optical Characterization of Real Surfaces and Films*, K. Vedam, Editor; (Vol. 19 of Physics of Thin Films), pp. 249-278, Academic Press, NY (1994).
4. Cross, L.E., Ceramic Capacitor Technology, Chapter in *Handbook of Solid State Batteries and Capacitors*, Editor M.Z.A. Munshi, World Scientific (1995).
5. Pandey, R.K. and Ruyan Guo, Current Issues on Crystal Growth of Novel Electronic Materials, *Ceramic Transactions*, Vol. 60, American Ceramic Society, Westerville, Ohio (1995).

**MATERIALS FOR ADAPTIVE STRUCTURAL
ACOUSTIC CONTROL**

Period February 1, 1995 to January 31, 1996

Annual Report

VOLUME I

OFFICE OF NAVAL RESEARCH

Contract No.: N00014-92-J-1510

APPROVED FOR PUBLIC RELEASE — DISTRIBUTION UNLIMITED

Reproduction in whole or in part is permitted
for any purpose of the United States Government

L. Eric Cross

PENNSSTATE



THE MATERIALS RESEARCH LABORATORY
UNIVERSITY PARK, PA

**GENERAL
SUMMARY
PAPERS**

APPENDIX 1

Ferroelectric Materials for Electromechanical Transducer Applications

Leslie Eric CROSS

Intercollege Materials Research Laboratory, The Pennsylvania State University, University Park, PA 16802, USA

(Received November 30, 1994; accepted for publication March 18, 1995)

Many advantages of ferroelectric compositions in the lead zirconate:lead titanate (PZT) solid solutions for both sensing and actuation are explored. The state of understanding of both intrinsic single domain and extrinsic domain wall and phase boundary contribution to response is described, and the composition manipulations used to modify the extrinsic responses explored. In lead magnesium niobate (PMN) based solid solution a nanometer scale ordering of Mg:Nb cations breaks up the conventional ferroelectric coupling leading to glass like relaxor ferroelectric response. The fact that problems arising from density and rigidity of PZT for large area transducers are markedly worked out in piezoceramic:polymer composites is also briefly explored.

KEYWORDS: ferroelectric materials, electromechanical transducer, lead zirconate:lead titanate (PZT), lead magnesium niobate (PMN), electrostrictive relaxor, piezoceramic compositions

1. Introduction

Interest in electromechanical transduction has recently increased markedly with the realization of the possibility to use electro-active sensors and actuators, coupled through sophisticated solid state electronics, to modify and control the mechanical behavior of complex materials and structures. The phenomenon of piezoelectricity is exciting in this context as the converse effect gives direct conversion of electric field into elastic strain (shape change) for the actuation function and the direct effect permits conversion of elastic stress into electrical polarization (electric field) for the sensing function. For a randomly axed ceramic polycrystal the spherical texture symmetry forbids piezoelectricity irrespective of the symmetry of the ceramic grain, however in some ferroelectric ceramics, the reorientable domain structure permits the induction of a macroscopic polar axis, reducing the symmetry to conical and producing very strong piezoelectric response.

This review talk will explore the many advantages of ferroelectric compositions in the lead zirconate:lead titanate (PZT) solid solutions for both sensing and actuation. The state of understanding of both intrinsic single domain and extrinsic domain wall and phase boundary contributions to response will be examined, and the composition manipulations used to modify the extrinsic responses explored. In lead magnesium niobate (PMN) based solid solutions a nanometer scale ordering of Mg:Nb cations breaks up the conventional ferroelectric coupling leading to glass like relaxor ferroelectric response.

The absence of stable macro domains in certain composition:temperature regions leads to highly reproducible electrostriction properties. The performance will be compared and contrasted to the more conventional PZTs.

For large area transducers, the density and rigidity of PZT gives problems and the manner in which this may be addressed and at the same time properties markedly improved in piezoceramic:polymer composites will be briefly explored.

2. Material Considerations

For an insulating crystal the piezoelectric and electrostrictive responses may be completely defined by a simple tensor equation

$$x_{ij} = s_{ijkl}X_{kl} + d_{mij}E_m + M_{mmij}E_mE_n. \quad (1)$$

x_{ij} , X_{kl} are components of elastic strain and elastic stress respectively.

E_mE_n are components of electric field.

S_{ijkl} the conventional elastic compliances in infinitesimal strain.

d_{mij} the piezoelectric tensor components.

M_{mmij} the electrostriction tensor components.

In eq. (1) the Einstein summation convention is assumed so that as $ijklmn$ run from 1-3 a set of nine equations for the components of x_{ij} are generated.

If the crystal symmetry is such that third rank polar tensor components are permitted the crystal is piezoelectric so that when all component of stress are zeros.

$$x_{ij} = d_{mij}E_m \quad (2)$$

describes the actuating function, again mij run from 1-3. Frequently eq. (2) is constructed in matrix form $x_o = d_{mo}E_m$ (3) where now o runs from 1-6, and m from 1-3. From energy consideration one may derive a complementary equation

$$P_m = d_{mij}X_{ij}, \quad (3)$$

which delineates the sensing function.

For higher crystal symmetries (such as centric) where all $d_{mij} \equiv 0$ the strain then depends on the higher order effect

$$x_{ij} = M_{mmij}E_mE_n \quad \text{for all } X_{nkl} \equiv 0, \quad (4)$$

which defines electrostriction and dielectric susceptibility.

$$\eta_{mn} = M_{mmij}X_{ij} \quad (5)$$

defines the converse effect which is the elastic stress dependence of dielectric permittivity. In a single crystal such as quartz, the non zero d_{mij} depend on the symmetry and are well determined material constants.

For a randomly axed polycrystal ceramic, the spheri-

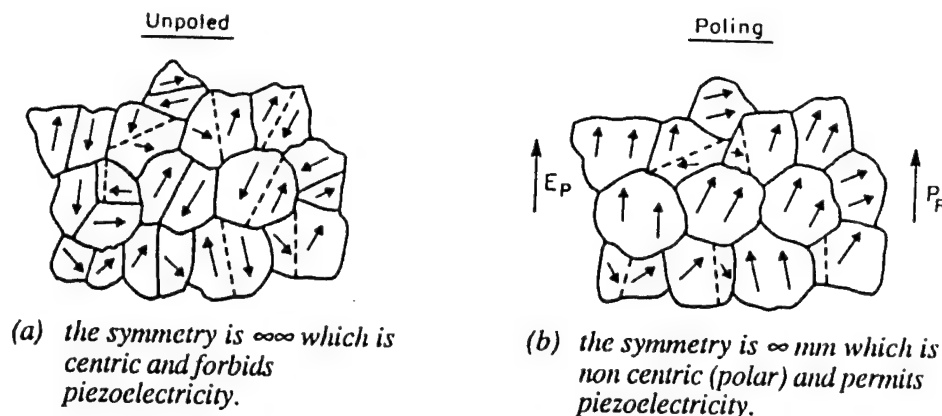


Fig. 1(a). The importance of domain structure in the ferroelectric ceramic to permit poling to a piezoelectrically active state.

cal texture symmetry (Curie group $\infty\infty$) forbids piezoelectricity however in a ferroelectric ceramic domain switching permits the induction of a polar axis which remains remanent after the field is removed lowering the symmetry to Curie group ∞mm which permits non zero piezoelectric d_{33} , $d_{31}=d_{32}$, $d_{24}=d_{15}$ constants [Fig. 1(a)]. The need to pole the electroceramic leads to many important consequences.

(a) For effective poling in a randomly axed structure there is a need for many possible domain orientations so that P_r may thread through making only small angles with the poling E field. Such a requirement favors ferroelectric states from a high symmetry paraelectric prototype hence the popularity of the simple cubic mixed oxide perovskite structure ferroelectrics.

(b) Unlike ferromagnets, the ordering in a ferroelectric domain is "soft" so that the P vector may be sensibly changed in both magnitude and direction by quite realizable E fields. This intrinsic softening becomes strongly enhanced near ferroelectric phase transitions and close to the transition can contribute in a major way to both dielectric and piezoelectric activity.

(c) After poling the ferroelectric ceramic can settle into any one of the very large family of metastable complex domain configurations. Thus the measured property constant $\bar{\epsilon}_{11}$, $\bar{\epsilon}_{33}$, \bar{d}_{33} , \bar{d}_{31} , \bar{d}_{15} , \bar{s}_{11} , \bar{s}_{12} ... are in fact orientational averages which depend in a complex manner on fabrication, grain size, poling conditions etc.

(d) Since the domain structure must be changeable at high electric fields to permit the poling, it is sensible to expect that there may be ancillary (extrinsic) shape change due to reversible domain wall motion and that these extrinsic effects may contribute strongly to dielectric and piezoelectric performance.

3. Advantages of the $\text{PbZrO}_3\text{:PbTiO}_3$ (PZT) System

From the phase diagram of the PZT solid solution system, several advantages for this system are immediately evident [Fig. 1(b)].

(a) Above the Curie temperatures the symmetry is cubic, the structure is perovskite.¹⁾

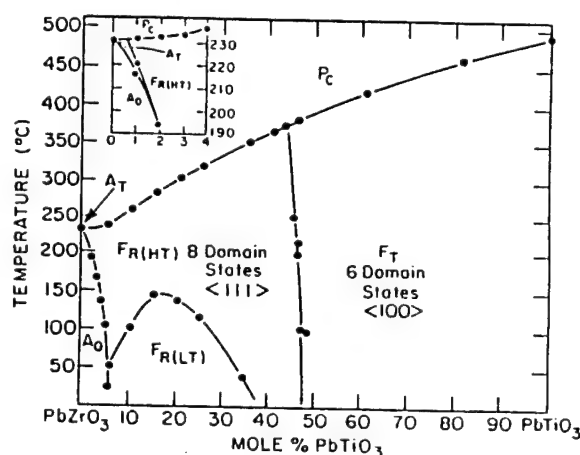


Fig. 1(b). The lead zirconate:lead titanate (PZT) solid solution phase diagram.

(b) The high Curie temperatures across the whole diagram lead to stable ferroelectric states over wide usable temperature ranges.

(c) The morphotropic phase boundary²⁾ separating rhombohedral (8 domain states) and tetragonal (6 domain states) ferroelectric forms is first order so there is necessarily a two phase region near this 52/48 Zr/Ti composition.

(d) In the two phase region the poling field may draw upon 14 orientation states leading to exceptional ceramic polability [Fig. 1(c)].

(e) As the MPB is near vertical on the phase diagram intrinsic property enhancement for compositions chosen near to the boundary persists over a wide temperature range.

PZT compositions have been studied for more than 40 years, and a huge library of empirical data involving a vast range of PZTs and additive and substitutional compositions is available, however some facets of the basic understanding are very fragile. Looking just at the possible polarization changes under electric field

POSSIBLE ORIENTATION STATES IN PEROVSKITES

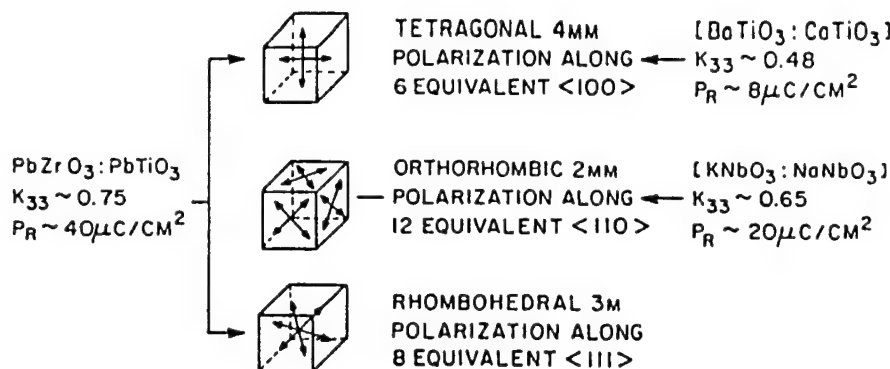
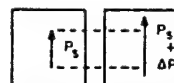


Fig. 1(c). The value of the mixed phase region at the morphotropic phase boundary (MPB) in poling of PZT vs other perovskite ferroelectrics.

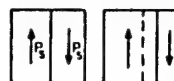
POLARIZATION MECHANISMS IN PIEZOCERAMICS

(A) HIGH FIELD

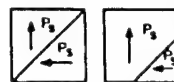
(1) INTRINSIC SINGLE DOMAIN POLARIZABILITY

 α_1 

(2) 180° DOMAIN WALL MOTION

 $\alpha_{D(180)}$ 

(3) FERROELASTIC WALL MOTION

 $\alpha_{D(e)}$ 

(4) FERROELECTRIC PHASE CHANGE

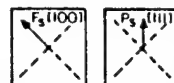
 α_{FE} 

Fig. 2. Possible contributors to the dielectric polarizability in an MPB composition of PZT.

(Fig. 2). Polarization in the domain itself may be changed [Fig. 2(1)], 180° domain walls may move [Fig. 2(2)], non 180° walls which must also be shape changing may move Fig. 2(3) and for MPB compositions, the balance of phases may be changed [Fig. 2(4)] also leading to shape change.

The intrinsic polarizability and associated piezoelectric responses have been difficult to evaluate as there are no good single crystals of the appropriate compositions. However, intensive studies by Haun *et al.*³⁻⁹⁾ have developed a framework of Landau-Ginsburg-Devonshire theory that provides a function which fits well with all aspects of the phase diagram (Fig. 3) and permits evaluation of the intrinsic component of response at any composition or temperature within the phase field.

During the course of many years of empirical development a wide range of low level additives (0-5 mol%)

have been found to have a marked influence upon the extrinsic contributions to dielectric and piezoelectric response.¹⁰⁾ In general, the aliovalent oxides fall into two distinct groups. Electron donors where the charge on the cation is larger than that which it replaces, and electron acceptor additives where the charge on the cation is smaller than that which it replaces. The donor additions enhance both dielectric and piezoelectric response at room temperature and under high fields show symmetric unbiased hysteresis loops with good squareness and lower coercivity (hence the name soft PZTs).^{11,12)} The acceptor additives in general reduce both dielectric and piezoelectric response, give rise to highly asymmetric hysteresis, larger electrical coercivity (hence the name hard PZTs) and much higher mechanical Q . That the dopants effect largely the extrinsic properties may be judged from low temperature measurement of the response for different dopants in

$$\begin{aligned}
\Delta G = & \alpha_1[P_1^2 + P_2^2 + P_3^2] + \alpha_{11}[P_1^4 + P_2^4 + P_3^4] \\
& + \alpha_{12}[P_1^2 P_2^2 + P_2^2 P_3^2 + P_3^2 P_1^2] + \alpha_{111}[P_1^6 + P_2^6 + P_3^6] \\
& + \alpha_{112}[P_1^4(P_2^2 + P_3^2) + P_2^4(P_1^2 + P_3^2) + P_3^4(P_1^2 + P_2^2)] \\
& + \alpha_{123}[P_1^2 P_2^2 P_3^2 + \sigma_{11}(P_1^2 + P_2^2 + P_3^2) + \sigma_{111}(P_1^4 + P_2^4 + P_3^4)] \\
& + \sigma_{12}[P_1^2 P_2^2 + P_2^2 P_3^2 + P_3^2 P_1^2] + \sigma_{111}[P_1^6 + P_2^6 + P_3^6] \\
& + \sigma_{112}[P_1^4(P_2^2 + P_3^2) + P_2^4(P_1^2 + P_3^2) + P_3^4(P_1^2 + P_2^2)] \\
& + \sigma_{123}[P_1^2 P_2^2 P_3^2 + \mu_{11}(P_1^2 P_2^2 + P_2^2 P_3^2 + P_3^2 P_1^2)] \\
& + \mu_{12}[P_1^2(P_2^2 + P_3^2) + P_2^2(P_1^2 + P_3^2) + P_3^2(P_1^2 + P_2^2)] \\
& + \mu_{44}[P_1 P_2 P_3 P_1 + P_2 P_3 P_2 P_1 + P_3 P_1 P_3 P_1] + \beta_1[\theta_1^2 + \theta_2^2 + \theta_3^2] \\
& + \beta_{11}[\theta_1^4 + \theta_2^4 + \theta_3^4] + \gamma_{11}[P_1^2 \theta_1^2 + P_2^2 \theta_2^2 + P_3^2 \theta_3^2] \\
& + \gamma_{12}[P_1^2(\theta_1^2 + \theta_2^2) + P_2^2(\theta_1^2 + \theta_3^2) + P_3^2(\theta_2^2 + \theta_3^2)] \\
& + \gamma_{44}[P_1 P_2 \theta_1 \theta_2 + P_2 P_3 \theta_2 \theta_3 + P_3 P_1 \theta_3 \theta_1] \\
& - \frac{1}{2} S_{11}[X_1^2 + X_2^2 + X_3^2] - S_{12}[X_1 X_2 + X_2 X_3 + X_3 X_1] \\
& - \frac{1}{2} S_{44}[X_1^2 + X_2^2 + X_3^2] - Q_{11}[X_1 P_1^2 + X_2 P_2^2 + X_3 P_3^2] \\
& - Q_{12}[X_1(P_2^2 + P_3^2) + X_2(P_1^2 + P_3^2) + X_3(P_1^2 + P_2^2)] \\
& - Q_{44}[X_1 P_2 P_3 + X_2 P_1 P_3 + X_3 P_1 P_2] - Z_{11}[X_1^2 p_1 + X_2^2 p_2 + X_3^2 p_3] \\
& - Z_{12}[X_1(P_2^2 + P_3^2) + X_2(P_1^2 + P_3^2) + X_3(P_1^2 + P_2^2)] \\
& - Z_{44}[X_1 p_2 p_3 + X_2 p_1 p_3 + X_3 p_1 p_2] - R_{11}[X_1 \theta_1^2 + X_2 \theta_2^2 + X_3 \theta_3^2] \\
& - R_{12}[X_1(\theta_2^2 + \theta_3^2) + X_2(\theta_1^2 + \theta_3^2) + X_3(\theta_1^2 + \theta_2^2)] \\
& - R_{44}[X_1 \theta_2 \theta_3 + X_2 \theta_1 \theta_3 + X_3 \theta_1 \theta_2]
\end{aligned}$$

Fig. 3(a). Thermodynamic function.

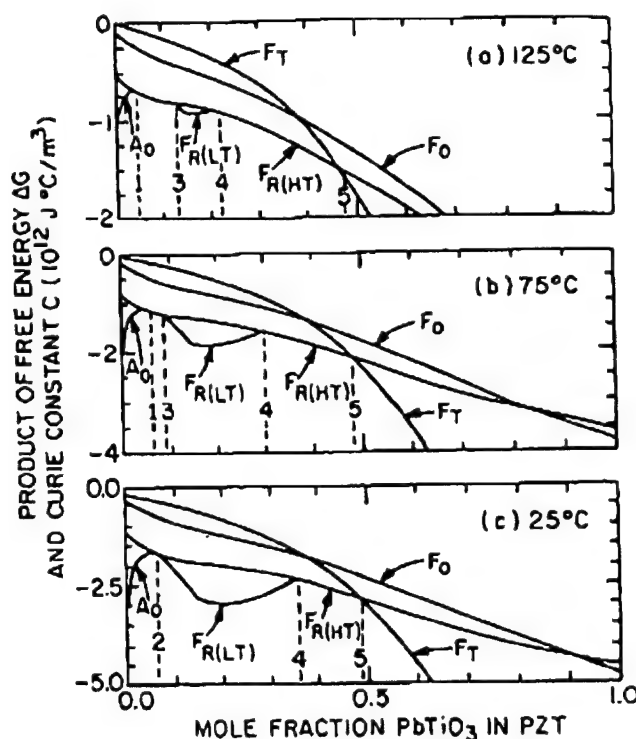


Fig. 3(b). Free Energy as a function of composition and temperature.

	Mole Fraction PbTiO ₃ in PZT										
	0.0	0.1	0.2	0.3	0.4	0.5	0.6	0.7	0.8	0.9	1.0
T_c (°C)	231.5	256.5	300.6	334.4	364.3	392.6	418.4	440.2	459.1	477.1	492.1
C (10 ⁵ °C)	2.027	2.050	2.083	2.153	2.424	4.247	2.664	1.881	1.642	1.547	1.500
Q_{11} (10 ⁻² m ⁴ /C ²)	4.620	5.080	5.574	6.175	7.260	9.660	8.116	7.887	8.142	8.504	8.900
Q_{12} (10 ⁻² m ⁴ /C ²)	-1.391	-1.540	-1.720	-1.997	-2.708	-4.600	-2.950	-2.480	-2.446	-2.507	-2.600
Q_{44} (10 ⁻² m ⁴ /C ²)	4.664	4.900	5.165	5.522	6.293	9.190	6.710	6.356	6.417	6.569	6.750
α_1 (10 ⁷ m/F) at 25°C	-4.582	-6.376	-7.470	-8.116	-7.904	-4.887	-8.340	-12.47	-14.84	-16.17	-17.05
α_{11} (10 ⁷ m ³ /C ² F)	62.35	41.25	31.29	22.30	13.62	4.764	3.614	0.6458	-3.050	-5.845	-7.253
α_{12} (10 ⁸ m ³ /C ² F)	-16.71	-4.222	-0.0345	1.688	2.391	1.735	3.233	5.109	6.320	7.063	7.500
ζ (10 ⁹ m ³ /C ² F)	-34.42	-0.2897	9.284	11.75	11.26	6.634	10.78	15.52	18.05	19.44	20.32
α_{111} (10 ⁸ m ³ /C ⁴ F)	5.932	5.068	4.288	3.560	2.713	1.336	1.859	2.348	2.475	2.518	2.606
α_{112} (10 ⁸ m ³ /C ⁴ F)	311.2	34.45	18.14	15.27	12.13	6.128	8.503	10.25	9.684	8.099	6.100
α_{123} (10 ⁹ m ³ /C ⁴ F)	-104.1	-8.797	-7.545	-7.052	-5.690	-2.894	-4.063	-5.003	-4.901	-4.359	-3.660
ζ (10 ⁹ m ³ /C ⁴ F)	84.41	13.39	4.627	3.176	2.402	1.183	1.595	1.851	1.652	1.256	0.7818

Fig. 3(c). Values of coefficients to fit the properties of PZTs.

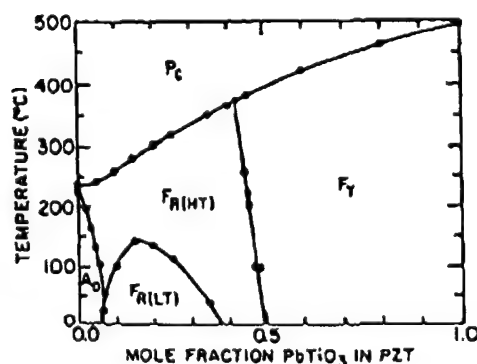


Fig. 3(d). Comparison of observed and calculated phase diagram for PZT.

the same Zr/Ti ratio (PZT) (Fig. 4). The weak field permittivity has a very large difference at room temperature (3000 ~ 750) which is completely absent at helium temperature where domain and phase boundary contributions are lost and the level agrees well with calculated intrinsic response.

In the acceptor modified compositions there are very good explanations of how the domain (not the domain wall) is stabilized.^{13,14} Essentially the charged acceptor associates with an oxygen vacancy to produce a slowly moving defect dipole pair which orients in the field of the domain slowly stabilizing the existing variant over other possible domain states. Bias phenomena in both poled and unpoled samples are logically explained as are facets of the aging behavior and the time depen-

dence of mechanical Q . For donor doped samples there are only "hand waving" arguments as to why the domain walls should become more mobile at weak fields, and much work needs to be done to determine the physics of the softening in these materials. An alternative approach to formulating ultra soft compositions has been the combination of PZT with a relaxor ferroelectric in a three component solid solution. A very wide range of compositions with complex chemistry on the B site of the ABO_3 perovskite have been explored. In general the effect is to lower the Curie point T_c , raise ϵ , raise d_{33} and d_{31} , K_t and K_p .

4. Electrostrictive Relaxor Ferroelectrics

In the $Pb(B_1B_2)O_3$ perovskites for which $PbMg_{1/3}Nb_{2/3}O_3$ (PMN) is a useful prototype it is clear from the dielectric response.¹⁵ Figure 5(a) that a new type of dis-

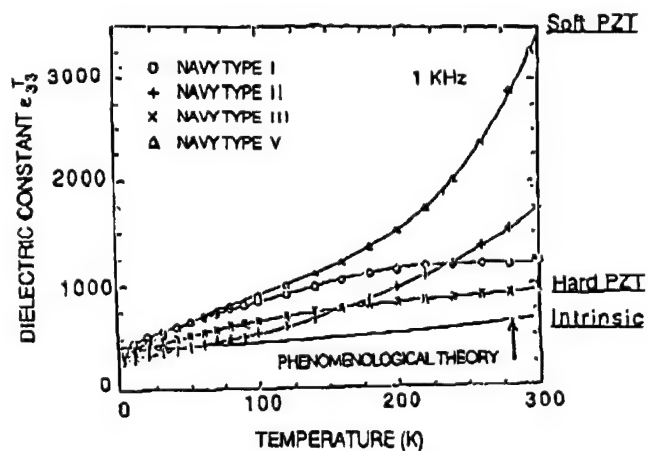


Fig. 4(a). Freeze out of extrinsic contributions to dielectric response in several PZTs at the 52:48 Zr/Ti ratio.

persive high permittivity response occurs. At low temperatures PMN is a ferroelectric as evidenced by pronounced dielectric hysteresis [Fig. 5(b)] however for zero field cooled samples there is no evidence of a non cubic structure nor is there any optical birefringence in the single crystal [Fig. 5(c)]. The origin of this unusual behavior has been traced by careful TEM studies to an unusual self limiting nanoscale ordering of the B site cations. In PMN contrary to expectation the Mg:Nb order 1:1 rather than 1:2, leading to strong short range chemical inhomogeneity.¹⁶ Presumably the local charge unbalance limits the scale of ordering to ~ 5 nm and it cannot be changed even by very long thermal annealing. On cooling the wide difference in Curie temperature between ordered and disordered regions gives rise to local polar regions in a paraelectric matrix which are on a scale where the electro crystalline anisotropy energy is comparable to thermal energy.¹⁷ At higher temperature this gives rise to super paraelectric like behavior, but on cooling the polar fluctuations freeze out in a glass like Vogel-Fulcher freezing in the dielectric response [Fig. 6].^{18,19}

The very high polarizability over a wide temperature range gives rise to massive electrostriction in PMN based compositions [Fig. 7] and the absence of stable domain structure leads to highly reproducible an-hysteretic strain behavior. Under bias fields the PMNs can be induced into very strong piezoelectric response giving a family of potential agile transducers.

5. Piezoceramic Composites

As was evident in eq. (1), dielectric, piezoelectric and elastic properties of the poled piezoceramic are tensor quantities and for many types of application it is possible to spell out a figure of merit which often requires the enhancement of some components of the ten-

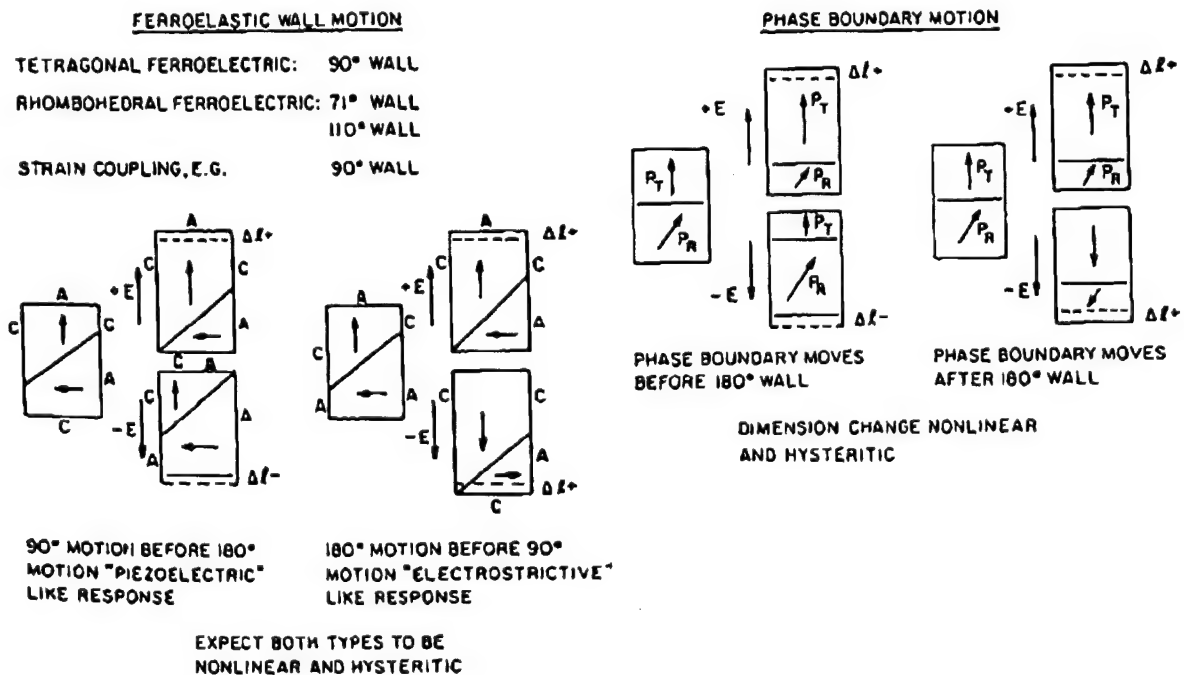


Fig. 4(b). Mechanisms which can contribute to the extrinsic response in PZT ceramic piezoelectrics.

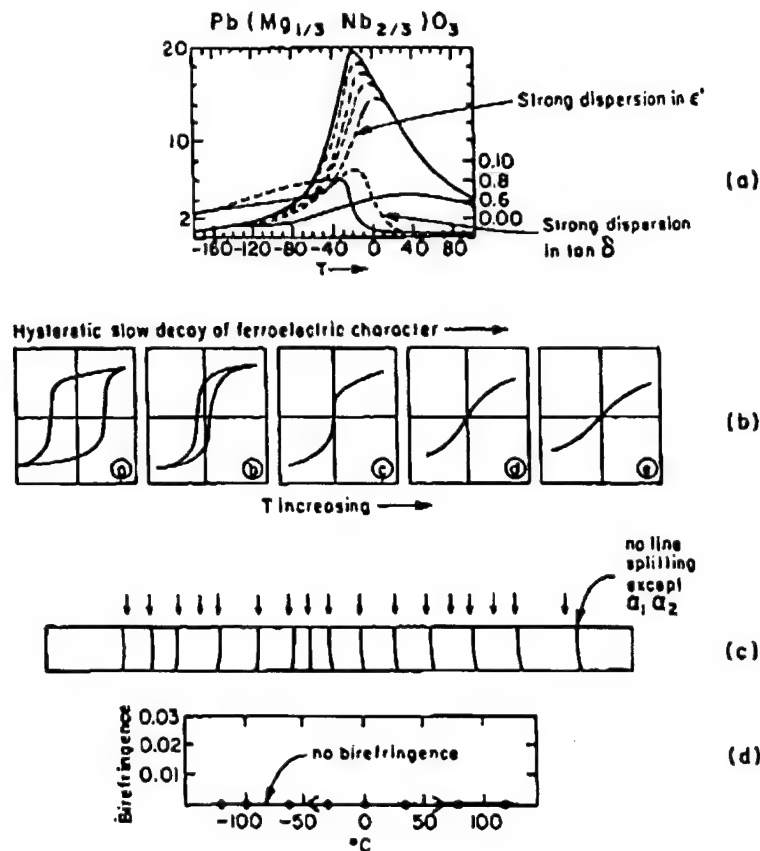


Fig. 5. Special features of relaxor ferroelectrics. (a) Weak field dielectric permittivity vs T . (b) High field hysteretic behavior vs T . (c) Low temperature X-ray and single crystal optics showing 'cubic' macro properties down to below -100°C .

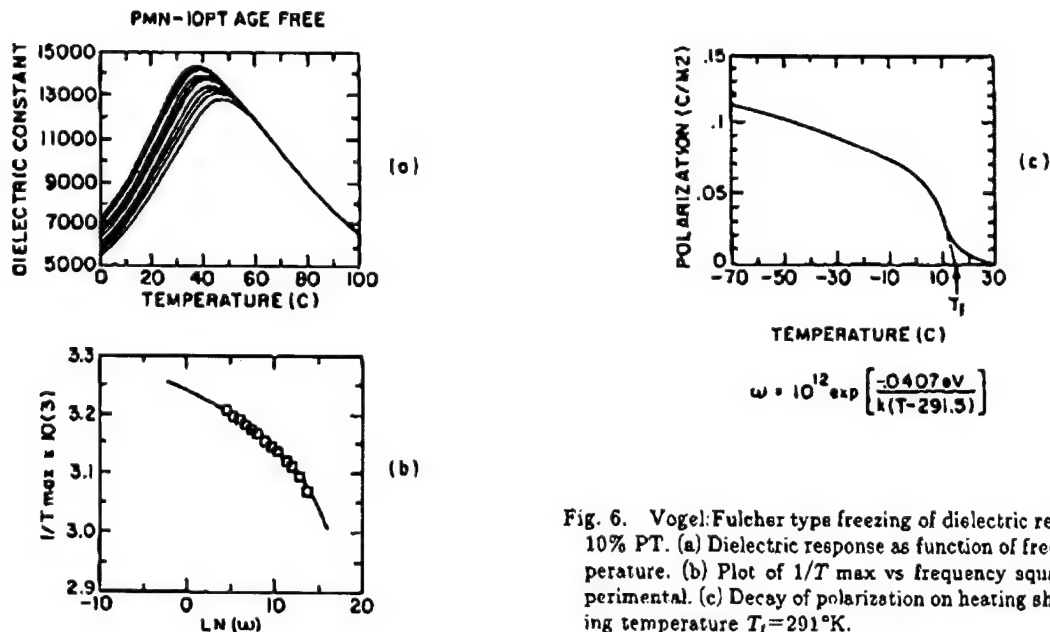


Fig. 6. Vogel-Fulcher type freezing of dielectric response in PMN: 10% PT. (a) Dielectric response as function of frequency and temperature. (b) Plot of $1/T_{\text{max}}$ vs frequency square dots are experimental. (c) Decay of polarization on heating showing the thawing temperature $T_f = 291^{\circ}\text{K}$.

sor and the diminution of others.

A typical example is the Navy requirement for sensing very weak hydrostatic pressure waves in water. For hydrostatic pressure the stress $X_{11} = X_{22} = X_{33} = -p$, where p is the pressure, thus the change of polarization ΔP from equation 3 is

$$\Delta P = d_{33}(-p) + d_{31}(-p) + d_{31}(-p) \\ = (d_{33} + 2d_{31})(-p) = d_h(-p),$$

where d_h is the hydrostatic d coefficient.

The voltage generated by the hydrophone is

$$(-p)g_h = (d_{33} + 2d_{31})(-p)$$

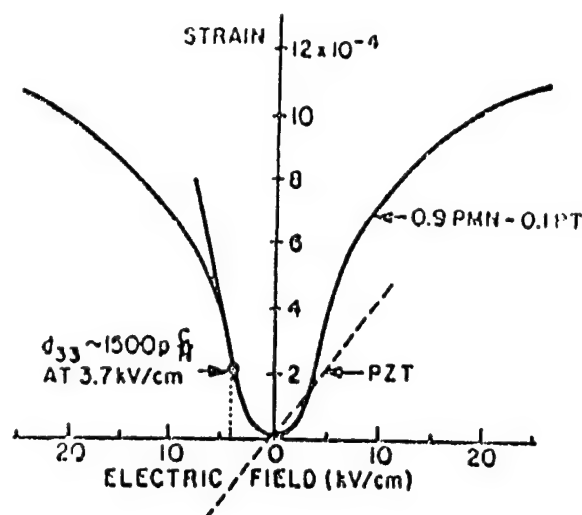


Fig. 7. Electrostrictive deformation x_3 for field applied along E_3 in lead magnesium niobate: 10% lead titanate ceramics.

where g_h is the hydrostatic voltage coefficient.

Often the figure of merit $d_h g_h$ (roughly a power figure) is used, i.e.

$$\frac{d_h g_h = (d_{33} + 2d_{31})^2}{\epsilon_{33}}$$

Unfortunately for PZT even though both d_{33} and d_{31} are large $d_{33} \approx -2d_{31}$ so that d_h is small and ϵ_{33} is large just the wrong combination for a hydrophone.

In exploring composites for hydrophone applications it would be advantageous from density and flexibility considerations to combine the ceramic with a dielectric polymer. Comparing dielectric and elastic properties for these two systems a fascinating juxtaposition is evident PZT is very soft dielectrically, ($\epsilon \sim 3,000$) whilst the average polymer is very stiff ($\epsilon \sim 10$). Conversely

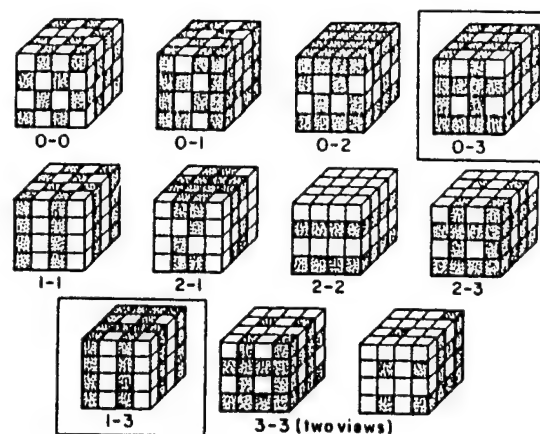


Fig. 8. Parameter considerations in polymer:piezoceramic composites and the simple cubes model illustrating phase self connectivity concept.

the polymer is very soft elastically ($s_{11} \sim 30 \cdot 10^{-11} \text{ m}^2/\text{N}$), but the ceramic is very stiff ($s_{11} \sim 2 \cdot 10^{-11} \text{ m}^2/\text{N}$). Thus by careful control of the mode in which each phase is self connected in the composite it is possible to "steer" the fluxes and fields as to enhance wanted coefficients and diminish unwanted responses.²⁰⁾

The important concepts are summarized in Fig. 8 together with the simple cubes model for connectivity²¹⁾ which is such an aid in thinking and which has given rise to the now internationally accepted notation for the designation of phase self connection in three dimensions.

Comparison of $d_h g_h$ product for some early composites as compared to single phase materials are given in Fig. 9.

A significant advantage has been demonstrated for the use of fine scale 1:3 composites produced by a "dice and fill" method²²⁾ from bulk PZT. This trans-

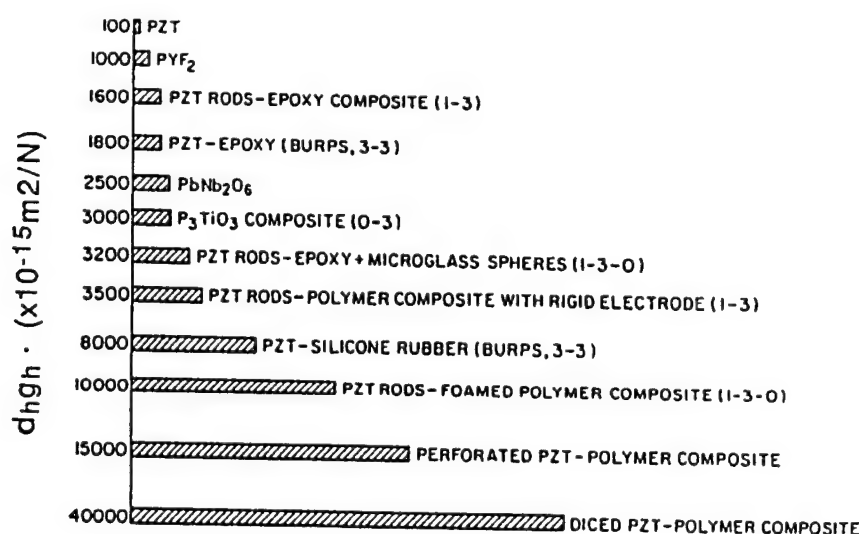


Fig. 9. Improvement in figure out of merit for hydrophone operation ($d_h g_h$) in composites of different connectivities.

ducer structure provides strong enhancement of k_t and the lowering of acoustic impedance both of which carry important gains for electromedical tomography systems.

New ceramic injection molding methods are now being applied to the fabrication of both large area and fine scale 1:3 transducers and promise a revolution in the economics of fabricating these most useful electromechanical elements.^{23,24)}

- 1) F. S. Galasso: *Structure Properties and Preparation of Perovskite Type Compounds* (Pergamon, Oxford, 1969).
- 2) B. Jaffe, W. R. Cooke, Jr. and H. Jaffe: *Piezoelectric Ceramics* (Academic Press, London, 1971).
- 3) M. J. Haun, E. Furman, H. A. McKinstry and L. E. Cross: *Ferroelectrics* **99** (1989) 27.
- 4) M. J. Haun, E. Furman, S. J. Jang and L. E. Cross: *Ferroelectrics* **99** (1989) 13.
- 5) M. J. Haun, E. Furman, S. J. Jang and L. E. Cross: *Ferroelectrics* **99** (1989) 55.
- 6) M. J. Haun, E. Furman, T. R. Halemane and L. E. Cross: *Ferroelectrics* **99** (1989) 74.
- 7) M. J. Haun, Q. Zhang, E. Furman, S. J. Jang and L. E. Cross: *Ferroelectrics* **99** (1989) 45.
- 8) M. J. Haun, T. R. Halemane, R. E. Newnham and L. E. Cross: *Jpn. J. Appl. Phys.* **24** (1985) 209.
- 9) M. J. Haun, E. Furman, S. J. Jang and L. E. Cross: *IEEE Trans. UFFC* **36** (1989) 393.
- 10) J. Herbert: *Ferroelectric Transducers and Sensors Electrocomponent Monograph* (Gordon Breach, London) Vol. 3.
- 11) R. Gerson and H. Jaffe: *J. Phys. Chem. Solids* **24** (1963) 979.
- 12) R. Gerson: *J. Appl. Phys.* **31** (1960) 188.
- 13) K. Carl and K. H. Hardtl: *Ferroelectrics* **17** (1978) 472.
- 14) D. Dederichs and G. Arlt: *Ferroelectrics* **68** (1986) 281.
- 15) G. A. Smolensky, V. A. Isupov, A. I. Agranovskaya, S. N. Popov: *Sov. Phys. Solid State* **2** (1960) 2906.
- 16) C. Randall, D. Barker, R. Whatmore and P. Groves: *Ferroelectrics* **76** (1987) 277.
- 17) L. E. Cross: *Ferroelectrics* **76** (1987) 241.
- 18) D. Viehland: PhD Thesis, Penn State University, 1991.
- 19) D. Viehland, S. J. Jang, L. E. Cross and M. Wuttig: *J. Appl. Phys.* **68** (1991) 2916.
- 20) R. E. Newnham, D. P. Skinner and L. E. Cross: *Mater. Res. Bull.* **13** (1978) 525.
- 21) D. P. Skinner, R. E. Newnham and L. E. Cross: *Mater. Res. Bull.* **13** (1978) 599.
- 22) W. A. Smith: *Proc. ISAF* (Lehigh University, 1986).
- 23) L. J. Bowen and K. French: *Proc. Int. Symp. Appl. Ferroelectrics* **10** (1993) 160.
- 24) L. J. Bowen, R. L. Gentleman, H. T. Phan, D. F. Fiore and K. French: *Proc. IEEE Ultrasonics Symp.* (IEEE, New York, 1993) p. 499.

APPENDIX 2

HOLLOW PIEZOELECTRIC COMPOSITES

J. F. Fernandez*, A. Dogan, Q. M. Zhang, J. F. Tressler and R. E. Newnham.

Intercollege Materials Research Laboratory, The Pennsylvania State University, University Park, PA 16802.

* (Current address: Electroceramic Department, Instituto de Ceramica y Vidrio, CSIC, 28500 Arganda del rey, Madrid, SPAIN)

Abstract

Current research activity in piezoelectric sensors and actuators is moving toward better resolution and higher power densities. Higher resolution and smaller sizes are needed in applications such as biomedical ultrasound, probes for invasive procedures, flow noise control, non-destructive testing, and automotive instrumentation. Piezoelectric transducers with enclosed hollow space offer several special advantages including low acoustic impedance, reduced mass, sensitivity to weak hydrostatic waves, and enlarged displacements through flexensional and rotational motions.

This paper describes recent advances in the processing and properties of five types of hollow piezoelectric composites with connectivity patterns of 0(0)-3, 1(0)-3, 2-0-2, 3-1(0) and 2(0)-2-2(0). Piezocomposites with hollow space included within the structure clearly demonstrate the advantages of functional composites in the field of smart systems.

Keywords: piezoelectrics, piezocomposites, actuators, hydrophones.

1. INTRODUCTION

An electromechanical transducer is a device that converts mechanical energy into electrical energy and vice versa. In a passive mode, operating at a low frequency, it can function as a hydrophone, detecting sound underwater. Typical operating frequencies lie in the low kilohertz range; since the acoustic wavelengths in that range are much larger than the transducer, it must respond to an isotropic stress. Sonar transducers are quite large. For ultrasonic imaging applications, piezoelectric composites must transmit a strong acoustic pulse, and then detect the weak echoes reflected from the internal organ of the human body. Typical medical ultrasonic probes are a few centimeters in size and operate in the low megahertz range. Closely allied to medical ultrasonics are the pulse-echo acoustic imaging system used in non-destructive testing. These applications range from inspecting casting for internal flaws to the processing of integrated circuits. The operating frequencies extend to much higher values, nearing gigahertz in some cases. Another interesting class of pulse-echo devices that requires frequencies down to the mid kilohertz range involves imaging through air. Typical examples are autonomous vehicle guidance and manufacturing assembly. When designing a transducer for a particular application, the choice of transducer material is critical. Ideally the properties include high piezoelectric response in both transmission and receiving modes, while maintaining low density and high flexibility.

Lead Zirconate Titanate ceramic, PZT, is widely used as a transducer material because of its high piezoelectric coefficients. However, for hydrophones applications, PZT is a poor material for several reasons. The hydrostatic piezoelectric coefficient, $d_h (=d_{33}+2d_{31})$, is very low. The piezoelectric voltage coefficients, g_{33} and g_h , are also low because of the high dielectric constant of PZT (1800). Moreover, the acoustic matching of PZT with water is poor because of its high density (7.9 g/cm^3), and the mechanical properties leave much to be desired because it is a brittle, inflexible ceramic.

In the last decade, a number of investigators have fabricated composites of PZT and polymers to overcome the aforementioned problems of PZT. The manufacture of piezoelectric composites requires careful replacement of a portion of the ceramic with polymer. This

replacement reduces the acoustic impedance of the piezoelectric ceramic, bringing it closer to that of water and the human body. It has been shown that it is possible to improve upon the piezoelectric properties of homogeneous PZT by the composite approach [1]. The concept that the connectivity of the individual phases controls the resulting properties has been demonstrated in a number of composites with different geometry and different connectivity patterns of the individual phases. The hydrostatic piezoelectric properties of these composites are far superior to those of single-phase PZT. However, some of the earlier composites are difficult to prepare and suffer a reduction in hydrostatic sensitivity with increasing pressure.

Early investigators concentrated on polymer-ceramic composites for use as hydrophones [2]. Several interesting connectivity patterns [3] were developed including 3-3 structures made by the replamine process [4] and by the fugitive phase technique [5,6]. Then came the more widely used 1-3 composites consisting of parallel PZT fibers embedded in a polymer matrix. These structures were made by extrusion [7], by dicing [8], and more recently by injection molding and lithographic lost-wax techniques [9]. The coupling between the ceramic fibers and the polymer matrix is important [10]. In optimizing hydrophone performance, the $d_h g_h$ product was chosen as a figure of merit. The 1-3 composite increases effective values of d_h and g_h by reducing the d_{31} piezoelectric coefficient and the dielectric constant while maintaining the large d_{33} coefficient.

The usefulness of the 1-3 composite in high frequency applications for non-destructive testing and medical diagnostics was recognized later [1-14]. Biomedical transducers require resonant frequencies in the 1-10 MHz range, high electromechanical coupling coefficients, low acoustic impedance, and broad bandwidth. The 1-3 transducers manufactured by Siemens [9] have thickness resonances of 5-10 MHz, coupling coefficient $k_t=0.67$, $K=600$, $\tan \delta < 0.025$, and a mechanical Q of about 10. Other variants on the basic 1-3 structure include the 1-2-3 composite with transverse load bearing fibers [14], and the 1-3-0 composite with a foamed polymer matrix [15], and the interesting woven fiber composites devised by Safari and co-workers [16-18].

Perhaps the simplest piezoelectric composite is the 0-3 transducer made by dispersing ceramic particles in a polymer matrix [19]. The NTK Piezo-Rubber films and cables are used as flexible hydrophones, keyboards, blood pressure cuffs, and musical instruments. They are made by hot-rolling $\text{PbTiO}_3/\text{PZT}$ ceramic powder mixtures into a chloroprene rubber matrix [19-20]. New piezoelectric mechanical dampers have been produced using composites of piezoelectric-polymer-carbon black [21]. Damping characteristics are controllable by changing the conductivity through the carbon black concentration.

It was demonstrated by Safari [22] that based on the theory of connectivity, new composites with different connectivity patterns could be fabricated with enhanced performance. Most of the work involved composites with 3-1 and 3-2 connectivity. These composites were prepared by drilling either circular or square holes in poled PZT blocks, in a direction perpendicular to the poled axis, and by filling the drilled holes with epoxy. On the samples optimized for hydrophone performance, the g_h and $d_h g_h$ coefficients were about 4 and 40 times greater, respectively, for the 3-1 composites; and 25 and 150 times greater for the 3-2 composites compared to those of solid PZT. For 3-1 composites, there was practically no variation of g_h with pressure up to 8.4 MPa. In the case of 3-2 composites, there was a slight variation of g_h with pressure.

A new type of 2-2 piezoelectric ceramic polymer composite operated at the transverse piezoelectric mode has exceptionally high hydrostatic response, high reliability, and can be made at low cost [23]. This type of composite made of PZT plates in a soft polymer matrix with elastically unidirectional face plates yield effective hydrostatic piezoelectric coefficient d_h of 6,000 pC/N and hydrostatic figure of merit $d_h g_h$ higher than $30,000 \cdot 10^{-15} \text{ m}^2/\text{N}$.

There still exists a need to further improve the piezoelectric properties of these composites. A primary goal is to reproducibly fabricate composite transducers with high figures of merit and minimal pressure sensitivity, under hydrostatic loading, for hydrophone applications. On the other hand, there is also a need of new systems that can afford more complex functions combining sensing and actuating capabilities. This paper reviews recent advances in the

processing and properties of different connectivity pattern composites based on the idea of hollow space within the structure.

2. HOLLOW PIEZOCOMPOSITES

Current research on piezoelectric sensors and actuators is moving toward miniaturized devices to achieve better resolution and higher power densities. High resolution and small sizes are needed in applications such as biomedical ultrasound, ultrasonics, probes for invasive procedures, flow noise control, nondestructive testing of composites, and automotive instrumentation. Higher frequencies and better impedance matching are specially advantageous in underwater transducers and biomedical ultrasonics. The introduction of open space in piezocomposites meets both of these criteria. In most of the cases, careful design of piezocomposites with open spaces leads to the development of reliable, robust, low cost transducers with improved piezoelectric properties. Table I summarizes recent trends in the design of piezocomposites with open spaces.

Perhaps, the first hollow piezoelectric composite were piezoelectric rings, ring stacks and tubes, thin wall or stripe electrode. In that cases the hollow space allows reduction of the piezoelectric radial mode. At the same time, these structures permit the introduction of a stress bolt. This basic configuration is common to tunable transducers [24], active vibration control devices [25] and ultrasonic motors [26]. Another hollow piezoelectric family are the etched PZTs[27], in which hollow spiral patterns eliminate radial modes. Etched piezoelectric are utilized at higher frequencies for biomedical ultrasound diagnosis. Hollow piezoelectric composites possess many of the advantages of other composites and make possible the reduction of undesirable modes of vibration and most important, act as an amplifiers of the sensing and actuating characteristics of ceramics. Metals and epoxies contribute to the amplification factor by different mechanisms depending on the design.

3. BB TRANSDUCERS

BBs are hollow spherical transducers a few millimeters in diameter, about the same size as the metallic pellets used in air rifles (BB guns). PZT BBs are mass produced, by a patented forming process in which air is blown through a PZT slurry of carefully controlled viscosity [28]. The hollow spheres are 1-6 mm in diameter with wall thickness of 0.1 mm. Densities are about 1.3 g/cm^3 giving the BB a low acoustic impedance close to that of water and human tissue.

Two poling configurations were investigated (figure 1): radial poling and external top-to-bottom poling. Electroding the inside of the sphere was necessary to pole in the radial direction. A circular hole was drilled in the wall such that silver electrode could be injected into the sphere. The outside surface was also electroded, leaving a small, uncoated region around the hole. The two principal vibration modes associated with this configuration were a volumetric expansion mode or breathing mode and a wall thickness mode at much higher frequency. Top-to-bottom poling was accomplished using silver caps on opposite sides of the sphere, figure 1B. The principal mode of vibration was the distortion of the sphere to an ellipsoidal shape.

When electroded inside and out, and poled radially the BB becomes an omnidirectional transducer suitable for underwater or biomedical applications. For spheres with a 2.6 mm diameter and 90 μm thick walls, the resonant frequencies are 700 kHz for the breathing mode (d_{31}) and 10 MHz for the wall thickness mode (d_{33}) [29].

When embedded in a polymer matrix to form a 0-3 composite the BB spheres are surprisingly strong, and able to withstand large hydrostatic pressure without collapse. Close-packed transducer arrays are easily assembled [29]. Hydrostatic piezoelectric coefficients well in excess of 1000 pC/N have been measured.

BBs are small enough to be used in catheters for non-invasive surgery to act as beacons, sensors, and actuators [30]. More than a million such procedures are now carried out annually in the United States.

4. PZT MACARONI

Poling is sometimes difficult for the long, slender PZT fibers used in 1-3 composites. Electric breakdown often occurs before poling is complete, and the transducer is ruined. Lower poling and driving fields are obtained when the spaghetti-like PZT fibers are replaced with macaroni-like PZT tubules [31]. When electroded inside and outside, the thin-walled tubes are poled and driven radially at relatively modest voltages (figure 2). The effective piezoelectric constant in the radial direction can be tuned to positive, zero, and negative values by varying the ratio of the outer radius (R) to the inner radius (r) of the tube. For a suitable ratio of R/r , this effective constant can also be adjusted in sign and magnitude with a DC bias field for tubes made of electrostrictive materials [31]. Endcapped thin wall tubes (figure 2) also exhibit exceptionally high hydrostatic response with an effective d_h coefficient of $-14,000$ pC/N and effective figure of merit $d_h g_h$ higher than $10,000 \cdot 10^{-15} \text{ m}^2/\text{N}$.

For large area applications, these tubes can be readily integrated into a 1-3 composite structure to provide low acoustic impedance and high piezoelectric activity. Acoustic transmitters requiring large uniaxial strains utilize the d_{31} constant of transverse piezoelectric mode composites. The effective d_{33} is proportional to the dimensional amplification factor, $L/(R-r)$ where L is the length of the tube. A d_{33} constant of $-10,000$ pC/N [32] about 16 times greater than that of a conventional PZT ceramic, has been obtained for 1-3 tubular composites with $R=1.27$ mm, $r=0.76$ mm and $L=13.5$ mm.

A different approach to the 1-3 composites was recently reported [33] and consist of PZT rods covered by compliant soft epoxy sandwiched between stiffnes polycarbonate sheets machined to give grooves. The PZT rods extend beyond the polymer matrix and were capped with flat cover. This structure generates an air cavity. The figure of merit is $22,460 \cdot 10^{-15} \text{ m}^2/\text{N}$, about six times larger than similar configurations without cavities. This composite, however, showed instability under steady state hydrostatic preassure, but the approach suggested new designs for tubular 1-3(0) piezocomposites with improved properties.

5. ZIG- ZAGs.

Zig-zag actuators are split bimorphs in which two ceramic legs are driven independently to generate synchronized horizontal and vertical displacements. The legs are joined in a teepee-like configuration which imparts a rolling motion to the load. Typical motions are in the 1-30 μm range and look to be useful in piezomotor and conveyor belt applications because of the ability to drive a load in two directions [34]. The required motion for a linear motor can be achieved by driving one leg with a sine wave and the other leg with a sine wave that is 90° out of phase. If the second leg is 90° ahead of the first, the resulting motion will be clockwise, and moves the load from right to left. If the second leg is 90° behind the first, the resulting motion will be counterclockwise and the load will be moved from left to right. A schematic view of the resulting motion when the actuator is driven in this manner is shown in figure 3. The mechanical impedance can be optimized by changing the angle between the legs, and the actuator's working parameter controlled by changing the driving voltage and frequency.

6. HONEYCOMB CERAMIC COMPOSITES

The basic structure of this composite is schematically illustrated in figure 4, where the ceramic is poled perpendicular to the z-direction as indicated [35]. The transducer is operated in the transverse piezoelectric mode (TP). It should be mentioned that two types of honeycomb composite transducers were investigated earlier [36-37]. The earlier honeycomb transducers were operated in the longitudinal piezoelectric mode. Due to the limitations of this mode, the effective hydrostatic piezoelectric response of the earlier honeycomb composite transducers are an order of magnitude smaller than that of the TP honeycomb transducers. An endcapped honeycomb structure was made by placing thin layers of epoxy over the two ends to block the openings. When this endcapped honeycomb is subjected to hydrostatic pressure, the d_{33} response is eliminated and the piezoelectric response comes from the d_{31} component of the piezoelectric. This is due to fact that the stress component perpendicular to the wall is zero because the interior is filled with air. The stress field in the x-, y- and z-directions induces three d_{31} responses in the corresponding ceramic plates. Exceptionally high hydrostatic

piezoelectric d_h values up to -4,700 pC/N were obtained. One of the biggest advantages of such a composite is the extrusion process that permits the development of complex geometries by a cost effective procedure.

7. MOONIES AND CYMBALS.

In recent years, piezoelectric and electrostrictive ceramics have been used in many actuator applications. To meet these needs a new type of composite actuator based on a flextensional transducer has been developed [38-42]. This ceramic-metal composite actuator, or "moonie", consists of either a piezoelectric ceramic disc or a multilayer stack, sandwiched between two specially designed metal end caps. The basic configuration of the moonie is shown in figure 5. The metal endcaps serve as mechanical transformers for converting and amplifying the lateral motion of the ceramic into a large axial displacement normal to the end caps. Both the d_{31} ($=d_{32}$) and d_{33} coefficients of the piezoelectric ceramic contribute to the axial displacement of the composite. Figure 6 shows the enhanced displacement of the moonie actuator compared to that of a PZT ceramic. This design provides a sizable displacement, as well as a large generative force. In other words, it bridges the gap between the two most common types of actuators, the multilayer and the bimorph [43]. The shallow spaces under the end caps produce a substantial increase in strain by combining the d_{33} and d_{31} coefficients of the ceramic. It is attractive for hydrophone, transceiver and actuator applications, and is especially advantageous for use as a non-resonant, low frequency projector in deep water.

Hydrophone sensitivity depends on d_h , the hydrostatic piezoelectric charge coefficient, and g_h , the hydrostatic piezoelectric voltage coefficient. The moonie transducer was introduced as a hydrophone having the highest figure of merit, $d_h g_h = 50,000 \times 10^{-15} \text{ m}^2/\text{N}$ [44], about 500 times larger than the uncapped PZT ceramic. The moonie also possesses high capacitance and excellent pressure tolerance. The stress distribution within the moonie hydrophone under a hydrostatic pressure was determined using Finite Element Analysis. Extensional stresses along the radial and tangential directions are generated under a hydrostatic pressure, and contribute significantly to the very high figure of merit of the moonie.

In addition to this, the effect on prestresses caused by thermal treatment of the moonie were also estimated. The maximum stress concentration reached several hundred MPa. Compressive stresses of 300 MPa are generated along the radial direction at the inner bonding edge, and 400 MPa extensive stresses occur in the cavity near the top of the endcap.

The combined effect of high hydrostatic pressure (7 MPa corresponding to a 700 m water depth), and thermal processes were also estimated. Even 7 MPa hydrostatic pressure causes little deformation to the moonie hydrophone because the effect of relatively large prestress pressures exceed those of the hydrostatic environment. This is one of the reasons that the moonie hydrophone has high pressure tolerance.

Moonie actuators also have very high effective d_{33} coefficients depending on the geometry. Effective d_{33} coefficients as large as 13,000 pC/N were obtained with brass caps 0.3 mm thick, but the value decreases rapidly toward the edge of the transducer. This is approximately thirty times higher than the d_{33} of a PZT-5A ceramic. The characteristics of the moonie actuator depend markedly on both the geometry and the choice of materials. Among the geometric parameters, cavity diameter, cavity depth, and cap thickness are the main parameters which control the displacement of a moonie actuator. An applied 1 kV/mm electric field produces a displacement of 22 μm at the center of a carefully designed brass-capped moonie actuator. By stacking two identical single moonies with these dimensions, the double stacked moonie actuator produces a 40 μm displacement, (figure 6).

The generative force of the moonie was measured experimentally and calculated by FEA. The calculated maximum force (30 N) at the effective working area of 3 mm² agrees with that obtained by the extrapolation of the experimental data.

For actuators, however, the stress concentration on the brass endcap just above the bonding layer reduces the effective force transfer from the PZT to the cap. It is possible to eliminate part of the stress concentration by removing a portion of the endcap just above the bonding region where the maximum stress concentration is observed. An enhancement in properties has been obtained by introducing a ring shaped groove on the exterior of the end caps [44]. The largest displacement was achieved when the groove was positioned above the

bonding layer. The deeper and wider the groove, the higher the displacement. Since the stress concentrates at the groove edges, this becomes a potential source of fatigue and may eventually produce failure under long term usage.

The effect of cavity diameter on the piezoelectric coefficient of moonie transducers with different cavity depths is shown in figure 7 and 8 [45]. The effective piezoelectric coefficient decreases with increasing the cavity diameter and cavity depth. After a certain cavity depth, the cavity does not transfer the applied stress to the ceramic efficiently.

Figure 9 shows the fatigue test of a moonie actuator with different end cap thicknesses under a high cyclic electric field (1kV/mm, 100 Hz) [45]. Experiments were carried out at room temperature with no load. After cycling 10^7 times, a deviation in displacement of only $\pm 0.8\%$ was observed. The reason for the deviation is probably due to the effect of environmental temperature change on the bonding layer. Before and after the cycling test, the admittance spectra of the actuators were recorded with no significant changes. The resonant and anti-resonant frequencies as well as their peak amplitudes were the same as the original values observed before the fatigue test.

A modified moonie with "cymbal" shaped endcaps has recently been developed [45-46], figure 10. The endcaps are fabricated by punching metal sheets. The cymbal design removed most of the region with stress concentration, and yields higher and more reproducible displacements. Even though this new design looks similar to the earlier moonie design, it has a different displacement mechanism. Displacement is primarily a result of flexural motion of moonie endcaps. For the cymbal, the displacement is created by the combination of flexural and rotational motion of the endcaps. Figure 11 shows the displacement values and the position dependence of the different endcap designs with fixed cavity depth (0.2 mm) and cavity diameter (0.9 mm). The cymbal actuator generated a $40\text{ }\mu\text{m}$ displacement which is about twice the moonie displacement. Because of its flexural nature, the displacement of the moonie actuator is highly dependent on position. Displacement decreases dramatically away from the center of the endcap, where the maximum displacement is observed, at the edge of the moonie actuator the displacement is equal to that of the PZT. A moonie with grooved endcaps

show significantly less position dependence of displacement. The cymbal actuator exhibits a more uniform displacement over a wide section about 4 mm in diameter at the center of the endcap. The large flat contact surface of the new endcap design makes it more practical to stack the individual actuators together to achieve higher displacement. Additionally, the new multistacked cymbal structure is more stable under uniaxial external loading. This actuator consists of five elements, 12.7 mm in diameter, 10 mm total thickness, and exhibits a displacement of 175 μm .

Properties and performance of ceramic-metal composites such as the moonie and cymbal, can be tailored through geometrical design and material selection [47]. Because of their large displacement and charge, moonie and cymbal composites show great potential for several applications [44-49], including hydrophone sensors with figure of merit higher than 100,000 $10^{-15} \text{ m}^2/\text{N}$, transceivers for fish finders, positional actuators and highly sensitive accelerometers [49].

8. SMART MATERIALS

Smart materials [50] have the ability to perform both sensing and actuating functions. Passively smart materials respond to external change in a useful manner without assistance, whereas actively smart materials have a feedback loop which allows them to both recognize the change through an actuator circuit. Many smart materials are analogous to biological systems; the piezoelectric hydrophones described earlier are similar to the thin fibers and air bladders by which a fish senses vibrations. Piezoelectrics with electromechanical coupling, shape memory materials that can "remember" their original shape, electrorheological fluids with adjustable viscosities, and chemical sensors which act as synthetic equivalents to the human nose are examples of smart electroceramics. "Very smart" materials, in addition to sensing and actuating, have the ability to "learn" by altering their property coefficients in response to the environment. Integration of these different technologies into compact, multifunction packages is the ultimate goal of research in the area of smart materials. Hollow

piezoelectric composites introduce new tools in the search of smart and very smart materials. The possibility of integrating piezoelectric composites with open space introduces another family of sensors and actuators with complex functions. Substantial progress in this field will occur during the coming decades.

A new vibration control device based on the moonie actuator has been developed by Tressler [51], figure 12. The actuator portion of the device consist of the standard (11 mm diameter, 2 mm thick) moonie, with a small piezoelectric ceramic embedded in the upper end cap to serve as a sensor (0.1 mm thick). This prototype sensor/actuator piezocomposite is capable of detecting and suppressing in real time, small vibration displacements ($< 1 \mu\text{m}$), with low force ($< 100 \text{ gf}$). The dynamic frequency range of the device spans from 100 Hz to at least 2500 Hz. The sensor detects sinusoidal vibrations normal to the actuator surface, via a feedback loop, and sends a signal of appropriate amplitude and phase shift to the actuator so that it effectively cancel is the external vibration. Potential applications for this device include active optical systems, rotor suspension systems, and other low level vibration suppression devices

ACKNOWLEDGMENTS

The authors would like to express their gratitude for the support to the following agencies and organizations: Office of Naval Research Contract no. N00014-92 J 1510, National Science Foundation Grant no. DMR-9223847, Spanish Science Ministry (CICYT MAT94-807 and DGICYT PR94-028), Turkish Science and technology Council and Middle East Technical University, Ankara.

REFERENCES

- [1] R. E. Newnham, Composite Electroceramics, *J. Mat. Education*, 7 (1985) 605-651.
- [2] T. R. Gururaja, R. E. Newnham, K. A. Klicker, S. Y. Lynn, W. A. Schulze, T. R. Shrout and L. J. Bowen, Composite Piezoelectric Transducers, in *Proceedings of the IEEE Ultrasonics Symposium*, vol. 2 (1980) 576-581.
- [3] R. E. Newnham, D. P. Skinner and L.E. Cross, Connectivity and Piezoelectric-Pyroelectric Composites, *Mat. Res. Bull.* 13 (1978) 525-536.
- [4] D. P. Skinner, R. E. Newnham and L. E. Cross, Flexible Composite Transducers, *Mat. Res. Bull.* 13 (1978) 599-607.
- [5] T. R. Shrout, W. A. Schulze and J. V. Biggers, Simplified Fabrication of PZT/polymer composites, *Mat. Res. Bull.* 14 (1979) 1553-59.
- [6] K. Rittenmyer, T. R. Shrout, W. A. Schulze and R. E. Newnham, Piezoelectric 3-3 Composites, *Ferroelectrics* 41 (1982) 189-195.
- [7] K. A. Klicker, J. V. Biggers and R. E. Newnham, Composites of PZT and Epoxy for Hydrostatic Transducer Applications, *J. Am. Ceram. Soc.* 64 (1981) 5-9.
- [8] H. P. Savakus, K. A. Klicker and R. E. Newnham, PZT Epoxy Piezoelectric Transducers: A Simplified Fabrication Procedure, *Mat. Res. Bull.* 16 (1981) 677-680.
- [9] G. Gu, A. Wolff, D. Cames and U. Bast, Microstructuring of Piezoelectric Composites, *Euro-Ceramics II* Vol.3 (1991) 2005-10.
- [10] C. Richard, P. Eyraud, L. Eyraud, A. Pelourson and M. Richard, A Pressure Dependence Approach of New 1.3.1 Piezoelectric Polymer Composite for Hydrophone, *Euro-Ceramics II* Vol.3 (1991) 2001-4.
- [11] T. R. Gururaja, W. A. Schulze, L. E. Cross, R. E. Newnham, B. A. Auld and Y. J. Wang, Piezoelectric Composite Materials for Ultrasonic Transducer Applications. Part I: Resonant Modes of Vibration of PZT Rod-Polymer Composites, *IEEE Transactions on Sonics and Ultrasonics*, Vol. 32, no. 4 (1985) 481-498.
- [12] T. R. Gururaja, W. A. Schulze, L. E. Cross, R. E. Newnham, B. A. Auld and Y. J. Wang, Piezoelectric Composite Materials for Ultrasonic Transducer Applications. Part

- II: Evaluation of Ultrasonic Medical Applications, *IEEE Transactions on Sonics and Ultrasonics*, 32, 4 (1985) 499-513.
- [13] W. Smith, The Role of Piezocomposites in Ultrasonic Transducers, *Proceedings of the 1988 IEEE Ultrasonics Symposium* (1988) pp. 755-66.
- [14] M. J. Haun, R. E. Newnham and W. E. Schulze, 1-2-3 and 1-2-3-0 Piezoelectric Composites for Hydrophone Application, *Adv. Ceram. Mat.* 1, 4 (1986) 361-365.
- [15] M. J. Haun and R. E. Newnham, An Experimental and Theoretical Study of 1-3 and 1-3-0 Piezoelectric PZT-Polymer Composites for Hydrophone Applications, *Ferroelectrics* 68 (1986) 123-129.
- [16] R. J. Card, M. P. O'Toole and A. Safari, Method of Making Piezoelectric Composites, U.S. pat # 4,726,099 (1988).
- [17] J. Giniewicz, R. E. Newnham and A. Safari, (Pb,Bi)(Ti,Fe,Mn)O₃ -Polymer 0-3 Composites for Hydrophone Applications, *Ferroelectrics* 73 (1987) 405-418.
- [18] S. S. Livneh, S. M. Ting and A. Safari, Development of Fine Scale and Large Area Piezoelectric Ceramic Fiber Polymer Composites for Transducer Applications, *Ferroelectrics* 157 (1994) 421-426.
- [19] H. Banno, Recent Developments of Piezoelectric Ceramic Products and Composite of Synthetic Rubber and Piezoelectric Ceramic Particles, *Ferroelectrics* 50 (1993) 329-338.
- [20] H. Banno and K. Ogura, Piezoelectric Properties at Polarization Reversal Process and Coercive Force of 0-3 Composite Polymers and Ceramic Powder Mixture of PZT and PbTiO₃, *Jap. J. Applied Physics* 30,93 (1991)2250-52.
- [21] Y. Suzuki, K. Uchino, H. Gouda, M. Sumita, R. E. Newnham and A. R. Ramachandran, Mechanical Damper Using Piezoelectric Composites, *J. Ceram. Soc. Jap. (Int. Ed.)* 99 (1991) 1096-98.
- [22] A. Safari, Perforated PZT-Polymer Composites with 3-1 and 3-2 Connectivity for Hydrophone Applications, Ph.D. Thesis, The Pennsylvania State University, University Park, PA (1983).

- [23] Q. M. Zhang, J. Chen, H. Wang, J. Zhao, L. E. Cross and M. C. Trottier, A Transverse Piezoelectric Mode 2-2 Piezocomposite for Underwater Transducer Applications, *IEEE Transactions on Ultrasonics, Ferroelectric and Frequency Control* (in press).
- [24] M. A. Blaskiewicz, Tunable Transducers, Ph.D. Thesis, The Pennsylvania State University, University Park, PA (1994).
- [25] A. R. Ramachandran, Complex Electromechanical Coefficients of Piezoelectric Composites: Applications to Passive Vibration Damping, Ph.D. Thesis, The Pennsylvania State University, University Park, PA (1992).
- [26] S. Ueda and U. Tomikawa, Ultrasonic Motor: Theory and Applications, Oxford University Press, (1993) Oxford.
- [27] S. Troiler, Q. C. Xu and R. E. Newnham, Preparation of Chemically Etched Piezoelectric Resonator for Density Meter and Viscosimeters, *Mat Res. Bull.* 22,4(1987)1267-1274.
- [28] L.B. Torobin, Methods of Making Hollow, Porous Microspheres, U.S. Patent #4,671,909, (1987).
- [29] R. Meyer Jr, H. Weitzing, Q. Xu, Q. Zan and R. E. Newnham, Lead Titanate hollow Sphere Transducers, *J. Am. Ceram. Soc.* 77,6 (1994) 1669-72.
- [30] D. Kilkomerson, B. Gardineer and H. Hojeibane, Quasi-Omnidirectional Transducers for Ultrasonic Electro-Beacon Guidance of Invasive Devices, *Proceedings of SPIE* 1733 (1992) 154-65.
- [31] Q. M. Zhang, H. Wang and L. E. Cross, Piezoelectric Tubes and Tubular Composites for Actuator and Sensor Applications, *J. Mater. Sci.* 28 (1993) 3962-68.
- [32] H. Wang, Q. M. Zhang, L. E. Cross and M. C Trottier, Transverse Piezoelectric Mode Composites: A New Design Approach for Smart Material Applications", *Proceedings of SPIE Conference on Smart Structures and Materials.* (1995)
- [33] C. Kim, K. M. Rittenmeyr and M. Kahn, 1-1-3 Piezocomposite for Hydrophone Transducer, *Ferroelectrics* 156 (1994) 19-24.

- [34] M.G. Matsko, Q. C. Xu and R. E. Newnham, Zig-Zag Piezoelectric Actuators: Geometrical Control of Displacement and Resonance, *J. of Intelligent Mat. Systems and Structures*, (in press).
- [35] Q.M. Zhang, H. Wang, J. Zhao, J. T. Fielding, R. E. Newnham and L. E. Cross, A High Sensitivity Piezoelectric Transducer Based on Transverse Piezoelectric Mode Honeycomb Ceramic Composites, *IEEE Transactions on Ultrasonics, Ferroelectric and Frequency Control* (in press).
- [36] T. R. Shrout, L.J. Bowen and W. A. Schulze, Extruded PZT-Polymer Composites for Electromechanical Transducer Applications, *Mater. Res. Bull.* vol 15 (1980) 1371-80.
- [37] A. Safari, A. Halliyal, R. E. Newnham and I. M. Lachman, Transverse Honeycomb Composite Transducers, *Mater. Res. Bull.* Vol 17 (1982) 301-9.
- [38] R. E. Newnham, Q. C. Xu and S. Yoshikawa, Transformed Stress Direction-Acoustic Transducer, U.S. Patent # 4,999,819, March 12, (1992).
- [39] Q. C. Xu, S. Yoshikawa, J. Belsick and R. E. Newnham, Piezoelectric Composites with High Sensitivity and High Capacitance for Use at High Pressures, *IEEE Transactions on Ultrasonics, Ferroelectrics and Frequency Control*, 38, 6 (1991) 634-639.
- [40] Y. Sugawara, K. Onitsuka, S. Yoshikawa, Q. Xu, R. E. Newnham and K. Uchino, Metal-Ceramic Composite Actuators, *J. Am. Ceram. Soc.* 75, 4 (1992) 996-998.
- [41] A. Dogan, Q. C. Xu, K. Onitsuka, S. Yoshikawa, K. Uchino and R. E. Newnham, High Displacement Ceramic-Metal Composite Actuators (Moonie), *Ferroelectrics* 156 (1994) 1-6.
- [42] K. Onitsuka, A. Dogan, Q.C. Xu, J. Tressler, S. Yoshikawa, and R.E. Newnham, Design Optimization for Ceramic-Metal Composite Actuators (Moonie), *Ferroelectrics* 156 (1994) 37-42.
- [43] K. Uchino, Piezoelectric and Electrostrictive Actuators, Morikita Publication, Tokyo, Japan (1986).

- [44] K. Onitsuka, Effects of Bonding and Geometry on the Flextensional Transducer, "Moonie", Ph.D. Thesis, The Pennsylvania State University, University Park, PA (1993).
- [45] A. Dogan, Flextensional Moonie and Cymbal Actuators, Ph.D. Thesis, The Pennsylvania State University, University Park, PA (1994).
- [46] A. Dogan and R. E. Newnham, Flextensional Cymbal Transducer, U.S.A. Patent, PSU Invention Disclosure No 94-1395 (1994).
- [47] J. F. Fernandez, A. Dogan, J. T. Fielding, K. Uchino and R. E. Newnham, "Tailoring High Displacement Performance of Ceramic-Metal Composite Actuators "Cymbals", *IEEE UFFC*, .submitted.
- [48] R. E. Newnham, A. Dogan, J. T. Fielding, J. F. Fernandez, D. Smith, J. Tressler, J. Wallis, K. Uchino, W. Zhu, Moonies, Cymbals and BB's, *Office of Naval Research Transducer Materials and Transducers Workshop*, April 1995 State College, PA, USA.
- [49] B. Koc, A. Dogan, J. F. Fernandez, K. Uchino and R. E. Newnham, "Accelerometer Application of the Moonie and Cymbal" *in preparation*.
- [50] R. E. Newnham and G. Ruschau, Smart Electroceramics, *J. Am. Ceram. Soc.* 74, 3 (1991) 463-480.
- [51] J. F. Tressler, Q. C. Xu, S. Yoshikawa, K. Uchino and R. E. Newnham, Composite Flextensional Transducer for Sensing and Actuating, *Ferroelectrics* 156 (1994) 67-72.

Jose F Fernandez was born in Madrid, Spain on September 23, 1961. He received the B. S. degree in applied physics in 1985, M.S. degree in physics in 1987 and Ph.D in physics in 1990, all of them from Autonomous University of Madrid, Spain.

He is a staff member of the Electroceramics Department at the Instituto de Ceramica y Vidrio, CSIC, Arganda del Rey, Madrid, Spain. In 1994-95 he was a Visiting Scientist at the Materials Research Laboratory, Pennsylvania State University. His research interest are in the processing of ceramics, dielectric and piezoelectric ceramics and composite materials for electronic applications.

He is a member of the American Ceramic Society and Spanish Ceramic and Glass Society.

Aydin Dogan was born in Ankara, Turkey, on February 22, 1966. He received the B.S. degree in materials science & metallurgical engineering in 1988 and the M.S. degree in 1990, both from Middle East Technical University in Ankara-Turkey. He received its Ph.D. in Solid State Science at the Pennsylvania State University, University Park, PA, in 1994. His research interests include electronic ceramics, sensors and actuators, smart materials and systems, and ferroelectrics.

He is a member of the Materials Research Society and is a NATO- TUBITAK science fellowship recipient.

Q. M. Zhang was born in ZeiJian, China in 1957. He received the B.S. degree from Nanjing University, China in 1981 and Ph. D. degree from Pennsylvania State University, University Park, in 1986. From 1986 to 1988, he was a Post-Dr at Materials Research Laboratory at Penn State. From 1988 to 1991, he was a research scientist at Brookhaven National Laboratory, NY, conducting research on interface, surface, and thin film with neutron and synchrotron X-ray scattering techniques.

He is currently an Associated Professor of Materiales and Senior Research Associate at the Intercollege Materials Research Laboratory of the Pennsylvania State University. His research interest invlove piezoceramic and polymer actuator, sensor, and transducer applications: new design and modeling of piezocomposites: smart materials and structures: novel, artificial, and nano-composite materials; effects of defect structure on the dielectric, piezoelectric, and elastic properties of ferroelectric materials; and structure studies on the interfaces and defects in ferroelectrics.

Dr. Zhang is member of American Ceramic Sociaty, American Physical Society, Materials Ressearch Society, and Neutron Scattering Society of America.

James F. Tressler was born in Lock Haven, PA, on May 2, 1968. He received the B.S. degree in ceramic science and engineering in 1991 and the M.S. degree in 1993, both from the Pennsylvania State University, University Park, PA. In 1994, he was a Visiting Scientist at the Sony Corporation Research Center in Yokohama, Japan, where he was involved in the processing of dielectric thin films. His research interests are in the areas of smart materials and systems, composites, and thin films.

Robert E. Newnham was born in Amsterdam, NY, on March 28, 1929. He received the B.S. degree in mathematics in 1950 from Hartwick College, Oneonta, NY, the M.S. degree in physics and mineralogy from the Colorado State University, Fort Collins, CO, and the Ph.D. in crystallography in 1960 from Cambridge University, Cambridge, England.

He is ALCOA Professor of Solid State Science at the Materials Research Laboratory at the Pennsylvania State University, University Park, PA. Previously, he was a staff member of the Laboratory for Insulation Research at the Massachusetts Institute of Technology, Cambridge, MA. His research interests are in structure-property relations, electroceramics, and composite materials for electronic applications.

TABLE I
New trends in piezocomposite design with open spaces

Previous			New design		
Connectivity pattern	Type	Name	Connectivity pattern	Type	Name
0-3	PT/PZT in polymer	Piezorubber	0(0)-3	PZT hollow spheres	BBs
1-3	PZT fiber in polymer	PZT spaghetti	1(0)-3	PZT tubules in polymer	PZT macaroni
3-1	PZT with drilled holes	Perforated PZT	3-1(0)	PZT honeycomb skeleton	Honeycomb
2-2	Cantilever	PZT bimorph	2-0-2	split bimorph	Zig Zag
2-2	Tape cast PZT multilayer	PZT actuator	2(0)-2-2(0)	Capped PZT	PZT moonie and cymbal

FIGURE CAPTIONS

Figure 1 Electrode design for (A) the radial poling configuration showing the small uncoated ring used to separate the inner and the outside electrode, and (B) the electrode configuration for top-to-bottom poling. Shaded areas represent the air-dry silver coating.

Figure 2 Schematic of capped 1(0)-3 piezocomposite configuration showing a single PZT tube poled radially.

Figure 3 Schematic view of the Zig-Zag Actuator motion being driven by sine and cosine waves.

Figure 4 Schematic drawing of a honeycomb ceramic structure. Poling directions are indicated in the insert of the figure. Notice the difference in the poling directions between neighboring cells.

Figure 5. The geometry of the ceramic-metal composite actuator "Moonie". The arrows describe the displacement directions when the moonie is driven by a field parallel to the poling direction of the ceramic.

Figure 6. The displacement characteristics of the moonie actuator as a function of the applied electric field. Dimensions: $d_m=12.7$, $d_p=12.7$, $d_c=9.0$, $h=0.2$, $t_p=1.0$, $t_m=0.3$ (all in mm).

Figure 7. Effect of cavity diameter and cavity depth on the effective piezoelectric coefficient of the moonie. Dimensions: $d_m=12.7$, $d_p=12.7$, $t_p=1.0$ (all in mm).

Figure 8. Effect of End cap thickness on the effective piezoelectric coefficient of the moonie. Dimensions: $d_m=12.7$, $d_p=12.7$, $d_c=9.0$, $t_p=1.0$ (all in mm).

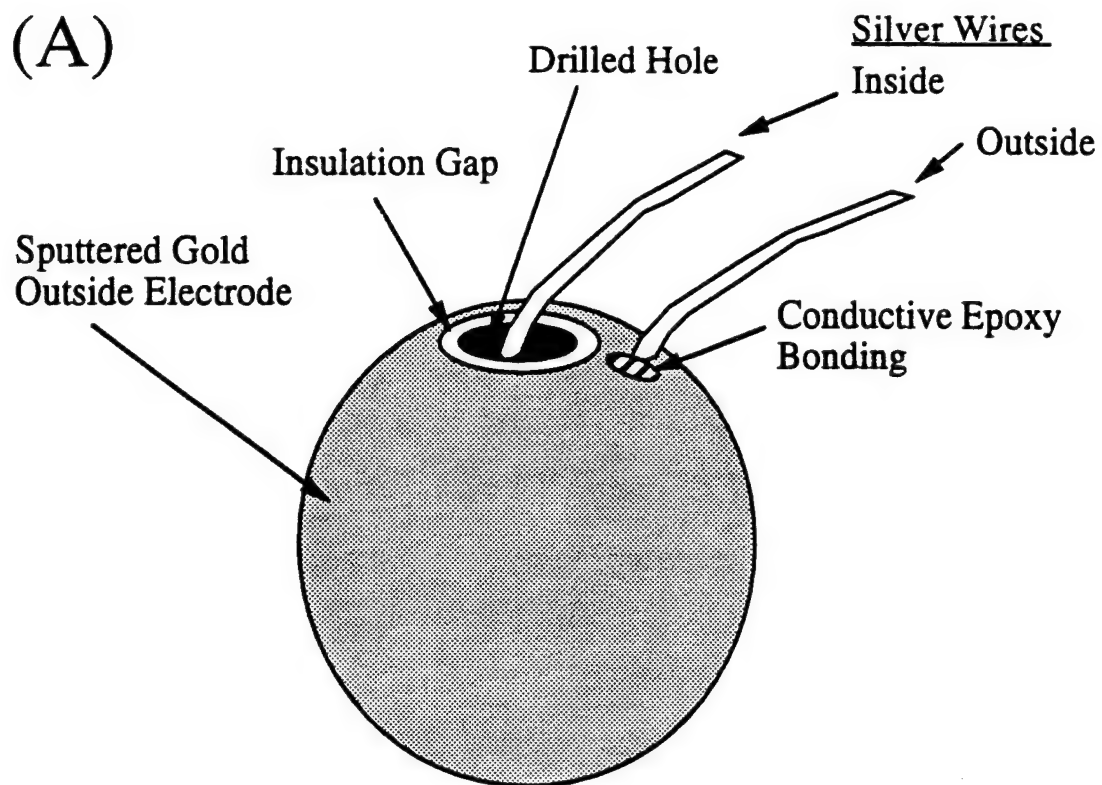
Figure 9. Fatigue characteristics of the moonie actuators.

Figure 10. The geometry of the ceramic-metal composite actuator "Cymbal". The arrows describe the displacement directions when the moonie is driven by a field parallel to the poling direction of the ceramic.

Figure 11. The position dependence of displacement for different endcap designs.

Figure 12. Integrated sensor and actuator for active vibration control.

(A)



(B)

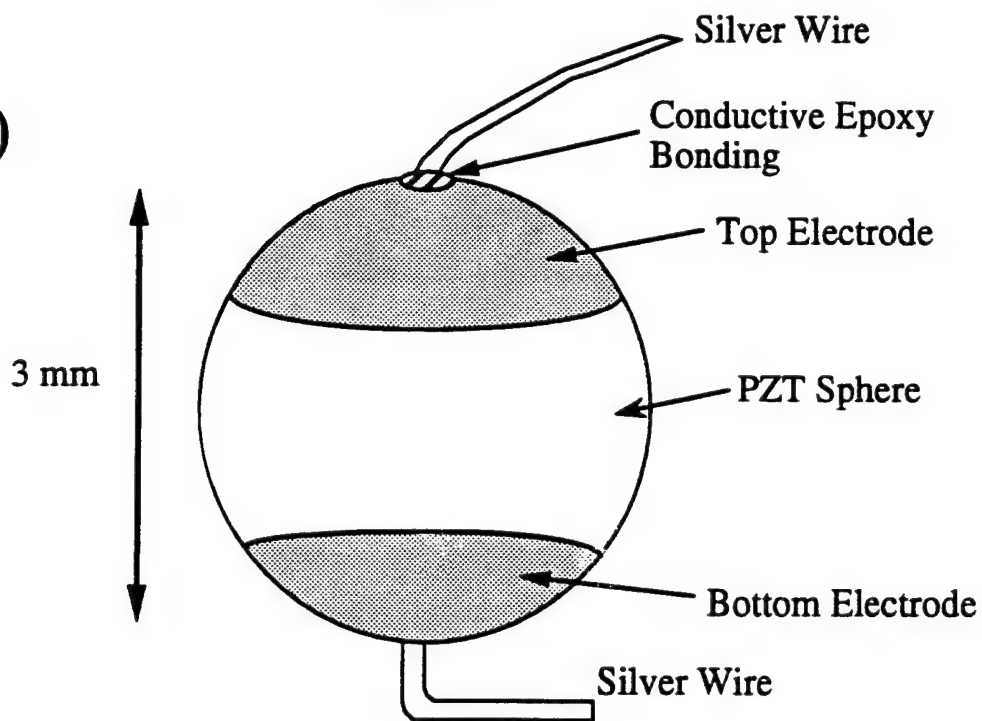
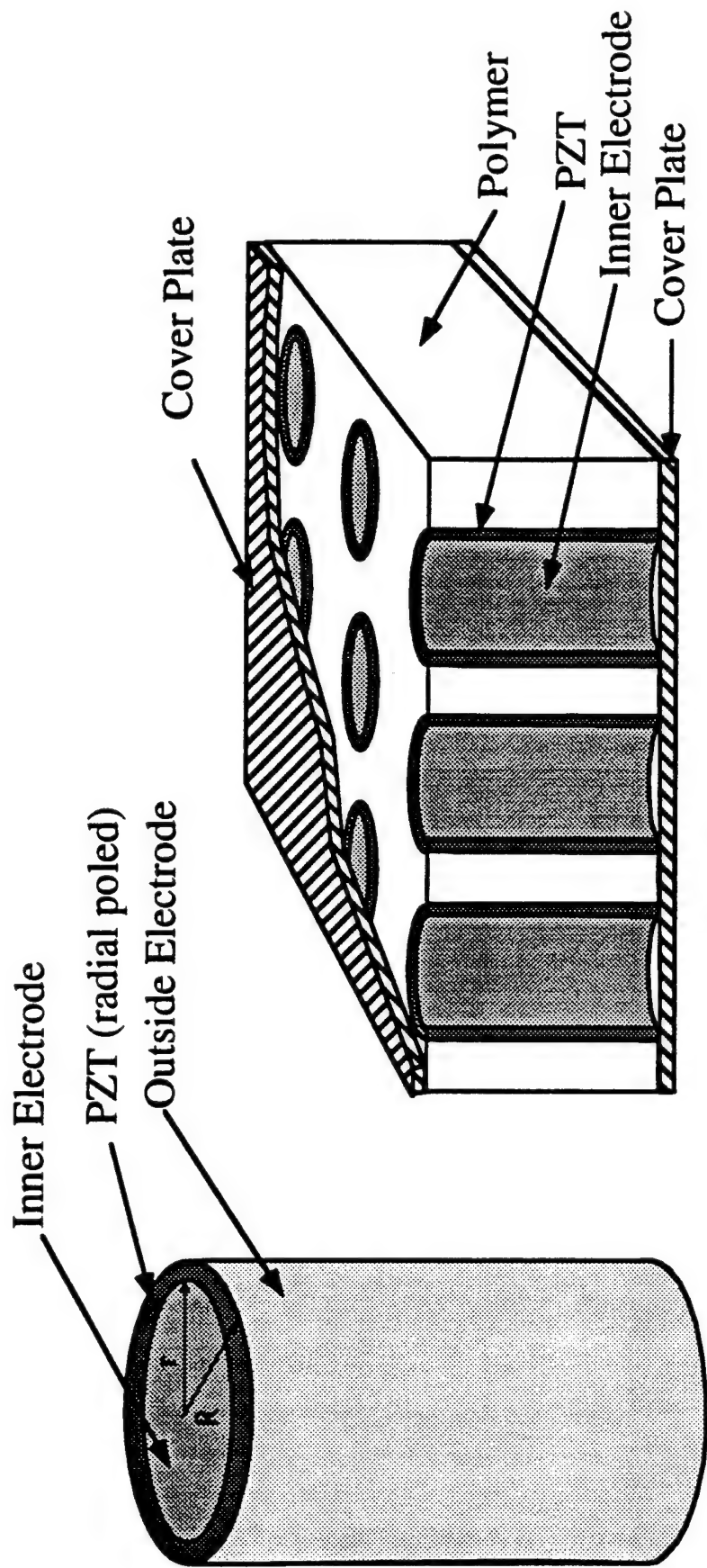
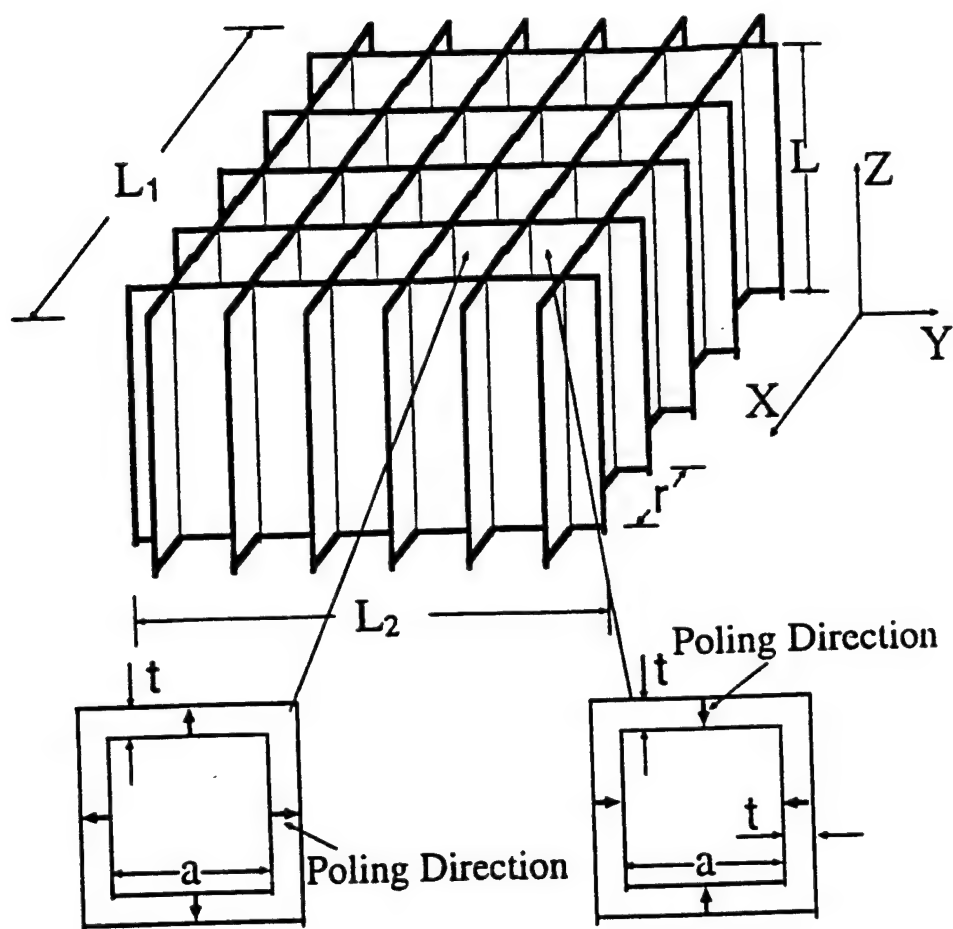


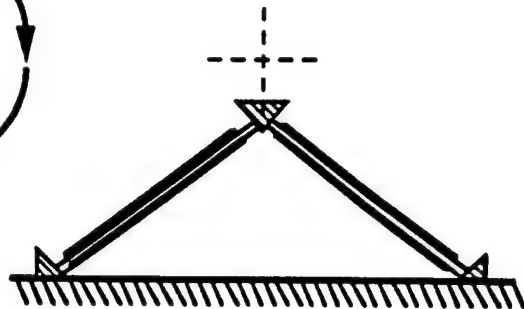
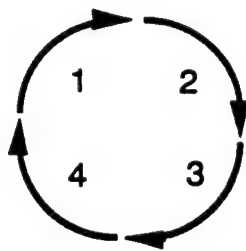
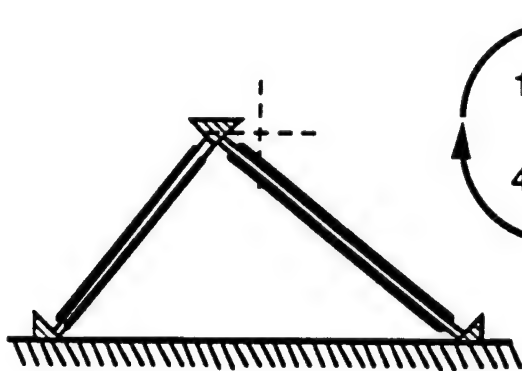
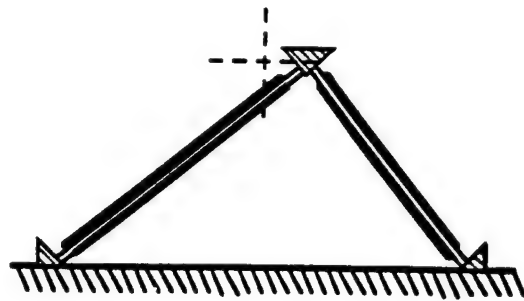
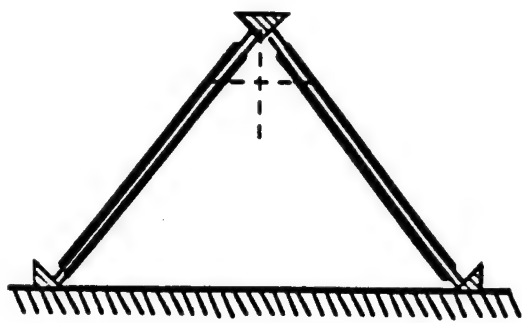
Figure 1



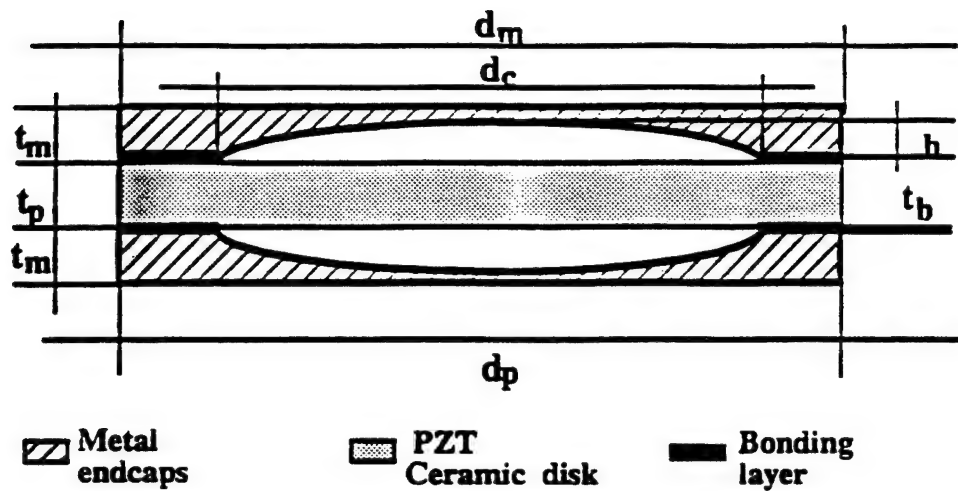
Single Tube Capped 1(0)-3 Composite



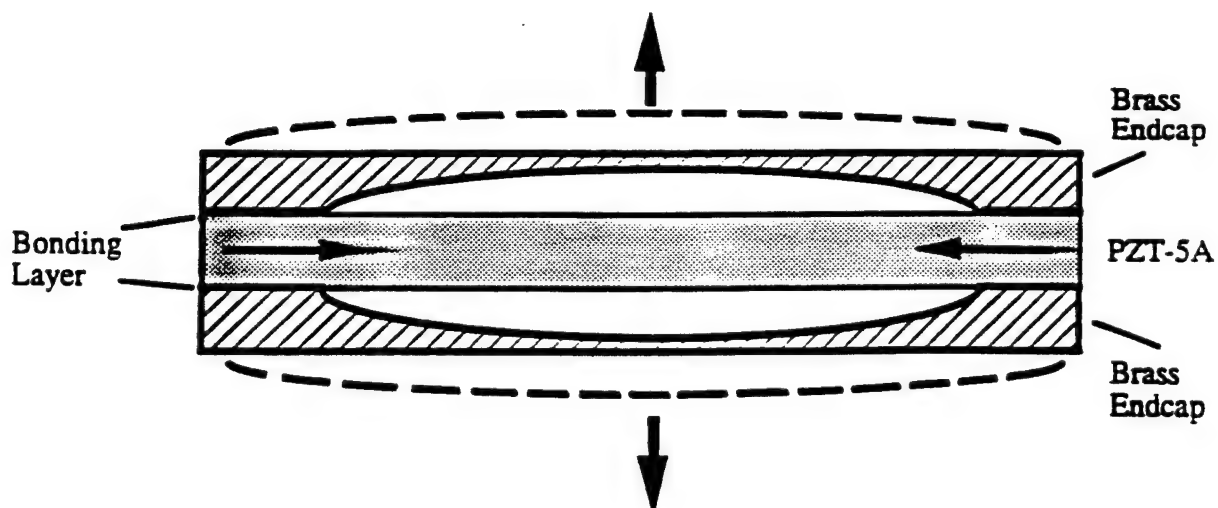
F 3

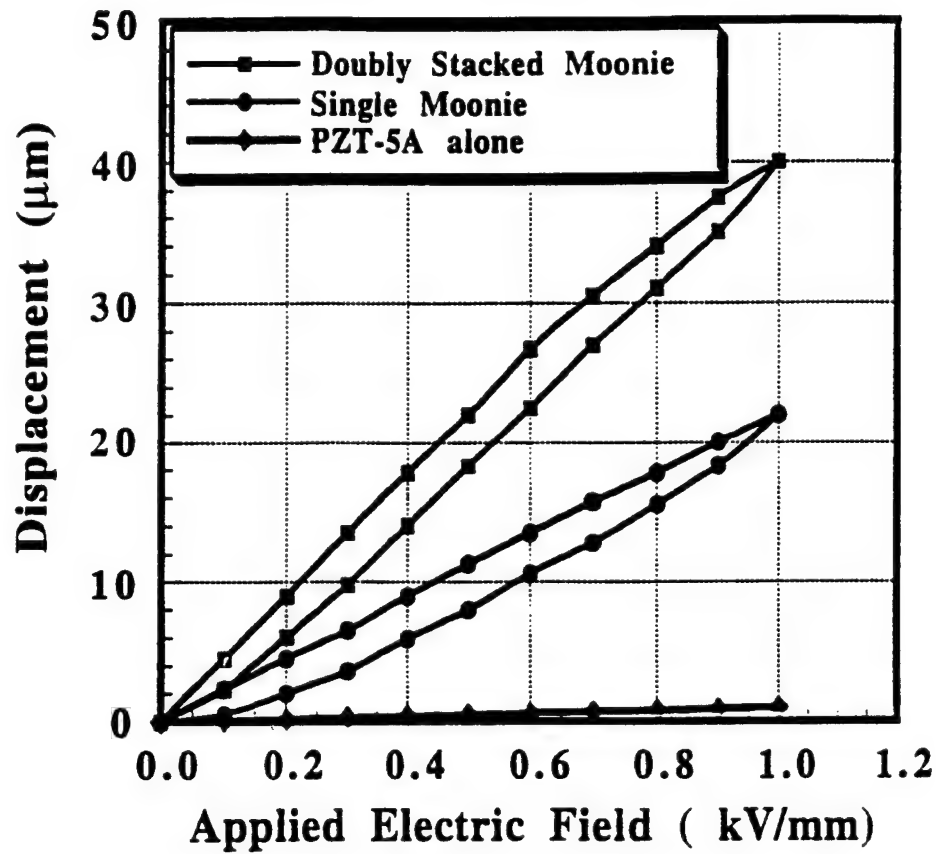


F 4



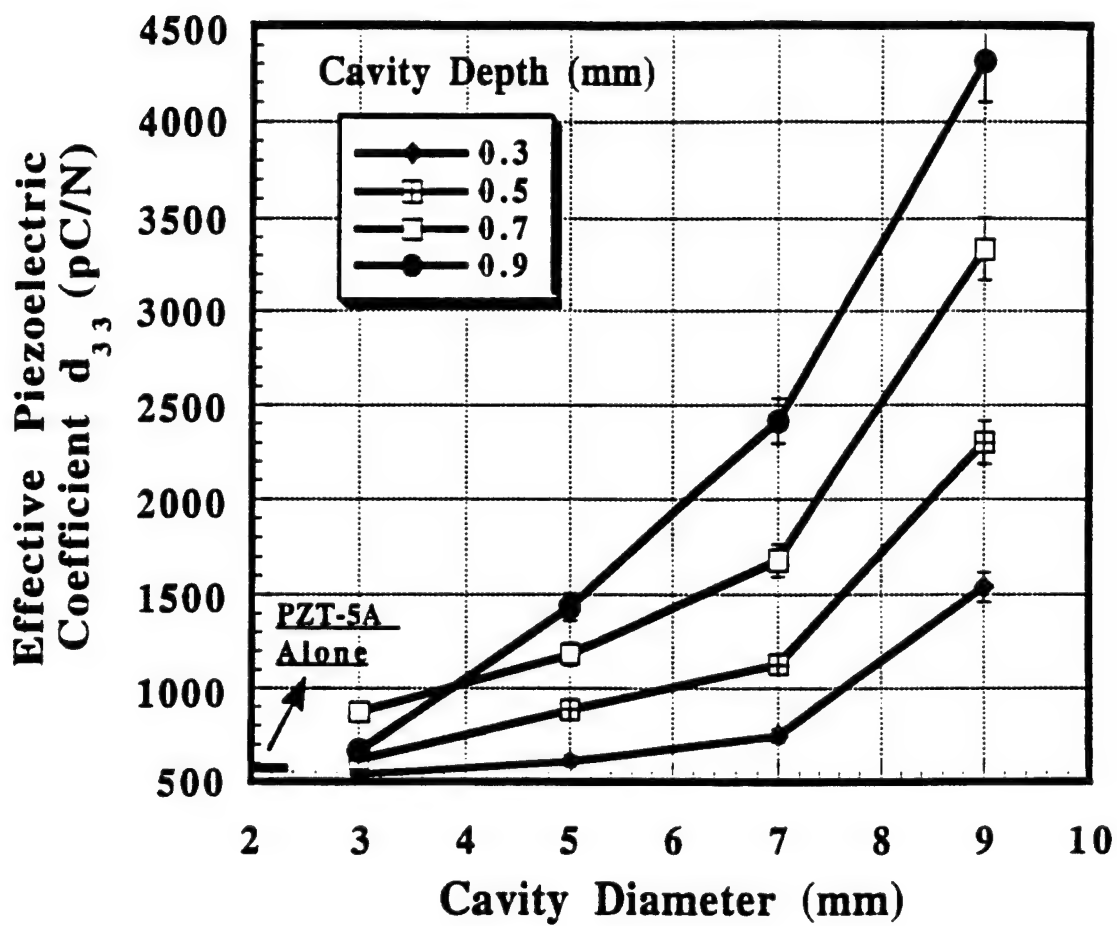
Dimensions: Endcap diameter, $d_m = 12.7$ mm PZT diameter, $d_p = 12.7$ mm
 Cavity diameter, $d_c =$ variable; 3.0, 5.0, 7.0, 9.0 mm
 Cavity depth, $h =$ variable; 0.3, 0.5, 0.7, 0.9 mm
 Metal cap thickness, $t_m = 1.0$ mm PZT thickness, $t_p = 1.0$ mm
 Bonding layer thickness, $t_b = 0.01$ mm



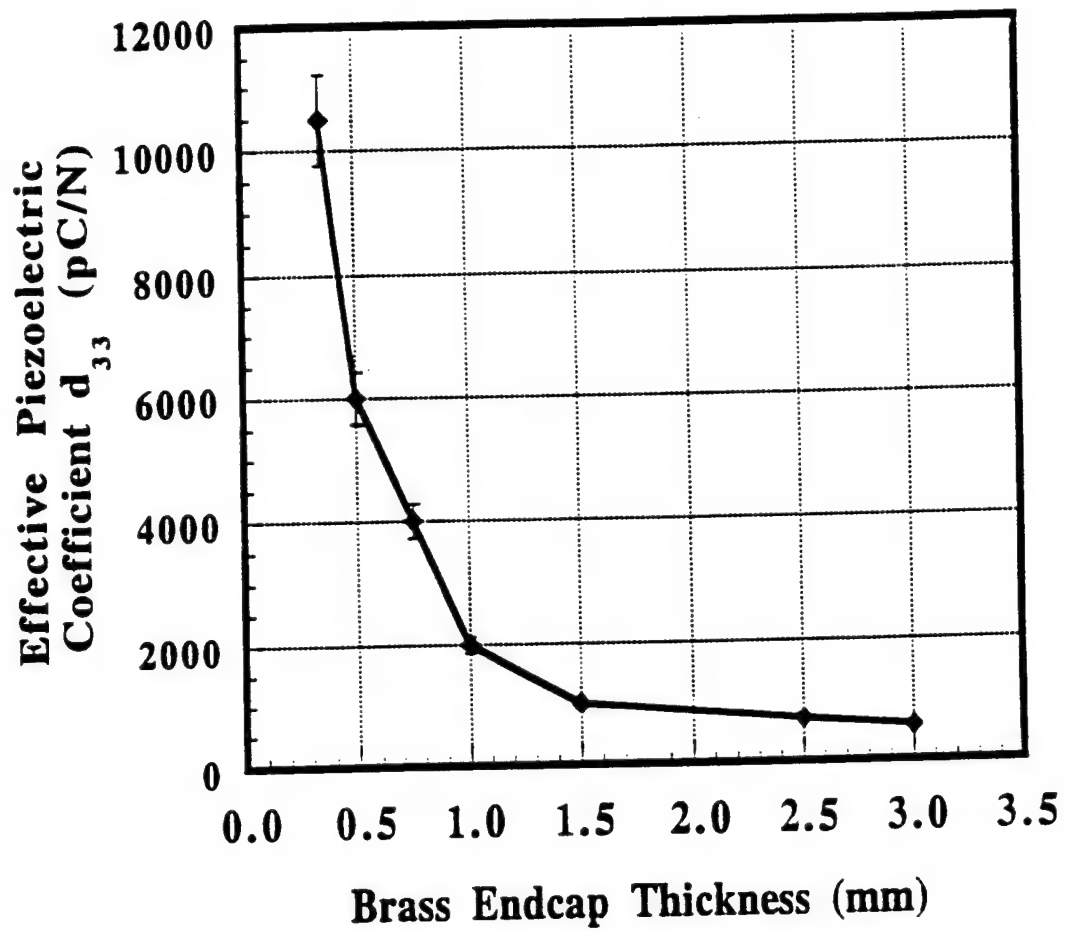


Dimensions: $d_m = 12.7$, $d_p = 12.7$, $d_c = 9.0$, $h = 0.2$, $t_p = 1.0$, $t_m = 0.30$ (all in mm)

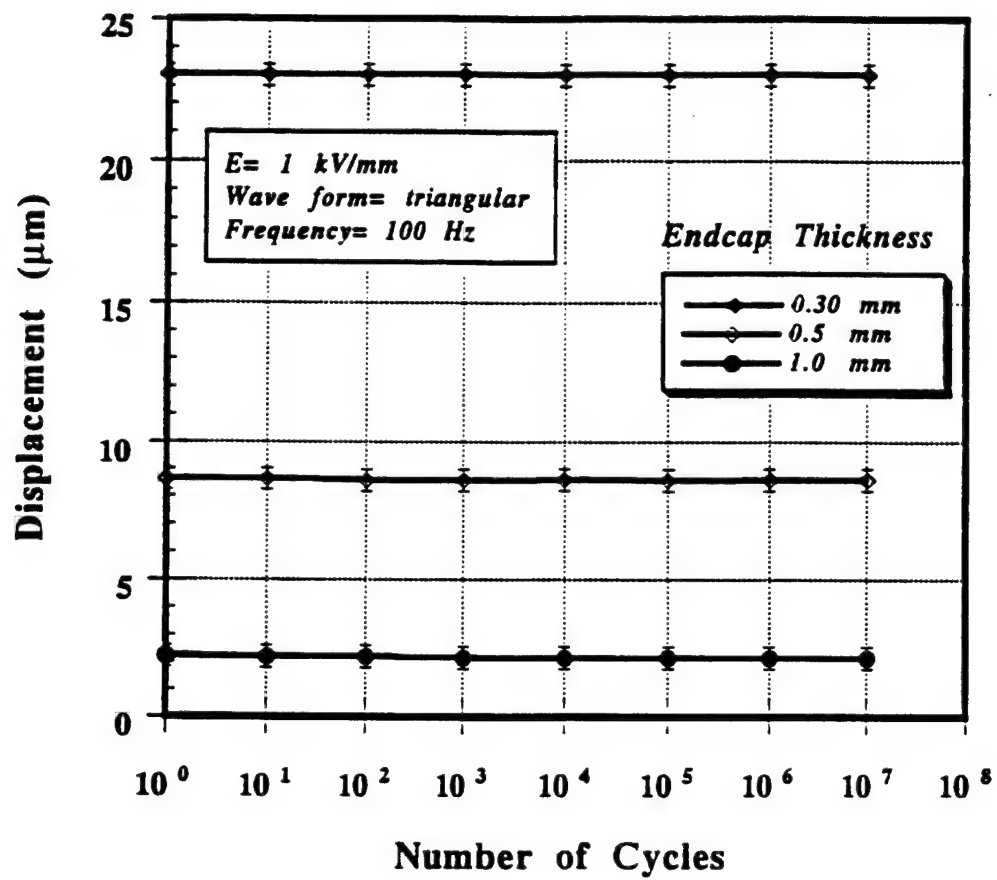
t_b (Ceramic-metal bonding layer) = 0.020, t_{bi} (inter-stack bonding layer) = 0.040



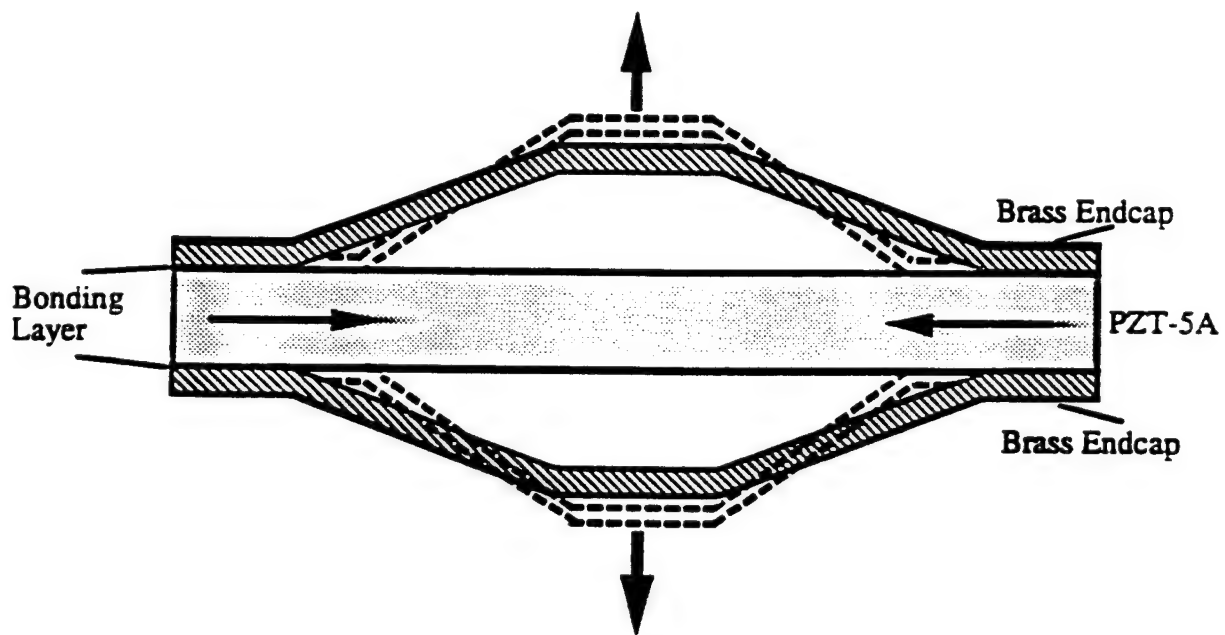
Dimensions: $d_m = 12.7$, $d_p = 12.7$, $t_p = 1.0$ (all in mm)



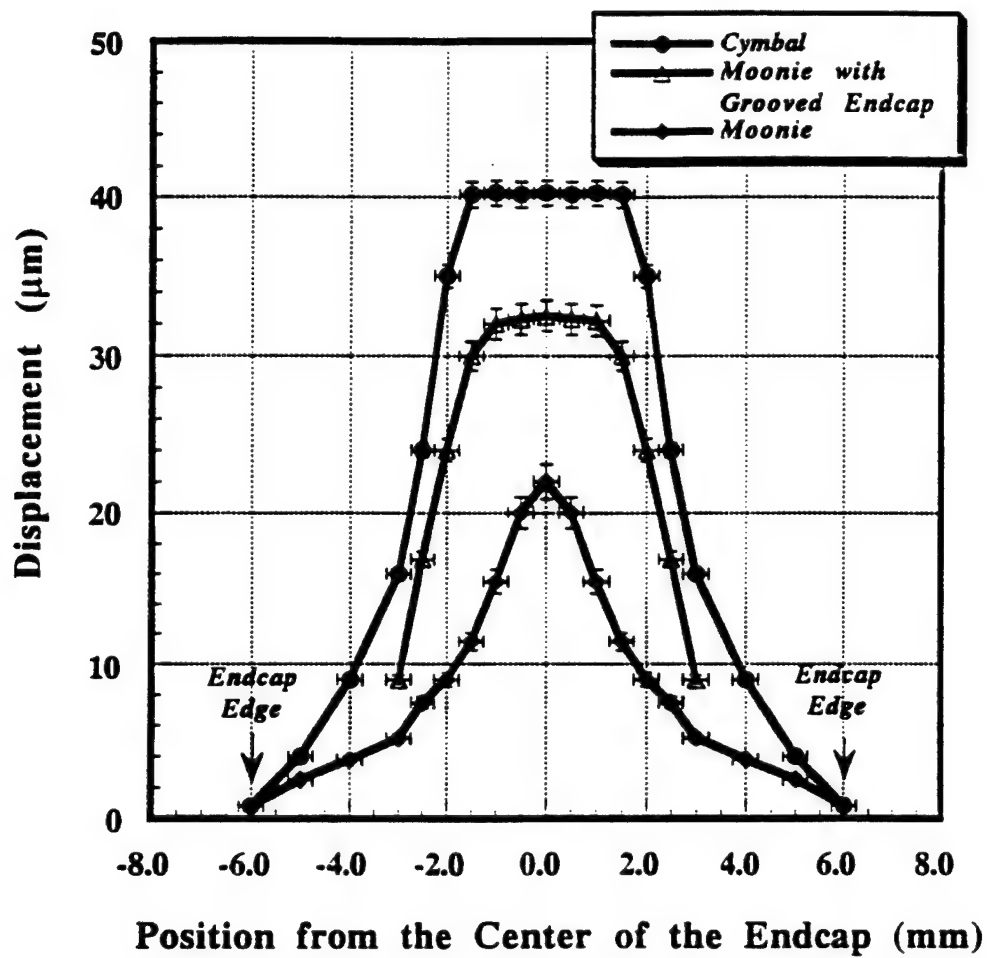
Dimensions: $d_m = 12.7$, $d_p = 12.7$, $d_c = 9.0$, $h = 0.2$, $t_p = 1.0$, (all in mm)



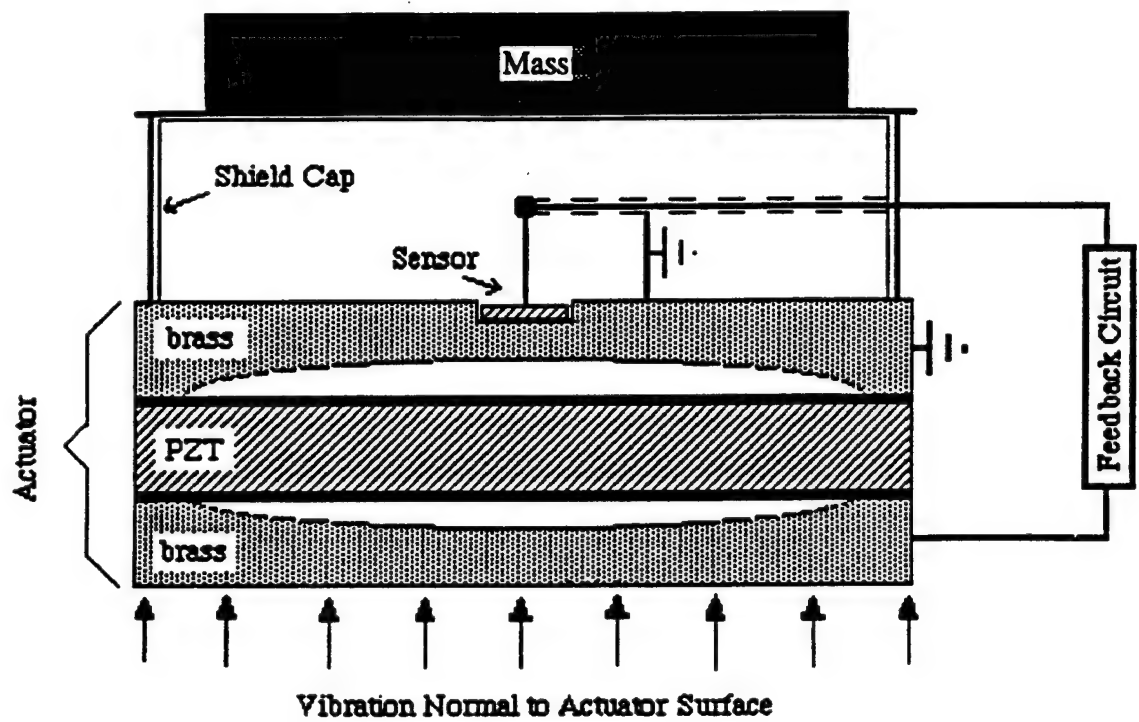
F9



F 10



Dimensions: $d_m = 12.7$, $d_p = 12.7$, $d_c = 9.0$, $h = 0.2$, $t_p = 1.0$, $t_m = 0.30$ (all in mm)



F.12

APPENDIX 3

RECENT DEVELOPMENTS IN CERAMIC ACTUATORS - COMPARISON AMONG USA, JAPAN AND EUROPE -

Kenji Uchino
International Center for Actuators and Transducers
Materials Research Laboratory, The Pennsylvania State University
University Park, PA 16802, USA

Abstract. In these several years, piezoelectric and electrostrictive materials have become key components in smart actuator/sensor systems such as precision positioners, miniature ultrasonic motors and adaptive mechanical dampers. This paper reviews recent developments of piezoelectric and related ceramic actuators with particular focus on the improvement of actuator materials, device designs and drive/control techniques of actuators. Developments will be compared among USA, Japan and Europe.

1 Introduction

Piezoelectric actuators are forming a new field between electronic and structural ceramics [1-4]. Application fields are classified into three categories: positioners, motors and vibration suppressors. The manufacturing precision of optical instruments such as lasers and cameras, and the positioning accuracy for fabricating semiconductor chips, which must be adjusted using solid-state actuators, is of the order of $0.1\ \mu\text{m}$. Regarding conventional electromagnetic motors, tiny motors smaller than $1\ \text{cm}^3$ are often required in office or factory automation equipment and are rather difficult to produce with sufficient energy efficiency. Ultrasonic motors whose efficiency is insensitive to size are superior in the mini-motor area. Vibration suppression in space structures and military vehicles using piezoelectric actuators is also a promising technology.

This article reviews recent applications of piezoelectric and related ceramics to smart actuator/sensor systems, including the improvement of actuator materials, design of the devices, drive/control techniques and integration of actuators and sensors. The developments are compared among USA, Japan and Europe.

2 Ceramic Actuator Materials

2.1 PRACTICAL ACTUATOR MATERIALS

Actuator materials are classified into three categories; piezoelectric, electrostrictive and phase-change materials. Modified lead zirconate titanate [PZT, $\text{Pb}(\text{Zr,Ti})\text{O}_3$] ceramics are currently the leading materials for piezoelectric applications. The PLZT $[(\text{Pb,Lu})(\text{Zr,Ti})\text{O}_3]$ 7/62/38 compound is one such composition [5]. The strain curve is shown in Fig.1(a) left. When the applied field is small, the induced strain is nearly proportional to the field ($x = dE$). As the field becomes larger (i.e., greater than about $100\ \text{V/mm}$), however, the strain

curve deviates from this linear trend and significant hysteresis is exhibited due to polarization reorientation. This sometimes limits the usage of this material in actuator applications that require nonhysteretic response.

An interesting new family of actuators has been fabricated in Germany from a barium stannate titanate system $[\text{Ba}(\text{Sn},\text{Ti})\text{O}_3]$ [6]. The useful property of $\text{Ba}(\text{Sn}_{0.15}\text{Ti}_{0.85})\text{O}_3$ is its unusual strain curve, in which the domain reorientation occurs only at low fields, and there is then a long linear range at higher fields (Fig.1(a) right); i.e., the coercive field is unusually small. Moreover, this system is particularly intriguing because no Pb ion is contained, which will be essential as ecological materials in the future.

On the other hand, electrostriction in PMN $[\text{Pb}(\text{Mg}_{1/3}\text{Nb}_{2/3})\text{O}_3]$ based ceramics developed in USA, though a second-order phenomenon of electromechanical coupling ($x = \text{ME}^2$), is extraordinarily large (more than 0.1 %) [7]. An attractive feature of these materials is the near absence of hysteresis (Fig.1(b)). The superiority of PMN to PZT was demonstrated in a Scanning Tunneling Microscope (STM) [8]. The PMN actuator could provide extremely small distortion of the image even when the probe was scanned in the opposite direction.

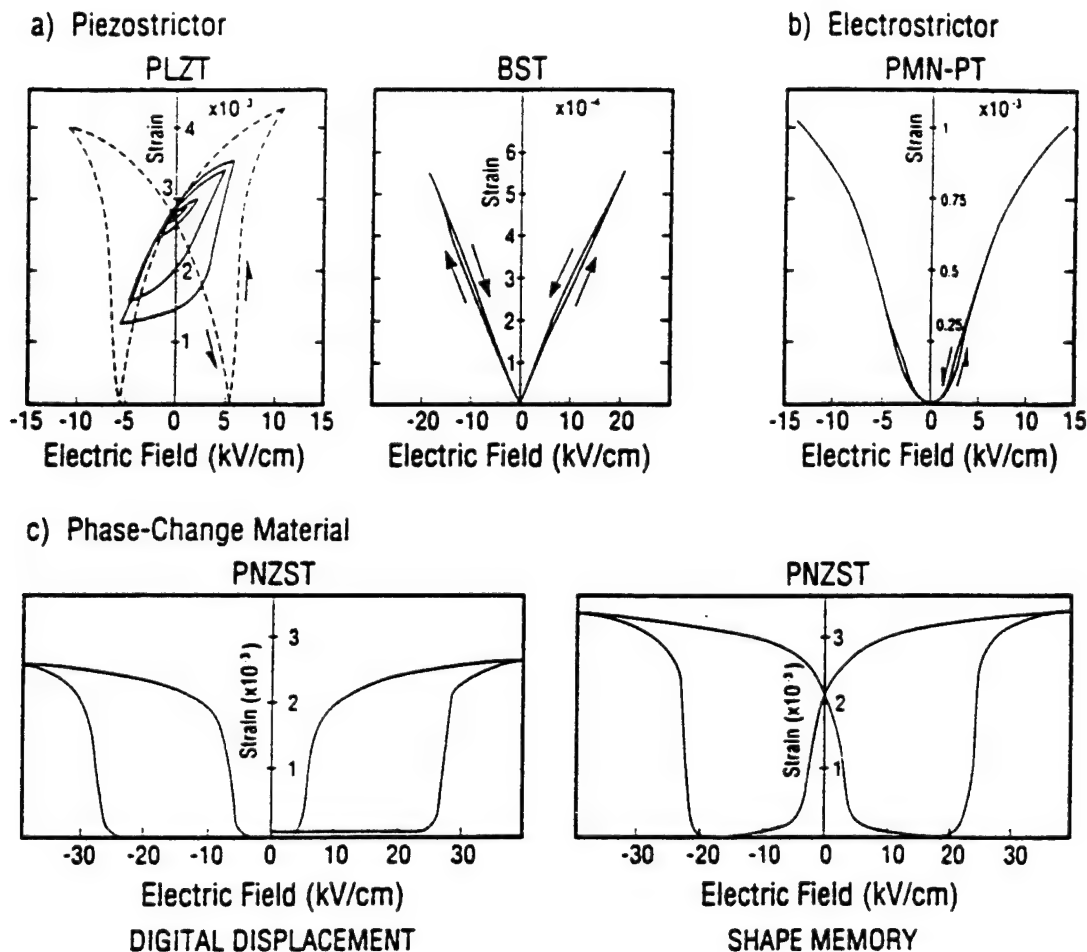


Fig.1 Electric field-induced strains in ceramics; (a) Piezoelectric $(\text{Pb},\text{La})(\text{Zr},\text{Ti})\text{O}_3$ and $\text{Ba}(\text{Sn},\text{Ti})\text{O}_3$. (b) Electrostrictive $\text{Pb}(\text{Mg}_{1/3}\text{Nb}_{2/3},\text{Ti})\text{O}_3$. (c) Phase-change material $\text{Pb}(\text{Zr},\text{Sn},\text{Ti})\text{O}_3$.

Concerning the phase-change-related strains, polarization induction by switching from an antiferroelectric to a ferroelectric state, has been proposed by our group[9]. Figure 1(c) shows the field-induced strain curves taken for the lead zirconate stannate based system $[\text{Pb}_{0.99}\text{Nb}_{0.02}((\text{Zr}_x\text{Sn}_{1-x})_1\text{yTi}_y)_{0.98}\text{O}_3]$. The longitudinally induced strain reaches up to 0.4%, which is much larger than that expected in normal piezoelectric or electrostrictors. A rectangular-shape hysteresis in Fig.1(c) left, referred to as a "digital displacement transducer" because of the two on/off strain states, is interesting. Moreover, this field-induced transition exhibits a shape memory effect in appropriate compositions (Fig.1(c) right). Once the ferroelectric phase has been induced, the material will "memorize" its ferroelectric state even under zero-field conditions, although it can be erased with the application of a small reverse bias field [10]. This shape memory ceramic is used in energy saving actuators. A latching relay in Fig.2 is composed of a shape memory ceramic unimorph and a mechanical snap action switch, which is driven by a pulse voltage of 4ms. Compared with the conventional electromagnetic relays, the new relay is much simple and compact in structure with almost the same response time.

2.2 NOVEL ACTUATOR MATERIALS

A monomorph device has been developed to replace the conventional bimorphs, with simpler structure and manufacturing process. The principle is a superposed effect of piezoelectricity and semiconductivity (Fig.3) [11]. The contact between a semiconductor and a metal (Schottky barrier) causes non-uniform distribution of the electric field, even in a compositionally uniform ceramic. Suppose that the ceramic possesses also piezoelectricity, only one side of a ceramic plate tends to contract, leading to a bending deformation in total. A monomorph plate with 30mm in length and 0.5 mm in thickness can generate 200 μm tip displacement, in equal magnitude of that of the conventional bimorphs [12]. The "rainbow" actuator by Aura Ceramics [13] is a modification of the above-mentioned semiconductive piezoelectric monomorphs, where half of the piezoelectric plate is reduced so as to make a thick semiconductive electrode to cause a bend.

A photostrictive actuator is a fine example of an intelligent material, incorporating "illumination sensing" and self production of "drive/control voltage" together with final "actuation." In certain ferroelectrics, a constant electromotive force is generated with exposure of light, and a photostrictive strain results from the coupling of this bulk photovoltaic effect to inverse piezoelectricity. A bimorph unit has been made from PLZT 3/52/48 ceramic doped with slight addition of tungsten [14]. The remnant polarization of one PLZT layer is parallel to the plate and in the direction opposite to that of the other plate. When a violet light is irradiated to one side of the PLZT bimorph, a photovoltage of 1 kV/mm is generated, causing a bending motion. The tip displacement of a 20mm bimorph 0.4mm in thickness was 150 μm , with a response time of 1 sec.

A photo-driven micro walking device, designed to begin moving by light illumination, has been developed [15]. As shown in Fig.4, it is simple in structure, having neither lead wires nor electric circuitry, with two bimorph legs fixed to a plastic board. When the legs are irradiated alternately with light, the device moves like an inchworm with a speed of 100 $\mu\text{m}/\text{min}$.

Table I summarizes the material developments in USA, Japan and Europe.

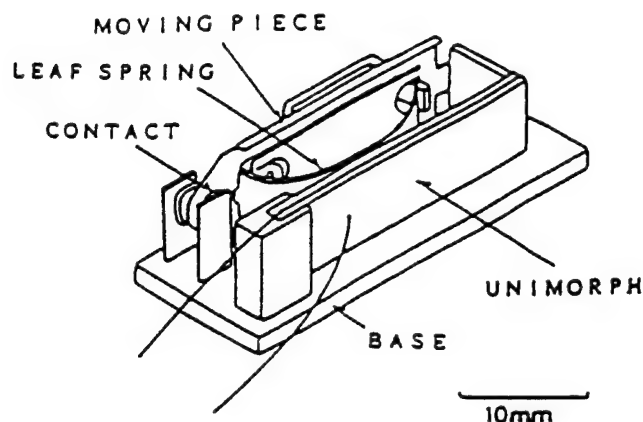


Fig.2 Latching relay using a shape memory ceramic unimorph.

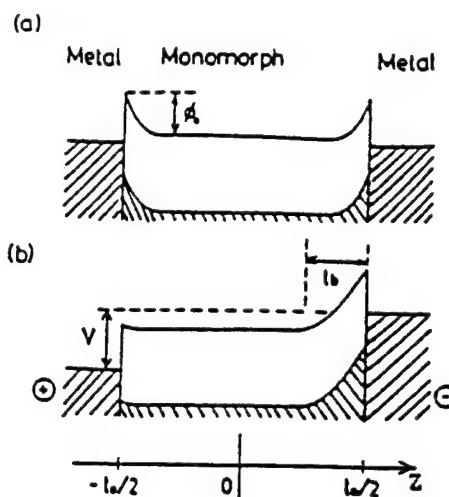


Fig.3 Electron energy band (Schottky barrier) model in monomorph devices (n-type semiconductor).

Table I Actuator materials developments.

US	JAPAN	EUROPE
*POSITIONER		
Pb(Mg _{1/3} Nb _{2/3})O ₃ -PbTiO ₃ Electrostrictor - Low hysteresis, non-linear	Pb(Zr,Ti)O ₃ -based Piezostrictor - Large strain (0.15%)	Ba(Sn,Ti)O ₃ Piezostrictor - Low hysteresis
*ULTRASONIC MOTOR		
	Pb(Zr,Ti)O ₃ -based Piezostrictor - high Q _m , low loss	
*SPECIAL PURPOSE		
Pb(Zr,Sn,Ti)O ₃ -based Phase change material - Large strain (0.4%) - Shape memory effect		
(Pb,Ln)(Zr,Ti)O ₃ -based Photostrictor - Remote control (photo-driven)		

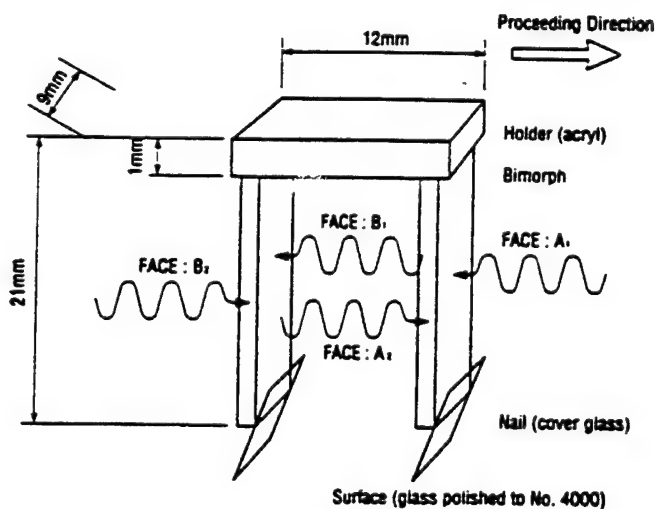


Fig.4 Structure of a photo-driven walking device and the illumination directions.

3 Actuator Designs

Two of the most popular actuator designs are multilayers and bimorphs (see Fig.5). The multilayer, in which roughly 100 thin piezoelectric/electrostrictive ceramic sheets are stacked together, has advantages in low driving voltage (100V), quick response (10 μ sec), high generative force (100kgf) and high electromechanical coupling. But the displacement in the range of 10 μ m is not sufficient for some applications. This contrasts with the bimorph, consisting of multiple piezoelectric and elastic plates bonded together to generate a large bending displacement of several hundred μ m, but the response (1msec) and the generative force (100gf) are low.

A composite actuator structure called the "moonie" has been developed at Penn State to provide characteristics intermediate between the multilayer and bimorph actuators; this transducer exhibits an order of magnitude larger displacement than the multilayer, and much larger generative force with quicker response than the bimorph [16]. The device consists of a thin multilayer piezoelectric element and two metal plates with narrow moon-shaped cavities bonded together as shown in Fig.5. The moonie with a size of 5 x 5 x 2.5 mm³ can generate a 20 μ m displacement under 60V, eight times as large as the generative displacement of the multilayer with the same size [17]. This new compact actuator has been applied to make a miniaturized laser beam scanner.

A 3-D positioning actuator with a stacked structure was also proposed by a German company as in Fig.6, where shear strain was utilized to generate the x and y displacements.

Table II summarizes the developments in actuator designs compared among USA, Japan and Europe.

4 Drive/Control Techniques

Piezoelectric/electrostrictive actuators may be classified into two categories, based on the type of driving voltage applied to the device and the nature of the strain induced by the voltage (Fig.7): (1) rigid displacement devices for which the strain is induced unidirectionally along an applied dc field, and (2) resonating displacement devices for which the alternating strain is excited by an ac field at the mechanical resonance frequency (ultrasonic motors). The first can be further divided into two types: servo displacement transducers (positioners) controlled by a feedback system through a position-detection signal, and pulse-drive motors operated in a simple on/off switching mode, exemplified by dot-matrix printers.

The materials requirements for these classes of devices are somewhat different, and certain compounds will be better suited to particular applications. The ultrasonic motor, for instance, requires a very hard type piezoelectric with a high mechanical quality factor Q, leading to the suppression of heat generation. Driving the motor at the antiresonant frequency, rather than at the resonant state, is also an intriguing technique to reduce the load on the piezo-ceramic and the power supply [18]. The servo-displacement transducer suffers most from strain hysteresis and, therefore, a PMN electrostrictor is used for this purpose. The pulse-drive motor requires a low permittivity material aiming at quick response with a certain power supply rather than a small hysteresis so that soft PZT piezoelectrics are preferred to the high-permittivity PMN for this application.

Fig.5 Typical designs for ceramic actuators: multilayer, moonie and bimorph.

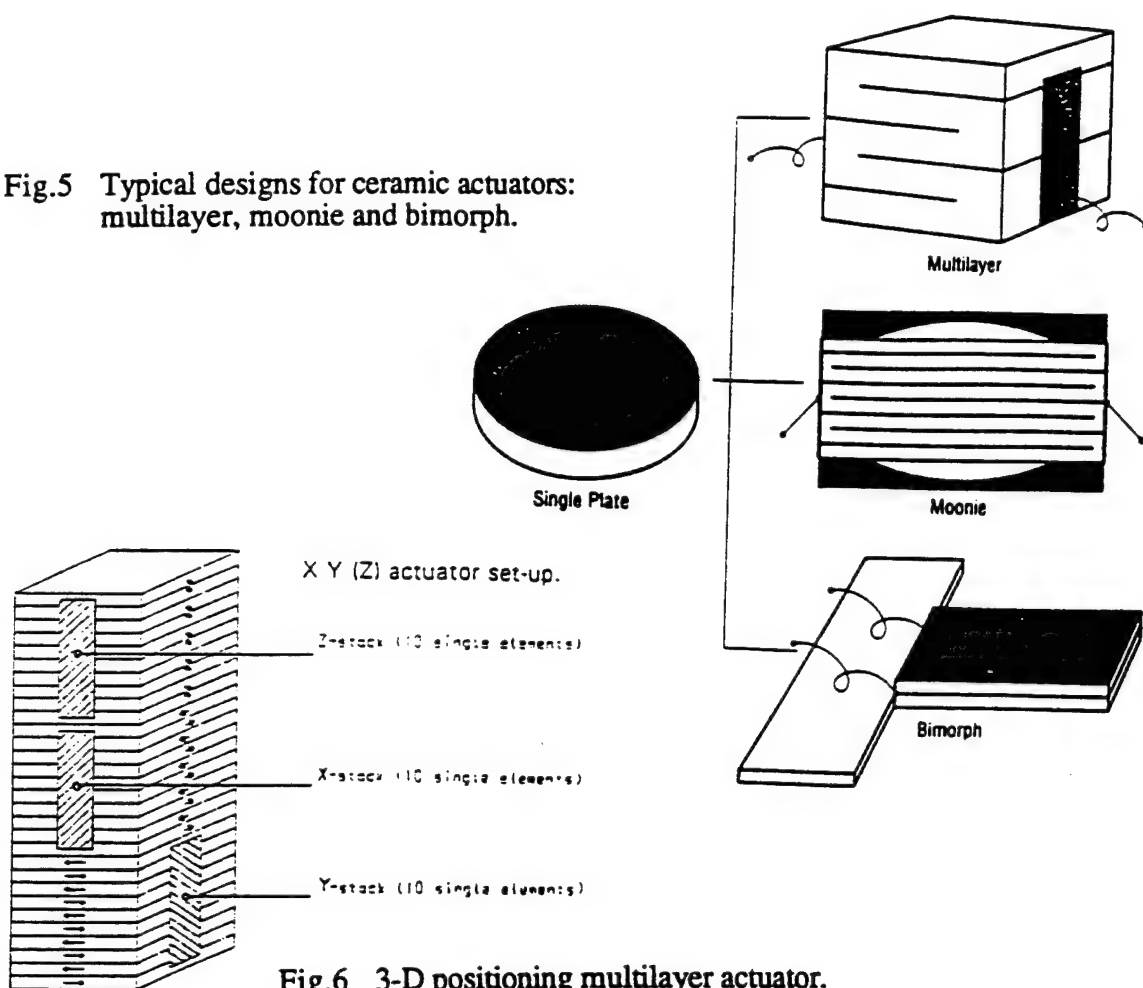


Fig.6 3-D positioning multilayer actuator.

Table II Actuator design developments.

DEVICE DEVELOPMENT

<u>US</u>	<u>JAPAN</u>	<u>EUROPE</u>
*RELIABILITY		
Multilayer with float electrodes	Multilayer with plate-through electrodes	Multilayer with very thin layers
Monomorph Rainbow		
*AMPLIFICATION MECHANISM		
Moonie, cymbal	Multilayer & Impact mechanisms	
*SPECIAL FUNCTION		
		Multilayer with 3-D function

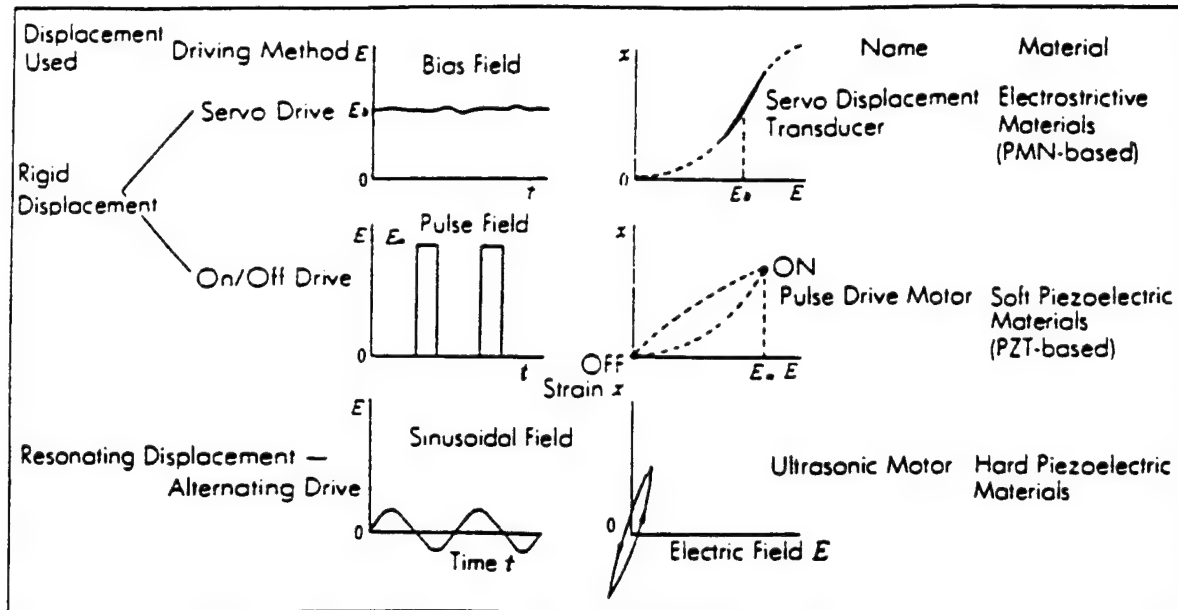


Fig.7 Classification of piezoelectric/electrostrictive actuators.

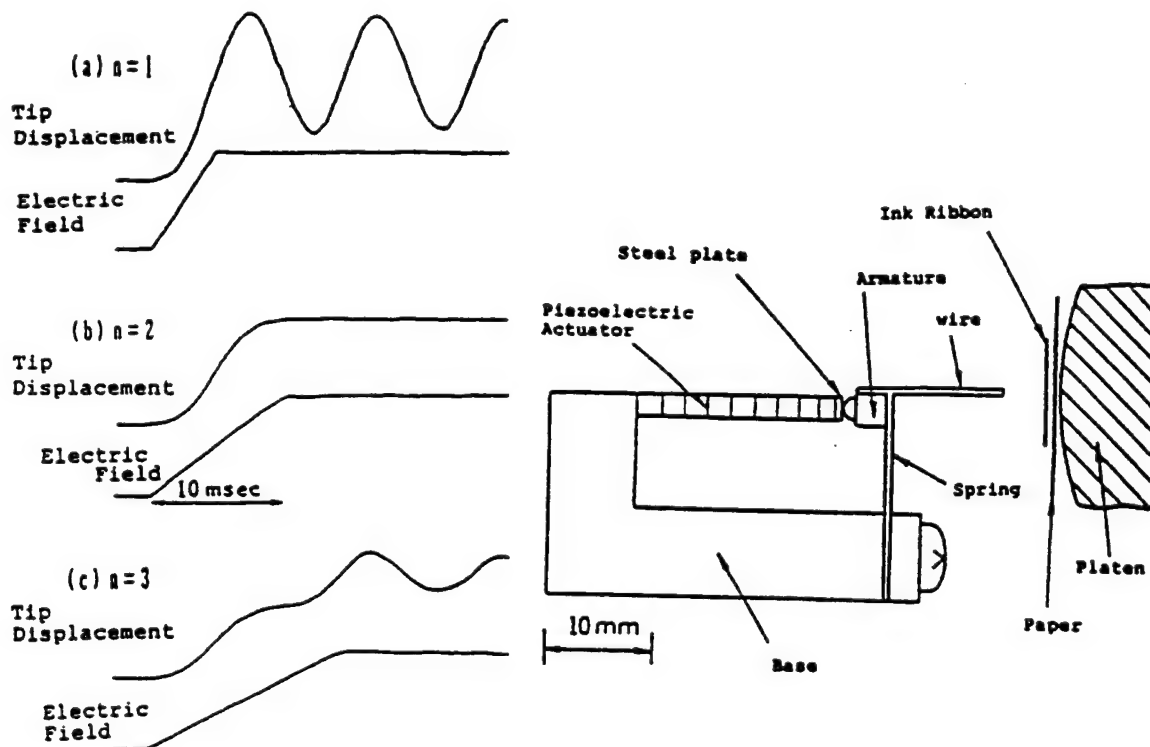


Fig.8 Transient vibration of a bimorph excited after a pseudo-step voltage applied. ($2n$ =resonance period)

Fig.9 Dot-matrix printer head using a flight actuator mechanism.

Pulse drive techniques of the ceramic actuator is very important for improving the response of the device [19]. Figure 8 shows transient vibrations of a bimorph excited after a pseudo-step voltage is applied. The rise time is varied around the resonance period. It is concluded that the overshoot and ringing of the tip displacement is completely suppressed when the rise time is precisely adjusted to the resonance period of the piezo-device. A flight actuator was developed using a pulse-drive piezoelectric element and a steel ball. A 2mm steel ball can be hit up to 20mm by a 5 μ m displacement induced in a multilayer actuator with quick response [19]. A dot-matrix printer head has been trially manufactured using a flight actuator as shown in Fig.9 [20]. By changing the drive voltage pulse width, the movement of the armature was easily controlled to realize no vibrational ringing or double hitting.

5 Device Applications

Table III compares the difference in the ceramic actuator developments among USA, Japan and Europe. The details will be described in this section.

5.1 USA

The target of the development is mainly for military-oriented applications such as vibration suppression in space structures and military vehicles. Notice the up-sizing trend of the actuators for these purposes.

A typical example is found in a space truss structure proposed by Jet Propulsion Laboratory [21]. A stacked PMN actuator was installed at each truss nodal point and functioned actively so that unnecessary mechanical vibration was suppressed immediately. A "hubble" telescope has also been proposed using multilayer PMN electrostrictive actuators to control the phase of the incident light wave in the field of optical information processing (Fig.10)[22]. The PMN electrostrictor provided superior adjustment of the telescope image because of negligible strain hysteresis.

Passive damper application is another smart usage of piezoelectrics, where mechanical noise vibration is radically suppressed by the converted electric energy dissipation through Joule heat when a suitable resistance, equal to an impedance of the piezoelectric element $1/\omega C$, is connected to the piezo-element [23]. Piezoceramic:carbon black:polymer composites are promising useful designs for practical application. Figure 11 shows the damping time constant change with volume percentage of the carbon black. The minimum time constant (i.e. quickest damping) is obtained at 6 % of carbon black, where a drastic electric conductivity change is observed (percolation threshold) [24].

5.2 JAPAN

Japanese industries seek to develop mass-consumer products, and the categories are only limited to mini-motor and positioner areas, aiming at the applications to office equipment and cameras/video cameras. In that sense, tiny actuators smaller than 1cm are the main focus.

A dot matrix printer is the first widely-commercialized product using ceramic actuators. Each character formed by such a printer is composed of a 24 x 24 dot matrix. A printing ribbon is subsequently impacted by a multiwire array. A sketch of the printer head appears

Table III Difference in the ceramic actuator developments among USA, Japan and Europe.

	US	Japan	Europe
TARGET	Military-oriented product	Mass-consumer product	Lab-equipment product
CATEGORY	Vibration suppressor	Mini-motor Positioner	Mini-motor Positioner Vibration suppressor
APPLICATION FIELD	Space structure Military vehicle	Office equipment Camera Precision machine Automobile	Lab stage/stepper Airplane Automobile Hydraulic system
ACTUATOR SIZE	Up-sizing (30cm)	Down-sizing (1cm)	Intermediate size (10cm)
MAJOR MANUFACTURER	AVX/Kyocera Morgan Matroc Itek Opt. Systems Burleigh AlliedSignal	Tokin Corp. NEC Hitachi Metal Mitsui-Sekka Canon Seiko Instruments	Philips Siemens Hoechst CeramTec Ferroperm Physik Instrumente

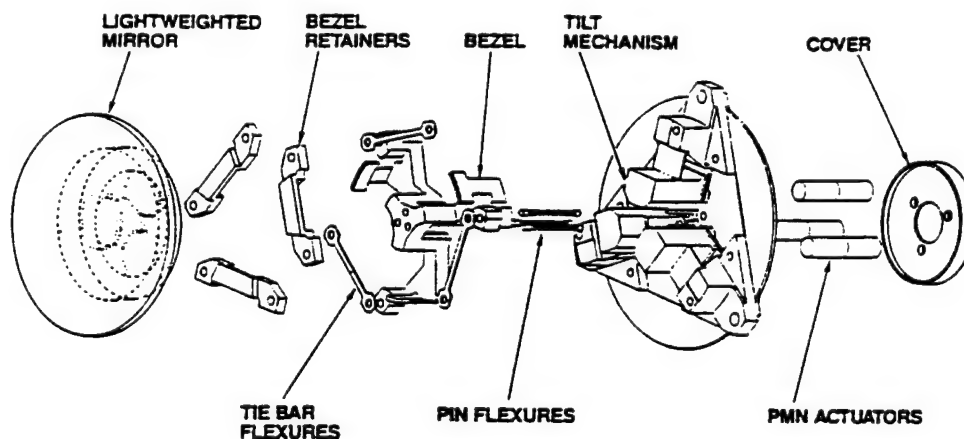


Fig.10 "Hubble" telescope using PMN electrostrictive actuators.

in Fig.12(a) [25]. The printing element is composed of a multilayer piezoelectric device, in which 100 thin ceramic sheets 100 μ m in thickness are stacked, together with a sophisticated magnification mechanism (Fig.12(b)). The magnification unit is based on a monolithic hinged lever with a magnification of 30, resulting in an amplified displacement of 0.5 mm and an energy transfer efficiency greater than 50%. A piezoelectric camera shutter is currently the largest production quantity item (Fig.13). A piece of piezoelectric bimorph can open and close the shutter in a milli-second through a mechanical wing mechanism [26]. Piezoelectric gyro-sensors are now widely used to detect the noise motion of a handy video camera. Figure 14 shows a Tokin's cylinder type gyroscope [27]. Among the 6 electrode strips, two of them are used to excite total vibration and the other two pairs of electrode are used to detect the Coriolis force or the rotational acceleration caused by the hand motion. By using the gyro signal, the image vibration can be compensated electrically on a monitor display.

Efforts have been made to develop high-power ultrasonic vibrators as replacements for conventional electromagnetic motors. The ultrasonic motor is characterized by "low speed and high torque," which is contrasted with "high speed and low torque" of the electromagnetic motors. Two categories are being investigated in Japan for ultrasonic motors: a standing-wave type and a propagating-wave type.

The standing-wave type is sometimes referred to as a vibratory-coupler type or a "woodpecker" type, where a vibratory piece is connected to a piezoelectric driver and the tip portion generates flat-elliptical movement. Attached to a rotor or a slider, the vibratory piece provides intermittent rotational torque or thrust. The standing-wave type has, in general, high efficiency, but lack of control in both clockwise and counterclockwise directions is a problem. An ultrasonic linear motor equipped with a multilayer piezoelectric actuator and fork-shaped metallic legs has been developed as shown in Fig.15 [28]. Since there is a slight difference in the mechanical resonance frequency between the two legs, the phase difference between the bending vibrations of both legs can be controlled by changing the drive frequency. The walking slider moves in a way similar to a horse using its fore and hind legs when trotting. A trial motor 20 x 20 x 5 mm³ in dimension exhibited a maximum speed of 20 cm/s and a maximum thrust of 0.2 kgf with a maximum efficiency of 20%, when driven at 98kHz of 6V (actual power = 0.7 W). This motor has been employed in a precision X-Y stage.

By comparison, the propagating-wave type (a surface-wave or "surfing" type) combines two standing waves with a 90 degree phase difference both in time and in space, and is controllable in both rotational directions (Fig.16) [29]. By means of the traveling elastic wave induced by a thin piezoelectric ring, a ring-type slider in contact with the "rippled" surface of the elastic body bonded onto the piezoelectric is driven in both directions by exchanging the sine and cosine voltage inputs. Another advantage is its thin design, which makes it suitable for installation in cameras as an automatic focusing device. 80 % of the exchange lenses in Canon's "EOS" camera series have already been replaced by the ultrasonic motor mechanism.

5.3 EUROPE

Ceramic actuator development has started relatively recently in Europe, and the research topics diverges very widely. However, the current focus by major manufacturers is probably put on lab-equipment products such as lab-stages and steppers with sophisticatedly complicated structures.

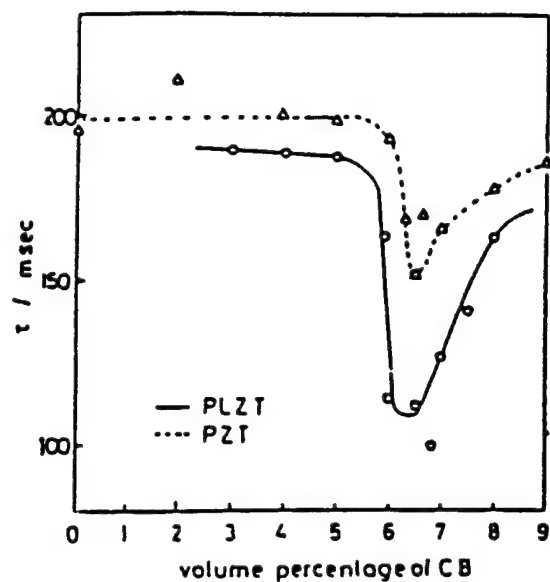


Fig.11 Damping time constant change with volume percentage of carbon black in piezoelectric composite dampers.

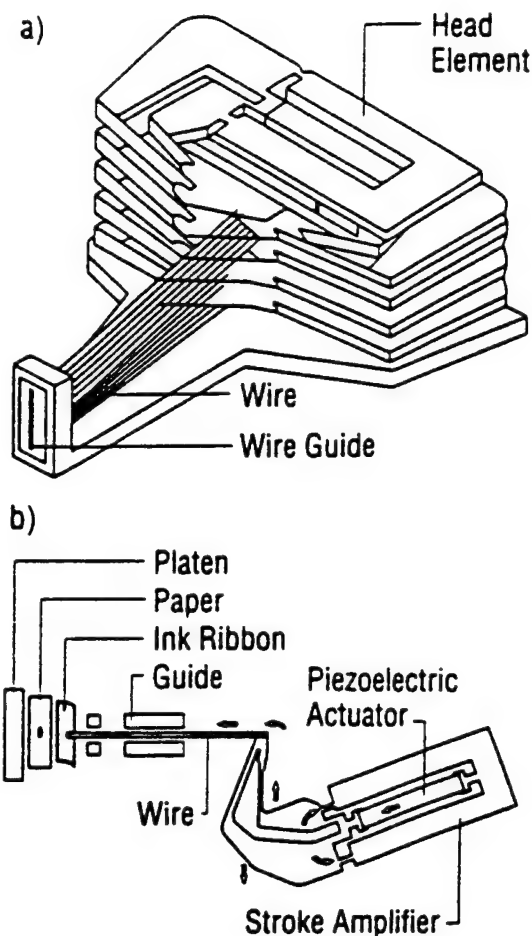


Fig.12 Structure of a printer head (a), and a differential-type piezoelectric printer-head element (b).

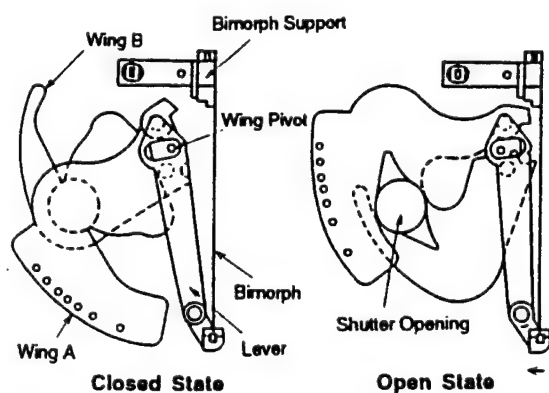


Fig.13 Piezoelectric camera shutter.

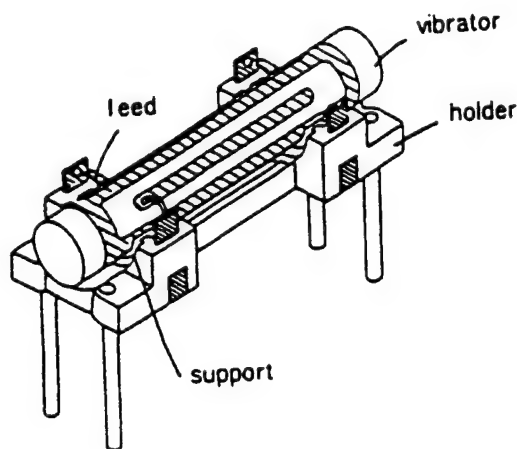


Fig.14 Piezo-ceramic cylinder vibratory gyroscope.

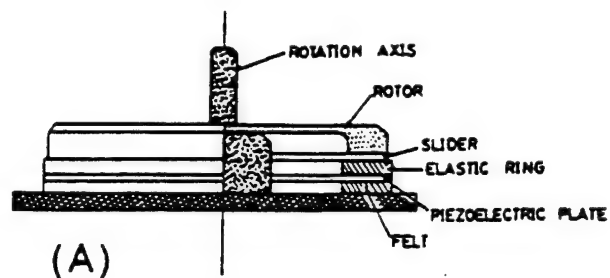


Diagram (B) illustrates a circular waveguide structure. The waveguide is divided into segments with alternating '+' and '-' signs. The slot is labeled with dimensions $(3/4)\lambda$ and $(1/4)\lambda$. The polarization direction is indicated by an arrow. The input and output ports are labeled A and B, with signals $\sin \omega t$ and $\cos \omega t$ respectively. The back side is labeled BACK SIDE.

12

Figure 17 shows a walking piezo motor with 4 multilayer actuators [30]. Shorter two are used to function as claspers and longer two provide the proceeding distance in an inchworm mechanism.

6 Future of Ceramic Actuators

18 years have passed since the intensive development of piezoelectric actuators began in Japan, then spreaded worldwide. Presently, the focus has been shifted to practical device applications.

The markets in USA is limited to military and defense applications, and it is difficult to estimate the sales amount. The current needs from Navy are smart submarine skins, hydrophone actuators, prop noise cancellation etc., and smart aircraft skins from Air Force, while Army requires helicopter rotor twisting, aeroservoelastic control and cabin noise/seat vibration cancellation.

On the contrary in Japan, piezoelectric shutters (Minolta Camera) and automatic focusing mechanisms in cemerars (Canon), dot-matrix printers (NEC) and part-feeders (Sanki) are now commercialized and mass-produced by tens of thousands of pieces per month. During the commercialization, new designs and drive-control techniques of the ceramic actuators have been mainly developed in the past few years. A number of patent disclosures have been found particularly in NEC, TOTO Corporation, Matsushita Electric, Brother Industry, Toyota Motors, Tokin, Hitachi Metal, Toshiba etc.

Several years ago Mr. T. Sekimoto, Former President of NEC, expressed his desire to the piezoelectric actuators in his New Year's speech that the market-share of piezoelectric actuators and their employed devices would reach up to \$10 billion (\$10¹⁰) in the future. If we estimate the annual sales in 2000 (without considering the current serious economical recession in Japan), ceramic actuator units, camera-related devices and ultrasonic motors will be expected to reach \$500 million, \$300 million and \$150 million, respectively. Regarding the final actuator-related products, \$10 billion will not be very different from the realistic amount.

Future research trends will be divided into two ways: up-sizing in space structures and down-sizing in office equipment. Further down-sizing will also be required in medical diagnostic applications such as blood test kits and surgical catheters. Piezoelectric thin films compatible with silicon technology will be much focused in micro-electromechanical systems. An ultrasonic rotary motor as tiny as 2 mm in diameter fabricated on a silicon membrane is a good example (see Fig.18) [31].

With expanding the application field of ceramic actuators, the durability/reliability issue becomes more important. The final goal is, of course, to develop much tougher actuator ceramics mechanically and electrically. However, the reliability can be improved significantly if the destruction symptom of the actuator is monitored.

Safety systems or health monitoring systems have been proposed with two feedback mechanisms: position feedback which can compensate the position drift and the hysteresis, and breakdown detection feedback which can stop the actuator system safely without causing any serious damages onto the work, e.g. in a lathe machine [32]. Acoustic emission and internal potential measurements, and resistance monitoring of a strain-gauge type internal electrode embedded in a piezo-actuator under a cyclic electric field drive are good predictors for the life time [33].

Future research and development should focus on superior systems ecologically (i.e. fit for human!) as well as technologically. Safety systems, which can monitor the fatigue or the destruction symptom of materials/devices, and stop the equipment safely without causing serious problems, will be desired.

7 References

- [1] K.Uchino, Piezoelectric/Electrostrictive Actuators, Morikita Publishing, Tokyo 1986
- [2] K.Uchino, Bull.Am.Ceram.Soc., 65(4), 647 (1986)
- [3] K.Uchino, MRS Bull., 18(4), 42 (1993)
- [4] K.Uchino, Proc. 4th Int'l Conf. Electronic Ceramics & Appl., p.179(1994)
- [5] K.Furuta and K.Uchino, Adv.Ceram.Mater., 1, 61 (1986)
- [6] J.von Cierninski and H.Beige, J.Phys.D, 24, 1182 (1991)
- [7] L.E.Cross, S.J.Jang, R.E.Newnham, S.Nomura and K.Uchino, Ferroelectrics, 23(3), 187(1980)
- [8] K.Uchino, Ceramic Data Book'88 (Chap.:Ceramic Actuators), Inst. Industrial Manufacturing Tech., Tokyo 1988
- [9] K.Uchino and S.Nomura, Ferroelectrics, 50(1), 191 (1983)
- [10] A.Furuta, K.Y.Oh and K.Uchino, Sensors and Mater., 3(4), 205 (1992)
- [11] K.Uchino, M.Yoshizaki, K.Kasai, H.Yamamura, N.Sakai and H.Asakura, Jpn.J.Appl.Phys., 26(7), 1046 (1987)
- [12] K.Uchino, M.Yoshizaki and A.Nagao, Ferroelectrics, 95, 161 (1989)
- [13] Aura Ceramics, Inc., Catalogue "Rainbow"
- [14] M.Tamura and K.Uchino, Sensors and Mater., 1, 47 (1988)
- [15] K.Uchino, J.Rob.Mech., 1(2), 124 (1989)
- [16] Y.Sugawara, K.Onitsuka, S.Yoshikawa, Q.C.Xu, R.E.Newnham and K.Uchino, J.Am.Ceram.Soc., 75(4), 996 (1992)
- [17] H.Goto, K.Imanaka and K.Uchino, Ultrasonic Techno, 5, 48 (1992)
- [18] N.Kanbe, M.Aoyagi, S.Hirose and Y.Tomikawa, J.Acoust.Soc.Jpn.(E), 14(4), 235 (1993)
- [19] S.Sugiyama and K.Uchino, Proc.Int'l.Symp.Appl.Ferroelectrics'86, IEEE, p.637 (1986)
- [20] T.Ota, T.Uchikawa and T.Mizutani, Jpn.J.Appl.Phys., 24, Suppl.24-3, 193 (1985)
- [21] J.T.Dorsey, T.R.Sutter and K.C.Wu, Proc. 3rd Int'l Conf. Adaptive Structures, p.352 (1992)
- [22] B.Wada, JPL Document D-10659, p.23 (1993)
- [23] K.Uchino and T.Ishii, J.Jpn.Ceram.Soc., 96(8), 863 (1988)
- [24] Y.Suzuki, K.Uchino, H.Gouda, M.Sumita, R.E.Newnham and A.R.Ramachandran, J.Jpn.Ceram.Soc., 99(11), 1135 (1991)
- [25] T.Yano, I.Fukui, E.Sato, O.Inui and Y.Miyazaki, Proc. Electr. & Commun.Soc., p.1-156 (Spring, 1984)
- [26] Y.Tanaka, Handbook on New Actuators for Precision Control, Fuji Technosystem, p.764 (1994)
- [27] Tokin Corporation, Catalogue "Ceramic Gyro"
- [28] M.Tohda, S.Ichikawa, K.Uchino and K.Kato, Ferroelectrics, 93, 287 (1989)
- [29] Y.Akiyama (Editor), Ultrasonic Motors/Actuators, Triceps, Tokyo 1986
- [30] M.P.Koster, Proc. 4th Int'l Conf. New Actuators, Germany, p.144 (1994)
- [31] A.M.Flyn, L.S.Tavrow, S.F.Bart, R.A.Brooks, D.J.Ehrlich, K.R.Udayakumar and L.E.Cross, J. Microelectromechanical Systems, 1, 44 (1992)
- [32] K.Uchino, J.Industrial Education Soc. Jpn., 40, 28 (1992)
- [33] K.Uchino and H.Aburatani, Proc. 2nd Int'l Conf. Intelligent Materials, p.1248 (1994)

APPENDIX 4

In Situ Annealing Studies of Sol-Gel Ferroelectric Thin Films by Spectroscopic Ellipsometry

Susan Trolier-McKinstry,^{*} Jiayu Chen, Kuppuswami Vedam, and Robert E. Newnham^{*}

Intercollege Materials Research Laboratory, The Pennsylvania State University, University Park, Pennsylvania 16802

Spectroscopic ellipsometry was utilized to follow *in situ* the annealing of sol-gel $\text{Pb}(\text{Zr,Ti})\text{O}_3$ films on sapphire and platinum-coated silicon substrates. Low-temperature processes, such as pyrolysis of organics and film densification, could be identified readily. Crystallization of the perovskite phase was initiated between 500° and 600°C for the film on sapphire. This was coincident with the roughening of the film surface. Identification of higher-temperature processes in the film on platinum-coated silicon was complicated by temperature-dependent changes in the substrate. *In situ* annealing studies on the substrate alone confirmed that, for the lengthy annealing profiles utilized in these experiments, substantial and irreversible changes in the effective substrate dielectric function occurred at temperatures >550°C. In addition, the role of extended, high-temperature annealing on the optical frequency dielectric properties of the films was investigated.

I. Introduction

SOL-GEL processing has emerged as one of the preferred methods for preparing ferroelectric thin films. As with other deposition techniques, the properties of the films are expected to be closely related to the structural and microstructural quality of the sample. Consequently, an understanding of the factors that control the development of the perovskite phase, grain size, and evolution of microstructural features such as incorporated porosity or surface roughness, in sol-gel films is important.

In this work, spectroscopic ellipsometry (SE) has been utilized to follow changes in the optical properties and the physical structure of sol-gel films on both platinum-coated silicon and sapphire substrates during annealing. SE is a light reflection technique that, in conjunction with computer modeling of the experimental data, is capable of nondestructively depth profiling thin-film samples with depth resolution in the Angstrom range. Fundamentally, this is done by measuring the relative changes in the amplitude and the phase of light polarized parallel (p) and perpendicular (s) to the plane of incidence, on reflection from the sample surface. The change in the light polarization state on reflection is determined by the depth profile of the dielectric function. The ellipsometric angles Δ and Ψ are related to the complex reflection coefficient \tilde{r} through

$$\tilde{p} = \tan \Psi e^{i\Delta} = \frac{\tilde{r}_p}{\tilde{r}_s}$$

where \tilde{r}_p and \tilde{r}_s are the reflection coefficients for p- and s-polarized light. Δ and Ψ are typically measured at ~100 wavelengths over the spectral range between ~400 and 800 nm.

A model describing the depth profile of the sample is then developed, and Δ and Ψ values are calculated using the Fresnel reflection coefficients. These values then are compared to the experimental data. Various parameters describing the depth profile (including layer thicknesses, optical properties of a given layer, or volume fraction of a second phase within a given layer) are optimized to obtain a best fit to the experimental data, using a nonlinear least-squares algorithm. Thus, SE offers a means of nondestructively depth profiling samples over the penetration depth of the light used. This technique is widely used in the study of semiconductor materials,^{1,2} and more recently for dielectrics.³⁻⁵ It has been shown previously that the depth profiles determined by SE correlate well with those measured directly using cross-sectional TEM.¹

II. Experimental Procedure

Sol-gel PZT films with a 52:48 zirconium:titanium ratio were prepared as described previously^{6,7} from lead acetate trihydrate, titanium isopropoxide, and zirconium propoxide precursors using methoxyethanol as a solvent. The solution was spun onto a platinum/titanium/silica/silicon wafer (obtained from Ramtron Corp., Colorado Springs, CO), and the film was heated rapidly to ~200°C, where it was held for 1–2 min to remove the solvent. This flash heating also helped densify the deposit and prevent cracks that would otherwise appear in thick sol-gel films. The process was repeated to build up a layer ~400 nm thick. The wafer was subsequently cut in several sections so that the effect of varying thermal treatments on film density and homogeneity could be determined on samples with identical preparation history. Similar films were prepared on a sapphire single crystal, although, in this case, the pyrolysis between coating cycles was performed at 400°C.

Descriptions of the rotating analyzer spectroscopic ellipsometer utilized in these experiments have been given previously.^{3,4} Sample-independent corrections were used to minimize error associated with changes in the ac/dc gain as a function of the voltage applied to the photomultiplier tube and the dark current. In addition, an effective source correction was utilized to account for wavelength-dependent changes in the ellipticity of the light output from the compensator. A complete description of the calibration procedures used is given elsewhere.⁴ With these corrections in place, Ψ and Δ can be measured on either transparent or opaque samples with an estimated accuracy of 0.01° and 0.03°, respectively, between 300 and 800 nm.

A windowless electrical-resistance furnace was built to house the sample for *in situ* annealing studies. A kanthal-wire-wrapped alumina tube was used as the heat source. Two outer cylinders were machined for incidence angles of 70° and 80°. These brass cylinders and the baseplate were electroplated with nickel to minimize oxidation of the copper and vaporization of the zinc at elevated temperatures. The furnace temperature was controlled by computer. Temperatures between 25° and 700°C could be achieved easily. However, a practical upper limit for *in situ* ellipsometric measurements was 450°C, where glow from the furnace interfered with the light reflected from the

L. C. Klein—contributing editor

Manuscript No. 193439. Received July 1, 1994; approved March 10, 1995.

Based in part on a thesis submitted by S. Trolier-McKinstry for the Ph.D. degree in Ceramic Science, The Pennsylvania State University, University Park, PA, 1993.

^{*}Member, American Ceramic Society.

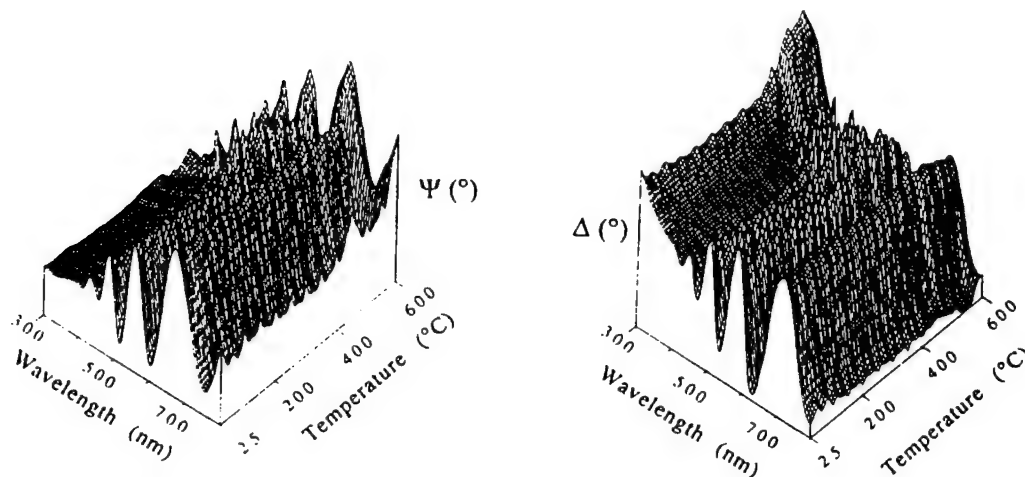


Fig. 1. Experimental data for the *in situ* annealing of a PZT film on sapphire. Ellipsometric spectra were collected every 50°C from room temperature to 600°C to obtain this graph.

sample surface. Below this cutoff, the furnace temperature did not significantly degrade the quality of the SE data.⁸

In these experiments, measurements were made at an incidence angle of 80°, with the compensator in place for the films on sapphire substrates. Films on platinum-coated silicon were measured at an incidence angle of 70°, without the compensator. *In situ* annealing studies were conducted by aligning the samples at room temperature and then assembling the furnace with the sample in place. SE data were first taken at room temperature. The film was heated to 100°C at the rate of 2°C/min without changing the sample position, realigned (to counteract drift in the screws controlling the angle of the sample mount), and remeasured. This process was repeated at 50°C temperature increments. Above 350°C, glow from the furnace contributed to the measured light signal. To eliminate errors associated with this, for anneals above 350°C, the samples were heated to the desired temperature, held for 0.5 h, and then cooled below 350°C for measurement. Ramp rates of 2°C/min were utilized during the annealing.

Modeling of the films was done using reference data for the substrates and a single oscillator of the form

$$n^2 = 1 + \frac{A\lambda^2}{\lambda^2 - B^2 - i2C\lambda}$$

to describe the unknown dielectric function of the films, where n is the complex index of refraction, λ is the wavelength (in nanometers), and A , B , and C are constants. Bruggeman effective medium theory was used to describe the optical properties of two phase mixtures.⁴ In all cases, the films and the substrates were treated as isotropic materials. Best-fit models were chosen by optimizing simultaneously the comparison between the experimental and modeled spectra, unbiased estimator for the differences between them, physical likelihood of the solution, 90% confidence limits on each fitting parameter, and correlation coefficient matrix describing the degree of interdependence between the parameters. The sum of the squares of the error (from which the unbiased error estimator is defined) between the experimental (exp) and calculated (calc) data sets was determined for films on transparent substrates from

$$\sum_m (\Delta_{\text{exp}} - \Delta_{\text{calc}})^2 + (\Psi_{\text{exp}} - \Psi_{\text{calc}})^2$$

where m is the number of wavelengths used in the fitting.

In contrast, for films on platinum-coated silicon substrates, the sum of the squares of the error used was determined from

$$\sum_m (\cos \Delta_{\text{exp}} - \cos \Delta_{\text{calc}})^2 + (\tan \Psi_{\text{exp}} - \tan \Psi_{\text{calc}})^2$$

This allows the experimental data to be weighted according to the accuracy with which it can be measured.⁴

III. Results

One section of the film on the platinum-coated silicon substrate and a similar sample deposited on sapphire were annealed *in situ* in the ellipsometer. Figure 1 shows the experimental data for the variation in the ellipsometric parameters Δ and Ψ as functions of wavelength and temperature. The spectrum at each temperature was modeled independently. It was found that PZT film was homogeneous throughout its thickness for both substrates at low temperatures (less than ~400°C), and could be well fitted by allowing the thickness and optical properties of the film to vary. Thus, for example, the best-fit model for the film on sapphire at 100°C gave a thickness of 258.6 ± 0.9 nm; the unbiased error estimator for the fit was 0.6° (see Fig. 2).

In Fig. 3, a plot of the film thickness as a function of the annealing temperature for films that had been heat-treated

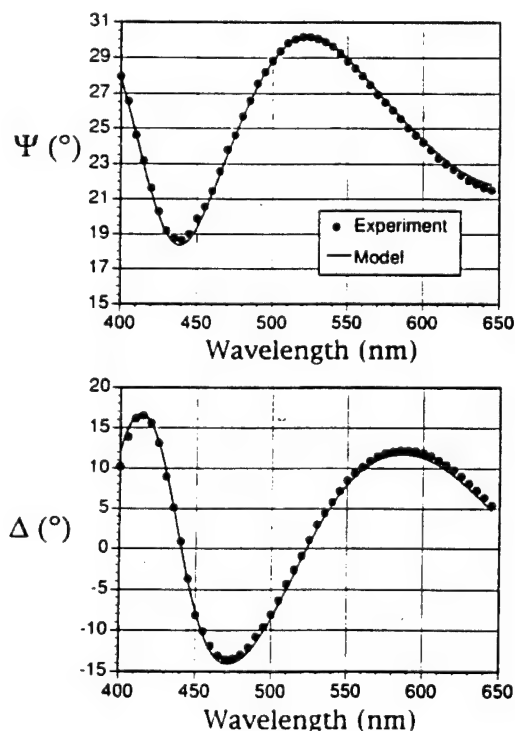


Fig. 2. Experimental and modeled values for the ellipsometric parameters Δ and Ψ for a PZT film on sapphire following a 100°C anneal. Film was modeled as a single layer on the substrate. Good agreement suggests that the film is well described as homogeneous through its thickness.

between spin coatings at $\sim 200^\circ$ and 400°C is shown. A large decrease in the film thickness occurred between 150° and 350°C for the film pretreated at lower temperatures; this temperature range also was marked by a substantial increase in parameters A and B , describing the effective film refractive index and its dispersion. The film pyrolyzed at 400°C , however, was fully collapsed, and did not show any change in the film depth profile or optical properties below the burnout temperature. The ellipsometric parameters Δ and Ψ changed continuously at low temperatures for the film heat-treated at 200°C because of structural and chemical changes in the film. Consequently, the models of the lower-temperature data on that film do not constitute equilibrium structures, but, rather, distinct points during the burnout process. At higher temperatures, the changes in both films were very rapid; therefore, Δ and Ψ were not observed to change with time once the measurement temperature had been reached.

In contrast to ion-beam-sputtered PZT films,⁵ the optical properties of sol-gel films at low temperatures were well described by a single oscillator. The fact that no additional optically lossy phase (such as the lossy lead oxide necessary in the sputtered films) was required to model the as-deposited films is probably a reflection of the excellent stoichiometry shown in most sol-gel films. Below 350°C , the refractive index of the film on sapphire was both low (~ 2.25 at 550 nm , as compared to ~ 2.6 for the perovskite phase) and nearly temperature independent. This film did not undergo a significant collapse in thickness at any temperature, including the crystallization temperature. Consequently, the low refractive index at low temperatures is probably associated primarily with the lack of crystallinity rather than low density.

The unbiased estimator of the error in the fit between calculated and experimental spectra, σ , began to increase above its average value at low temperatures for anneals between 350° and 400°C for the films on both sapphire and platinum-coated silicon. As discussed by An *et al.*,² in *in situ* SE measurements, transitions between different models are indicated by places where σ begins to diverge from a steady value. Additional analysis of the experimental data suggests that, for the PZT films, these changes did not correspond to the generation of surface roughness, interface porosity, or increased absorption in the film. One possible reason for this deviation could be the formation of heterogeneities within the film which lead to light scattering. In general, it was found that the presence of multiple phases within a film (in this case, probably the amorphous precursor and a pyrochlore phase) leads to an increase in σ which is difficult to eliminate through changes in the model depth profile.

At 450°C and above, however, the ongoing increase in σ could be eliminated by allowing a progressive roughening of the surface of the film on sapphire (i.e., at 450°C , σ could be

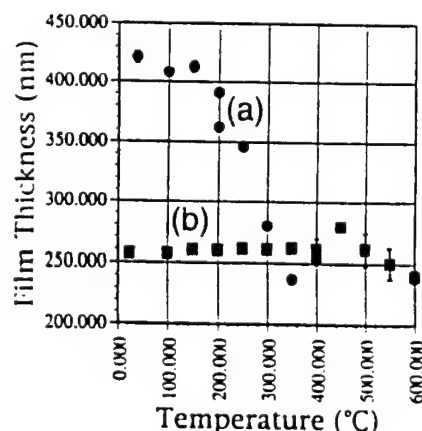


Fig. 3. Film thickness as a function of annealing temperature for sol-gel PZT films heat-treated between coatings at (a) 200° and (b) 400°C . Substrate in (a) is platinum-coated silicon and in (b) is sapphire.

lowered from 3.6° to 0.73° by adding a layer of surface roughness to the model). This continued until 550°C , above which the thickness and volume fraction of air in the roughness layer were approximately temperature independent. In all cases, an increase in the roughness, determined by SE, correlated with a visually observable increase in scattering from the surface of the sample, as observed in reflected light.

Initial fits of the data at 500°C and above with only a layer of surface roughness led to modeled refractive index values less than those for bulk PZT and relatively high σ values (2.6°). Given that Δ and Ψ could typically be determined with an accuracy better than 0.05° , such a fit was clearly unacceptable. This situation was improved significantly by incorporating an additional low-density layer in the film. For example, Fig. 4 shows a comparison of one-, two-, and three-layer models for the data set at 600°C . A three-layer model was required to adequately model the structure in the Ψ and Δ spectra. In terms of the unbiased error estimator for the fits to the 600°C data, addition of the third layer lowered σ to 0.36° . Because this is on the order of the accuracy of the experimental data, it was judged that additional complication of the model (beyond three layers) was not warranted. Similarly, three-layer models were required for data at 500° , 550° , and 650°C .

On the basis of the optical data alone, it was difficult to distinguish between two different three-layer models, one of which had a significantly lower refractive index than the other. Because SEM micrographs indicated a dense microstructure and XRD demonstrated that the film was crystalline (with a considerable amount of residual pyrochlore, in addition to the perovskite phase following the 650°C anneal (Fig. 5)), the model with the higher refractive index was chosen. The best-fit modeled depth profiles for the higher-temperature anneals are shown in Fig. 6. In each case, the quality of the fit to the experimental data was comparable to that shown in Fig. 4. Each of the models was consistent with the dense columnar microstructure previously reported for sol-gel films on single-crystal substrates.

The changes in the microstructure were coupled with a marked increase in the film refractive index between 500° and

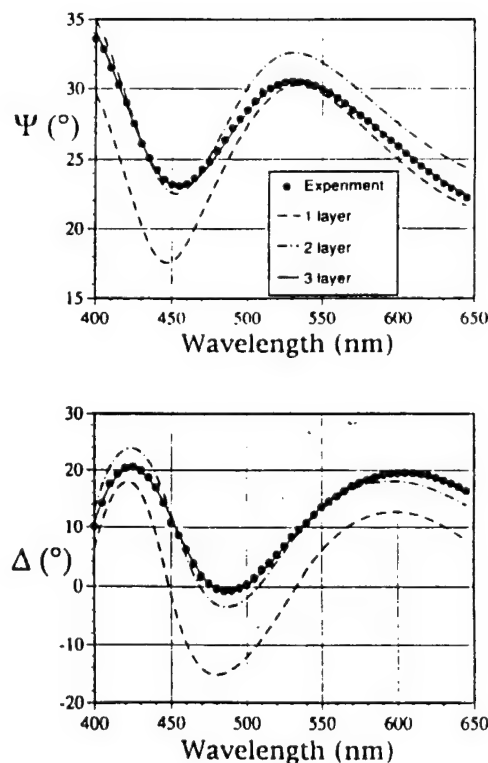


Fig. 4. Comparison of experimental Δ and Ψ spectra following the 600°C anneal with best-fit one-, two-, and three-layer models. Three-layer model is clearly superior.

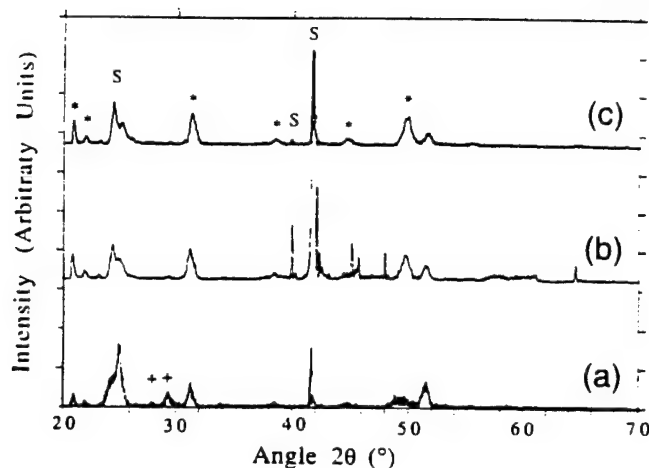


Fig. 5. XRD pattern following 650°C anneals: (a) 0.5, (b) 2, and (c) 3.5 h anneal ((*) denotes perovskite peaks, (+) denotes pyrochlore peaks, and (S) denotes substrate peaks).

600°C (see Fig. 7). This increase in the refractive index was associated with crystallization of the film. Independent X-ray studies on films prepared in a similar manner confirmed that the perovskite phase began to crystallize in this temperature range.⁹ In addition, a significant amount of pyrochlore was apparent in the XRD pattern of this film following the 600°C anneal. The pyrochlore was removed by *ex situ* annealing of the film in a conventional furnace at 650°C for 1.5 h (Fig. 5). The sample was remeasured using SE following this anneal. There was no large decrease in the refractive index of the type reported by Peng and Desu.¹⁰

These changes were more difficult to follow for the film on platinum-coated silicon. As for the film on sapphire, there was an increase in σ at 550°C, suggesting the need for a more-complex model. Although an increase in surface roughness and refractive index of the film partially counteracted the increase in σ , larger improvements were obtained by allowing the effective substrate optical properties to become less metallic in character. As shown in Fig. 8, the ellipsometric spectra for a platinum-coated silicon substrate exposed to the similar extended temperature profile underwent a notable transformation in this temperature range. Previous studies indicated that diffusion of the titanium bonding layer through the platinum, coupled with oxidation of the titanium, occurred at elevated temperatures in oxidizing atmospheres.^{11,12} The platinum thickness was much greater than the penetration depth of visible light in the metal for these substrates. Thus, the fact that changes in the substrate were detected optically indicated that the diffusion had progressed to the near surface region of the substrate (within the top few hundred Ångströms). Changes in the substrate were less marked in films annealed for shorter times at temperatures >500°C. Even in those cases, however, it was frequently found that the measured refractive index of the film was too high if changes in the substrate were neglected. Consequently, some care should be adopted in interpreting optical measurements of films on platinum-coated silicon substrates.

Because of this change in the substrate, determination of the exact microstructure or optical properties of the sol-gel film on platinum-coated silicon annealed at (or above) this temperature was not possible, given the large number of unknowns in both the film and substrate properties. This prohibited an estimation of the bulk density of the film, measurement of the degree of surface roughness, and determination of whether there is a reaction layer formed between the ferroelectric film and the electrode during the long annealing profile utilized. As was the case for the film on sapphire, it was believed that an increase in the film refractive index and a roughening of the film surface occurred associated with crystallization of the perovskite phase. The XRD pattern of this film, after completion of the heating

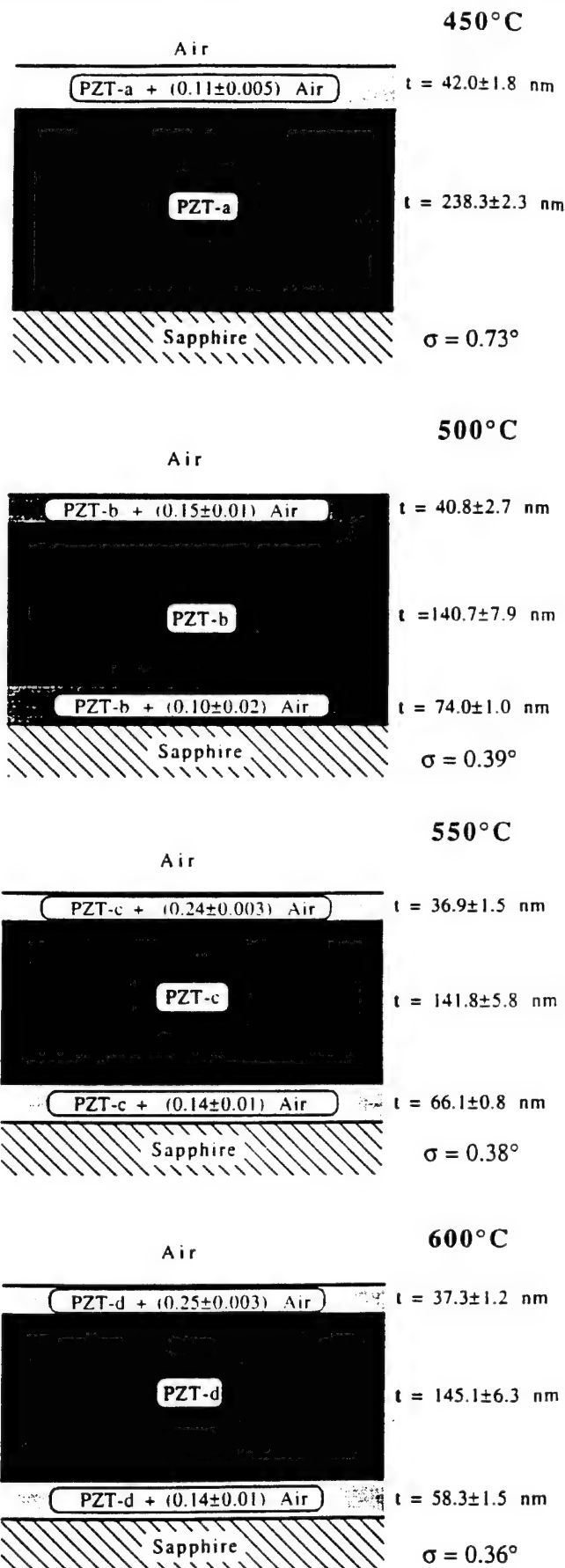


Fig. 6. Depth profiles of sol-gel films as a function of annealing temperature. Notations PZT-a, PZT-b, PZT-c, and PZT-d denote that refractive index of the film material is different for different annealing temperatures (see Fig. 6).

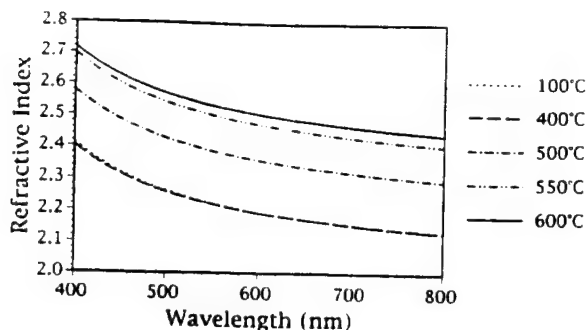


Fig. 7. Refractive index of a PZT film on sapphire versus annealing temperature (corrected for inhomogeneities).

run, showed that the film consisted largely of a crystalline perovskite phase with a small amount of poorly crystallized pyrochlore.

IV. Extended Anneal at 600°C

Measurements of the dielectric constant as a function of frequency on similar sol-gel PZT films showed that there was a high-frequency roll-off in the dielectric constant of films fired at high temperatures.⁷ In an attempt to determine the mechanism causing this phenomenon, a second piece of the sample was examined by SE at several points during an extended anneal at 600°C.

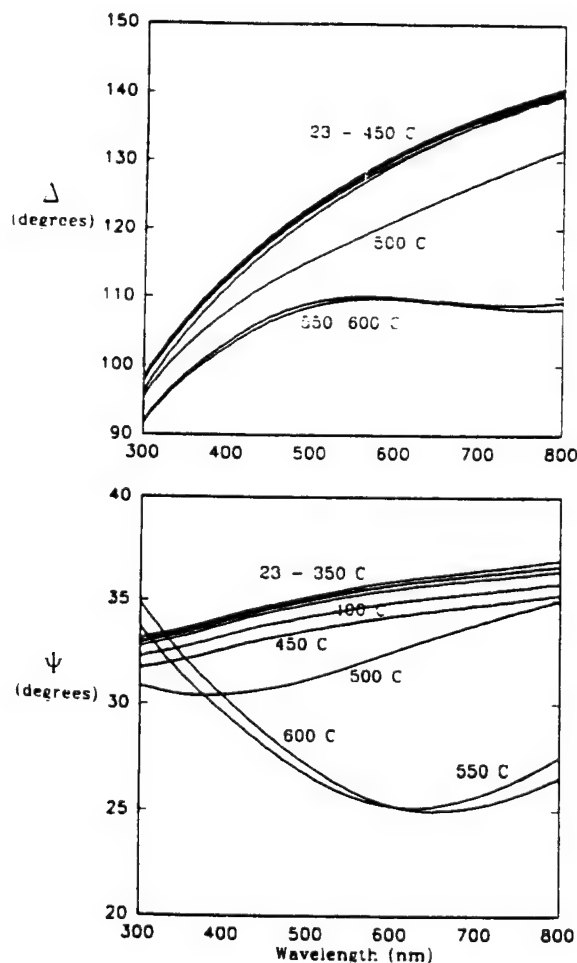


Fig. 8. Ellipsometric spectra as a function of temperature for a platinum-coated silicon substrate exposed to long-time anneals.

After 0.5 h at 600°C, the film had collapsed to its final thickness, and the high refractive index suggested that the perovskite phase was both well-crystallized and fairly dense. The best-fit model of the film consisted of two layers, with the majority of the film surmounted by a thin layer of surface roughness. There was no systematic change in the film microstructure with increased annealing time, and all of the parameters describing the depth profile remained approximately constant for all subsequent heat treatments. The film depth profile was fixed for all times >0.5 h to eliminate some of the uncertainty in the refractive index determination, and the film was modeled by permitting the optical properties to vary. The refractive index was found to change regularly as the annealing time increased for all of the microstructures chosen.

As shown in Fig. 9, after 0.5 h, the effective film refractive index decreased for longer anneals. Given the volatility of lead at these temperatures, it seemed possible that this was associated with the depletion of lead from the film surface, possibly accompanied by the formation of a pyrochlore phase. Lead volatility may be related to the formation of an electrically lossy layer in series with the remainder of the film at elevated temperatures.⁷ Because these types of changes could have a substantial effect on the utility of ferroelectric films, further study of these phenomena to elucidate the mechanisms for the variations in dielectric constant, dielectric loss, and optical properties with firing time would be fruitful.

V. Discussion

SE can be used to follow evolution in the structure and microstructure of ferroelectric films during the annealing process. Because the properties of the films are expected to depend on both of these factors,^{5,13-16} SE should be helpful in identifying processing conditions that facilitate preparation of high-quality films. In addition, the technique should be very useful in drawing correlations between the thin-film microstructure and the resulting properties of the films.^{5,14}

Schematics describing the proposed set of reactions occurring during the slow annealing of sol-gel PZT films on sapphire and platinum are shown in Fig. 10. As described in the previous section, the as-deposited sol-gel films were homogeneous throughout their thickness. On annealing, the microstructure remained largely unchanged until the temperature at which crystallization of the perovskite phase should occur. At that point, the surface became progressively rougher. A layer with a

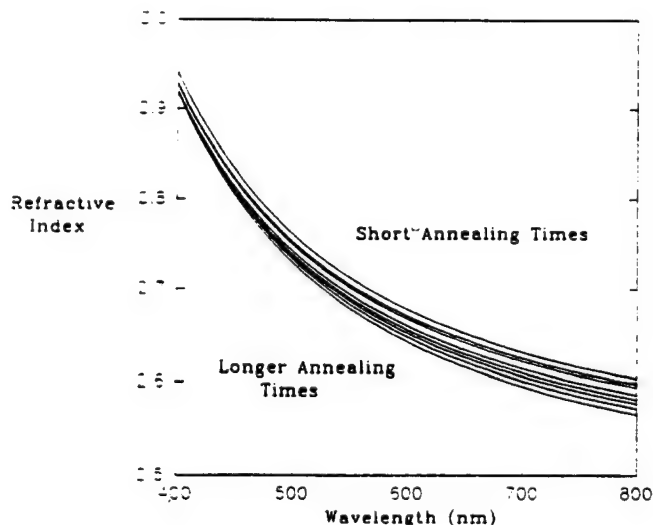


Fig. 9. Effective refractive index versus temperature for a PZT film on platinum-coated silicon annealed for varying times at 600°C. Changes in the substrate properties were not compensated for in the calculation of the effective refractive index.

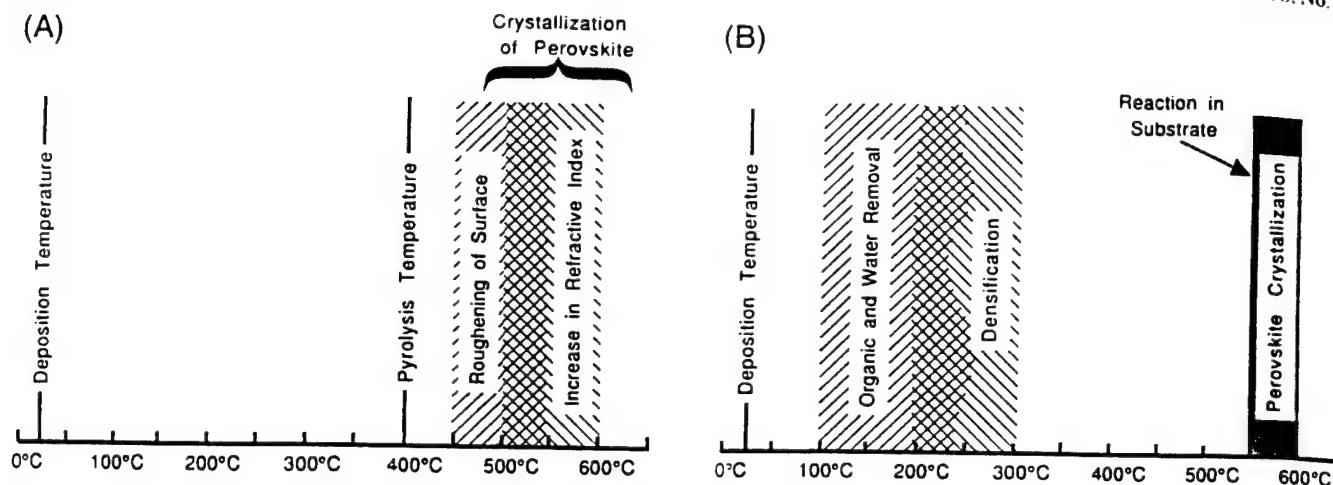


Fig. 10. Reaction schemes for annealing of sol-gel PZT films on (A) sapphire and (B) platinum-coated silicon.

lower refractive index also developed near the substrate. Additional experiments on sol-gel films demonstrated that the measured roughness depended on the annealing profile utilized. Consequently, for electrooptic applications where scattering from nonplanar surfaces could lower the performance of the device, it will be important to develop processing conditions that minimize the roughening of the film during crystallization.

The changes in the refractive index of the film on sapphire as a function of annealing are largely comparable to those reported by Budd and Payne¹⁷ and Peng and Desu.¹⁰ As shown in Fig. 7, the largest increase occurs where the film crystallizes. The primary advantage to the use of SE over other optical characterization methods for such studies is that no a priori assumption on the film homogeneity as a function of depth is required. The importance of this becomes apparent in a comparison of the present work with that of Peng and Desu, who used optical transmission data to study microstructure development in PZT films on sapphire substrates for several zirconium:titanium ratios. Many of the refractive indices reported by Peng and Desu are low, probably as a result, at least in part, of the implicit assumption that their films are homogeneous. This is particularly notable for the lead titanate film, which should have a refractive index of >2.65 at 632.8 nm if dense and smooth, as opposed to the reported value of ~ 2.3 . The presence of surface roughness, or any other type of low-density region in the film, decreases the effective index determined from transmission data. Because surface roughness develops over approximately the same temperature range that the perovskite phase crystallizes in many PZT films,³ the effective refractive index determined in transmission measurements contains information on both phase change and microstructure change. Thus, it also is possible that the decrease in the refractive index for annealing temperatures greater than $\sim 520^\circ\text{C}$ reported by those authors is due to the generation of surface roughness as the grain structure evolves, rather than a pyrochlore \rightarrow perovskite transition. In contrast, because SE entails measurements of both relative phase and amplitude, it is possible to decouple the presence of inhomogeneities from changes in the film refractive index. Consequently, it is possible to simultaneously depth profile the inhomogeneities in the film and determine the refractive index of the densest regions of the film. This minimizes a significant source of error in the optical characterization of thin films. In addition, the ability to decouple the index of the dense material from the effective index for an inhomogeneous film is very helpful in identifying structural changes in the film material.

SE data on the annealing of the platinum-coated silicon substrate alone (Fig. 8) showed substantial changes during annealing. Thus, by 550°C , the curves for Δ and Ψ had both developed interference oscillations associated with reflections from the top and bottom surfaces of a transparent film on the metal. Comparable oscillations were found on a sample heated in a

conventional furnace using a similar temperature profile. Auger spectroscopy measurements on the annealed substrate confirmed that titanium from the bonding layer had migrated through the film to the surface.¹² The oxygen content of the film tracked the titanium depth profile, suggesting that the transparent layer observed in these experiments was due to titania.

The reaction in the substrate was less apparent in SE measurements when a thin film was deposited on the platinum surface. The reaction also was less important for substrates held at elevated temperatures for comparatively short times. Substrates heated quickly to 600°C and held only 0.5 h did not show the onset of interference fringes characteristic of a transparent overlayer. Nevertheless, even thin or patchy layers of an insulating material between the electrode and a ferroelectric film would result in an increase in the apparent coercive field and a decrease in the apparent dielectric constant of the film. Consequently, deposition techniques that rely on heating platinum-coated silicon substrates before deposition is initiated could lead to serious degradation in the apparent properties of the resultant films.

VI. Conclusions

A rotating analyzer spectroscopic ellipsometer was utilized to nondestructively depth profile sol-gel ferroelectric films on sapphire and platinum-coated silicon substrates during the annealing process. It was possible to identify the burnout of organics, collapse of the film to a dense amorphous state, crystallization, and evolution of surface roughness in the films. Crystallization occurred between 500° and 600°C for PZT 52/48 films on sapphire substrates and was associated with generation of surface roughness. Excessive roughness would be deleterious in situations where the ferroelectric was either integrated into a complex multilayer structure or used in an electrooptic device (where roughness would lead to additional signal attenuation). Consequently, for these applications, control of the nucleation and growth of the perovskite phase is expected to be important in eliminating microstructural defects from ferroelectric thin films. In all cases, it is important to utilize some microstructure-sensitive technique to examine the role of processing conditions in controlling the electrical properties of ferroelectric films.

References

- P. J. McMarr, K. Vedam, and J. Narayan, "Spectroscopic Ellipsometry: A New Tool for Nondestructive Depth Profiling and Characterization of Interfaces," *J. Appl. Phys.*, **59** [3] 694-701 (1986).
- I. An, H. V. Nguyen, N. V. Nguyen, and R. W. Collins, "Microstructural Evolution of Ultrathin Amorphous Silicon Films by Real-Time Spectroscopic Ellipsometry," *Phys. Rev. Lett.*, **65** [18] 2274-77 (1990).
- P. Chindaudom and K. Vedam, "Determination of the Optical Function $n(\lambda)$ of Vitreous Silica by Spectroscopic Ellipsometry with an Achromatic Compensator," *Appl. Opt.*, **32**, 6391-97 (1993).

⁴P. Chindaudom and K. Vedaam, "Optical Characterization of Inhomogeneous Transparent Films on Transparent Substrates by Spectroscopic Ellipsometry"; in *Optical Characterization of Real Surfaces and Films*; pp. 191-247. Edited by M. H. Francombe and J. L. Vossen. Academic Press, New York, 1994.

⁵S. Trolier-McKinstry, H. Hu, S. B. Krupanidhi, P. Chindaudom, K. Vedaam, and R. E. Newnham, "Spectroscopic Ellipsometry Studies on Ion-Beam-Sputtered Pb(Zr,Ti)O₃ Films on Sapphire and Pt-Coated Silicon Substrates," *Thin Solid Films*, **230**, 15-27 (1993).

⁶K. R. Udayakumar, J. Chen, S. B. Krupanidhi, and L. E. Cross, "Sol-Gel-Derived PZT Thin Films for Switching Applications," *Proc. IEEE Int. Symp. Appl. Ferroelectr.*, **7th**, 741-43 (1990).

⁷J. Chen, K. R. Udayakumar, K. G. Brooks, and L. E. Cross, "Rapid Thermal Annealing of Sol-Gel-Derived Lead Zirconate Titanate Thin Films," *J. Appl. Phys.*, **71**, 4465-69 (1992).

⁸S. E. McKinstry, "Characterization of Ferroelectric Surfaces and Thin Films by Spectroscopic Ellipsometry"; Ph.D. Thesis. The Pennsylvania State University, University Park, PA, 1992.

⁹N. Tohge, S. Takahashi, and T. Minami, "Preparation of PbZrO₃-PbTiO₃ Ferroelectric Thin Films by the Sol-Gel Process," *J. Am. Ceram. Soc.*, **74** [1] 67-71 (1991).

¹⁰C. H. Peng and S. B. Desu, "Structure Development Study of Pb(Zr,Ti)O₃ Thin Films by an Optical Method," *J. Am. Ceram. Soc.*, **77** [6] 1486-92 (1994).

¹¹R. Bruchhaus, D. Pitzer, O. Eibl, U. Scheithauer, and W. Hoesler, "Investigation of Pt Bottom Electrodes for "In Situ" Deposited Pb(Zr,Ti)O₃ (PZT) Thin Films," *Mater. Res. Soc. Symp. Proc.*, **243**, 123-28 (1992).

¹²G. R. Fox, S. Trolier-McKinstry, L. M. Casas, and S. B. Krupanidhi, "Pt/Ti/SiO₂/Si Substrates," *J. Mater. Res.*, **10** [6] 1508-15 (1995).

¹³V. P. Dudkevich, V. A. Bukreev, V. M. Mukhortov, Yu. I. Golovko, Yu. G. Sindeev, V. M. Mukhortov, and E. G. Fesenko, "Internal Size Effect in Condensed BaTiO₃ Ferroelectric Films," *Phys. Status Solidi A*, **65**, 463-67 (1981).

¹⁴S. Trolier-McKinstry, "Spectroscopic Ellipsometry Studies of Ferroelectric Thin Films," *Ferroelectrics*, **152**, 169-74 (1994).

¹⁵H. Hu, C. J. Peng, and S. B. Krupanidhi, "Effect of Heating Rate on the Crystallization Behavior of Amorphous PZT Thin Films," *Thin Solid Films*, **223**, 327-33 (1993).

¹⁶S. A. Mansour and R. W. Vest, "The Dependence of Ferroelectric and Fatigue Behaviors of PZT Films on Microstructure and Orientation," *Integr. Ferroelectr.*, **1**, 57-69 (1992).

¹⁷K. D. Budd and D. A. Payne, "Optical Properties and Densification of Sol-Gel-Derived PbTiO₃ Thin-Layers," *Proc. SPIE-Int. Soc. Opt. Eng.*, **1326**, 450-55 (1990). □

APPENDIX 5

Inorganic Lead Compounds in Electroceramics and Glasses

Although many electroceramics and glasses have greater lead by weight than low-technology materials, these high-technology materials have less significant environmental impact and cannot be regulated in the same manner as low-technology materials.

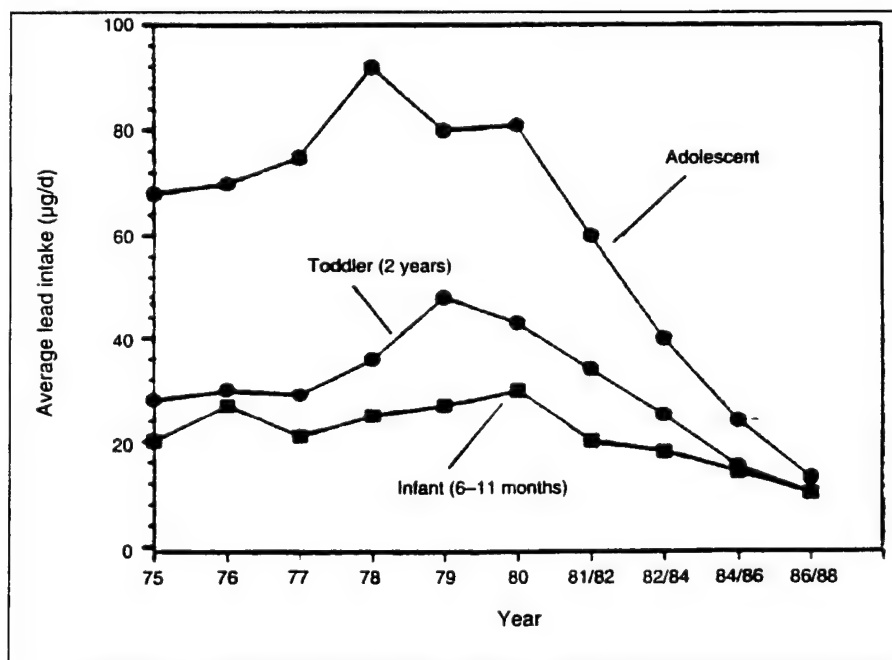
Nathan Nair, Amar Bhalla and Rustum Roy
The Pennsylvania State University, University Park, Pa.

Lead-based compounds are numerous. When the toxicological effects of lead compounds are studied, a distinction between organic and inorganic lead compounds appears because each group behaves differently in biological systems.¹ Examination of inorganic lead compounds exposes additional differences in their stability, modes of human exposure and socioeconomic importance.

Lead-based electroceramics and glasses include inorganic lead compounds that can be controlled in the future when restrictions on lead use are enacted. The compounds widely used in electronics pose minimal health risks because of their stability. The socioeconomic impact of restricting these compounds could be significant because of their widespread use and the difficulty of locating replacement materials.

Environment & Health Issues

Environment and human health effects are intricately linked. As inorganic lead compounds enter the environment, they also enter the biologic chain. Once within



Average daily lead intake. Source: U.S. Department of Health and Human Services, Public Health Service, Food and Drug Administration, Center for Food Safety and Applied Nutrition. FDA Total Diet Study, Washington, D.C., 1989.

the chain, inorganic lead eventually is absorbed by humans. Where is the inorganic lead retained in the body? What are the effects of lead in the body?

Natural sources of inorganic lead atmospheric pollution include volcanic debris and erosion of certain soils and clays. Human sources include industrial processes, such

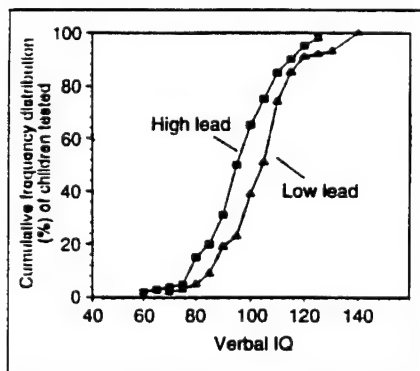
as lead battery manufacturing. Atmospheric lead concentration adjacent to smelters may be as high as 93 mg/m^3 .² These sources significantly affect only the local atmosphere. Cigarette smoke also contains lead compounds.¹

The largest general source of lead in the atmosphere has been the combustion of organic-lead-containing gasoline. In 1974, before the leaded gasoline ban, American cities had an average level of 0.89 mg/m^3 and rural areas, 0.11 mg/m^3 .³

Except for those individuals who live or work near sources, population exposure to atmospheric lead is minor compared to subsequent pathways. The major significance is that heavy metals, including lead, have a tendency to concentrate in the lower atmosphere and contaminate surrounding soil layers.⁴ Soil lead contamination is, under certain circumstances, a direct effect of atmospheric pollution.

Lead can be stabilized by soil humus, and it remains in the upper 2.5 cm of the soil. If disturbed, the lead may move deeper into the soil. Ground water supplies can be contaminated by municipal or hazardous dump sites.⁴

Inhalation and ingestion are the two routes for human exposure to lead. For adults, inhalation is the more efficient mode of absorption—



Comparison of verbal IQ scores of children with high- and low-lead levels. Source: H. L. Needleman, C. Gunnoe, A. Leviton et al., "Deficits in Psychologic and Classroom Performance of Children with Elevated Dentine Lead Levels," *N. Engl. J. Med.*, 300: 689-95 (1979).

Environmental Lead Intake and Absorption*	
Source of lead exposure	Absorption (%)
Foods and beverages ($10\text{--}30 \text{ }\mu\text{g/L}$)	5-15
U.S. city air ($1\text{--}6 \text{ }\mu\text{g/m}^3$)	25-50
Cigarette smoke ($1 \text{ }\mu\text{g/cigarette}$)	10-15
Industrial air (200 mg/m^3)	15
*Reference 7.	

30%–37% absorption rate into the blood stream through the respiratory tract. Ingestion causes 10% lead absorption into the blood stream. However, for children, ingestion may cause up to 50% absorption of lead into the blood stream.⁵

Lead in water is absorbed at a higher rate, 35%–50% for adults and >50% for children.⁶ Although inhalation of lead has a greater absorption rate, ingestion is the more significant route of human exposure for those who are not exposed to direct sources of atmospheric lead pollution.

Inhalative absorption occurs in the microscopic air sacs of the lungs, where blood gases are exchanged with atmospheric gases. Analysis of air lead vs blood lead levels is described as generally curvilinear. As air lead concentration arithmetically increases, blood level concentration increases at a greater rate.⁸

The derivative of this function for males is greater than for females. The derivative is higher for children.⁹ Adults, without prior lead exposure, experience a 1 mg/dL increase in blood lead concentration for every 1 mg/m^3 increase in air lead concentration. For children, there may be 2 mg/dL or greater increase in blood lead.¹⁰

The ingestive absorption of lead from food and beverages is variable. The lead concentration of foods and beverages may increase after handling, processing and storage, so that it is significantly greater than the raw-food concentration. Blood absorption of lead from food varies with consumer age, sex and eating habits.

Children may be further exposed to lead while ingesting soil and dust. For children who live near

smelters, this accounts for a major source of lead absorption. When soil lead concentrations reach 500 ppm, a 2 mg/dL increase in blood lead levels of children occurs for every 100 ppm increase in soil concentration. However, since 1980, the average lead intake of adolescents, toddlers and infants has decreased.

Health Effects

Certain metals are required for normal physiological activity. Lead is not required for regular activity. It is a cumulative poison that is retained by tissue and can cause acute and chronic illnesses. Blood, soft tissues and skeletal tissues each have a different normal level and different retention rates.

Once lead exposure reaches significant levels, dose-effect correlations are used to establish the human health effects. Individual dosages of lead are related to specific human effects. Blood lead level is used to establish the dosage. Dose-effect studies are specified for three primary body systems: blood, specifically heme synthesis; central nervous system; and kidneys.

Normal blood lead concentrations vary considerably among individuals. Geographic location, occupation and living habits affect the blood lead concentration, from 11 to $38 \text{ }\mu\text{g/dL}$.⁷

Lead can enter blood from lead stored in bones or soft organs. During the early stages of lead exposure, blood lead levels correspond to the concentrations of recently inhaled or ingested lead.¹¹ For individuals who have had long-term lead exposure, blood lead levels correspond to the amount of lead stored in bones or soft organs.¹²

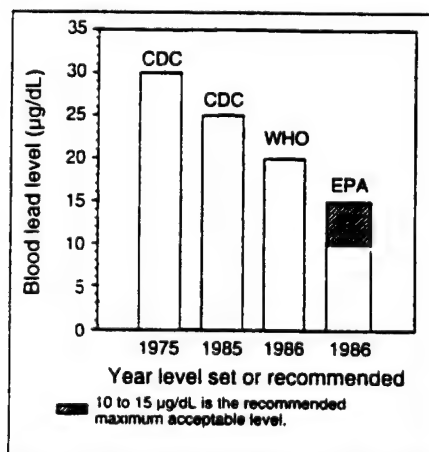
Ninety percent of blood lead is bound to red blood cells, where it has a half-life of 36 ± 5 d.¹³ The remaining blood lead is in plasma, where the half-life is minutes to hours.¹⁴ Lead leaves blood mainly from the plasma portion and is excreted in urine.

The half-life of lead in soft tissue is 40 d. Some of this is rapidly exchanged with blood plasma. Lead is excreted from soft tissues into gastrointestinal secretions, sweat, hair and nails.¹⁴

Ninety-nine percent of lead absorbed from the environment is eventually deposited in skeletal tissues.¹⁵ The half-life of skeletal lead is 10,000 d and can be considered inactive once deposited.

Anemia, or the lack of hemoglobin, is a major symptom of lead exposure. Hemoglobin is an iron-based bio-molecule that is the primary mode of oxygen transport from lungs to tissues. Increased lead concentrations in the blood stream correspond to decreased hemoglobin levels.^{16,17} Blood lead levels as low as 5 µg/dL cause decreased hemoglobin levels.¹⁸

Frank anemia in adults has been observed at lead levels as low as 50 µg/dL. Children display less tolerance for blood lead.¹⁹ Lead inhibits the enzymatic or catalytic activity of two molecules that are necessary for hemoglobin production. The primary enzyme is *d*-aminolevulinic



Changes in blood lead level guidelines. Source: U.S. Congress, Office of Technology Assessment, Neurotoxicity: Identifying and Controlling Poisons of the Nervous System. OTA-BA-436, 271, 1990.

Lead Content of Unexposed Adult Human Tissues ²¹	
Tissue	Lead content (mg/100g wet tissue) ¹
Blood	11-38
Soft tissue	
Liver	0.40-0.28
Lung	8×10^{-5} - 3×10^{-2}
Hilar lymph nodes	4×10^{-6} - 4×10^{-2}
Kidney	5×10^{-2} - 1.6×10^{-1}
Spleen	1×10^{-2} - 7×10^{-2}
Brain	1×10^{-2} - 8×10^{-2}
Skeletal tissue	
Bone	6.7×10^{-1} -3.59
Teeth	7×10^{-3} -1.17

¹Reference 7. ²Except blood, in µg/dL.

acid dehydratase (ALAD) found in red blood cells.²⁰ Lead prevents ALAD activity in the red blood cells and inhibits ALAD activity of the brain in children.

The other enzyme affected is ferrochelatase. Ferrochelatase catalyzes the reaction between ferritin and protoporphyrin to form heme, a component in hemoglobin. Ferrochelatase is inhibited by lead, causing an excess of another bio-molecule, protoporphyrin, in red blood cells. Increased levels of protoporphyrin may be found at blood lead levels of 15 µg/dL.

Acute lead alteration of the brain structure has been reported at lead levels >120 µg/dL in adults.^{21,22} Children again appear to be at greater danger, with levels as low as 80 µg/dL.¹⁰

Lower lead levels also can cause neurological problems. Children who have elevated dentine lead levels, have, on average, 4.5 points lower IQ verbal examination scores than students with lower dentine lead levels.²³

Asymptomatic adults with elevated blood lead levels may exhibit memory, attention or concentration difficulties.¹⁴ The hypothesized mechanism for lead neuropathy, or subtle brain alteration, is attributed to damaged endothelial cells of blood capillaries in the brain. Lead causes these cells to expand, which increases the permeability of the blood-brain barrier to other substances that can cause acute encephalopathy or more subtle alterations.

Newly developing capillaries appear more vulnerable to the

effects of lead than already formed vessels.²⁴ This may explain why suckling infants are at greater risk than the mother who is directly intaking lead.

One of the major functions of the kidneys is nitrogenous waste removal. Nitrogenous wastes are formed during the metabolism of proteins. Lead affects the proximal convoluted tubules of kidneys.¹⁵ The primary function of these proximal tubules is to reabsorb water, sodium ions and amino acids back into the bloodstream so that these metabolically important chemicals are not excreted in urine.

Lead inhibits an enzyme of the cells lining the inner wall of the proximal tubules. This reduces the ability of the tubules to reabsorb amino acids, leading to aminoaciduria or acidic urine.¹⁴ Long-term, high-dose exposure to lead eventually causes partial renal fibrosis, which results in irreversible reduction of kidney function and finally chronic renal failure.²⁵

Stability

Two significant lead-based pigments used in paints are lead carbonate (basic white lead) and lead oxide (red lead). Both compounds are soluble under acidic conditions.

The solubility of lead solders is similar to that of metallic lead, which dissolves in slightly acidic pH. Lead sulfate, used in storage batteries, is soluble in water in either neutral or acidic pH.²⁶ Because the pH of rain and ground

water is slightly acidic, they cause some lead compounds to dissolve and enter the environment.

Lead-based electroceramics—including lead titanate, lead zirconium titanate, lead lanthanum zirconium titanate and lead magnesium niobate—are water insoluble. The leachability of lead ions from these compounds is minimal because of their complex crystal structure. Lead-based glasses—including lead aluminum silicates, lead aluminum borosilicates and lead boro-composites—are water insoluble, and leachability is minimal because of their complex structure.

Human Exposure to Lead

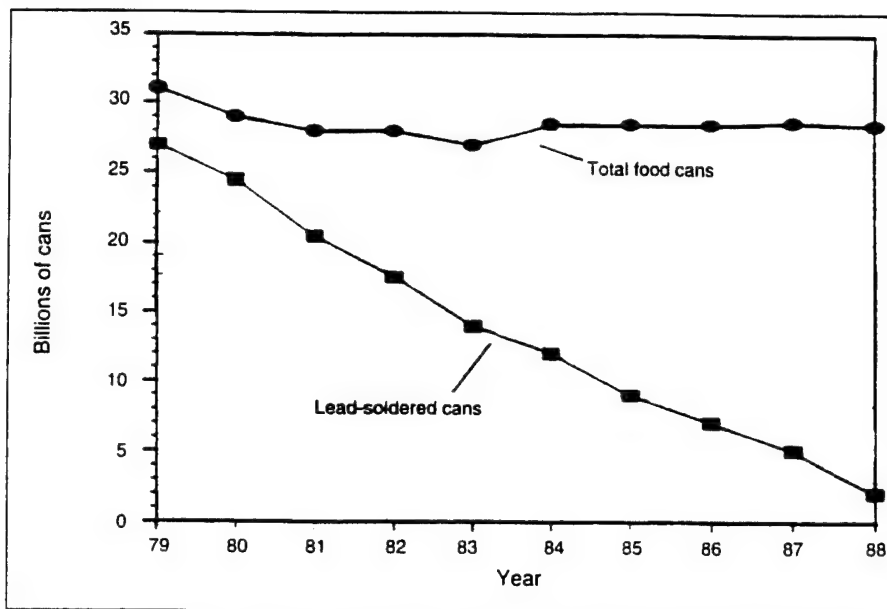
The two major sources of human exposure to inorganic lead are from lead-based paints and lead piping used in many public water distribution systems. These sources of exposure should then be compared to lead-based electroceramics and lead glasses.

Children are at the most significant risk of lead exposure from lead-based paints. Fourteen million housing units in the United States contain lead paint that is deteriorating, and 3.8 million of them are the homes of young children.⁴ Children in these conditions are susceptible to lead exposure through ingestion of lead-contaminated dust particles.

Children prone to the regular ingestion of nonfood materials also are at risk if paint chips are consumed. Houses renovated using lead paint, which includes most homes constructed before 1980, is another possible source of exposure for children.⁴

Drinking water is a possible source of human exposure. Lead levels in ground water are typically low. However, public water distribution systems may contain lead connector, piping and copper-piping soldered joints. Housing units built before 1920 contain mostly lead piping. After 1950, lead piping was generally replaced by copper piping that used lead-based solder.

Cisterns for water storage or collection are another possible source of lead when lead solder is used in



Total number of cans produced vs lead-soldered cans. Source: U.S. Congress, Office of Technology Assessment, *Neurotoxicity: Identifying and Controlling Poisons of the Nervous System*, OTA-BA-436, 271, 1990.

their construction or for repairs.⁴ The probability of significant exposure is greater if the plumbing is used only intermittently and the system is not flushed prior to use.

Lead-based electroceramics are used in capacitors, transducers, sensors, phase shifters, pyro-detectors, thermistors, memory devices and medical diagnostic devices. Lead-based glasses are major ingredients in display sealing, integrated circuit packages and coatings. Electroceramic components are incorporated into cardiac pacemakers, analog devices, telecommunication systems and many consumer electronic systems.^{27,28}

Worker exposure during production is minimized through proper handling, protection and efficient production methods. Humans are exposed during product use to minimal amounts of lead, because the actual lead components are inside the consumer product.

Certain medical products, such as pacemakers or transducers, significantly increase the risk of human exposure. However, in these situations product use is necessary and the risk of exposure is warranted.

Industrial disposal of waste materials from production of lead-containing compounds is a source

of human exposure. Processing steps—including melting, preparing slurries and mixing powders—can cause lead contamination. Finishing steps—including cutting, polishing and molding—create waste materials that are not used in the final products. Disposal of lead-containing components after their life span further contaminates the environment.

Federal Regulations

Lead-based paints containing >0.06 wt% lead were banned by the Consumer Product Safety Commission in 1978 for consumer products or for residential purposes under the Federal Hazardous Substances Act. Before 1950, paints may have contained nearly 50 wt% lead.³⁰ Exceptions were given to paints used for industrial, military or marine use.⁴

Although the Act prohibits future use of lead-based paints, 74% of existing housing units contain ~3 million tons of lead. Acceptable lead levels set by federal agencies have decreased since 1975. Presently, there is no standard for safe lead levels for existing painted surfaces.

Most existing standards are based primarily on practical issues instead

of health concerns.⁴ In 1992, the Lead-Based Paint Exposure Reduction amendment to the Toxic Substances Control Act was passed by Congress.³¹ The amendment required the Department of Health and Human Services and Department of Housing and Urban Development to develop regulations concerning lead-based paint activities, including training programs and home renovation.³¹

The 1986 Safe Drinking Water Act banned lead in water distribution systems, and it limited the amount of lead in brass plumbing to 8%.⁴

In 1993, a bill was proposed in the U.S. Senate to create comprehensive regulations concerning a wide range of lead-containing compounds. The Lead Reduction Exposure bill was passed by the Senate, but the House of Representatives did not pass this amendment to the Toxic Substance Control Act before the session ended.

If passed in a later session of Congress, it would place restrictions on lead solders, paints and piping. It also would restrict the manufacture of lead-based electroceramics and glasses because of their relatively high lead content by weight.³²

Socioeconomic Effects

In 1970, the Consumer Product Safety Commission banned the use of lead-based paints containing >0.06 wt% lead by 1978 for most uses.

The production of lead sulfate for storage batteries accounts for the largest single use of lead.⁷ Lead storage batteries are widely used because of their convenience.³³

Metallic lead and lead alloys are used in lead piping and solder.

A major similarity between all of these compounds is that they each have specific, usually low-technology, uses.

Lead-based electroceramics and glasses are multiuse compounds. In general, these compounds are widely used in high-technology applications.

Non-lead-containing pigments can be used to effectively replace

Solubility of Inorganic Lead Compounds*				
Material	Cold water	Hot water	Acid	Base
Metallic Lead	Insoluble	Insoluble	Nitric and acetic	Insoluble
Lead-tin soft solder	Insoluble	Insoluble	Nitric and acetic	Insoluble
Lead arsenate	Insoluble	Slightly	Soluble	Soluble
Lead carbonate	Insoluble	Insoluble	Soluble	Soluble
Lead chromate	Slightly	Slightly	Soluble	Soluble
Lead oxide	Insoluble	Insoluble	Soluble	Insoluble
Lead silicate	Insoluble	Insoluble	Decomposes	Soluble

Reference 26.

lead-based pigments without excessive expense.

Storage batteries are more difficult to replace, because an oxidation-reduction reaction that produces one compound is necessary for rechargeable batteries. Because of the expense and inefficiency of lead storage batteries, research for other storage batteries has continued.

Photovoltaic cells have been studied extensively. Nickel-iron batteries are lighter than lead storage batteries and are presently used in telephone exchanges and other heavy-duty situations. Nickel-cadmium batteries are used in spacecraft and may last up to 25 years. However, they may not be an alternative because of the extreme toxicity of cadmium.

Lead solder and piping are being replaced by copper, brass or poly(vinyl chloride). Lead solders used in food containers are being replaced.

Replacement materials for lead-based electroceramics and glasses that have equivalent efficiency are not presently being used or phased into use. Research is being conducted to produce suitable replace-

ment materials. However, unlike other lead-containing compounds, replacements for electroceramics and glasses must meet a higher or equivalent standard of efficiency and should be inexpensive. Lower quality or more expensive compounds could not effectively be phased into electronic devices that presently use electroceramics and glasses without creating economic problems.

Changes in production and disposal methods may be an alternative to replacement. Low-temperature processing of lead-based compounds reduces the vapor pressure and the amount of lead lost from vaporization.

Clean cutting methods with lasers reduce the amount of material wasted. If possible, avoiding cutting and polishing can significantly reduce the amount of waste material containing lead. Proper packaging of final components may reduce environmental contamination at the end of their life span.

Industrialized nations continue to use and develop electroceramics and glasses that contain lead compounds to defend their

Standards and Regulations for Lead		
Agency	Focus	Lead level
CDC	Blood	25 mg/dL; level of concern
OSHA	Air	50 mg/m ³
OSHA	Blood	60 µg/dL; removal from exposure
ACGIH	Air	150 mg/m ³
EPA	Air	1.5 mg/m ³ ; 3 month average
EPA	Water	50 mg/L
FDA	Food	100 mg/d
CPSC	Paint	0.06 wt%

*Reference 29.

technological competitiveness. However, these nations are more able to replace low-technology products containing lead, including paints, piping, and gasoline. Thus, production and disposal of high-technology products containing lead remains the major source of lead pollution.

Developing nations are more concerned with the disposal of these high-technology products, rather than production. The major concern of these nations are the low-technology products containing lead, including paint, piping and gasoline.

Conclusion

Three basic criteria should be used to determine whether a compound is sufficiently hazardous to be restricted.

The primary criterion is the human health effect of a compound. Certain compounds inflict serious health problems after minimal, short-term contact. Inorganic lead is a cumulative poison that causes widespread health effects after long-term exposure to significant doses. Once in the human body, all inorganic lead compounds act similarly. However, proper lead concentration monitoring and medical treatment can avert serious effects in almost all situations.

The second criterion is the stability of the compound and at what concentrations humans are exposed. Unstable compounds that readily enter the environment pose a more serious threat to the community than compounds that remain inert. An additional aspect of this criterion is the relative human exposure to these substances. Compounds—such as lead oxide, lead carbonate, metallic lead and lead alloys—readily enter the environment, and humans are widely exposed to consumer products that contain these inorganic compounds. However, lead-based electroceramics and glasses do not enter the environment as readily, and human exposure is variable. Human exposure to lead-containing compounds used in electronic

components is minimal. When used in medical applications, exposure increases but is offset by the necessity of the product and stability of the compounds.

The third criterion is a cost-of-replacement vs benefits analysis. Inorganic lead compounds used in lead paints, batteries or piping already have available replacement materials in use. In addition, these compounds perform narrow functions. The cost of new product development and implementation have a lesser effect on society and the economy. However, lead-based electroceramics and glasses are used widely as the basic components of many electronic devices. These compounds are not as readily replaced by similar quality materials. If effective replacement materials are not found, phasing out these compounds in the United States could have serious socioeconomic effects. Other nations that have not restricted the use of lead-based ceramics and glasses will produce either higher quality or less expensive electronics. Even if society is willing to accept these consequences, a separate socioeconomic problem is created with medical applications. A more costly or less effective pacemaker or transducer will have a serious effect on the cost and quality of health care in the United States. In the present climate, these are not options that American society will find acceptable.

These three criteria support the idea that certain inorganic lead compounds are extremely hazardous and warrant regulation. Most of these compounds have been restricted or banned by the U.S. federal government after individual consideration. However, multilateral regulation of inorganic lead compounds cannot be supported by the presented data.

The enormous differences in chemistry, uses and importance of inorganic lead compounds should be considered before the federal government acts. The federal government does have a responsibility to act on the prevailing public opinion if society is completely

aware of the future consequences that may be involved.

However, society has not been exposed to accurate information concerning the dangers of inorganic lead compounds, and, in this situation, the federal government has two other responsibilities. The first is to correctly inform the public of the different types of lead compounds and their uses. The second is to act carefully and cautiously, rather than submit to a public opinion that is based on incomplete data.

Lead-based electroceramics and glasses should not be placed in the hazardous materials category with other described inorganic lead compounds, but the regulation of raw-material supply, production and disposal is desirable. Lead-based electroceramics and glasses have too many important uses to be banned in an attempt to completely eliminate lead contamination and human exposure. Careful, specific action against harmful compounds is a more reasonable solution than adopting legislation affecting the element lead and all of its compounds. ■

For the complete set of references to this article, please FAX or mail your request with your name and address to Editorial Assistant at 614-899-6109 or headquarters, respectively. Request ACerS Data Depository File No. 234.

Your Comment

Please use the Reader Service Card on page 17 to circle numbers that pertain to this article.

It was useful and/ or interesting	Circle 291
It was not useful and/ or interesting	Circle 290
I would like more articles on this topic	Circle 289

APPENDIX 6

9 Single Crystals

Anthony L. Gentile

American Association for Crystal Growth, Thousand Oaks, CA, U.S.A.

Frank W. Ainger

Materials Research Laboratory, The Pennsylvania State University, University Park, PA, U.S.A.

List of Symbols and Abbreviations	314
9.1 Introduction	315
9.2 Crystals and Crystallography	316
9.2.1 Ferroelectricity in Crystals	317
9.3 Growth of Single Crystals	319
9.4 Classification of Crystal Growth Techniques	320
9.5 Brief Fundamental Aspects for Selection of Crystal Growth Parameters ...	321
9.6 Phase Equilibria and the Gibbs Phase Rule	322
9.6.1 Solid Solution Series	324
9.7 Crystal Growth Techniques	326
9.7.1 Growth from a Melt	326
9.7.1.1 Directional Solidification	326
9.7.1.2 Bridgman–Stockbarger Technique	326
9.7.1.3 Verneuil Flame Fusion Technique	327
9.7.1.4 Czochralski Technique	328
9.7.1.5 Skull Melting	329
9.7.1.6 Zoning Techniques	330
9.7.2 Indirect Crystal Growth – Growth from Solution	331
9.7.2.1 Top-Seeded Solution Growth	331
9.7.2.2 Hydrothermal Growth	333
9.7.2.3 The Sol-Gel Process and Its Derivatives	333
9.7.3 Crystal Growth from the Vapor Phase	334
9.7.3.1 Physical Vapor Deposition	334
9.7.3.2 Vapor Deposition of Single-Crystal Thin Films	334
9.7.3.3 Metal-Organic Chemical Vapor Deposition	334
9.7.3.4 Atomic Layer Epitaxy	336
9.7.4 Solid-to-Solid Crystal Growth	336
9.8 Distribution Coefficient and Mass Transport	337
9.9 Heat Transfer	339
9.10 Crystal Growth Theory Versus Experiment	340
9.11 References	340

List of Symbols and Abbreviations

A, B	component of a mixture
C	number of compounds
E	eutectic point
F	degrees of freedom
k	distribution or segregation coefficient
P	number of phases present at equilibrium pressure
T	temperature
T_c	Curie temperature
ΔT	change in temperature
$\Delta T/\Delta x$	thermal gradient
Δx	distance in furnace
X	composition

ACRT	accelerated crucible rotation technique
ALE	atomic layer epitaxy
BST	barium strontium titanate
CVD	chemical vapor deposition
EO	electro-optic
KTN	potassium (K) tantalate niobate
LEC	liquid encapsulated Czochralski
LHPG	laser heated pedestal growth
MBE	molecular beam epitaxy
MOCVD	metal-organic chemical vapor deposition
MOMBE	metal-organic molecular beam epitaxy
OMVPE	organo-metallic vapor phase epitaxy
PC	polycrystal
PVD	physical vapor deposition
PZT	lead (Pb) zirconate titanate
rf	radio frequency
TSSG	top-seeded solution growth
YBCO	yttrium barium copper oxide (superconductor)

9.1 Introduction

A ceramic has been defined (NAS, 1968) as an inorganic non-metallic material or article. Ceramics may be polycrystals, glasses, or combinations thereof, or single crystals. A single crystal is defined as the macroscopic extension of a regular repeated geometric network of atoms (called the crystal lattice), consisting of one or more elements, from a microscopic scale to a unit ingot (or film). Therefore, the bulk single crystal (ingot) as well as the single crystal thin film is expected to contain no crystal grain boundaries and to have a continuous, repeated symmetry of its constituent atoms. In contrast, a ceramic body may be seen as a consolidation of many small single crystal grains, a polycrystalline form, with the grains having random crystallographic orientation. Ceramic Processing is defined (NAS, 1968) as a combination of science and engineering that is directed initially toward developing – and ultimately of reliably manufacturing – a ceramic product with specific desirable properties tailored to its application. The processing equivalent for single crystals is the synthesis or growth procedure known as crystal growth.

Many materials which have been thought of as traditional ceramic materials have extensive applications in single crystal form. Some devices, e.g., lasers, pyroelectric detectors, have been demonstrated using both single crystal and ceramic forms. However, the efficiency of the devices in most cases has been lower for the ceramic body than for the single crystal, lower even than predicted by calculations taking into account differences based on anisotropic properties.

The materials which we will stress in this chapter are the refractory (high melting point) oxides, both simple and complex.

These materials include simple oxides of the type A_xO_y , e.g., SiO_2 , Al_2O_3 , MgO , TiO_2 , ZrO_2 , and complex structures of the formula type ABO_3 where B may be Nb, Ta, Ti, or Zr; and A may be Na, K, Ca, Ba, Sr, Pb. Other refractory materials including spinel structures such as $MgAl_2O_4$, garnets (including aluminosilicates and rare earth garnets), and other aluminates, borates, silicates, and aluminosilicates as well as carbides, borides, and nitrides would fit into this chapter but would require extensive discussion to cover. Many of the growth techniques discussed are applicable to these compounds.

In these materials, bonding occurs primarily between charged atoms or groups of atoms, i.e., ionic bonding. Data on ionic radii and coordination numbers are available. The coordination number represents the number of surrounding cations around a positive metal ion or anion. It is believed to be a major factor in the determination of certain properties, e.g., ferroelectric and nonlinear properties.

Polar materials are of great interest because of their nonlinear optical properties (large nonlinear coefficients) leading to efficient electro-optic modulation, second (or higher) harmonic generation, frequency conversion, and optical parametric oscillation, operating in wavelengths from the visible to near infrared. In these processes, energy exchange between a number of optical fields of different frequencies is brought about by a field-dependent dielectric constant. Electro-optic modulation is based on manipulation of the optical properties of crystals by means of external electric fields. In optical parametric oscillation, a fixed frequency pump wave is converted to a higher frequency signal and a lower frequency idler wave. Phase matching conditions are altered by changes in temperature or orientation (angular posi-

tion) of the crystal which allows tuning of the signal or idler wavelength. It is not surprising then that the demand for optical quality (striae free) crystals applicable to electro-optic devices has also advanced the techniques for the growth of oxide single crystals.

Some aspects of crystal growth are also treated in Vol. 16 (Chap. 2, Sec. 2.7) of this Series.

9.2 Crystals and Crystallography

From a crystallographic point of view, the spatial arrangement of atoms in a crystal forms a unit cell which is defined as the smallest crystallographic "repeat" unit, i.e., a sufficient number of atoms are repeated to define the 3-dimensional relationship of the atoms throughout the crystal when the unit cell is reproduced by simple translations in the same orientation. The unit cell for perovskites which represent an important family of ferroelectric structures is shown in Fig. 9-1. The name is derived from the mineral perovskite CaTiO_3 which is isostructural with other ABO_3 crystals where $A = \text{Ca, Ba, Sr, K, Na, Li}$, and $B = \text{Nb, Ta, Ti, Zr}$. The unit cell of a cubic perovskite shows a metal ion $B (= \text{Ca})$ at the center of the basic cube, and an anion $X (= \text{O})$ at the center of the cube faces, yielding an octahedron with the metal ion (B) in its center, the BX_6 octahedra.

The unit cell usually is not the simple chemical formula which designates the overall ratios of its constituent elements. The 3-dimensional extension of a unit cell in an infinite pattern produces a single crystal. The unit cell defines the basic symmetry of the crystal which classifies the crystal into one of seven crystal systems.

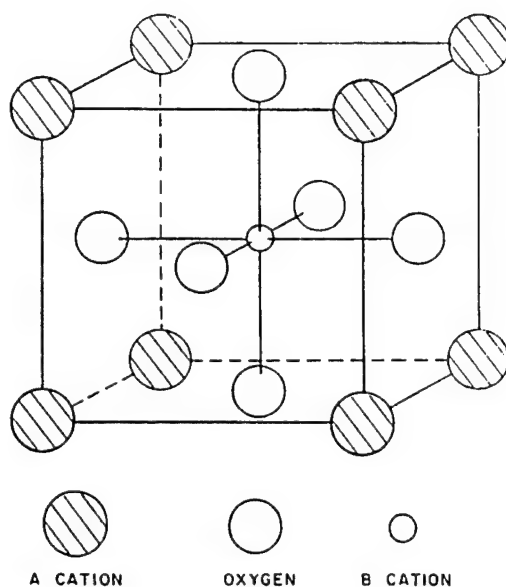


Figure 9-1. Perovskite (ABO_3) structure.

An extended discussion of crystallography appears in Chap. 1, Vol. 1, of this Series.

For many electronic and optical applications, one can select useful crystals based on their chemical and structural makeup. The linear electro-optic (EO) effect is observed in crystals which lack inversion symmetry (noncentrosymmetric); in crystals which possess inversion symmetry, the linear electro-optic effect vanishes (Yariv, 1967) and the dominant term describing the dependence of the dielectric tensor on the electric field is a quadratic term. Some of the best 'quadratic' EO materials are ferroelectric when operated above their Curie temperature, i.e., in a paraelectric phase. This indicates that changes in the optical index are linked more fundamentally to the induced polarization than to the applied electric field. In this region, susceptibility is temperature dependent. As illustrated in Fig. 9-2 for the longitudinal electro-optic effect, specific point groups will contain crystal compounds having longitudinal (modulator field and

CRYSTAL SYMMETRY						
SYSTEM	POINT GROUP					
CUBIC	23,	M3,	432,	$\bar{4}3M$,	M3M	
HEXAGONAL	(6,	$\bar{6}$,	6/M,	(622,	6MM,	$\bar{6}M2$, 6/MMM
TRIGONAL	(3,	$\bar{3}$,	(32,	3M,	$\bar{3}M$	
TETRAGONAL	(4,	($\bar{4}$,	4/M,	(422,	4MM,	($\bar{4}2M$, 4/MMM
ORTHORHOMBIC	(222,	MM2,	MMM			
MONOCLINIC	(2,	M,	2/M			
TRICLINIC	(1,	$\bar{1}$				

Figure 9-2. Point groups of longitudinal electro-optic crystals.

light propagation in same direction) or transverse (field normal to direction of light propagation) electro-optical effects. Although we can select EO crystals from these groups, rarely can we predict the magnitude of the effect based on present-day knowledge. However, in the case of EO coefficients, theoretical calculations based on structural properties (especially bond length and angle) of the electro-optic coefficient made by Shih and Yariv (1980, 1982) for binary compounds including GaAs and CdTe have compared favorably with measured results. The calculations for compounds of the type ABO_3 have not been as accurate. Additional theoretical and experimental work is required for ultimate device advancement in many fields including the synthesis and characterization of single crystal materials. The continuity of the internal structure of a single crystal explains the many observed differ-

ences in properties compared to its chemically-similar ceramic body, especially regarding optical, optoelectronic, and ferroelectric properties.

9.2.1 Ferroelectricity in Crystals

A crystal is *ferroelectric* if it demonstrates reversible spontaneous polarization (Megaw, 1957). A ferroelectric is a pyroelectric with a reversible spontaneous polarization which goes to zero at temperatures higher than T_c , the Curie temperature. At T_c the polar phase becomes non-polar, i.e. centrosymmetric, and is represented by a dielectric anomaly whereby the dielectric constant reaches a maximum value and then decreases above T_c according to the Curie-Weiss law. When a ferroelectric crystal is cooled through T_c , it spontaneously polarizes into domains, the directions of which are dictated by the

space group and crystal structure. In order to minimize the internal strain, the domains adopt those polar crystallographic structures which lead to this condition. Therefore in order to obtain a single domain crystal either an electrical or mechanical stress is applied in the required polar direction on cooling through T_c .

There are related materials which contain aligned dipoles on the lattice dimension but are non-polar owing to their compensating antiparallel arrangement. These are known as *antiferroelectrics* and frequently have free energies near to those of a polar form. Some antiferroelectrics may be disposed into a polar form by stress, electric field or chemical modification—induced ferroelectricity; lead zirconate PbZrO_3 is a prime example.

In ABO_3 compounds, where $B = \text{Ti}, \text{Nb}$, six-fold coordination is typical, consisting of an octahedral arrangement of oxygen atoms around niobium or titanium atom as shown in Fig. 9-3. The shape or distortion of this atomic arrangement relative to the position of the B atom, is considered to have an essential role in ferroelectric transi-

sitions as well as nonlinear properties. The movement of the B ion in its oxygen cage constitutes a simple microscopic description of ferroelectricity in perovskite compounds.

The sequence of ferroelectric transitions:

cubic \rightarrow tetragonal \rightarrow orthorhombic
 \rightarrow rhombohedral

such as observed in BaTiO_3 and KNbO_3 , is readily understood if one pictures the B ion (Nb^{5+} , Ti^{4+}) being successively displaced along (100), then (110), and finally (111). This mechanism is typical of a displacive ferroelectric transition. A distinction between *displacive* and *order-disorder ferroelectrics* can be made. The order-disorder type is characterized by the existence of permanent dipoles primarily in the ferroelectric phase (Rytz, 1983). Thermal agitation competes with the dipole-dipole interaction and, at the Curie temperature, the alignment of the dipoles (perfect at absolute zero) disappears. In the paraelectric phase, dipole orientation is disordered. In displacive ferroelectrics, dipoles induced in the ferroelectric phase disappear in the paraelectric phase via a displacement of atoms towards a position of higher symmetry.

Recent work (Müller, 1981; Müller et al., 1982; Burns and Dacol, 1982) indicates that a ferroelectric transition demonstrates simultaneously both displacive and order-disorder characteristics, with one dominating but not excluding the other. This is why BaTiO_3 is not a simple example and points to the need for further investigations of polycrystalline and single crystal ferroelectrics.

Many oxide ferroelectrics exhibit the perovskite structure and possess high spontaneous polarization and dielectric constants which determine their pyroelec-

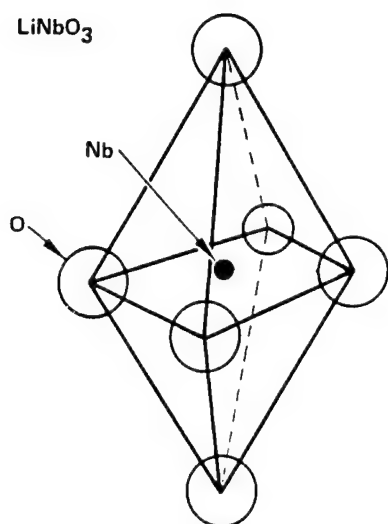


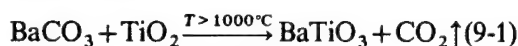
Figure 9-3. Niobium (Nb) octahedron.

tric, piezoelectric and electro-optic properties. Although the polycrystalline ceramic form has been successfully commercialized for components such as capacitors, thermal detectors, and piezoelectric elements because of its low-cost, high-volume production technology, there exist important applications for ferroelectric single-domain crystals where high coefficients and/or optical quality are deemed necessary. Such crystals may be either in bulk or thin film form according to the application.

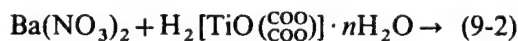
9.3 Growth of Single Crystals

The process of forming a single crystal is referred to as crystal growth. The processing of ceramic oxides is done by chemical synthesis and two examples of ways in which polycrystalline barium titanate is made are given below:

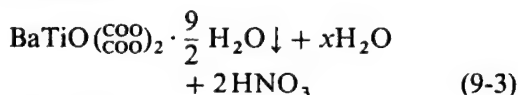
Solid state reaction:



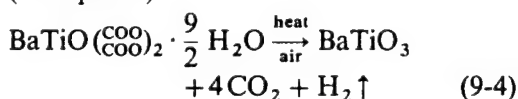
Chemical precipitation from solution:



in solution



(Precipitate)



The solid-state reaction [Eq. (9-1)] is commonly used for commercial ceramics because it is inexpensive and facilitates the inclusion of numerous other oxides by substitution or doping, whilst the chemical precipitation [Eq. (9-2) to (9-4)] provides a high-purity form which can be used in the growth of single crystals. Crystal growth is

linked with chemical synthesis; numerous methods are available for the formation of single crystals.

Crystal growth occurs through a controlled accumulation of atoms or ions or molecules around a unique nucleus. The nucleus or nucleation site may be self-induced or introduced as a seed. The methods of single crystal growth involve a controlled change of state, or phase change, to the solid (condensed) state. This transition may occur from the vapor, liquid, or, in certain cases, within the solid state itself. The growth of crystals occurs through the application of many disciplines within chemistry and physics including thermodynamics, kinetics, and fluid dynamics. Essentially, the crystal grower uses the information available in these fields to develop techniques to react components to form a single compound, to create a physico-chemical environment for controlled nucleation, and to apply (or remove) heat to transform the compound to a condition wherein programmed heat transfer will yield a condensed state accruing on the nucleation site to form a single crystal.

The emphasis in this chapter is primarily on the practical aspects of single crystal growth as related to the synthesis of refractory oxide crystals and thin films. Crystal growth theory, although rapidly developing today, is also changing, and is somewhat limited in its applicability to the *practice* of crystal growth. Most theoretical models are successful in two dimensions but do not carry over as well to the third dimension.

Before we get into a detailed discussion of crystal growth, we present a classification of crystal growth techniques with examples from a variety of materials in order to give the reader an overall view of crystal growth. Following that, we discuss growth

parameters, phase equilibria, and then present specific examples of some of the common growth techniques in use today to produce single crystals of refractory oxides and mixed crystal species which have interesting properties applicable to devices in use in many modern technologies.

9.4 Classification of Crystal Growth Techniques

The classification of crystal growth techniques presented here (Table 9-1) is based on that developed by Laudise (1967, 1970). The various crystal growth approaches are

illustrated for specific materials often representative of a group chosen from the most popular among those in practice. The selection of a growth technique is discussed in terms of phase equilibria. The description of crystal growth techniques is followed by a brief introduction to the roles of energy and mass transport.

The various chemical thermodynamic and kinetic influences are pointed out as we develop the determination of the parameters of crystal growth. A short section points out some recent work which has shown remarkable correlation between crystal growth theory and experiment. Single crystals may be grown by many tech-

Table 9-1. Classification of crystal growth techniques (Gentile, 1983).

Phase	Direct		Indirect	
	Source	Growth technique	Source	Growth technique
Liquid	Melt ^a	Verneuil	Flux-solution (solid solution)	Slow cooling
		Pedestal		Temp. differential
		Directional solidification		Solvent evaporation
		Bridgman		Top seeded (isothermal)
		Stockberger		Hydrothermal
		Cooled seed		Any solvent: aqueous, molten flux, etc.
		Kyropoulos		
		Pulling		
		Czochralski		
		Zoning techniques	Reaction	Chemical, electrochemical
Vapor	Constituent gas (Epitaxy)	Float zone		
		LHPG		
		Skull melting		
		Sublimation-condensation	Compound gas	Reaction-condensation CVD, MOCVD, (MOVPE), etc.
Solid	Solid	PVD ^b , MBE, ALE		
		Recrystallization	Solid solution	Exsolution Spinodal decomposition
		Strain		
		Polycrystal		

^a Melt may be off stoichiometry but direct if composition is same as growing crystal; ^b PVD, physical vapor deposition; MBE, molecular beam epitaxy; ALE, atomic layer epitaxy; CVD, chemical vapor deposition; MOCVD, metal-organic chemical vapor deposition; MOVPE, metal-organic vapor phase epitaxy.

Reproduced from *Tutorial Lectures in Electrochemical Engineering and Technology II*, AIChE Symposium Series, Vol. 19, No. 229 (1983) page 144 by permission of the American Institute of Chemical Engineers, © 1983, AIChE, all rights reserved.

niques, some of which will be discussed comprehensively in this article.

Crystal growth techniques are generally named after the first person to describe them (e.g., Czochralski, Bridgman) or a descriptive phrase of the process, e.g., physical vapor deposition (PVD), chemical vapor deposition (CVD). The classification shown in Table 9-1 (Gentile, 1983) is a slightly modified version of the classification first presented by Laudise (1967, 1970) with some of the ideas of Thurmond (1959). The principal difference is that crystal growth techniques have been separated initially into two categories: direct and indirect. However, the techniques have not been separated into single and multicomponent types. The direct techniques are those which do not contain any components other than those of the desired crystal product. This accords with Thurmond's "conservative" system which is similarly defined "when nothing is added to or taken from the melt except by the freezing process". The phase from which the crystal is growing, whether it is vapor, liquid, or solid, has the same overall constitution (excluding trace impurities whether added for doping purposes or inadvertently present) as the growing crystal. A common and simple example is the melt growth of single crystals of sapphire (α - Al_2O_3) from a molten pool of Al_2O_3 which may (or may not) contain trace amounts of a "dopant" metal added in order to modify electronic and/or optical properties, such as the addition of Cr^{3+} to sapphire for the fabrication of ruby laser crystals. The Al_2O_3 system is considered simple because it contains one metallic element, melts congruently to form a liquid melt of the same composition and has no solid-solid phase transitions from room temperature to its melting point at 2050°C.

Indirect techniques, like Thurmond's "nonconservative" system, involve the use of either additional foreign components or excesses of constituent components which act as mineralizers, fluxes, solvents, or carriers of the constituents. These indirect techniques include ways of growing incongruently melting crystals which decompose upon melting to form a liquid and another solid of different compositions. Indirect techniques using solvents (fluxes or mineralizers) may be employed to grow crystals which can also be grown directly. Solvent or fluxes are frequently utilized to lower the growth temperature to more practical working levels which, in addition, may avoid subsolidus (solid-solid) phase transitions. The phases or states of matter (liquid, vapor, and solid) which are changed in order to obtain single crystals represent the phases present with the solid single crystal at the interface in both direct and indirect categories. The materials from which these phases are generated are referred to as *source materials*.

Off-stoichiometric melts, i.e., melts whose composition vary slightly from the precise chemical formula of the compound, are included here as direct techniques. Crystals such as LiNbO_3 and LiTaO_3 are grown from melt compositions which vary from formula but yield solid crystals of the same composition as the melt. Frequently, these compounds will demonstrate off-stoichiometric maximum melting compositions as well as an "existence region" wherein the solid compound exists with variations in stoichiometry.

9.5 Brief Fundamental Aspects for Selection of Crystal Growth Parameters

The selection of a specific technique for crystal growth and the source materials to

be used is based on the physical and chemical properties of the material to be grown, including melting point, component vapor pressures, and constituent reactivity. The final equilibrium state is that having the lowest free energy. Therefore, the thermodynamics of the reaction(s) must be taken into consideration and frequently may be used to calculate the first usable form of pertinent data to the crystal grower: the phase equilibrium diagram. Although crystal growth is not an equilibrium but rather a steady state process, the information required to engineer a crystal growth process appears in the phase equilibrium diagram. A simple binary phase diagram (Fig. 9-4) illustrates the temperature-composition (T - X) relationships for two components which may be compounds A and B. From the diagram, it appears that both compounds melt without decomposition (congruently) at temperatures T_A and T_B , respectively, and thus could be grown by direct techniques from the melt. In addition, this diagram illustrates a simple eutectic point, E ; i.e., a minimum melting mixture of the constituents at a temperature $T_E < T_A, T_B$. Therefore, either com-

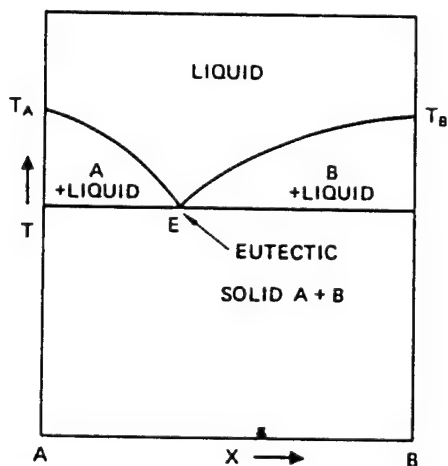


Figure 9-4. Phase diagram for binary systems.

pound may also be grown indirectly within the phase field where it is in equilibrium (as a solid) with a liquid in a temperature range lying below its melting point, but above T_E . The selection of this range depends upon the selection of the starting composition. However, below T_E , a solid mixture of A and B coexist. In order to grow a single crystal of one compound (A) from solution, the crystal must be separated from the remaining melt before T_E is reached. A pertinent method to grow single crystal A could be the Czochralski technique. Selection of crystal growth parameters and the allowed variations of parameters (degrees of freedom) are determined from the phase equilibrium diagram and governed by the Gibbs phase rule (see also Vol. 5, Chap. 1, Sec. 1.5.12, of this Series).

9.6 Phase Equilibria and the Gibbs Phase Rule

The Gibbs phase rule can be written as

$$P + F = C + 2 \quad (9-5)$$

where P = number of phases present at equilibrium; F = degrees of freedom of system (temperature, pressure, composition); and C = number of components of system.

The rule can be applied to all phase equilibrium diagrams to ascertain information concerning the phase relations and the remaining degrees of freedom which represent the control parameters of crystal growth. In practice, the Gibbs phase rule is frequently used in its reduced form derived by the removal of pressure as a variable. It can then be written as

$$P + F = C + 1. \quad (9-6)$$

Applying the reduced version of the phase rule, the eutectic point E in a binary

(two-component) phase equilibrium diagram (Fig. 9-4) is determined to be an invariant point, i.e., there are no degrees of freedom since three phases are present: two solid phases (A and B) and a liquid phase:

$$P = 3 \text{ (solid A, solid B, liquid);}$$

$$C = 2 \text{ (A, B).}$$

Thus,

$$F = 0.$$

This is obvious from the diagram itself, since at the point E both the composition and temperature (the degrees of freedom in a binary system) are fixed (invariant). However, along the curve $E-T_B$ there exist only 2 phases (solid B plus liquid), which leaves one degree of freedom. The selection of either a temperature within the range from T_B to T_E or a composition within the range from E to B fixes a point on the curve. In the phase field "B + liquid", the crystal grower may select a temperature and composition with some variability to optimize, for example, the indirect growth of solid B. The $T-X$ diagram is a result of the system thermodynamics in that it indicates the result of the equilibrium reaction for a given temperature and a specified mixture (composition) of the constituents. The phase diagram, however, tells us nothing about the kinetics of the reaction which includes the rates of the reaction, or the formation of metastable (intermediate) phases. In addition, the typical binary phase diagram represents an isobaric plane which may not be a true representation of reality for systems containing components with significant vapor pressures. In many crystal growth situations, the pressures generated at the indicated temperature and composition may be beyond the capability of the crystal

growth apparatus leading to an explosion; this is not usually a problem in refractory materials. In other cases, control of constituent overpressure may be required to achieve the desired phase, compound or stoichiometry.

Many of the systems of interest to the crystal grower today are indirect ones which include crystals which melt incongruently. A phase equilibrium diagram of a system containing an incongruently melting compound is illustrated in Fig. 9-5 (Reisman, 1970). The compound A_xB_y in the diagram melts at temperature T_i to form a solid of composition A in equilibrium with a liquid (melt) of composition i . In order to grow compound A_xB_y from the melt, an indirect approach is required utilizing a melt in the phase field " A_xB_y (solid) + liquid" under " $i-e$," liquidus line section.

A complex phase diagram such as the system BaO-TiO₂ (Fig. 9-6) (Kirby and Wechsler, 1991; Wechsler and Kirby, 1992)

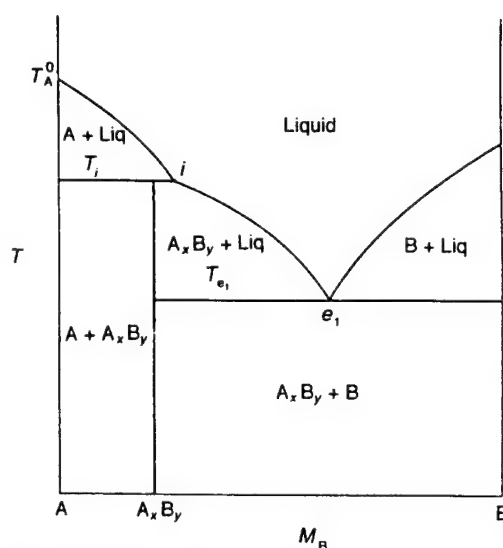


Figure 9-5. Phase diagram for incongruently melting compound. Reprinted with permission from Reisman (1970). © 1970, Academic Press, Orlando, FL; © 1990, MCNC, Research Triangle Park, NC.

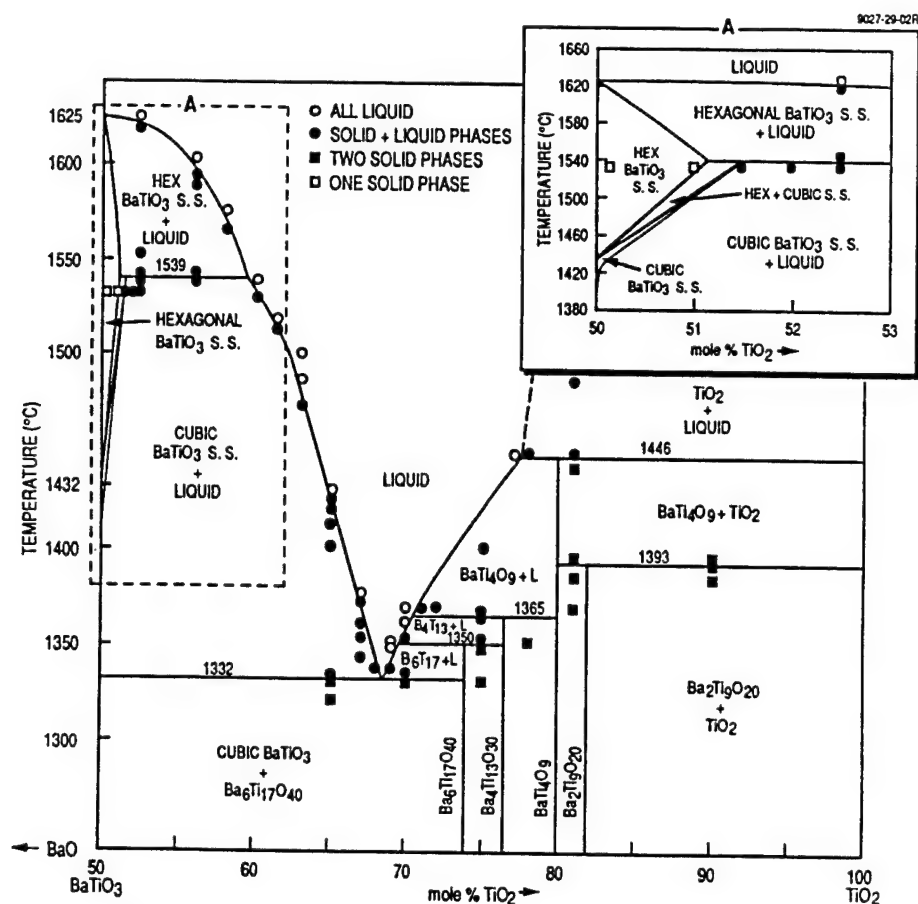


Figure 9-6. Phase diagram for the system $\text{BaTiO}_3\text{--TiO}_2$. From Kirby and Wechsler (1991) © 1991. Reprinted by permission of the American Ceramic Society.

shows the formation of many stoichiometric compounds and illustrates many features including incongruent melting. The diagram is used here to delimit the phase field wherein conditions exist for the growth of cubic BaTiO_3 from an off-stoichiometric melt, i.e., one rich in TiO_2 .

9.6.1 Solid Solution Series

In isostructural compounds such as $\text{BaTiO}_3\text{--SrTiO}_3$, $\text{KTaO}_3\text{--KNbO}_3$, $\text{PbZrO}_3\text{--PbTiO}_3$, a complete continuous series of quaternary compounds may ex-

ist, from one pure end member to the other, which is called a solid solution series. A series of the general formula $\text{KTa}_x\text{Nb}_{1-x}\text{O}_3$ where $0 < x < 1$ exists for all values of x in the designated range. This relationship can be shown as a phase equilibrium diagram (Fig. 9-7): a plot of temperature vs. mol% KTaO_3 in the liquid–solid thermal range (Fig. 9-7a), and the subsolidus phase equilibrium (Fig. 9-7b). The essential difference (see Fig. 9-7a) from most phase equilibrium diagrams is the constantly varying compositions of the liquid (shown by the liquidus curve) and

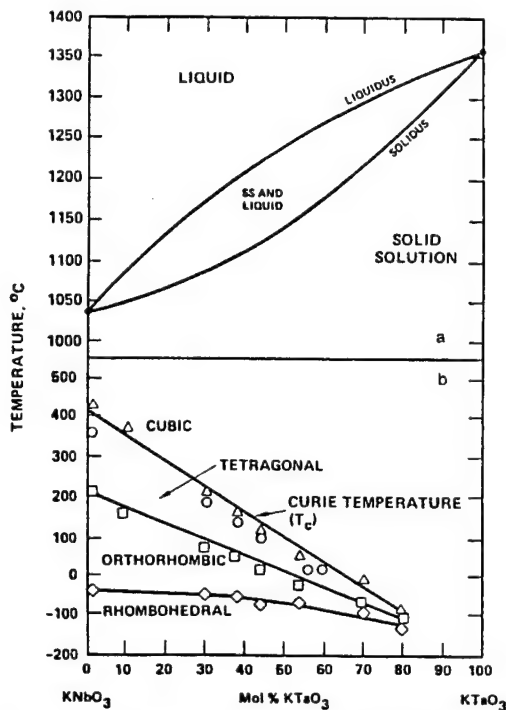


Figure 9-7. KTN phase diagrams. (a) Liquidus-solidus relations; (b) subsolidus relations.

the solid (solidus) with changes in temperature. The region between the curves represents solid in equilibrium with liquid. The area above the liquidus is entirely liquid; and that below the solidus is all solid. In Fig. 9-7b, we observe that the first-to-form solid is cubic. The transition boundary from cubic to tetragonal represents the Curie temperature which varies with composition (value of x). In this system, this is a nondestructive transition into the ferroelectric phase.

In the 'KTN' system shown in Fig. 9-8, a melt composition at A (approximately $\text{KTa}_{0.37}\text{Nb}_{0.63}\text{O}_3$) is entirely liquid above 1200°C. As the temperature is lowered to cross the liquidus curve, the first-to-freeze composition (approximately $\text{KTa}_{0.66}\text{Nb}_{0.34}\text{O}_3$) is designated by a' on the solidus curve; the tie line a - a' shows the liquid-solid equilibrium at temperature $T=1200^\circ\text{C}$. As the temperature is lowered, the composition of the liquid varies along the liquidus curve, and that of the solid along the solidus curve. For a starting composition A, solidification is complete when the vertical extension of A

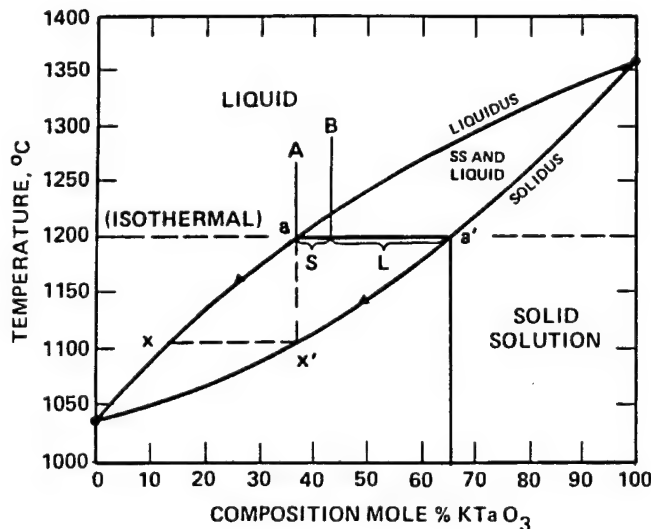


Figure 9-8. Phase diagram for the system KNbO_3 - KTaO_3 .

hits the solidus (x'); theoretically, the last drop of liquid has the composition x . The solid obtained by a slow cooling procedure varies continuously in composition.

In order to obtain a crystal or solid of composition a' at a working temperature of 1200°C , the selected melt composition must lie to the right of A, i.e., must be richer in Ta. This is shown for a composition at B ($\text{KTa}_{0.43}\text{Nb}_{0.57}\text{O}_3$). The intersection of B with the isothermal temperature (1200°C) line extension designates the proportional amounts of solid (S) and liquid (L) at that temperature. Starting with composition B, precipitation of solid material commences as the temperature is lowered just below the liquidus curve, approximately 1220°C . As discussed above for A, the first solid to crystallize lies at the intersection of a horizontal line (the 1220°C isotherm) with the solidus curve. As cooling continues, the compositions of both the liquid and solid continuously change along their respective curves. This relationship poses a significant problem for the crystal grower seeking a uniform single crystal and requires a technique which varies from the standard cooldown procedure. Techniques have been developed to overcome this problem and are discussed in Sec. 9.7.2.1.

9.7 Crystal Growth Techniques

9.7.1 Growth from a Melt

Direct crystal growth from a liquid melt to a solid involves the solidification by a controlled pass through the melting point of the compound. Typically, the source material is heated to melting and then cooled slowly by either lowering an ampoule through a suitable thermal gradient or lowering furnace temperature (ramping).

The selected growth technique may require an ampoule or container, or one may choose a "containerless" technique defined here as a method wherein the source material does not come into contact with a container in the region of the growth interface. Container selection is influenced by temperature and reactivity of the constituent materials. In many cases, the furnace may be used in either a vertical or horizontal position so long as the growth parameters may be stabilized and controlled.

9.7.1.1 Directional Solidification

Directional solidification involves cooling through the melting point of a liquid melt in an ampoule. The ampoule is frequently conically shaped at the bottom tip to achieve nucleation of a single crystal. This method is often used where no seed of the desired single crystal is available. When a seed is available, it may be encapsulated into the base of the ampoule for "seeded" growth. Solidification continues from the tip to the top of the ampoule by cooling and directing heat transfer or removal of heat through the growing crystal. Bridgman (1925) enhanced the direct solidification technique by invoking a thermal gradient profile initially accomplished by having the center of the furnace at maximum temperature and then allowing the natural cooling toward the ends to create the gradient. Thermal techniques have been applied to control growth gradients in both contained and containerless techniques.

9.7.1.2 Bridgman-Stockbarger Technique

In the Bridgman technique, the furnace temperature is kept constant and the ampoule is lowered at a controlled rate through a preset thermal profile. Stockbarger's (1936) interest in growing large

crystals (several inches in diameter) of alkali halides led him to take more drastic steps to remove heat and create a steeper thermal gradient (larger $\Delta T/\Delta x$, where ΔT is the change of temperature with distance in the furnace, Δx). He added baffles inside the furnace to assist in cooling the desired region. Today many variations of these methods are in practice and different ways are used to vary thermal gradients. A typical vertical crystal growth method using an ampoule and cooling in a modified-steep thermal gradient is commonly called Bridgman–Stockbarger (Fig. 9-9). Natural steep thermal gradients are typical of some of the containerless techniques because of their geometric configuration.

9.7.1.3 Verneuil Flame Fusion Technique

The growth of crystals from the melt is most easily achieved by the Bridgman–Stockbarger technique. However, the properties of refractory oxide materials rule out the use of conventional crucible (container) materials, e.g., fused silica, because of their high melting points and subsequent reactivity. Several approaches can be used to bypass these problems essentially by employing “containerless” techniques. The “flame fusion” or Verneuil technique (Verneuil, 1902) has been used extensively for the synthesis of sapphire, ruby, rutile (TiO_2), and spinel (MgAl_2O_4). The Verneuil technique represents one of the early direct crystal growth techniques from the melt. Growth takes place on a pedestal as shown schematically in Fig. 9-10. Verneuil used a hopper to hold and feed the Cr-doped aluminum oxide powder above a pedestal. Heat was provided by an oxy-hydrogen torch to initiate rapid melting of the powder at 2050°C . As the molten powder is distributed around the pedestal, it loses heat and solidifies.

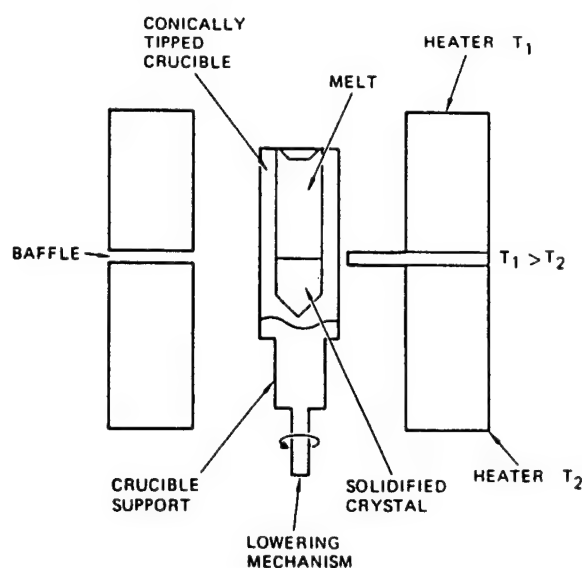


Figure 9-9. Bridgman–Stockbarger growth apparatus. Reprinted with permission from Academic Press, Inc., Orlando, FL, from Gentile (1987, 1992), © 1987, page 4; © 1992, page 712.

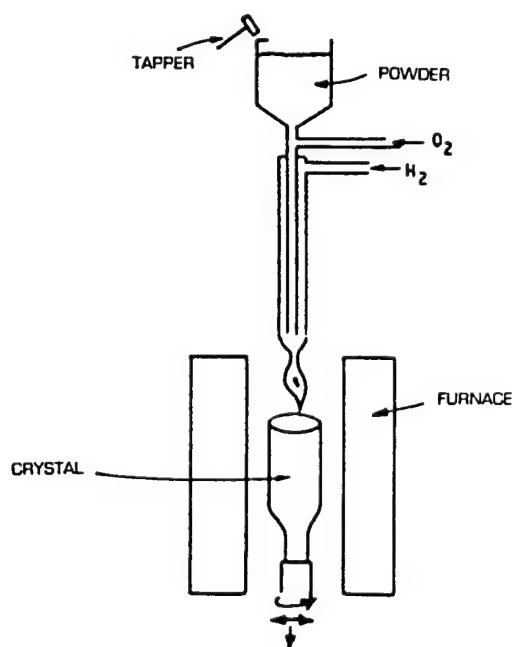


Figure 9-10. Verneuil flame fusion apparatus. Reprinted with permission from Hurle (1979), page 110, © 1979, Elsevier Science Publishers BV, Amsterdam.

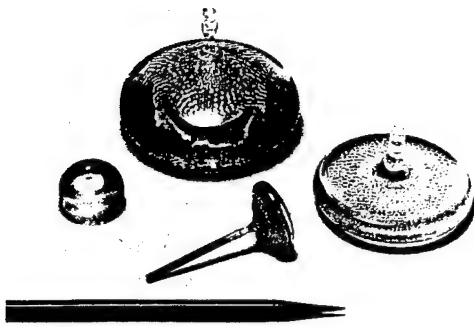


Figure 9-11. Verneuil-grown sapphire boules.

The pedestal for single crystal growth held a single crystal rod of sapphire or ruby to nucleate and promote continuous single crystal growth, yielding boules and rods of various sizes. Modification of the standard pedestal approach can yield disk-shaped sapphire boules as shown in Fig. 9-11. However, the fast cooling of the material in this zone of steep thermal gradients

causes the crystals to grow very highly strained. Crystals often split in half in storage to relieve the built-in strain. The Verneuil technique has been replaced (Charvat et al., 1967) for the most part by the Czochralski technique.

9.7.1.4 Czochralski Technique

The *Czochralski technique* (1918) (Fig. 9-12) employs the use of a crucible containing the melt from which a solid single crystal is pulled by controlled lifting after dipping of a seed (or a noble metal rod, e.g. Pt, when no seed is available) to induce nucleation. If multiple crystals nucleate, a "necking down" procedure is applied to restrict the growth to one single crystal. Heating of the crucible may be accomplished by use of a resistance-heated furnace or radio frequency (rf) induction in which case the crucible may act as an rf susceptor. Heat transfer through the growing crystal and holder rod is enhanced by the steep thermal gradient and causes so-

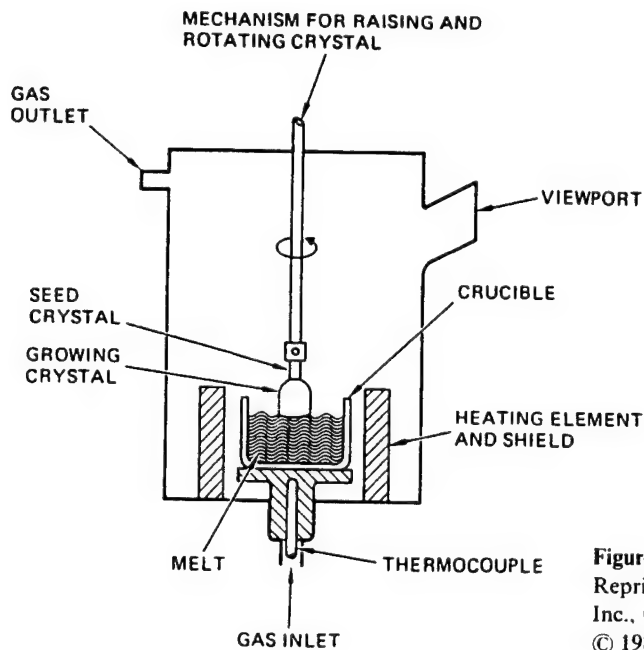


Figure 9-12. Czochralski crystal growth system. Reprinted with permission from Academic Press, Inc., Orlando, FL, from Gentile (1987, 1992), © 1987, page 5; © 1992, page 713.

lidification to occur. Constant temperature control (frequently automated) is necessary to continue growth as well as to maintain a uniform diameter of the growing ingot. This is the standard technique for commercial growth of ruby and sapphire from a melt contained in an iridium crucible.

The Czochralski technique was subsequently developed for commercial electronic-grade silicon pulled from fused silica crucibles. However, requirements for high-purity, "zero-defect" silicon free of oxygen impurity caused much of the production of silicon wafers to utilize the float zone technique, as described in Sect. 9.7.1.6, below.

A special variant of the Czochralski method, the *Kyropoulos technique*, utilizes a cooled seed to initiate single crystal growth within the melt-containing crucible. However, heat removal continues by controlled lowering of the furnace temperature (ramping) to grow the crystal within the crucible, without any pulling and rotation.

Other variations of both these techniques have been developed, one of which, *liquid encapsulated Czochralski (LEC) growth*, is especially useful for compound semiconductors which are volatile at their melting points, e.g., GaAs, GaP, InP, PbTe, Bi₂Te₃, etc. Boron oxide, which melts as a glass at 450°C, remains viscous to high temperatures and does not react with the above compounds, is most commonly used as a molten layer around the melt. Figure 9-13 shows the experimental setup for the growth of gallium phosphide in which an overpressure ($P > 30$ atmospheres) of inert gas is maintained in the closed system along with the B₂O₃ layer, to prevent loss of phosphorus. LEC is not usually required for the less volatile compounds such as the refractory oxides al-

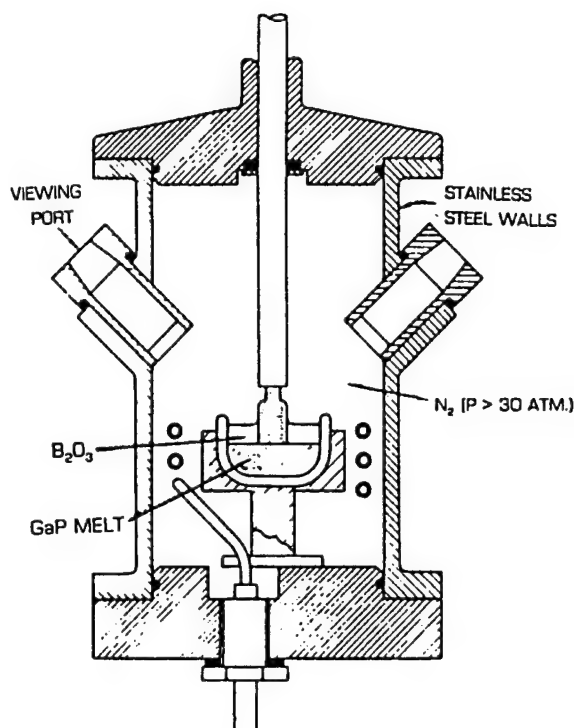


Figure 9-13. Liquid encapsulated Czochralski (LEC) apparatus. Reprinted with permission from Hurle (1979), page 99, © 1979, Elsevier Science Publishers BV, Amsterdam.

though some problems of constituent loss occur in certain systems which contain oxides which are volatile at growth temperatures. A major problem for the application of LEC is the reactivity of most refractory oxides with boric oxide as well as many other possible encapsulants (see also Vol. 16, Ch. 2, Sec. 2.5.4).

9.7.1.5 Skull Melting

A more controlled containerless (or actually "self-container") technique than the Verneuil method discussed above is *skull melting* (Aleksandrov et al., 1973). Skull melting has been demonstrated (Nassau, 1981; Wenckus et al., 1977) to produce very large crystals of such materials as cu-

bic zirconia (ZrO_2 stabilized in the cubic form by the addition of Y_2O_3 , CaO , or MgO). This method utilizes a cold crucible or skull to contain the melt inside a crust of its own powder. The skull is designed for the use of radio frequency (rf) energy to heat and melt the material inside, e.g., cubic zirconia. The skull consists of a split cup (usually split in half), closed at the bottom and open at the top, made up of numerous water-cooled copper tube fingers. The skull is placed inside a copper coil which is energized with an rf generator. Radio frequency penetrates into the skull filled with the zirconia powder containing a stabilizer and powdered zirconium metal. The metal is required to act as the initial susceptor because the zirconia powder is an insulator at room temperature. As the zirconia gets hot, it becomes conducting (similar to alumina) and melts in the rf field. Eventually, the zirconium metal reacts with oxygen from the surrounding air to form additional zirconia. A thin solid skin (less than 1 mm thick) remains next to the walls of the cup because it is cooled by contact with the water-cooled copper fingers. This skin, acting as a container, prevents contamination as well as reaction between the melt and the skull. The melt is maintained for several hours to ensure uniformity; then, it is slowly cooled. Self nucleation has been observed to start at the bottom of the cup; crystal growth proceeds from the bottom to the top until the melt is consumed. Columns of single crystals as large as 2 cm across and 1.5 cm long have been grown by this technique. This process has been commercialized for the growth of large cubic zirconia crystals (Wenckus, 1993).

9.7.1.6 Zoning Techniques

In the liquid-to-solid techniques discussed above, the source material exists

(just prior to crystal nucleation) completely in the liquid state and then proceeds to solidification. A different approach is involved in "zoning" techniques where only a narrow zone of liquid is made to travel through a polycrystalline ingot for transformation into a single crystal. The width of the molten zone is dependent on the viscosity/surface tension of the melt. The float zone technique shown in Fig. 9-14 employs rf heating of a polycrystalline ingot in contact at one end with a single crystal. Melting is accomplished at the interface and the zone is moved, by the motion of either the ingots or the furnace, to continue single crystal growth. Although performed vertically and containerless for silicon, horizontal zoning techniques similar to the zone-refining process

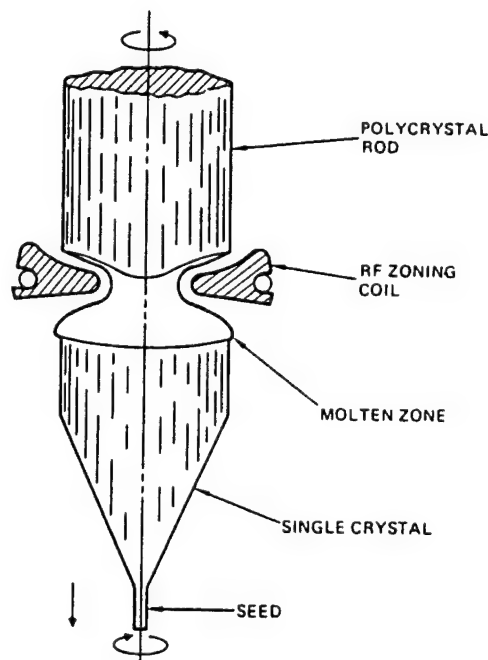


Figure 9-14. Float zone technique. Reprinted with permission from *Encyclopedia of Physical Science and Technology* Vol. 4, Academic Press, Inc., Orlando, FL, from Gentile (1987, 1992), © 1987, page 6; © 1992, page 714.

developed by Pfann and Olson (1953), primarily for purification, have been used for single crystal synthesis. The high melting points, reactivity, and relatively low viscosity of molten refractory oxides limit the application of zone melting techniques. Alternative methods of heating have been used, including lamps and lasers. Ainger et al. (1970) successfully grew ferroelectric tungsten bronze oxide crystals using an arc-image furnace.

A recent development (Feigelson, 1985) is *laser heated pedestal growth* (LHPG) which is a float zone technique for the growth of small diameter or fiber single crystals where the material is self contained by the surface tension of the melt. A laser, usually carbon dioxide, is used for oxide melts since the $10.6\text{ }\mu\text{m}$ photon energy is readily absorbed, making it relatively easy to grow crystals from ceramic feed rods and attain temperatures of more than 3000°C . LHPG is a versatile technique which enables the study of the melting behavior and crystallization of some of the more refractory oxide compounds and to access either those for which there is no suitable crucible, or those which do not lend themselves to skull-melting and where also small quantities of materials are available.

9.7.2 Indirect Crystal Growth – Growth from Solution

Indirect crystal growth is dominated by solution growth where a solid crystal (essentially, the solute) can be retrieved from a liquid solution by either cooling slowly and thus changing the solubility relations, or by evaporation of a solvent which is volatile under the conditions of crystal growth. The solvent can range in composition from one that varies slightly from the stoichiometric composition of the desired

crystal (an excess of one of its constituents) to a totally foreign material which dissolves the desired compound under certain conditions such as heating, but will allow it to solidify intact upon cooling.

An ideal solvent should meet the following requirements (Elwell & Scheel, 1975):

- high solubility for crystal constituent;
- crystal phase is only stable phase at growth temperature;
- appreciable change of solubility with temperature;
- low viscosity at the applied temperature;
- low melting point;
- low volatility;
- nonreactive with crucible;
- absence of elements which are incorporated into the melt;
- suitable density;
- ease of separation from crystal;
- low toxicity.

9.7.2.1 Top-Seeded Solution Growth

Top-seeded solution growth (TSSG) was first introduced by Linz et al. (1965) and described in detail by Belruss et al. (1971), and has been used successfully for many ABO_3 compounds (Rytz et al., 1990) including BaTiO_3 , KNbO_3 , SrTiO_3 , and solid solution series which include $\text{Ba}_{1-x}\text{Sr}_x\text{TiO}_3$, BST (Rytz et al., 1985), and $\text{KTa}_{1-x}\text{Nb}_x\text{O}_3$, KTN (Rytz, 1983; Gentile and Andres 1967). The substitution of Sr for Ba in BaTiO_3 stabilizes the cubic phase and allows solidification from a melt while avoiding excessive strain or cracking in the crystal. KTN grows in a cubic phase and the ferroelectric transitions are nondestructive.

Top-seeded solution growth utilizes a setup similar to that used for Czochralski growth except for a few significant differences. As illustrated in Fig. 9-15, the crucible is on an insulated stand within a

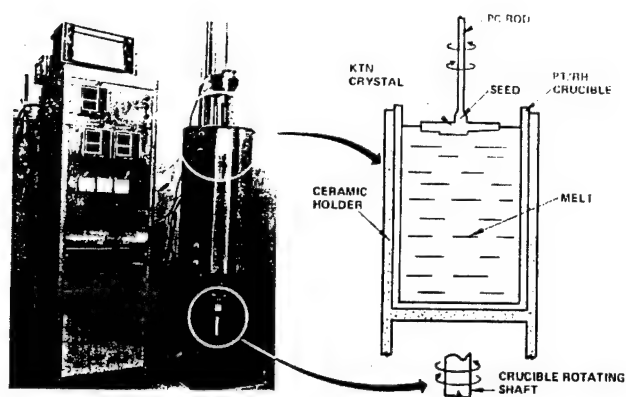


Figure 9-15. Apparatus for top-seeded solution growth.

resistance-heated furnace. Crucibles used for these materials can be platinum or platinum/rhodium alloys. The seed is suspended from a platinum rod which is not reactive with the melt and acts as a heat sink. The melt consists of the component oxides with an excess of one. A look at the phase diagram (Fig. 9-16) (Kirby and Wechsler, 1991) indicates that a solution of approximately 35 mol% BaO and 65 mol% TiO_2 yields the cubic phase of BaTiO_3 (Rytz et al., 1990) when cooled below the liquidus temperature (near

1400°C) but above the eutectic temperature (1332°C).

Solid-solution growth of either BST or KTN of compositions away from the end members is somewhat more complex. As described in Section 9.6 on phase equilibria, KTN solid solutions are grown from a melt whose composition is widely different from the solid material in equilibrium with it. In addition, lowering the temperature causes a large, continuous change in crystal composition. This would mean large variations in Curie temperature and

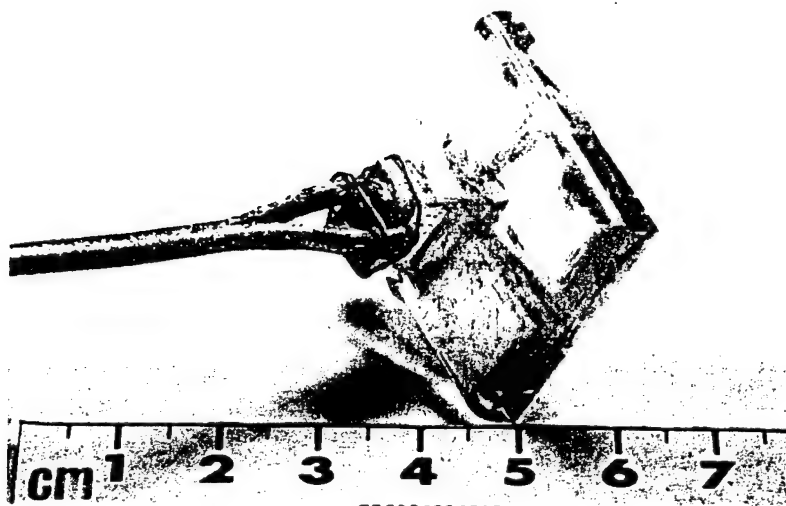


Figure 9-16. KTN single crystal.

other ferroelectric and optical inhomogeneities within the crystal. In order to maintain uniform composition, KTN is grown isothermally (see Fig. 9-8) from a melt rich in K_2O using solvent evaporation of the volatile K_2O (Gentile and Andres, 1967). The use of Pt/Rh crucibles holding as much as 800 g of melt yielded large KTN crystals as shown in Fig. 9-16. Because of the nature of the growth and a viscous melt, stirring is necessary to maintain a uniform melt. In addition to seed rotation at several rpm, ACRT (accelerated crucible rotation technique) developed by Scheel and Schulz-DuBois (1971) has been used with success (Scheel, 1972). Without effective stirring, depletion of required constituents can occur at the solid-melt interface which can slow down or stop continued crystal growth or cause constitutional supercooling, resulting in spurious deposition of undesired material on the growing crystal.

9.7.2.2 Hydrothermal Growth

Hydrothermal crystal growth is a special case of solution growth utilizing the increased solubility of many compounds in water under high pressures and temperatures. The technique is well-known for the synthesis of large quartz (SiO_2) crystals (Laudise, 1987; Laudise and Barns, 1988) weighing in the range of 5 to 8 kg (Laudise, 1994) for the electronic communications industry. Other oxide crystals including beryl ($Be_3Al_2Si_6O_{18}$) and ruby (chromium-doped sapphire, $\alpha-Al_2O_3:Cr$), have also been grown hydrothermally. An important advantage of the hydrothermal method is the use of pressure as a variable which adds an important dimension to process control and, in addition, may allow variations in product characteristics which are not attainable with other tech-

niques. A knowledge of the phase equilibrium conditions for the system involved is essential under critical and supercritical conditions. Autoclave containers for hydrothermal growth must be able to withstand high pressures at elevated temperatures while resisting attack from either acidic, basic or oxidizing hydrothermal solutions. Special stainless steel formulations have proven successful; however, for many materials, the container must be lined with a noble metal to prevent reaction.

9.7.2.3 The Sol-Gel Process and Its Derivatives

The sol-gel process is popular today for the growth of polycrystalline thick films of such materials as PZT, BST, and KTN for applications including non-volatile ferroelectric memory devices, pyroelectric detectors, and capacitors. The approach utilizes the chemistry of viscous solutions containing an intimate mixture of the constituent elements of interest (often as organo-metallic compounds) which are uniformly distributed so that upon calcination, the desired stoichiometric compound forms with little or no segregation. Although the sol-gel technique is not specifically aimed at the growth of thin single crystal films, many approaches towards growing ferroelectric thin films are based on a solution process with controlled viscosity – however, not always a gel. The viscosity controls the film thickness distributed on a substrate via a spinning technique as developed in the semiconductor industry. In this case, the solution is placed in the center of a wafer which is rotated at an appropriate velocity to spread the liquid uniformly across the surface. Highly preferred orientations of the films can be obtained by using a single crystal substrate with or without buffer layers.

9.7.3 Crystal Growth from the Vapor Phase

9.7.3.1 Physical Vapor Deposition

Crystal growth from a vapor phase has many complexities, some of which will be covered herein. The simplest case is the solidification or condensation of a constituent gas or gases; essentially the opposite of sublimation. Under certain conditions of temperature and pressure, for example, water vapor will form ice. Similarly, II–VI compounds, e.g., CdS, ZnS, will grow as single crystals from their constituent gases: Cd or Zn and S₂. The technique utilized is called *Physical Vapor Deposition* (PVD) and does not involve any extraneous compound formation or reactions. In the case of these II–VI compounds, the source material can also be the solid compound itself which sublimates upon heating to form the two gaseous species. Under the proper conditions of pressure and temperature, the gases will combine upon condensation in stoichiometric proportion to form single crystals of the compounds, or even mixtures (mixed crystals) of two or more compounds. This is a unique property of II–VI compounds. PVD as well as other vapor deposition techniques are not an applicable technique for the synthesis of single crystals of refractory oxide compounds since the vapor pressures of most constituents is extremely low even at elevated temperatures. However, many investigators are currently pursuing vapor deposition of thin single-crystal films of ferroelectric, nonlinear, and superconducting oxides using high-vacuum molecular beam epitaxy (MBE), metal-organic molecular beam epitaxy (MOMBE), and chemical vapor deposition (CVD) (MOCVD or OMVPE) techniques. These are covered briefly in the discussion that follows.

9.7.3.2 Vapor Deposition of Single-Crystal Thin Films

When the volatility of the constituents is insufficient to cause sublimation, as is the case for most refractory oxides, other techniques may be employed. The use of high vacuum frequently creates phase conditions where the constituents can be heated to vaporization. Such is the case in molecular beam epitaxy (MBE) where effusion cells containing elemental sources are heated to form directional beams of constituent atoms. A schematic diagram for a MBE system is shown in Fig. 9-17 (Panish, 1986) for GaAs/GaAlAs. Recently, investigators have used MBE for the synthesis of new high temperature superconductors including yttrium barium copper oxide (YBCO, YBa₂Cu₃O_{7-x}) and similar systems. Stoichiometry is controlled both by temperature of the substrate (where solidification is occurring) and concentration of the constituents in the vicinity of the substrate. In many experiments, the unsuitable properties of certain elements have been overcome by employing metal-organic (MO) sources creating a technique referred to as MOMBE. Under these conditions, MBE may be considered an indirect technique.

9.7.3.3 Metal-Organic Chemical Vapor Deposition

Approaches to the growth of single crystal films where the constituent elements are introduced as metal-organic compounds have been designated metal organic chemical vapor deposition (MOCVD) or organometallic vapor phase epitaxy (OMVPE). Gaseous compounds of the constituent elements are introduced in proportions calibrated to yield the desired stoichiometry under the growth conditions. A simplified schematic diagram for MOCVD utilizing three constituents is shown in Figure 9-18.

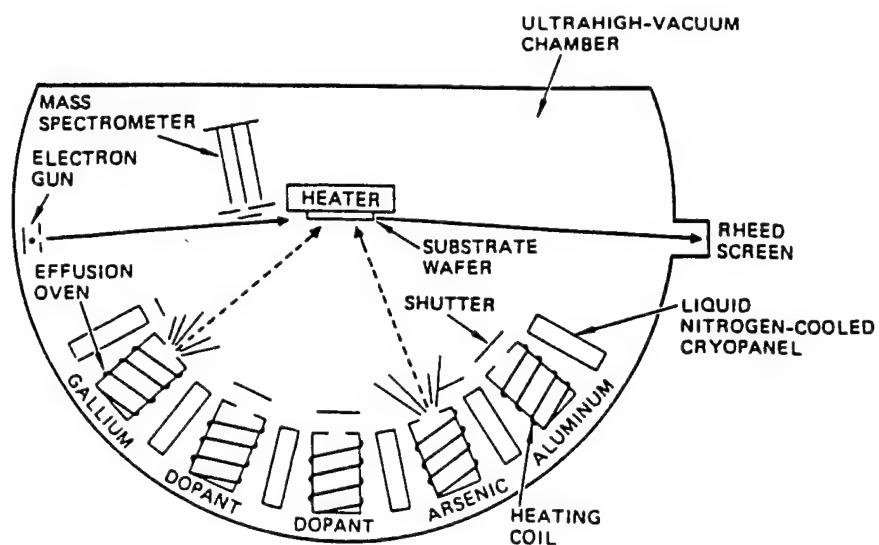


Figure 9-17. Molecular beam epitaxy (MBE) schematic. Reprinted from Panish (1986), © 1986, with permission from Pergamon Press Ltd., Oxford.

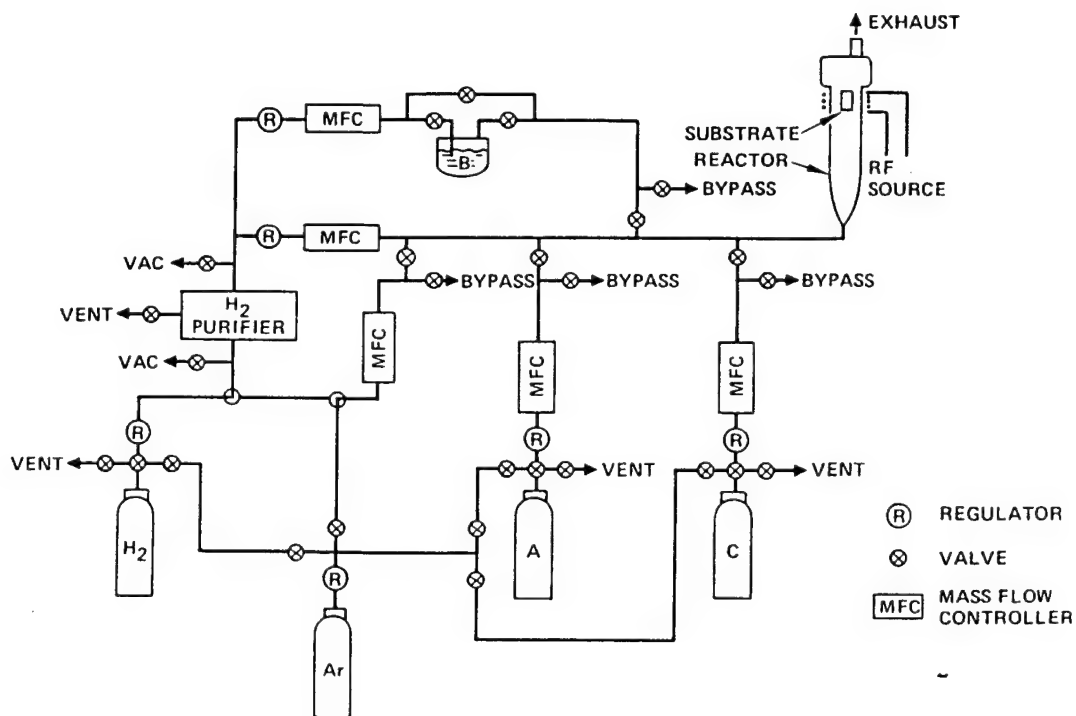


Figure 9-18. Simplified MOCVD apparatus.

In "cold wall" CVD techniques, the source gases are selected so that they decompose/react only when they come into contact with the hot substrate – usually a single crystal to nucleate epitaxial growth. Epitaxial growth occurs when the deposited layer follows the lattice network of the substrate whether the substrate is the same material (homo-epitaxy) or a different crystal substance (hetero-epitaxy). The major factors for substrate matching in order to obtain optimum layer quality are lattice parameters and coefficients of thermal expansion. In cold wall reactors, the substrate is heated usually by placing it on a susceptor, e.g., a carbon block, and using rf induction heating. In some cases, heating is accomplished or assisted by internal or external radiant lamps. Following the reaction and deposition of the desired layer, residual gaseous products are removed from the reactor by pumping or flowthrough of inert gases. Reactor shapes (geometries) may vary to accommodate the reaction relative to the surface of the substrate; they may be vertical or horizontal. Similar geometries may be used in "hot wall" reactors which are contained in furnaces. The entire reactor is heated to maintain constituent elements (or compounds) in the vapor state until they react and deposit on the substrate. This may result in deposition which is not restricted to the substrate.

9.7.3.4 Atomic Layer Epitaxy

Atomic Layer Epitaxy (ALE) (Suntola and Hyvarinen, 1985) is a vapor deposition technique applicable to MBE and/or MOCVD. A monolayer of each constituent is deposited either individually from an elemental source or as a reactant species to form the desired compound by reaction with a subsequent layer as illustrated in Fig. 9-19. In the figure, the reaction to form

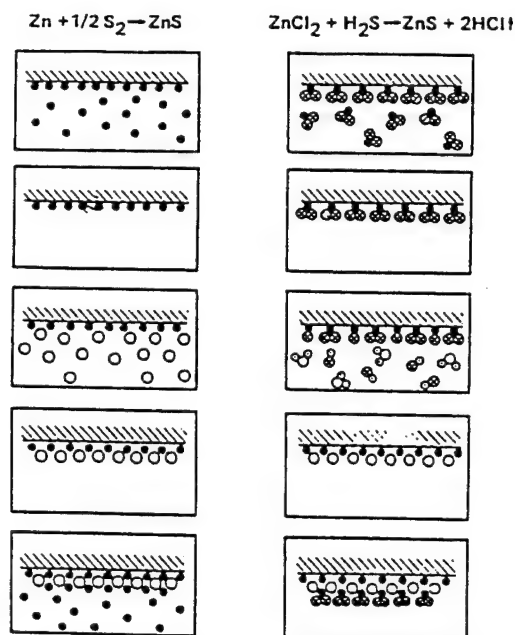


Figure 9-19. Atomic layer epitaxy (ALE). After Suntola and Hyvarinen (1985). Reproduced with permission from Annual Reviews Inc., © 1985.

ZnS is shown on the left by direct reaction of the elemental constituents, zinc and sulfur; the right side illustrates the layer-by-layer reaction of ZnCl_2 and H_2S . Conditions are established to remove excess atoms other than the desired monolayers. ALE has been extremely successful for synthesis of II–VI compound layers because of the properties of II–VI materials. The II–VI bond, e.g., Zn–S, is much stronger than either the Zn–Zn or the S–S bonds. The method could be extended to the ALE growth of oxides, for instance titanium tetrachloride could be reacted with wet air and/or oxygen to give titanium dioxide.

9.7.4 Solid-to-Solid Crystal Growth

Solid-to-solid crystal growth is dominated by recrystallization which is typically invoked by sintering to cause grain growth and may ultimately yield single crystal ma-

terial. Direct recrystallization begins and ends with the same compound but yields larger crystal grains. Grain growth occurs to reach a state of lowest free energy. Built-in strain in a polycrystalline mass activates the process of recrystallization. Gilman (1963) describes *exaggerated grain growth*: "...in certain cases, after prolonged annealing of a fine-grained matrix, only one (or a few) large grain grows at the expense of the whole specimen." (See also Vol. 15, Chap. 9, Sec. 9.6.3, of this Series.) Although first observed in metals where reorientation across grain boundaries leading to grains disappearing is more frequently observed, this process has been observed in semiconductors, organic materials, ice, and in some minerals when compressed and heated (McCrone, 1949). The latter include anhydrite (CaSO_4), fluorite (CaF_2), periclase (MgO), and corundum ($\alpha\text{-Al}_2\text{O}_3$). In addition, as a result of heat and compression of powders (Buckley, 1961), significant grain growth has been observed in rock salt (NaCl) and sylvite (KCl).

One of the most successful applications of solid-to-solid crystal growth has been in hexagonal ferrites. Single crystals of approximately 10 mm diameter by several centimeters in length have been reported (Lacour and Paulmus, 1968) for barium hexaferrite, $\text{BaFe}_{12}\text{O}_{19}$.

Indirect solid-to-solid crystal growth includes the phenomena of spinodal decomposition where a "mixed crystal" (a single crystal composed of the constituents of two isomorphous crystals) breaks down into its constituent compounds or different mixtures because the compounds formed are the equilibrium phases (lowest free energy states) under the conditions of temperature and pressure (see Vol. 5, Chap. 7 of this Series).

9.8 Distribution Coefficient and Mass Transport

The selective incorporation (or rejection) of components at a fluid-solid interface causes the interface of a growing crystal to represent not only a sink for matter, but also a source of both heat and matter. Latent heat that is released during the growth process (when atoms/ions are attaching to the solid) at the interface, together with matter that is not incorporated into the solid, must be transported away from the advancing interface. In this manner, heat transfer proceeds through both the fluid and the solid; the rejected constituents are transported through the fluid only. The rate with which constituent atoms (ions) are incorporated into the solid is governed by the difference in the chemical potentials of the two phases in contact. In turn, the chemical potentials depend on the concentration of all species present, as well as on the local temperature and pressure. Thus, the mass and heat transport problems are coupled. In order to determine the time-dependent position and shape of an interface, one must simultaneously consider the conservation of mass, momentum, and energy for the entire system. Macroscopic mass and heat transport play a central role in crystal growth. Molecules or atoms must be transported in the fluid over macroscopic distances toward the interface where they attach to the crystal. This transport can be fast or slow compared to the growth (attachment) kinetics. The rate at which a crystal grows can be limited by interfacial kinetics or by the transport process (diffusion limited). These are the factors which must be established by the crystal grower in terms of control of overall constituent concentration (source material), temperature, temperature gradient, pressure, and

growth rate. When growth is by an indirect method, there will be a buildup of those components that tend to be rejected from the solid adjacent to the growing interface.

If the distribution constant (or segregation coefficient) k , defined as the concentration of a constituent, A , in the solid over the concentration of that constituent in the liquid

$$k = \frac{[A_{\text{solid}}]}{[A_{\text{liquid}}]} \quad (9-7)$$

of a given component is less than unity, $k < 1$, then the component will be rejected from the solid and will tend to concentrate close to the growing interface. Conversely, if $k > 1$, there will be a depletion of that component close to the interface as compared to the bulk composition. The effective segregation coefficient k_{eff} in the real growth regime is different from the equilibrium k derived from the phase equilibrium diagram. Thus, k_{eff} can indicate the impact of crystallization rate, diffusion, and hydrodynamic processes at the crystal growth interface (Burton et al., 1953). Diffusion processes, activated by concentration and thermal gradients, are required to homogenize the composition at the growing interface. If crystal growth is so slow as to be almost at equilibrium, diffusion can readily counteract this effect. In most cases, however, severe build-up can occur. Build-up, in turn, leads to a morphological stability problem. This problem is commonly encountered in indirect crystal growth and can result in constitutional supercooling.

When the rate of growth is too rapid for the diffusion of the constituents of the growing crystal (in their proper proportions) for balance at the growth interface, the composition of the liquid becomes depleted of certain constituents. This leaves a composition which has a lower freezing

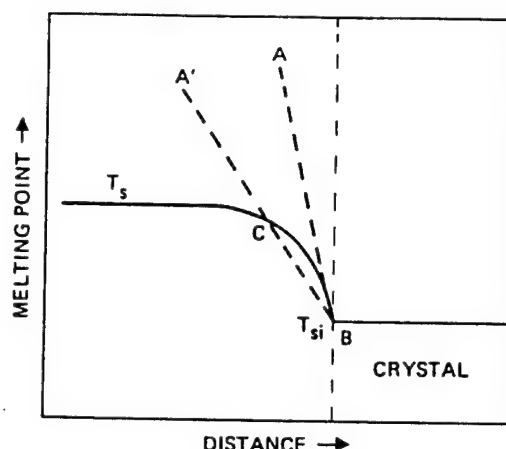


Figure 9-20. Composition melting points as a function of distance near the growing interface.

point and, therefore, tends to freeze out rapidly (Hurle, 1962). Such a case is illustrated in Fig. 9-20 which shows the melting point relationships of the compositions that exist near the interface of the growing crystal as a function of distance. The melting point of the solution (T_s) decreases as the interface is approached. Lines AB and $A'B$ represent two different possible temperature gradients in the solution. For the larger (steeper) gradient, AB , there is no supercooling at all positions in front of the interface. For the smaller gradient, $A'B$, the region CB is supercooled and crystallization will tend to take place in front of the solid interface at a rapid rate. Large temperature gradients as well as slower growth rates can be used to lessen the tendency toward constitutional supercooling. If the growing interface is not an "equilibrium form" of the crystal, it will usually change to a surface composed of facets whose faces are equilibrium faces, or at least faces of lower interfacial free energy. There exists a tendency toward runaway dendritic growth resulting in a mosaic structure. In addition to the thermal gradient (which may be furnace limited), the

control of crystal growth at this point depends on the growth rate and use of methods such as accelerated crucible rotation technique (ACRT) to enhance diffusion and mixing of the constituents. In essence, we must overcome the constitutional (composition) differences at the liquid–solid or liquid–vapor interface referred to as the “boundary layer.”

Crystal growth literature contains numerous mathematical treatments of the boundary layer. A good comprehensive treatment of the subject appears in the book by Rosenberger (1979). The relation of the boundary layer concept to real crystal growth situations is very complicated. In fact, crystal growth situations may or may not have boundary layers. If crystal growth rates are sufficiently slow, diffusive flow may spread over the entire region. The important and related roles of macroscopic mass and heat transport have been noted above for their central role in crystal growth processes. Molecules must be transported in the fluid over macroscopic distances to the crystal–fluid interface. From this position they take their (relatively) permanent position on the crystal surface. The control factor at this critical point is the boundary layer.

9.9 Heat Transfer

The transfer of thermal energy within materials and experimental setups is as important for the understanding of crystal growth as the transport of matter. Specific temperature ranges and thermal profiles (gradients) are selected. This is done to control interphase mass transport rates through the temperature dependence of the chemical potentials; to dissipate or supply latent heat that is generated or consumed at interfaces; and to control trans-

port properties such as diffusivities, viscosities, emissivities, and densities. This does not imply that these parameters can be controlled independently; indeed, they cannot. For this reason, modern crystal growth still depends largely on data derived from empirical investigations. Although there has been significant development in crystal growth theory, and many observed phenomena have been explained and even modelled in mathematical terms (Rosenberger, 1979), there still exists a large separation between experiment and theory. The gaps are being narrowed by many investigators (Koai et al., 1994a). In crystals grown from the melt utilizing such techniques as Bridgman, Czochralski (Derby, 1988; Brown, 1988) and float-zone, the uniformity of composition is strongly dependent on the pattern and intensity of flow in the melt (Oshima et al., 1994) as well as the shape of the solid–liquid interface (Koai et al., 1994b). The unequal distribution of a dopant between crystal and melt causes a concentration gradient normal to the interface which is influenced along the interface by convection in the melt and the interface shape. This concentration gradient represents the boundary layer discussed above. The boundary layer (or diffusion layer) decays exponentially with distance from the interface into the melt when the interface is planar. The melt is quiescent except for the motion caused by growth of the crystal. Analysis of the growth of a large diameter crystal with similar velocity field along the interface indicates that convection only alters the concentration field perpendicular to the interface. The idea of diffusion-controlled mass transfer was followed up with expressions to calculate the thickness of the axial boundary layer without consideration for the fluid motion in the melt. Investigators typically applied the concept of

a stagnant-film layer which masked a growing crystal from a well-mixed melt. Recently, some investigators (Hayakawa et al., 1993) have approached the problem by a consistent analysis between mass transfer and flow in the fluid.

9.10 Crystal Growth Theory Versus Experiment

Recent investigations utilizing computer-aided analysis of the interactions of natural convection and the shape of the crystal/melt interface have established the influence of these parameters in crystal growth from the melt particularly in Bridgman and Czochralski systems (Brown, 1988; Derby, 1988; Hurlé, 1983). New algorithms are currently being used which pertain to the mathematical free-boundary problem and simultaneously compute the interface shape, velocity and pressure fields in the melt, and the temperature distribution in both the crystal and the melt. Investigators using these algorithms have concluded that for moderate convection levels the boundary-layer model is an oversimplification of the interactions between complex flow patterns and the dopant field. An important difference revealed by this approach is that the concentration gradient next to the crystal is far from radially uniform; in fact, as much as 60% variation in radial segregation is calculated. For the most part, accurate comparisons with experimental values require the determination of the variation of thermophysical properties with temperature which are unknown to date. However, excellent agreement has been shown where experimental and property data exist.

Molecular dynamics simulations have been applied (Grabow and Gilmer, 1987;

Gilmer and Bakker, 1991) to vapor deposition using MBE in a study of effects of deposition on misfit surfaces. Simulations of MBE deposition of strained Si films provide information on the mobility of atoms at the surface and give insight into mechanisms by which strain relief can occur. In an investigation of columnar growth morphology in MBE-grown films (which is farthest from the equilibrium state of a film), molecular dynamics simulations show that the angle of the beam, interatomic forces, substrate temperature, and deposition rate all have a strong effect on the film structure.

Although many limitations remain in the experimental arena which require further engineering and control over interrelated parameters, some fall into an area over which we have some control, but require still more for the perfection of crystals. An insight into the fine tuning of these parameters is being attained by the theoretical work in progress.

9.11 References

- Ainger, F. W., Bickley, W. P., Smith, G. V. (1970), *Proc. Br. Ceram. Soc.* 18, 221–237.
- Aleksandrov, V. I., Osiko, V. V., Prokhorov, A. M., Tatarintsev, V. M. (1973), *Vestn. Akad. Nauk SSSR* 12, 29.
- Belruss, V., Kalnajas, J., Linz, A., Fotweiler, R. C. (1971), *Mater. Res. Bull.* 6, 899.
- Bridgman, P. (1925), *Proc. Am. Acad. Arts Sci.* 60, 305.
- Brown, R. A. (1988), *AIChE J.* 34, 881.
- Buckley, H. E. (1961), *Crystal Growth*, 5th ed. New York: Wiley, p. 294.
- Burns, G., Dacol, F. H. (1982), *Solid State Commun.* 42, 9.
- Burton, J. A., Prim, R. C., Slichter, J. (1953), *J. Chem. Phys.* 21, 1987.
- Charvat, F. R., Smith, J. C., Nestor, O. H. (1967), *Proc. Int. Conf. on Crystal Growth, Boston 1966; Suppl. J. Phys. Chem. Solids*. Oxford: Pergamon Press.
- Czochralski, J. (1918), *J. Phys. Chem.* 92, 219.
- Derby, J. J. (1988), *MRS Bull.* 13 (10), 29.

- Elwell, D., Scheel, H. J. (1975), *Crystal Growth from High-Temperature Solutions*. London: Academic Press.
- Feigelson, R. S. (1985), in: *Crystal Growth of Electronic Materials*: Kaldis, E. (Ed.). New York: Elsevier, Chap. 11.
- Gentile, A. L. (1983), *AIChE Symp. Series, Tutorial Lect. Electrochem. Eng. Technol.-II* 79, 144.
- Gentile, A. L. (1987), in: *Encyclopedia of Physical Science and Technology*, Vol. 4: *Crystal Growth*. Orlando, FL: Academic Press, pp. 1–14.
- Gentile, A. L. (1992), in: *Encyclopedia of Physical Science and Technology*, Vol. 4: *Crystal Growth*. Orlando, FL: Academic Press, pp. 709–725.
- Gentile, A. L., Andres, F. H. (1967), *Mater. Res. Bull.* 2, 853.
- Gilmer, J. J. (Ed.) (1963), *Art and Science of Growing Crystals*. New York: Wiley, p. 434.
- Gilmer, G. H., Bakker, A. F. (1991), in: *Computer Aided Innovation of New Materials*: Doyama, M., Suzuki, T., Kihara, J., Yamamoto, R. (Eds.). Amsterdam: North-Holland, p. 687.
- Grabow, M. H., Gilmer, G. H. (1987), in: *MRS Symp. Proc.* 94, 15.
- Hayakawa, Y., Asakawa, K., Torimoto, Y., Yamashita, K., Nakayama, A. (1993), *J. Cryst. Growth* 128, 159–162.
- Hurle, D. T. J. (1962), *Prog. Mater. Sci.* 10, 79.
- Hurle, D. T. J. (1979), *Crystal Growth: A Tutorial Approach*, North-Holland, Series in Crystal Growth, Vol. 2, W. Bardsley, D. T. J. Hurle, J. B. Muller (Eds.). Amsterdam: Elsevier Science Publishers, p. 110.
- Hurle, D. T. J. (1983), *J. Cryst. Growth* 65, 124.
- Kirby, K., Wechsler, B. A. (1991), *J. Am. Ceram. Soc.* 74, 1841–1847.
- Koai, K., Seidl, A., Leister, H.-J., Müller, G., Köhler, A. (1994a), *J. Cryst. Growth* 137, 41–47.
- Koai, K., Sonnenberg, K., Wenzl, H. (1994b), *J. Cryst. Growth* 137, 59–63.
- Lacour, C., Paulus, M. (1968), *J. Cryst. Growth* 3–4, 814–817.
- Laudise, R. A. (1967), *Proc. Int. Conf. on Crystal Growth, Boston 1966; Suppl. to J. Phys. Chem. Solids*. Oxford: Pergamon Press, 3–16.
- Laudise, R. A. (1970), *The Growth of Single Crystals*. Englewood Cliffs, NJ: Prentice-Hall.
- Laudise, R. A. (1987), *Chem. Eng. News* 65 (39), 30–43.
- Laudise, R. A. (1994), Private communication.
- Laudise, R. A., Barns, R. L. (1988), *IEEE Trans. Ultrasonics, Ferroelectrics, and Frequency Control* 35 (3), 277–287.
- Linz, A., Belruss V., Naiman, C. S. (1965), *Meeting of Electrochem. Soc. San Francisco. Extended Abstracts* 2, 87.
- Megaw, H. D. (1957), *Ferroelectricity in Crystals*. London: Methuen.
- McCrone, W. C. (1949), in: *Crystal Growth, Discussion of the Faraday Society, Vol. 5*. London: Butterworths, pp. 158–166.
- Müller, K. A. (1981), in: *Nonlinear Phenomena at Phase Transitions and Instabilities*: Riste, T. (Ed.). New York: Plenum Press.
- Müller, K. A., Luspín, Y., Servoin, J. L., Gervais, F. (1982), *J. Phys. Lett. (Paris)* 43, L-542.
- NAS (National Academy of Sciences, USA), (1968), *Ceramic Processing, Publication 1576*. Washington, D.C.: National Academy of Sciences.
- Nassau, K. (1981), *The Lapidary Journal* 35, 1194–1200, 1210–1214.
- Oshima, M., Taniguchi, N., Kobayashi, T. (1994), *J. Cryst. Growth* 137, 48–53.
- Panish, M. B. (1986), *Prog. Cryst. Growth Charact.* 12, 1.
- Pfann, W. G., Olsen, K. M. (1953), *Phys. Rev.* 89, 322.
- Reisman, A. (1970), *Phase Equilibria – Basic Principles, Applications, Experimental Techniques*. New York: Academic Press.
- Rosenberger, F. (1979), *Fundamentals of Crystal Growth I*. Berlin: Springer.
- Rytz, D. (1983), *Ferroélectricité Quantique dans $KTa_{1-x}Nb_xO_3$* , Thèse N° 475, Département de Physique, École Polytechnique Fédérale de Lausanne.
- Rytz, D., Wechsler, B. A., Kirby, K. W., Nelson, C. C. (1985), *Jpn. J. Appl. Phys.* 24, 622–624, *Proc. 6th Int. Mtg. on Ferroelectricity, Kobe, Japan 1985*.
- Rytz, D., Wechsler, B. A., Nelson, C. C., Kirby, K. W. (1990), *J. Cryst. Growth* 99, 864–868.
- Scheel, H. J., Schulz-DuBois, E. O. (1971), *J. Cryst. Growth* 8, 304.
- Scheel, H. J. (1972), *J. Cryst. Growth* 13/14, 560.
- Shih, C.-C., Yariv, A. (1980), *Phys. Rev. Lett.* 4, 281–284.
- Shih, C.-C., Yariv, A. (1982), *J. Phys. C: Solid State Phys.* 15, 825–846.
- Stockbarger, D. C. (1936), *Rev. Sci. Instrum.* 7, 133–136.
- Stringfellow, G. B. (1984), *J. Cryst. Growth* 68, 111–122.
- Stringfellow, G. B. (1993), *J. Cryst. Growth* 128, 503–510.
- Suntola, T., Hyvarinen, J. (1985), *Annu. Rev. Mater. Sci.* 15, 177.
- Thurmond, C. D. (1959), in: *Semiconductors*: Hannay, N. B. (Ed.). New York: Reinhold.
- Verneuil, A. (1902), *C. R. Acad. Sci. (Paris)* 135, 791–794.
- Wechsler, B. A., Kirby, K. W. (1992), *J. Am. Ceram. Soc.* 75, 981–984.
- Wells, A. F. (1984), in: *Structural Inorganic Chemistry*, 5th ed. Oxford: Clarendon Press; Chap. 2.
- Wenckus, J. F., Menashi, W. P., Castonguay, R. A. (1977), *U.S. Patent* 4049384.

- Wenckus, J. (1993), in: *Proc. 10th Int. Conf. on Crystal Growth, San Diego, CA, 1992*, *J. Cryst. Growth* 128, 13–14.
- Yariv, A. (1967), *Quantum Electronics*. New York: Wiley, Chap. 18.

General Reading

- Buckley, H. E. (1961), *Crystal Growth*, 5th ed. New York: Wiley.
- Elwell, D., Scheel, H. J. (1975), *Crystal Growth from High-Temperature Solutions*. London: Academic Press.
- Gilman, J. J. (Ed.) (1963), *Art and Science of Growing Crystals*. New York: Wiley.
- Hannay, N. B. (1967), *Solid State Chemistry*. Englewood Cliffs, NJ: Prentice Hall.
- Herbert, J. M. (1982), *Ferroelectric Transducers and Sensors*. London: Gordon and Breach.
- Hurle, D. T. J. (Ed.) (1992), *A Perspective on Crystal Growth*. Amsterdam: Elsevier.
- Jona, F., Shirane, G. (1962), *Ferroelectric Crystals*. Mineola, NY: Dover Press.
- Laudise, R. A. (1970), *The Growth of Single Crystals*. Englewood Cliffs, NJ: Prentice-Hall.
- Lines, M. E., Glass, A. M. (1977), *Principles and Applications of Ferroelectrics and Related Materials*. Oxford: Clarendon Press.
- Megaw, Helen D. (1957), *Ferroelectricity in Crystals*. London: Methuen.
- Nye, J. F. (1969), *Physical Properties of Crystals*. Oxford: Clarendon Press.
- Pfann, W. G. (1966), *Zone Melting*, 2nd ed. New York: Wiley.
- Rosenberger, F. (1979), *Fundamentals of Crystal Growth I*, Springer Series in Solid-State Sciences, Vol. 5. Berlin: Springer.
- Roy, R. (Ed.) (1994), *Crystal Chemistry of Non-Metallic Materials*, Vol. 4. Berlin: Springer.
- Wells, A. F. (1984), *Structural Inorganic Chemistry*, 5th ed. Oxford: Clarendon Press.
- Wilke, K.-T. (1963), *Methoden der Kristallzüchtung*. Berlin: VEB Deutscher Verlag der Wissenschaften.
- Wilke, K.-T. (1973), *Kristallzüchtung*. Berlin: VEB Deutscher Verlag der Wissenschaften.
- Crystals: *Growth, Properties, and Applications*, Volumes 1–13. Berlin: Springer.
- Crystal Growth, Discussions of the Faraday Society*, No. 5, 1949. London: Butterworths.

MATERIALS STUDIES

APPENDIX 7

6/12

DIELECTRIC, PYROELECTRIC AND PIEZOELECTRIC PROPERTIES OF CALCIUM-MODIFIED LEAD MAGNESIUM TANTALATE-LEAD TITANATE CERAMICS

S.W. CHOI, J.M. JUNG AND A.S. BHALLA*

Department of Physics, Dankook University,
29 Anseodong, Cheonan, Chungnam, Korea

*Material Research Laboratory, The Pennsylvania State University
University Park, PA 16802 USA

Abstract Dielectric, pyroelectric and piezoelectric properties of relaxor ferroelectrics in solid solution, formulated $0.65(\text{Pb}_{1-x}\text{Ca}_x)(\text{Mg}_{1/3}\text{Ta}_{2/3})\text{O}_3-0.35\text{PbTiO}_3$, have been investigated. Complete single-phase perovskite with high density was obtained with all samples fired at 1250°C . The Curie temperature and pyroelectric peak temperature decrease almost linearly as the amount of Ca in the compositions increases. The transition temperature of the solid solutions can easily be controlled by Ca additions in the PMT-PT. Dielectric, pyroelectric and piezoelectric constants achieved maximum values for $x=0.02$. Compositions near $0.65\text{PMT}-0.35\text{PT}-0.12\text{Ca}$ have been identified to have high dielectric constants (~ 15000) and low dissipation factors (~ 0.015) near room temperature.

INTRODUCTION

Relaxor perovskite $\text{Pb}(\text{Mg}_{1/3}\text{Ta}_{2/3})\text{O}_3$ -PMT was first synthesized by Soviet workers in the early 1960s¹. Relaxor ferroelectrics are typically characterized by the display of a broad dielectric peak with frequency dispersion of a paraelectric-ferroelectric phase transition. The main feature of the dielectric properties of PMT was a broad maximum of dielectric constant well below room temperature. However, with the addition of PbTiO_3 -PT (Curie temperature $\sim 490^\circ\text{C}$), the compositions in PMT-PT solid solution exhibit a morphotropic phase boundary between a rhombohedral and tetragonal phases at about 35 mol% PT².

In a well known $\text{Pb}(\text{Zr}_x\text{Ti}_{1-x})\text{O}_3$ piezoelectric material, the compositions near the morphotropic phase boundary separating rhombohedral and tetragonal phases exhibit large dielectric and piezoelectric anomalies³. Similar properties are also seen in other lead-based relaxor-lead titanate (PT) ferroelectric binary materials, such as $\text{Pb}(\text{Zn}_{1/3}\text{Nb}_{2/3})\text{O}_3$ - PbTiO_3 ⁴ and $\text{Pb}(\text{Mg}_{1/3}\text{Nb}_{2/3})\text{O}_3$ - PbTiO_3 ⁵. The compositions near the $0.65\text{PMT}-0.35\text{PT}$ solid solution morphotropic phase boundary, where large values of dielectric constants could be expected, have a transition into the paraelectric phase around 100°C . Thus, these compositions are not suitable for room temperature switching application. Previously, the effects of Ba, Sr and La additions on the dielectric properties of the system PMT-PT were studied, and the dielectric properties of the base composition were improved through selection of additives^{6,7,8}.

In the present work we have studied the effects of replacing of Pb by Ca on

7/12

DIE., PYRO., PIEZO. PROPERTIES OF Ca-MODIFIED PMT-PT CERAMICS

while the samples sintered at 1250°C for 4h resulted in almost complete formation of perovskite phase. Addition of Ca to the base composition apparently does not affect the pyrochlore-perovskite transformation.

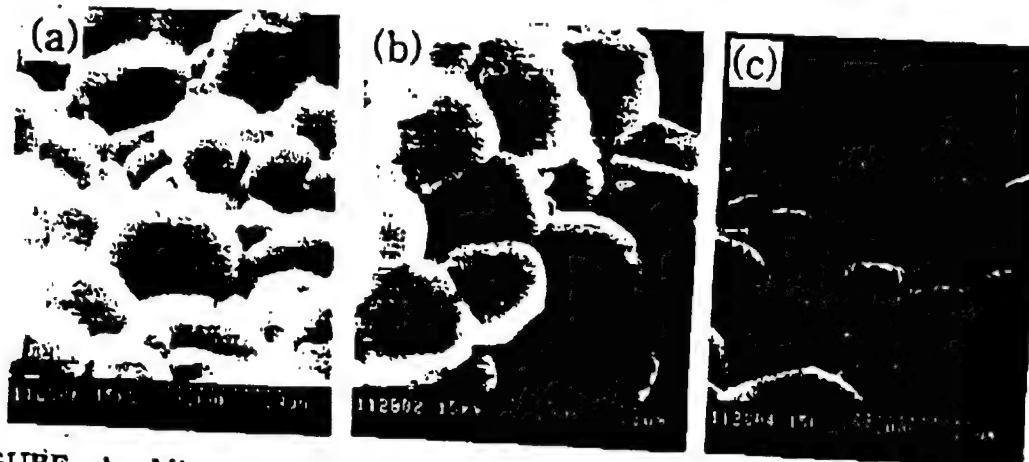


FIGURE 1. Microstructure of 0.65PMT-0.35PT-xCa ceramics sintered at 1250°C/4h. (a)x=0.0 (b)x=0.01 (c)x=0.05

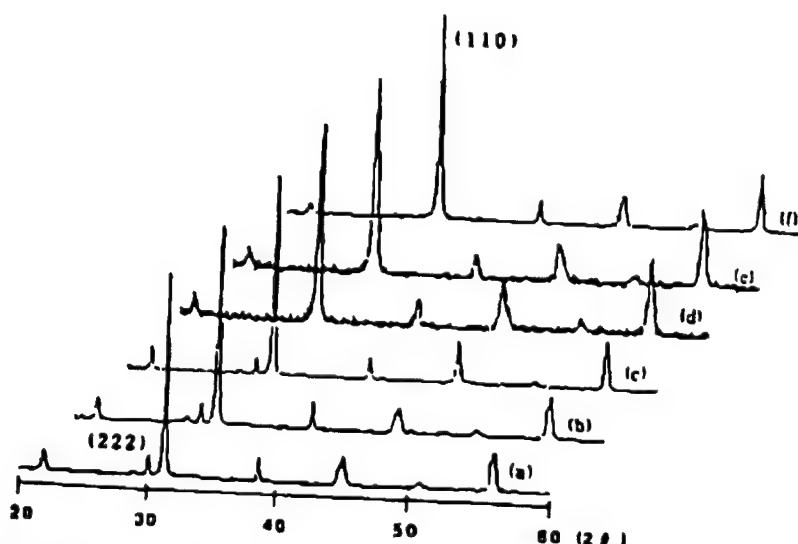


FIGURE 2. X-ray diffraction patterns for 0.65PMT-0.35PT-xCa ceramics. (a)x=0.0 (b)x=0.02 (c)x=0.12, calcined at 850°C/5h (d)x=0.0 (e)x=0.02 (f)x=0.12, sintered at 1250°C/4h

Dielectric properties

Fig.3 shows temperature dependence of dielectric constant and dissipation factor for the base composition modified with 0, 2 and 12 mol% Ca. All compositions show a broad maximum for the dielectric constant. All of the samples exhibited frequency dispersion behavior of both dielectric constant and dissipation factor, which is a characteristic of relaxor ferroelectrics. When the amount of Ca is increased to more than 2 mol%, the dielectric peak is lowered as well as broadened. It was also interesting to note that the substitution of

8/12

S.W. CHOI, J.M. JUNG AND A.S. BHALLA

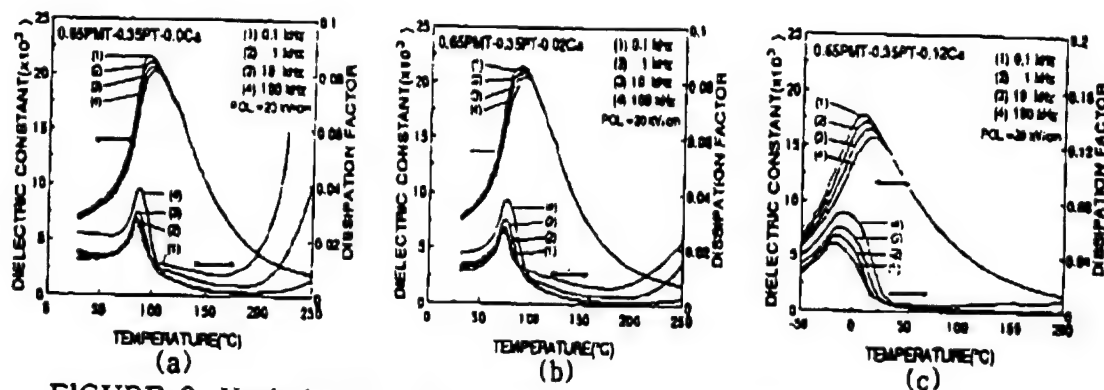


FIGURE 3. Variation of dielectric constant and dissipation factor with temperature and frequency for 0.65PMT-0.35PT- x Ca ceramics. (a) $x=0.0$ (b) $x=0.02$ (c) $x=0.12$

Ca in the composition enhanced broadening of the dielectric peak, and highly diffuse phase transition was observed for compositions having Ca content >2 mol%. It is clear that both the diffuseness and frequency dependence of Curie temperature become prominent as the amount of Ca increases. The increase in diffuseness with the amount of Ca corresponds to decrease in dielectric constant (K_{max}). In the compositions with higher than 2 mol% Ca, the decrease in the maximum value of the dielectric constant even when no pyrochlore phase was found to be present occurred mainly due to the detrimental effect of addition of Ca. Later Chen et al.^{12, 13} reported that the decrease in the dielectric constant is not only due to pyrochlore phase but also other factors such as lattice impurities and intergranular phases. It should be noted that we did not analysis the grain boundaries hear and further study is needed to determine the effect of intergranular phases.

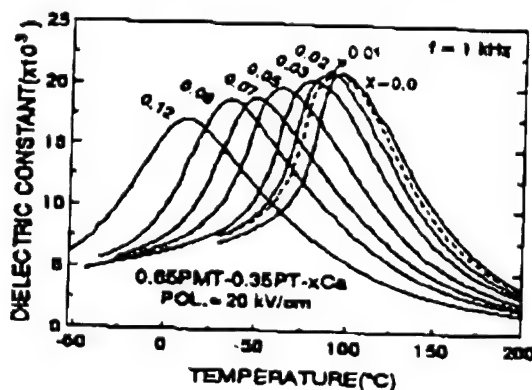


FIGURE 4. Dielectric constant as a function of temperature for 0.65PMT-0.35PT- x Ca ceramics.

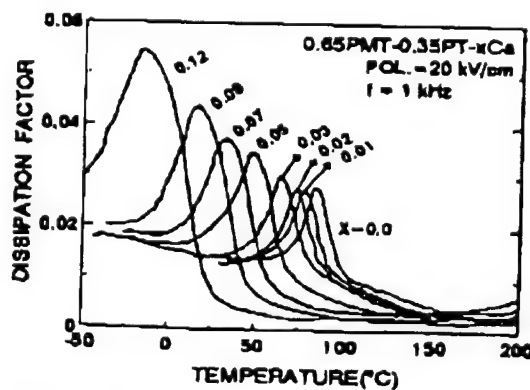


FIGURE 5. Dissipation factor as a function of temperature for 0.65PMT-0.35PT- x Ca ceramics.

Fig.4 shows plots of dielectric constant vs. temperature at 1 kHz for compositions 0.65PMT-0.35PT system containing different amounts of Ca. The

9/12

DIE., PYRO., PIEZO. PROPERTIES OF Ca-MODIFIED PMT-PT CERAMICS

dielectric constant slightly rises up to 2 mol% Ca and then decreases with further addition of Ca. The decrease in dielectric constant is accompanied by a lowering of the transition temperature. Small amounts of Ca act as fluxes, and Ca maintains its fluxing action up to 2 mol%.

Fig.5 shows plots of dissipation factor vs. temperature at 1 kHz for compositions 0.65PMT-0.35PT containing different amounts of Ca. The dissipation factor slightly decreases with additions of Ca up to 2 mol% and then increases with further additions of Ca. Further increase in Ca content appeared to be detrimental, as shown by the considerably lowered dielectric constant and increased dissipation factor. The composition 0.65PMT-0.35PT with 12 mol% Ca have been identified to have high dielectric constants (~15000) and low dissipation factors (~0.01) near room temperature. It was found that partial substitutions of Ca for Pb were quite effective in decreasing the Curie temperature. The Curie temperature decreases sharply with increasing Ca, the

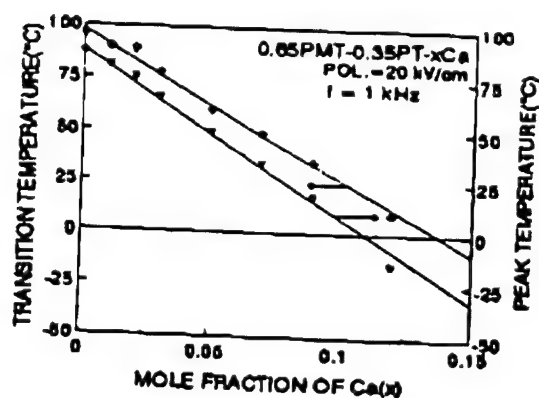


FIGURE 6. Variation of T_c and peak temperature as a function of x for 0.65PMT-0.35PT-xCa ceramics.

composition 0.65PMT-0.35PT-0.12Ca has its T_c value near room temperature. Curie temperature of the binary system vary almost linearly with amounts of Ca as can be seen in Fig.6. It is clear that the addition of Ca shift T_c downward significantly, about 8 °C/mol%, which is lower than the value reported in study using a nonstoichiometric doping of Sr in PMT-PT system⁷.

These two effects should be properly sorted out in order to obtain ceramics which can be utilized at room temperature.

Pyroelectric and piezoelectric properties

Fig.7 shows temperature dependence of pyroelectric coefficient for the base composition modified with Ca as a function of amount of additive from 0 to 12 mol%. Pyroelectric coefficient increases with increasing x until $x \sim 0.02$ is reached. However, for x more than ~ 0.02 , pyroelectric coefficient decreased. In most cases like in dielectric data, substitution of Ca in the composition enhanced broadening of the pyroelectric peak. The decrease in pyroelectric coefficient similar to that K vs T (Fig.4) data is accompanied by a lowering of the pyroelectric peak temperature. The pyroelectric peak temperature decreases with increase of Ca content as can be seen in Fig.6. The effects should be properly sorted out in order to obtain pyroactive ceramics, which can be utilized at room temperature. Composition 0.65PMT-0.35PT-0.09Ca has their pyroelectric peak value near room temperature. The results further indicated that it was necessary to have a nominal addition of 2 mol% Ca to obtain the

10/12

S.W. CHOI, J.M. JUNG AND A.S. BHALLA

the dielectric, pyroelectric, piezoelectric properties and microstructure of $0.65(\text{Pb}_{1-x}\text{Ca}_x)(\text{Mg}_{1/3}\text{Ta}_{2/3})\text{O}_3-0.35\text{PbTiO}_3$ composition near the morphotropic phase boundary(PMT-PT). The purpose of the investigation was to develop ceramics having higher dielectric properties near room temperature.

EXPERIMENTAL PROCEDURE

Reagent-grade oxide powders of PbCO_3 , TiO_2 , Ta_2O_5 , MgO and CaCO_3 with purity better than 99.8 % were used as starting raw materials. The columbite precursor method by Swartz and Shrout⁹ for the synthesis of the various compositions was used. The sintered samples were characterized by x-ray diffraction to insure phase purity. The grain size was determined on fracture surfaces of pellets using scanning electron microscopy(SEM). Opposite faces of the samples were coated with sputtered silver electrodes.

Dielectric properties were measured with an Impedance Analyzer(HP4192A), control unit and its interface. The dielectric constant and dissipation factor were measured as a function of temperature at various frequencies between 0.1 and 100 kHz with a temperature rate of 4 °C/min. The pyroelectric coefficient and spontaneous polarization were measured by the static Byer-Roundy method¹⁰ as the samples were heated, again at a rate of 4 °C/min, through the phase transition region. Prior to the dielectric, pyroelectric and piezoelectric measurements the specimens were poled by applying a DC field of 20 kV/cm at room temperature. Piezoelectric d_{33} was measured by using Berlincourt d_{33} meter. Electromechanical coupling factor k_p was measured by using resonance-antiresonance method¹¹.

RESULTS

Microstructure and X-ray analysis

Fig.1 shows SEM observations of the fractured surfaces of undoped and Ca-doped 0.65PMT-0.35PT, fired at 1250°C for 4h. Clearly, this sample reveals homogeneous microstructure consisting of large grains($\sim 3\mu\text{m}$) as the Ca content increased from 0 to 2 mol%. These ceramics have densities of more than 95% of the theoretical densities. A homogeneous grain structure was obtained with 2 mol% substitution of Ca for the composition 0.65PMT-0.35PT, which gave the highest percentage of theoretical density. From these data it may be concluded that small substitutions of Ca for Pb in the base composition improve the densification and grain refinement which related to dielectric properties.

Fig.2 shows the XRD patterns of the calcined powder and fired specimens for undoped, Ca-doped 0.65PMT-0.35PT. The 0.65PMT-0.35PT- $x\text{Ca}$ ($x=0\sim 0.12$) compositions calcined at 850°C for 5h contained >10% of pyrochlore phase

11/12

S.W. CHOI, J.M. JUNG AND A.S. BHALLA

high pyroelectric coefficient (Fig. 7).

Fig. 8 shows the room-temperature values of piezoelectric d_{33} and electromechanical coupling factor k_p of the composition $0.65\text{PMT}-0.35\text{PT}-x\text{Ca}$ as a function of mole fraction of Ca. The maximum piezoelectric d_{33} and electromechanical coupling factor k_p are observed at 2 mol% calcium doping. The foregoing composition is in good agreement with those exhibiting maxima in spontaneous polarization.

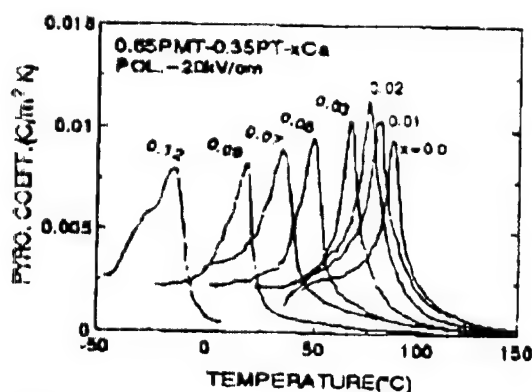


FIGURE 7. Pyroelectric coefficient as a function of temperature for $0.65\text{PMT}-0.35\text{PT}-x\text{Ca}$ ceramics.

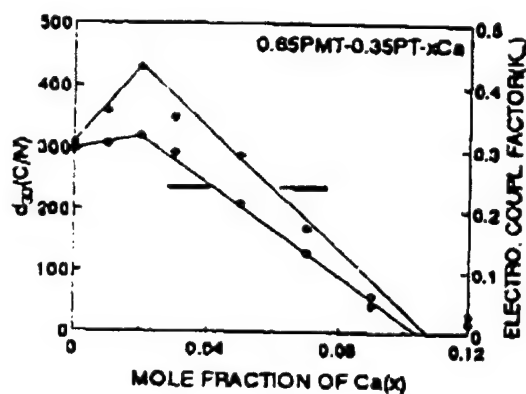


FIGURE 8. Piezo. d_{33} constant and electromechanical coupling factor k_p for $0.65\text{PMT}-0.35\text{PT}-x\text{Ca}$ ceramics at room temperature.

CONCLUSIONS

$0.65\text{PMT}-0.35\text{PT}-x\text{Ca}$ ($x=0\sim0.12$) ceramics fired at 1250°C showed a single-phase perovskite structure. These ceramics have densities of more than 95% of theoretical densities. The optimum amount of Ca added is about 2 mol% in this research. Further addition of Ca, however, caused a degraded dielectric, pyroelectric and piezoelectric constants even though no pyrochlore phase was found to be present. The Curie temperature and pyroelectric peak temperature decrease almost linearly as the amount of Ca in the compositions increases. Compositions near $0.65\text{PMT}-0.35\text{PT}-x\text{Ca}$ ($x=0.09\sim0.12$) have been identified to have high dielectric, pyroelectric constants and low dissipation factors near room temperature.

ACKNOWLEDGMENT

This work was supported by the Korea Science and Engineering Foundation (KOSEF) through the Research Center for Dielectric and Advanced Matter Physics (RCDAMP) at Pusan National University.

12/12

DIE., PYRO., PIEZO. PROPERTIES OF Ca-MODIFIED PMT-PT CERAMICS

REFERENCES

1. V.A. Bokov and I.E. Myl'nikova, Sov. Phys. Solid State, 2, 2428(1961)
2. Y.J. Kim and S.W. Choi, Ferroelectrics, 108, 241(1990)
3. B.Jaffe, R.S. Roth and S.Marzullo, J. Res. Natl. Bur. Stand., 55, 239(1955)
4. S.Nomura, T.Takahashi and Y.Yokomizo, J. Phys. Soc. Jpn., 27, 262(1969)
5. S.W. Choi, T.R. Shrout, S.J. Jang and A.S. Bhalla, Ferroelectrics, 100, 29(1969)
6. S.W. Choi and J.M. Jung, Proc. ISAF'94, 806(1994)
7. J.M. Jung, Y.H. Park and S.W. Choi, Proc. ISAF'94, 810(1994)
8. Y.J. Kim, S.W. Choi and A.S. Bhalla, Ferroelectrics; to be published
9. S.L. Swartz and T.R. Shrout, Mat. Res. Bull., 17, 1245(1982)
10. R.L. Byer and C.R. Roundy, Ferroelectrics, 3, 333(1972)
11. Proc. IRE. Inst. Radio Eng., 49(7), 1161(1961)
12. J. Chen and M.P. Harmer, J. Am. Ceram. Soc., 73, 68(1990)
13. J. Chen, A. Gorton, H.M. Chen and M.P. Harmer, J. Am. Ceram. Soc., 69, C303(1986)

APPENDIX 8

DIELECTRIC, PYROELECTRIC PROPERTIES, AND MORPHOTROPIC PHASE BOUNDARY IN La-DOPED $(1-x)\text{Pb}(\text{Mg}_{1/3}\text{Ta}_{2/3})\text{-}x\text{PbTiO}_3$ SOLID SOLUTION CERAMICS

Y. J. KIM and S. W. CHOI

*Department of Physics, Dankook University, Cheonan,
Chungnam 330-714, Korea*

and

A. S. BHALLA

*Materials Research Laboratory, Penn State University,
University Park, PA 16802 USA*

(Received November 18, 1994; in final form March 20, 1995)

Dielectric and pyroelectric properties of relaxor ferroelectric in the $(1-x)(\text{Pb}_{1-3y/2}\text{La}_y)(\text{Mg}_{1/3}\text{Ta}_{2/3})\text{-}x\text{PbTiO}_3$ (PMT-PT) solid solution series have been investigated. The dielectric constant and loss of ceramic samples were determined. The pyroelectric coefficient and spontaneous polarization were measured by the static Byer-Roundy method as a function of temperature for various compositions in the La-doped PMT-PT system. The position of the morphotropic phase boundary in PMT-PT appeared not to be affected by La_2O_3 addition. Lanthanum-doping resulted in a reduction of grain size and shifting of the T_c by about $25^\circ\text{C}/\text{mole}\%$ downward in the PMT-PT system. Dielectric constants and pyroelectric coefficients for La-doped PMT-PT are much larger compared to the undoped PMT-PT system. Further additions of La_2O_3 could be used to shift the T_c downward without significantly changing the dielectric behavior. In the present study no clear morphotropic phase boundary (MPB) has been identified. A two-phase region is indicated between $x \approx 0.27\text{--}0.4$.

Keywords: PMT-PT, morphotropic phase boundary, pyroelectric/dielectric properties.

INTRODUCTION

Perovskite lead magnesium tantalate [$\text{Pb}(\text{Mg}_{1/3}\text{Ta}_{2/3})\text{O}_3$ (PMT)] was first synthesized by Bokov and Myl'nikova.¹ The main feature of the dielectric properties of PMT as a function of temperature is a broad dielectric constant maximum at the transition temperature. The relaxor-like dielectric maximum at 1 kHz occurs at -100°C . However, with the addition of PbTiO_3 (PT) ($T_c = 490^\circ\text{C}$), PMT-PT solid solution exhibits a morphotropic phase boundary (MPB) between a rhombohedral phase and tetragonal phase at about 29–39 mole% PT.²

The effect of La-doping on the dielectric and pyroelectric properties of the PMT-PT system is discussed in the present work. The compositions $(1-x)\text{PMT-}x\text{PT}$ ($x = 0.25\text{--}0.4$) with 1–5 mole% La-doping have been selected, in accordance with the solid solution phase diagram.² In this investigation we have sought to locate the morphotropic phase boundary region using dielectric and pyroelectric results. It can qualitatively be predicted that extraordinarily large dielectric constants and

pyroelectric coefficients are expected when the composition is close to the morphotropic phase boundary.^{3,4}

It is of major interest to investigate the characteristics of such morphotropic phase boundary compositions in the PMT-PT-La system. The systematic study of PMT-PT-La in this work extends the already known behavior of the mixed B-site complex perovskites of general formula $A(B', B'')O_3$ to the mixed A-site/mixed B-site perovskites of general formula $(A', A'')(B' B'')O_3$. Thus, an additional compositional variable must be considered in order to explain the trends in the dielectric and pyroelectric response. A number of studies of mixed A-site relaxors have appeared in the literature, in particular concerning the effects of doping lead magnesium niobate (PMN) with La^{3+} ions.^{5,6}

A systematic study of La substitution in morphotropic phase boundary compositions in the PMT-PT system is described in this paper.

EXPERIMENTAL PROCEDURE

Ceramic samples were prepared by conventional sintering techniques.⁷ Reagent-grade oxide powders of $PbCO_3$, TiO_2 , La_2O_3 , Ta_2O_5 , and MgO with purity better than 98% were used as starting raw materials. The columbite precursor method was used for synthesis of various compositions.⁸⁻¹⁰ In the first stage, precursor was mixed in stoichiometric ratios with PbO , TiO_2 , and La_2O_3 . After ball-milling, the mixed oxides were calcined at 800°C for 2 h. The calcined powder was ground and ball-milled again, then pressed into disks 10 mm in diameter and about 2 mm in thickness.

The disks were placed in a capped Al_2O_3 crucible and sintered at 1100, 1200, 1250, or 1300°C for 2 h, PbO volatilization during sintering was minimized by surrounding each pellet with powder of identical composition.

The sintered samples were characterized by X-ray powder diffraction (XRD) to insure phase purity. The amount of perovskite phase was determined from the relative intensities of the (110) peak of the perovskite phase and (222) peak of the pyrochlore phase. The grain size was determined from fracture surfaces of the pellets using scanning electron microscopy (SEM). Weight loss and Archimedes density were measured for all samples.

For electrical measurements, samples of suitable dimensions were cut and polished. Opposite faces of the samples were coated with sputtered silver electrodes. Temperature dependences of the dielectric constant and loss tangent were measured at frequencies of 0.1, 1, 10 and 100 kHz at a heating/cooling rate of 4°C/min, using an automated dielectric measurement system with a multi-frequency LCR meter. The pyroelectric coefficient and spontaneous polarization were measured by the static Byer-Roundy¹¹ method as the poled samples were heated at a rate of 4°C/min, through the transition temperature.

Prior to dielectric and pyroelectric measurements the specimens were poled by applying a DC field of about 15 kV/cm while cooling from well above the transition to a temperature well below. In the present work, lanthanum doped PMT-PT compositions near the probable morphotropic phase boundary are studied.

RESULTS AND DISCUSSION

(a) Density and Grain Size

Modification of the PMT-PT system by the addition of lanthanum oxide has marked effects on the basic properties of the ceramics, such as increased dielectric constant, pyroelectric coefficient, and densification. As determined from X-ray powder diffraction patterns, less than 1% pyrochlore phase was detected for the various compositions. Typical SEM photomicrographs of the fractured surfaces are shown in Figure 1.

It is clearly evident that La-doped polycrystalline ceramics have smaller grain size than three of the undoped ceramics. As observed, the grain sizes were about 5 μm and 3.6 μm for PMT-PT and PMT-PT-La, sintered at 1300°C for 2 h, respectively. The optimum sintering temperatures were determined empirically, by systematically investigating the bulk density obtained for each composition. The resultant densities in the PMT-PT-La system were greater than 90% of the theoretical value.

(b) Dielectric Properties

Figure 2 shows a typical plot of dielectric constant and loss as functions of temperature and frequency for 0.64PMT-0.36PT-0.01La. These data also show typical

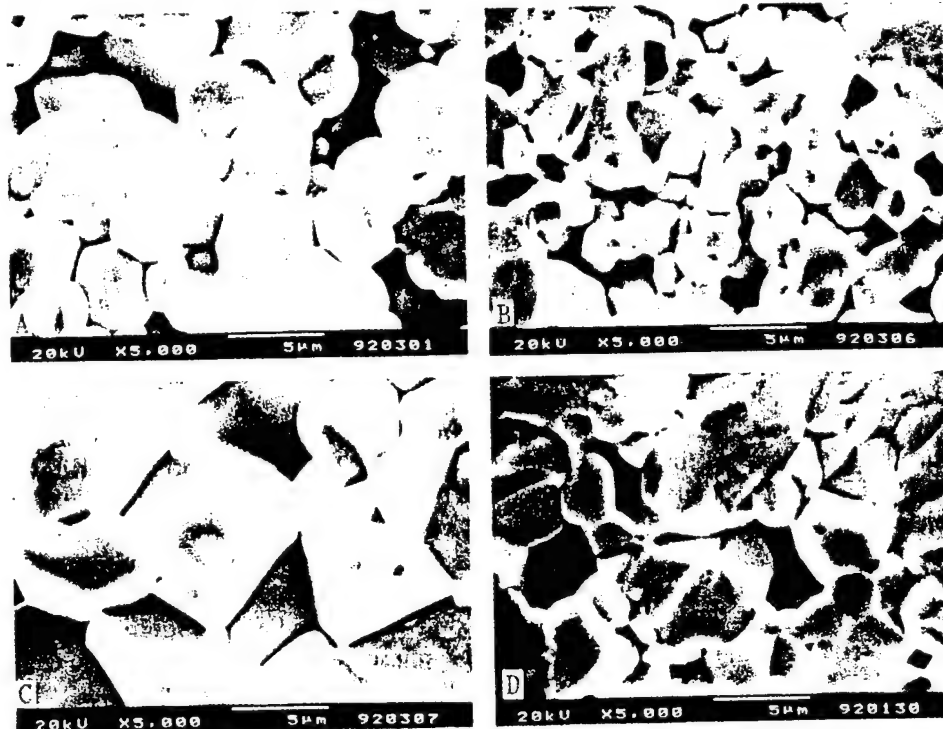


FIGURE 1 Scanning electron micrographs of fracture surfaces of (A) 0.66PMT-0.34PT, (B) 0.66PMT-0.34PT-0.01La, sintered at 1250°C for 2 h, and (C) 0.66PMT-0.34PT-0.01La, sintered at 1300°C for 2 h.

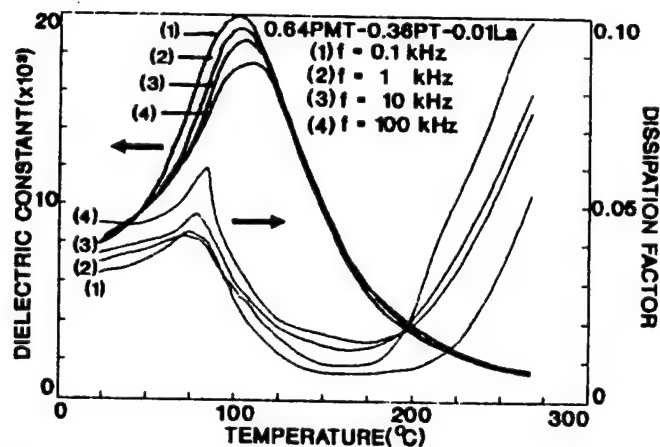


FIGURE 2 Dielectric constant and loss as functions of temperature and frequency for 0.64PMT-0.36PT-0.01La.

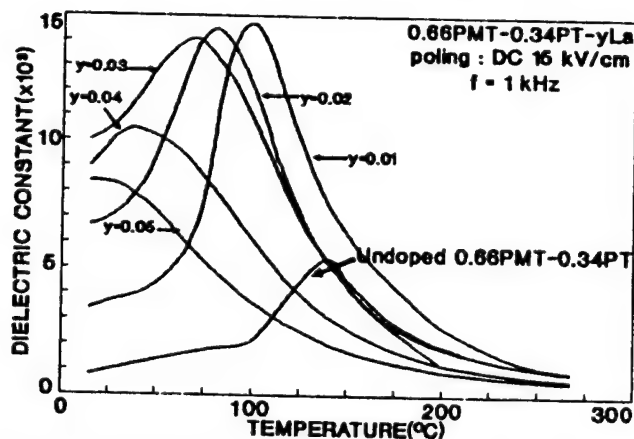


FIGURE 3 Dielectric constant as a function of temperature for 0.66PMT-0.34PT-yLa.

relaxor behavior (i.e.: diffuse dielectric maxima; dielectric maxima decreases and shifts upward with increasing frequency). No clear evidence of a rhombohedral to tetragonal phase transition was observed from the K vs. T plots for compositions near the MPB, as was found in the undoped PMT-PT system reported by Kim.²

The dielectric constants for La-doped PMT-PT are much larger compared to the values observed for the undoped PMT-PT system. La-doping also shifted the T_c downward, approximately 25°C/mole% La_2O_3 . The dielectric constant vs. temperature behavior at 1 kHz is shown in Figure 3 and 4 for various compositions across the 0.66PMT-0.34PT-yLa and 0.625PMT-0.375PT-yLa solid solution series, respectively, near the reported morphotropic phase boundary. The dielectric constants decrease as La-doping is increased. It is clear that PMT-PT compositions doped with lanthanum have increases in dielectric constant compared to the undoped PMT-PT system, with much more pronounced effects for 1 mole% lanthanum doping. We observed an increase in dielectric constant of a factor of 3, as shown in Figure 3 and 4.

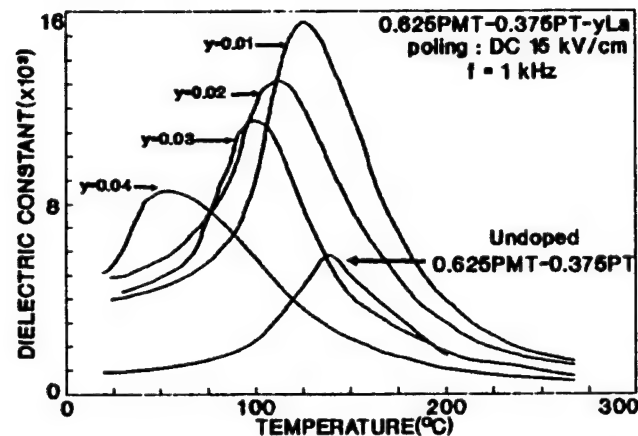
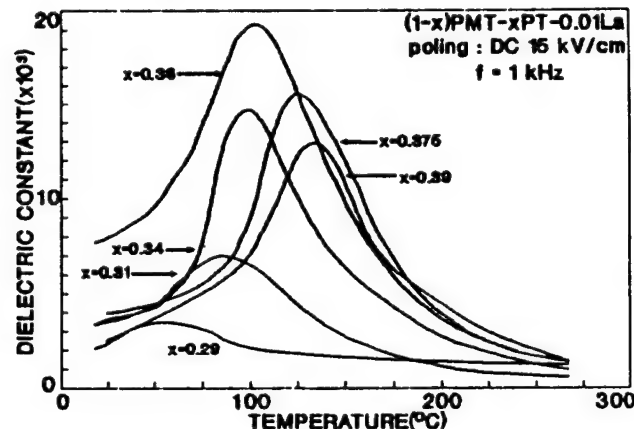


FIGURE 4 Dielectric constant as a function of temperature for 0.625PMT-0.375PT-yLa.

FIGURE 5 Dielectric constant as a function of temperature for $(1-x)\text{PMT}-x\text{PT}-0.01\text{La}$.

It was found that the room temperature dielectric constant increased by a factor of about 10 for 3 mole% lanthanum doping in 0.66PMT-0.34PT, as compared with that of the undoped system, as shown in Figure 3, which is associated with the decrease in T_c of the PMT-PT compositions.

Figure 5 shows the dielectric constant for various compositions in $(1-x)\text{PMT}-x\text{PT}-0.01\text{La}$ solid solutions as functions of temperature. The addition of La_2O_3 affects the dielectric properties of PMT-PT. The phase transition is continuously shifted to higher temperatures with increasing PbTiO_3 content. The dielectric behavior as a function of mole% PT is similar to that observed in the undoped PMT-PT system by Kim.²

The substitution of La^{3+} in PMT-PT is likely to influence the distribution of Ta^{5+} and Mg^{2+} ions over the B-sites. La^{3+} is also likely to couple the Ta_2O_6 octahedra together, just as the role of Pb^{2+} ion in the structure.

The PMT-PT solid solution exhibits a probable morphotropic phase boundary between rhombohedral and tetragonal phases at about 29–39 mole% PbTiO_3 .² An important advantage of these ceramics is that their dielectric constants and py-

roelectric coefficient can be tailored by minor modifications of the composition. The high values of the maximum dielectric constant obtained in the vicinity of the morphotropic phase boundary are worth noting, as they're indicative of possible large pyroelectric responses.

Figure 6 shows the maximum dielectric constant for various compositions in the $(1-x)\text{PMT}-x\text{PT}-0.01\text{La}$ and undoped $\text{PMT}-\text{PT}$ solid solutions as a function of mole fraction of PbTiO_3 . It is clear that the $\text{PMT}-\text{PT}$ system doped with lanthanum near the morphotropic phase boundary has larger dielectric constant than the corresponding undoped $\text{PMT}-\text{PT}$ system.

Figure 7 shows the variation in transition temperature for various compositions in the $(1-x)\text{PMT}-x\text{PT}-y\text{La}$ and undoped $(1-x)\text{PMT}-x\text{PT}$ solid solutions near the morphotropic phase boundary as a function of mole fraction of PbTiO_3 . The phase transition temperature is continuously shifted to higher temperature with increasing PbTiO_3 . It is also found that La-doping shifts the phase transition temperature downward. This variation is interesting and worth studying. The shift of

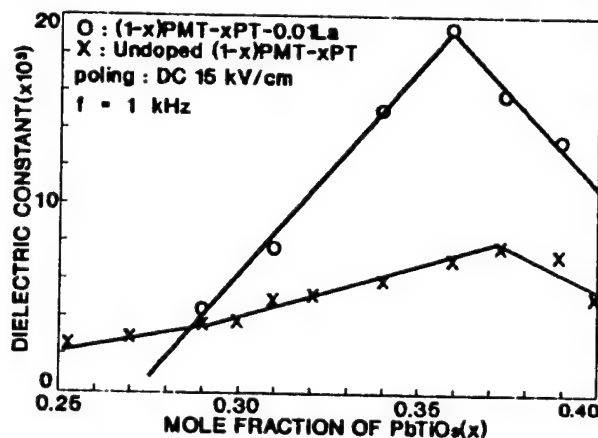


FIGURE 6 Maximum dielectric constant as a function of mole fraction of PT for La-doped and undoped $\text{PMT}-\text{PT}$ system.

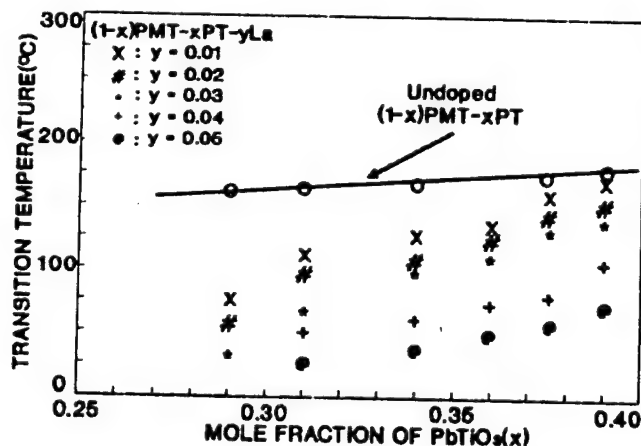


FIGURE 7 Transition temperature of dielectric constant plotted as a function of the mole fraction of PT for La-doped and undoped $\text{PMT}-\text{PT}$ system.

the morphotropic phase boundary with La-substitution for Pb may be related to the distribution of ions having different ionic radii in the same sublattice of the complex perovskite structure.

(c) *Pyroelectric Properties and Morphotropic Phase Boundary*

Temperature dependences of the pyroelectric coefficient and spontaneous polarization were measured from 25°C to 250°C by the Byer-Roundy technique. In the present work ceramic compositions from the solid solution system $(1 - x)\text{PMT} - x\text{PT} - y\text{La}$ ($x = 0.29 - 0.39$, $y = 0.01 - 0.05$) were measured in order to identify the MPM region and to monitor the effect of PbTiO_3 content on the pyroelectric response. With La_2O_3 addition, the transition temperature of PMT-PT can be suitably adjusted for room temperature pyroelectric applications.

In the present paper we focused our studies on the morphotropic phase boundary compositions only. The morphotropic phase boundary is important because most of the properties of interest can be optimized along it: e.g., dielectric constant, pyroelectric coefficient, and spontaneous polarization all increase to their maximum values. For the system PMT:PT, in most of the electrical measurements (e.g. pyroelectric data) two major anomalies corresponding to the rhombohedral \rightarrow tetragonal \rightarrow cubic phase transitions were observed.

Figures 8 and 9 show the pyroelectric coefficients for various compositions in the $0.66\text{PMT} - 0.34\text{PT} - y\text{La}$ and $0.625\text{PMT} - 0.375\text{PT} - y\text{La}$ solid solutions, respectively, as functions of temperature. Pyroelectric coefficient decreases with increasing mole% La are similar to the observed dielectric constant vs. temperature behavior. The broadening of the two peaks in the pyroelectric coefficient vs. temperature plots may be due to coexistence of the multiple phases. The presence of two peaks in the pyroelectric coefficient vs. temperature could be due to the curvature of the morphotropic phase boundary. As a result, the first peak may correspond to the transition from rhombohedral to tetragonal phase, and the second peak to the transition from tetragonal to cubic.

Figures 10 and 11 show pyroelectric coefficient and spontaneous polarization,

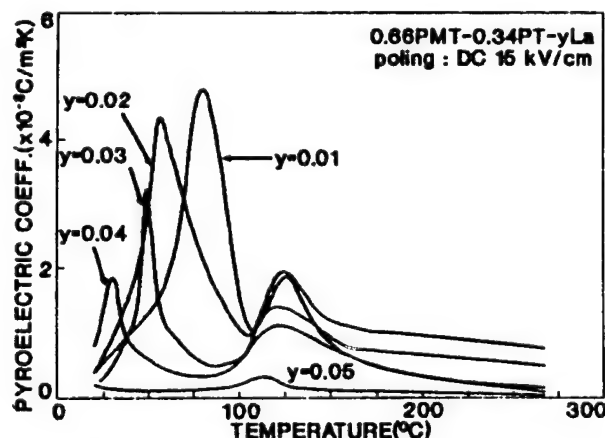


FIGURE 8 Pyroelectric coefficient as a function of temperature for $0.66\text{PMT} - 0.34\text{PT} - y\text{La}$.

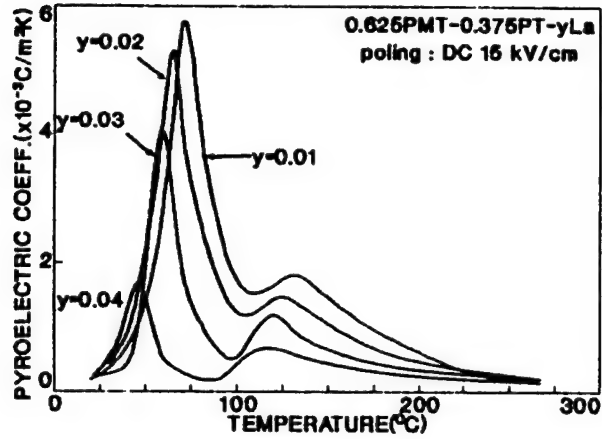
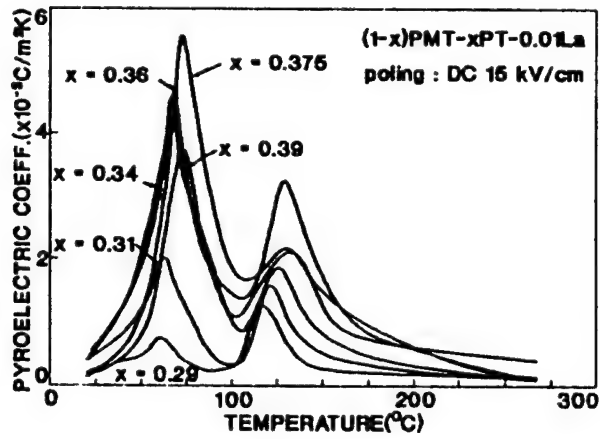
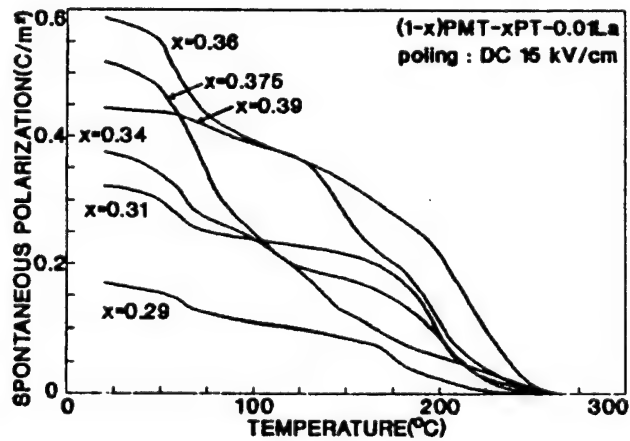


FIGURE 9 Pyroelectric coefficient as a function of temperature for 0.625PMT-0.375PT-yLa.

FIGURE 10 Pyroelectric coefficient as a function of temperature for $(1-x)\text{PMT}-x\text{PT}-0.01\text{La}$.FIGURE 11 Spontaneous polarization as a function of temperature for $(1-x)\text{PMT}-x\text{PT}-0.01\text{La}$.

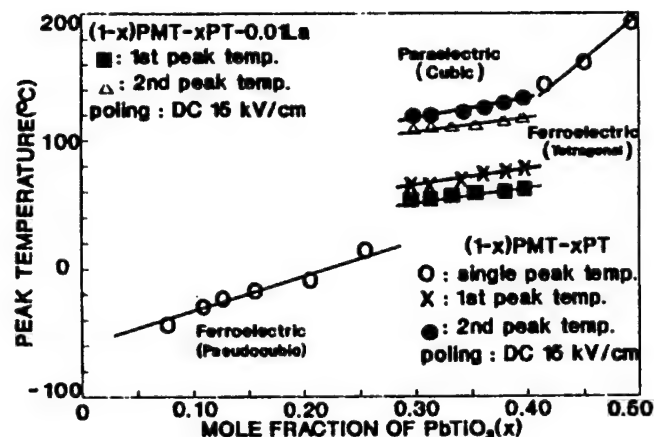


FIGURE 12 Phase diagram of La-doped and undoped PMT-PT solid solutions plotted from the pyroelectric data.

respectively, for various compositions in the $(1-x)\text{PMT}-x\text{PT}-0.01\text{La}$ series as functions of temperature. The peak temperatures do not change in the two-phase coexistence region for compositions between $x = 0.29-0.39$, as shown in Figure 12. For other compositions, the pyroelectric coefficient as a function of temperature has only a single peak.² This suggests successive phase transitions from ferroelectric rhombohedral at low temperature to ferroelectric tetragonal and finally to paraelectric cubic.

Figure 12 shows variation of the pyroelectric coefficient peak temperature with composition x in the $(1-x)\text{PMT}-x\text{PT}-0.01\text{La}$ and undoped $(1-x)\text{PMT}-x\text{PT}^2$ solid solutions near the morphotropic phase boundary. The position of the morphotropic phase boundary in PMT:PT appears to be unaffected by the addition of La_2O_3 , but the pyroelectric peak temperature was shifted downward by about $25^\circ\text{C}/\text{mole}\%$ La. It is observed that the peak temperature of each phase does not change much in the two phase region. The morphotropic phase boundary between two phases is not a line but a region similar to that observed in the undoped PMT-PT system by Kim.²

La-additions further allow flexibility in adjusting the transition temperature without significantly affecting the two-phase region or morphotropic phase boundary. The two phase region shifts by La-substitution for Pb may be related to the distribution of ions having different ionic radii in the same sublattice of a solid solution with perovskite structure.^{12,13} At present these phenomena cannot be fully explained.

CONCLUSIONS

Lanthanum-modification of PMT-PT ceramics was found to promote densification, inhibit grain growth, and shift $T_c \sim 25^\circ\text{C}/\text{mole}\%$ La_2O_3 downward. Also, it was found that PMT-PT ceramics doped with lanthanum have higher dielectric and pyroelectric constants than undoped PMT-PT compositions. The probable morphotropic phase boundary is not a line but a two-phase region similar to that

observed in the undoped PMT-PT system. A more detailed study is needed to understand this two-phase region.

ACKNOWLEDGEMENT

This work was supported by the Korea Science and Engineering Foundation (KOSEF) through the Science Research Center (SRC) of Excellence.

REFERENCES

1. V. A. Bokov and I. E. Myl'nikova, *Sov. Phys. Solid State*, **2**, 2428 (1961).
2. Y. J. Kim and S. W. Choi, *Ferroelectrics*, **108**, 241 (1990).
3. T. R. Shrout, Ph.D. Thesis, The Pennsylvania State University, 1981.
4. J. R. Oliver, R. R. Neurgaonkar and L. E. Cross, *J. Appl. Phys.*, **64**, 37 (1988).
5. L. E. Cross, *Ferroelectrics*, **76**, 241 (1987).
6. J. Chen, H. M. Chan and M. P. Harmer, *J. Am. Ceram. Soc.*, **72**, 593 (1989).
7. T. Takenaka, Y. Soma and K. Sakata, *Trans. Inst. Electron. Ceram. Eng. Jpn.*, **B**, **69**, 468 (1986).
8. S. L. Swartz, T. R. Shrout, W. A. Schulze and L. E. Cross, *J. Am. Ceram. Soc.*, **67**, 311 (1984).
9. T. R. Shrout and A. Halliyal, *Am. Ceram. Soc. Bull.*, **66**, 704 (1987).
10. S. L. Swartz and T. R. Shrout, *Mat. Res. Bull.*, **17**, 1245 (1982).
11. R. L. Byer and C. R. Roundy, *Ferroelectrics*, **3**, 333 (1972).
12. R. D. Shanonon and C. T. Prewitt, *Acta Crystallogr. B*, **25**, 925 (1969).
13. G. A. Smolenskii and A. I. Agranovskaya, *Sov. Phys. Solid State*, **1**, 1429 (1960).

APPENDIX 9

A PROCESSING AND ELECTRICAL PROPERTY INVESTIGATION OF THE SOLID SOLUTION: $(x) \text{Pb}(\text{In}_{1/2}\text{Nb}_{1/2})\text{O}_3 - (1-x) \text{Pb}(\text{Sc}_{1/2}\text{Ta}_{1/2})\text{O}_3$

EDWARD F. ALBERTA AND AMAR S. BHALLA
Materials Research Laboratory, The Pennsylvania State University,
University Park, Pennsylvania, 16802 USA

Ceramics in the solid solution system $(x) \text{Pb}(\text{In}_{1/2}\text{Nb}_{1/2})\text{O}_3 - (1-x) \text{Pb}(\text{Sc}_{1/2}\text{Ta}_{1/2})\text{O}_3$ [PIN:PST(x)] with compositions ranging from $x=0.0$ to $x=1.0$ have been fabricated. This paper presents the processing methods for producing 100% perovskite PIN and PST ceramics, as well as those for the PIN/PST solid solution. Various electrical properties including the dielectric constant and hysteresis, the pyroelectric and piezoelectric response, are measured on these compositions.

INTRODUCTION

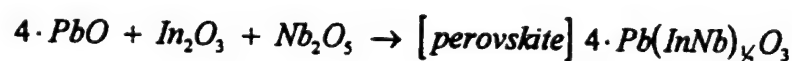
Earlier studies have shown that both $\text{Pb}(\text{In}_{1/2}\text{Nb}_{1/2})\text{O}_3$ [PIN] and $\text{Pb}(\text{Sc}_{1/2}\text{Ta}_{1/2})\text{O}_3$ [PST] are relaxor ferroics in which the degree of B-site cation ordering can be thermally controlled. Disordered PIN has been found to have a pseudo cubic perovskite structure, specifically, a rhombohedrally distorted space group of $R3m$ or $R3$. After thermal annealing, PIN has been shown to order into an antiferroelectric orthorhombic phase, isostructural with PbZrO_3 . Disordered PST has also been found to have a pseudo cubic structure. However, after ordering, the unit cell doubles into a ferroelectric phase. It is because of this difference in ordering behavior that the PIN:PST system looks to be of both theoretical and practical interest.

EXPERIMENTAL

1 Processing

i. Lead Indium Niobate Ceramics.

The processing of PIN powders evolved in this paper through a number of experimental steps. The first synthesis approach was through the common mixed oxide method. The starting materials for this procedure were reagent grade PbO, Nb₂O₅, and In₂O₃. Stoichiometric amounts of the raw materials were mixed with alcohol and ball-milled in Nalgene containers. Milling times were typically longer than 12 hours, followed by drying the powders at 100°C for 18 to 24 hours. After drying, the powder was re-ground with a mortar and pestle to 100 mesh. The PIN powder was then calcined on a platinum foil within a closed alumina crucible. The desired reaction for the mixed oxide method is as follows:



As with many other perovskite materials, a parasitic pyrochlore phase was concurrently produced. It was therefore important to determine the relative proportions of the two phases. This was accomplished using x-ray diffraction [XRD] and the method described by Swartz and Shrout (1982). From diffraction patterns the intensity of the 100% peaks of the two phases (110 and 022, respectively) were determined and the amount of perovskite present calculated by:

$$\% \text{ Perovskite} = I_{110} \left(\frac{I_{110}}{I_{011} + I_{022}} \right) \times 100$$

After calcining the powders with various soak times and temperatures, it quickly became apparent that lead and/or indium volatility was a serious problem. Atmospheric control was achieved by placing boats of PbO and In_2O_3 alongside the platinum foil. Eventually, the high temperature curing cement was used for better control of the atmosphere. In no case was phase pure PIN produced for reaction times up to 10 hours. An optimum soak condition of 4 hours at 1050°C was found to result in the production of only 80% perovskite phase. Further, any increase in either time or temperature resulted in an increase of pyrochlore concentration.

Further processing steps based on a precursor method for producing an intermediate "building block" phase for the synthesis of phase pure perovskite relaxor materials was used (Swartz and Shrout, 1982). For this wolframite precursor method, InNbO_4 was the choice for the intermediate phase. InNbO_4 was synthesized using the stoichiometric mixing and milling and drying of In_2O_3 and Nb_2O_5 . Von Liebertz (1972) cited a reaction temperature of 1100°C , so a sealed crucible with an indium source was employed. It was found (see figure 1) that production of InNbO_4 was reasonably (~90%) complete after 4 hours at 1200°C . Using these conditions InNbO_4 was synthesized and mixed with PbO and re-milled as previously mentioned. After drying the powder, various calcining conditions were evaluated using the sealed crucible method. It was found that soak times longer than four hours lead to increased concentration of the pyrochlore phase. Maximum perovskite phase content was found to be 85% at 1050°C (see figure 2.)

As suggested by Groves (1985) Li_2CO_3 was used to aid in forming PIN. In this paper the author reasons that the perovskite phase has a more "open" structure as compared to the pyrochlore. The small lithium ion should, therefore, add to the driving force for perovskite production due to its large kinetic energy at processing temperatures. This does seem to be the case as seen in figure 2. The addition of 3 weight percent of ultra-pure Li_2CO_3 increased the formation of the perovskite phase to about 90% with the

previously mentioned calcining conditions. Another problem realized at this temperature was the tendency for the powders to begin to sinter.

Another useful approach used both lithium and excess indium. Figure 1 shows the result of adding 2 excess weight percent In_2O_3 before the processing of InNbO_4 . It was found that >90% InNbO_4 was formed at 1100°C after 4 hours and the product showed greater crystallinity. This precursor was then mixed with PbO and 3 weight percent Li_2CO_3 . (Calcined powders and ceramics using this procedure will be referred to as PIN23). Figure 3 is a time and temperature diagram derived from PIN23 calcination study. At a temperature of 900°C PIN23 phase pure powders were produced after reacting the mixtures for 6 hours. Using this method, the need for sealed crucibles was eliminated; however, lead and indium sources were still used and precise temperature control was also required. A sample PIN23 XRD pattern is shown in figure 4.

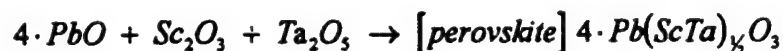
Currently sol-gel methods are also being investigated (Ravichandran, et al., 1995) for the production of PIN powder. It is hoped this will lead to a more robust processing method and larger batch sizes.

Sintering of PIN23 ceramics was done at 1050°C for 2 hours. This temperature was a trade-off between density and phase purity of the resulting ceramics. At 1050°C approximately 89 to 92% theoretical density was achieved while maintaining at least 98% of the perovskite phase in the bulk. Concentration of the pyrochlore phase on the surface tended to be slightly greater but could easily be polished off during sample preparation. Figure 5 shows an XRD pattern of a typical sintered PIN23 ceramic.

ii. Lead Scandium Tantalate Ceramics.

The production of PST has also evolved through a number of steps. Similar to PIN, the common mixed oxide method was used initially. Stoichiometric amounts of reagent grade PbO , Sc_2O_3 , and Ta_2O_5 was mixed and ball-milled for 12 hours with

zirconia media in alcohol. After drying 18 to 24 hours the powders were ground to 100 mesh and placed on a platinum foil in a closed alumina crucible. An alumina boat containing PbO was also placed in the crucible to control lead losses. The formation of PST is governed by the following formula:



This mixed oxide approach did not yield promising results. A maximum of 80% perovskite phase was achieved at 1000°C after calcining 4 hours (see figure 6.) Sealing the crucibles, as done with PIN, was found to have no effect on the amount of pyrochlore phase present.

The wolframite precursor method was also used for the synthesis of PST. The appropriate precursor phase for PST was found to be ScTaO₄. 90% Single phase ScTaO₄ was produced after calcining the oxides for 8 hours at 1500°C. (see figure 7) It was determined that highly crystalline, single phase ScTaO₄ could be produced from a two-step method. The first step was to calcine the powder at 1400°C for 4 hours to obtain 60% single phase ScTaO₄. The powder was then re-milled for 12 hours in alcohol and dried for 18 hours. After drying the powder was fully converted to ScTaO₄ when soaked at 1500°C for 4 hours.

PbO was added to the ScTaO₄ and was milled and dried. It was found that single phase PST could easily be produced at temperatures as low as 800°C and times as short as 2 hours. A sample XRD pattern of a PST powder produced by this method is shown in figure 8. Sintering of PST ceramics, however, has proven to be more difficult. The maximum density found after sintering for 8 hours at 1400°C was 65 to 70% theoretical. Fielding et al. (1995) has shown that highly dense single phase PST ceramics can be produced after sintering pellets between 1500°C and 1600°C in double sealed crucibles. In addition, work by Ravichandran et al. (1995) has shown sol-gel derived PST can be sintered in a phase pure perovskite pellets at a temperature of approximately 1400°C.

iii. PIN:PST ceramics.

PIN:PST (x) ceramics (x representing the concentration of PIN in mole percent) were fabricated using the single phase powders as discussed previously. Appropriate amounts of the end members were mixed and milled for 6 hours and a binder was added. Once the powder was dried it was ground to 100 mesh and pressed. Weight loss of the ceramics was in all cases less than 2%. Pellets were placed in alumina crucibles on platinum foils and lead and indium sources were added. All of the ceramics (x = 100.0, 97.5, 50.0 and 2.5) retained at least 98% of the perovskite phase and were between 85 and 80% of the theoretical density.

2 Electrical

Electrical measurements including the dielectric constant and loss, dielectric hysteresis, and pyroelectric coefficient were made on the sintered pellets. The experimental setup to measure the dielectric constant and loss included a Hewlett Packard 4271A capacitance bridge and liquid nitrogen feed furnace. The Byer-Roundy method was used for the pyroelectric measurements. This setup involved a Hewlett Packard 4192A picoammeter and a similar furnace setup. Data was collected by Hewlett Packard 200 series micro computer. A modified Sawyer-Tower circuit was used for the hysteresis measurements. It included a Trek 2000 voltage amplifier and an MS-DOS based computer equipped with analog to digital converters for data collection.

Room temperature dielectric constant measured at 1 kHz were found to be 3845 (near the peak) and 1267 (in the paraelectric region) for ceramics with x = 97.5 and 2.5, respectively. The transition temperatures for the two ceramics were determined for the two ceramics to be 20°C and 10°C, respectively. Transition temperatures from

pyroelectric data were found to be slightly lower, with values of 10°C and 0°C, respectively. As expected from the dielectric and pyroelectric data, only limited room temperature hysteresis was noticed. Upon cooling to -30°C, PIN:PST(2.5) shows a remnant polarization of 4.5 $\mu\text{C}/\text{cm}^2$, and reaches a saturated value of 5.7 $\mu\text{C}/\text{cm}^2$. The coercive field was found to be 9.86 kV/cm. No piezoelectric response has been detected in these compositions at room temperature. Further studies on the temperature dependence of the ferroelectric properties and the similar measurements on other compositions across the phase diagram are in progress.

SUMMARY

The experimental approach describes a suitable method for fabricating phase pure perovskite ceramics in the PIN:PST solid solution system. It is shown that high quality ceramics with less than 2% pyrochlore phase can be produced by a suitable multi-step process. Future work will focus on the order-disorder behavior and the electromechanical properties of these and other compositions across the PIN:PST phase diagram.

REFERENCES

- [1] Fielding, J.F., *Proceedings of the Amer. Ceram. Soc. Meeting*, April 1995.
- [2] Groves, P., "Fabrication and Characterization of Ferroelectric Perovskite Lead Indium Niobate," *Ferroelectrics*, **65** 67-77 (1985).
- [3] Park, S.S., and W.K. Choo, "Pyroelectric and Dielectric Properties of Lead Indium Niobate Ceramics," *Ferroelectrics*, **118** 117-122 (1991).
- [4] Setter, N., Ph.D. Thesis, The Pennsylvania State University, 1980.

- [5] Swartz, S.L., and T.R. Shrout, "Fabrication of Perovskite Lead Magnesium Niobate," *Mat. Res. Bull.*, **17** 1245 (1982).
- [6] Von Liebertz, J., "Gitterkonstanten von InNbO_4 und InTaO_4 ," *Acta. Cryst. B* **28** 3100 (1972).
- [7] Ravichandran, D., A.S. Bhalla, and R. Roy, "Sol-Gel Derived $\text{Pb}(\text{Sc}_{0.5}\text{Ta}_{0.5})\text{O}_3$ Powders," *Materials Letters* (to be published).

FIGURES

Figure 1. Formation of InNbO_4 with a soak time of 4 hours.

● → stoichiometric, ○ → 2wt% excess In_2O_3 .

Figure 2. Formation of $\text{Pb}(\text{In}_{1/2}\text{Nb}_{1/2})\text{O}_3$ with a soak time of 4 hours.

● → stoichiometric, ○ → 3wt% excess Li_2CO_3 .

Figure 3. Formation of $\text{Pb}(\text{In}_{1/2}\text{Nb}_{1/2})\text{O}_3$ with 2wt% excess In_2O_3 and 3wt% excess Li_2CO_3 . 100% Perovskite forms at 900°C after 6 hours.

Figure 4. X-Ray diffraction pattern of a calcined $\text{Pb}(\text{In}_{1/2}\text{Nb}_{1/2})\text{O}_3$ powder.

Figure 5. X-Ray diffraction pattern of a sintered $\text{Pb}(\text{In}_{1/2}\text{Nb}_{1/2})\text{O}_3$ ceramic.

Figure 6. Formation of $\text{Pb}(\text{Sc}_{1/2}\text{Ta}_{1/2})\text{O}_3$ by the mixed oxide method.

Figure 7. Formation of ScTaO_4 by the mixed oxide method.

Figure 8. X-Ray diffraction pattern of a calcined $\text{Pb}(\text{Sc}_{1/2}\text{Ta}_{1/2})\text{O}_3$ powder.

Figure 9. Dielectric constant and loss of (a) PIN:PST (2.5) and (b) PIN:PST (97.5).

Figure 10. Pyroelectric constant and remnant polarization of (a) PIN:PST (97.5) and (b) PIN:PST (2.5).

Figure 11. Room temperature dielectric hysteresis loop of (a) PIN:PST (97.5) and (b) PIN:PST (2.5).

Figure 12. Dielectric hysteresis loop of PIN:PST (2.5) measured at -30°C .

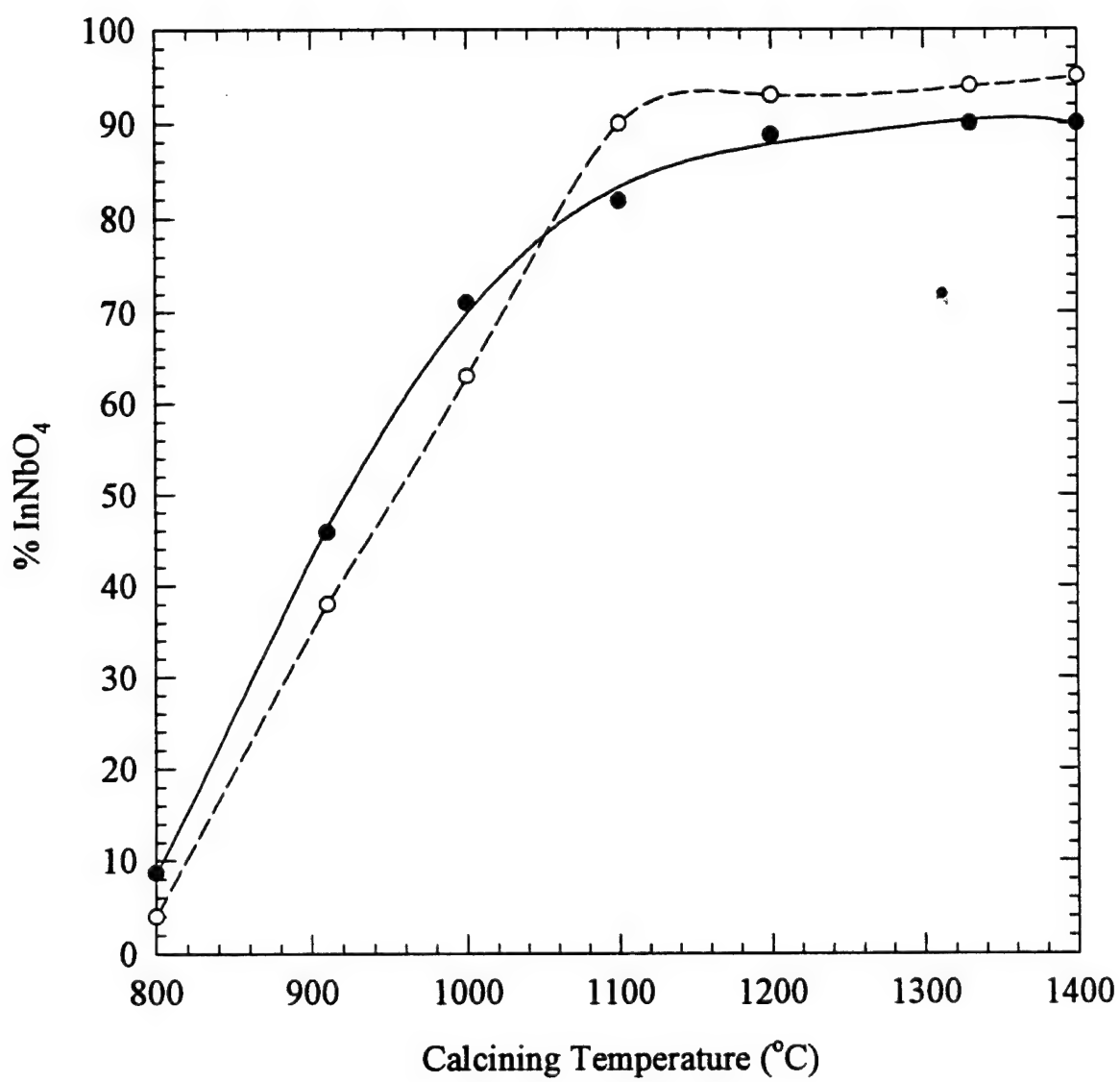


Figure #1

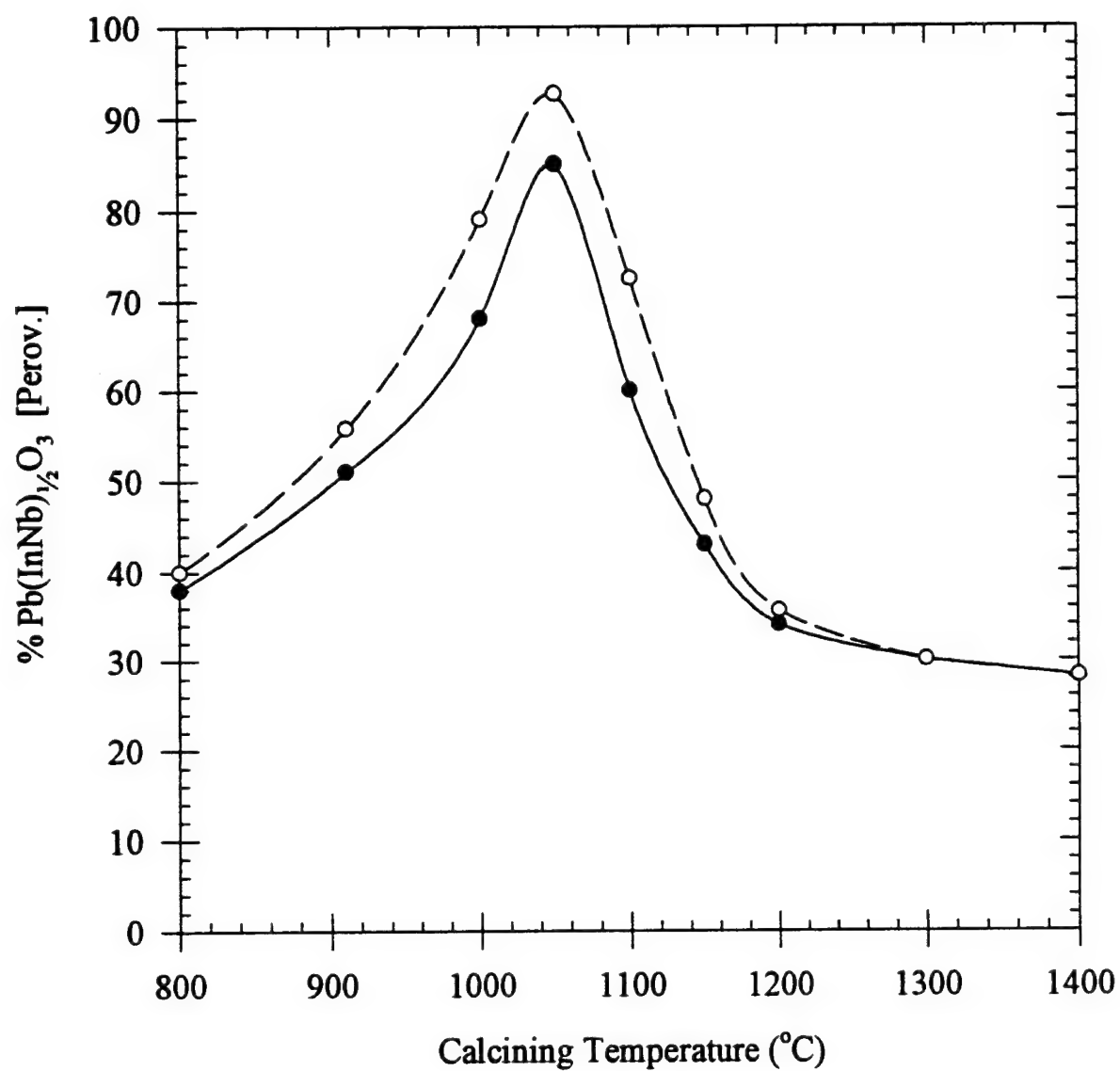


figure 712

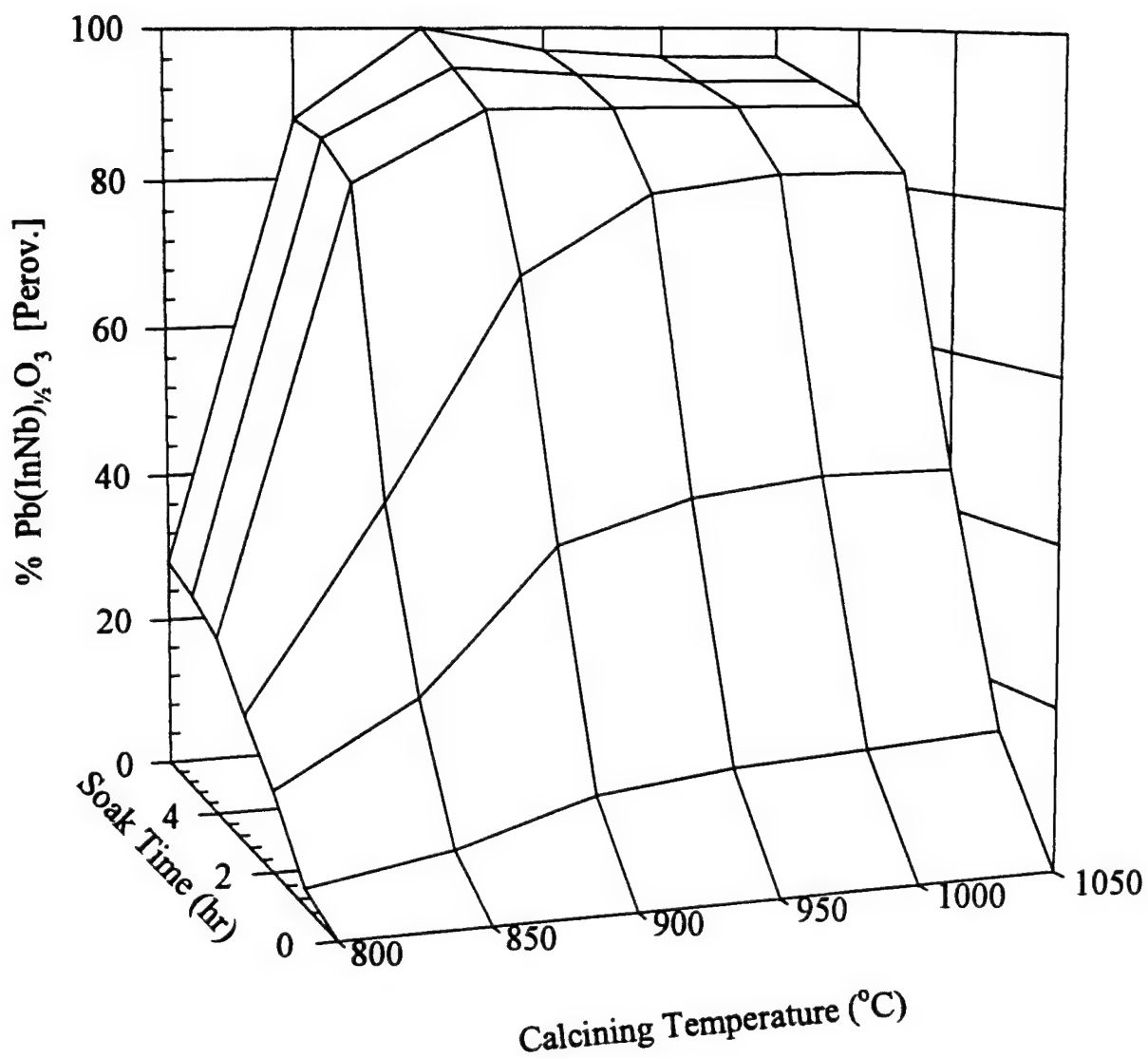
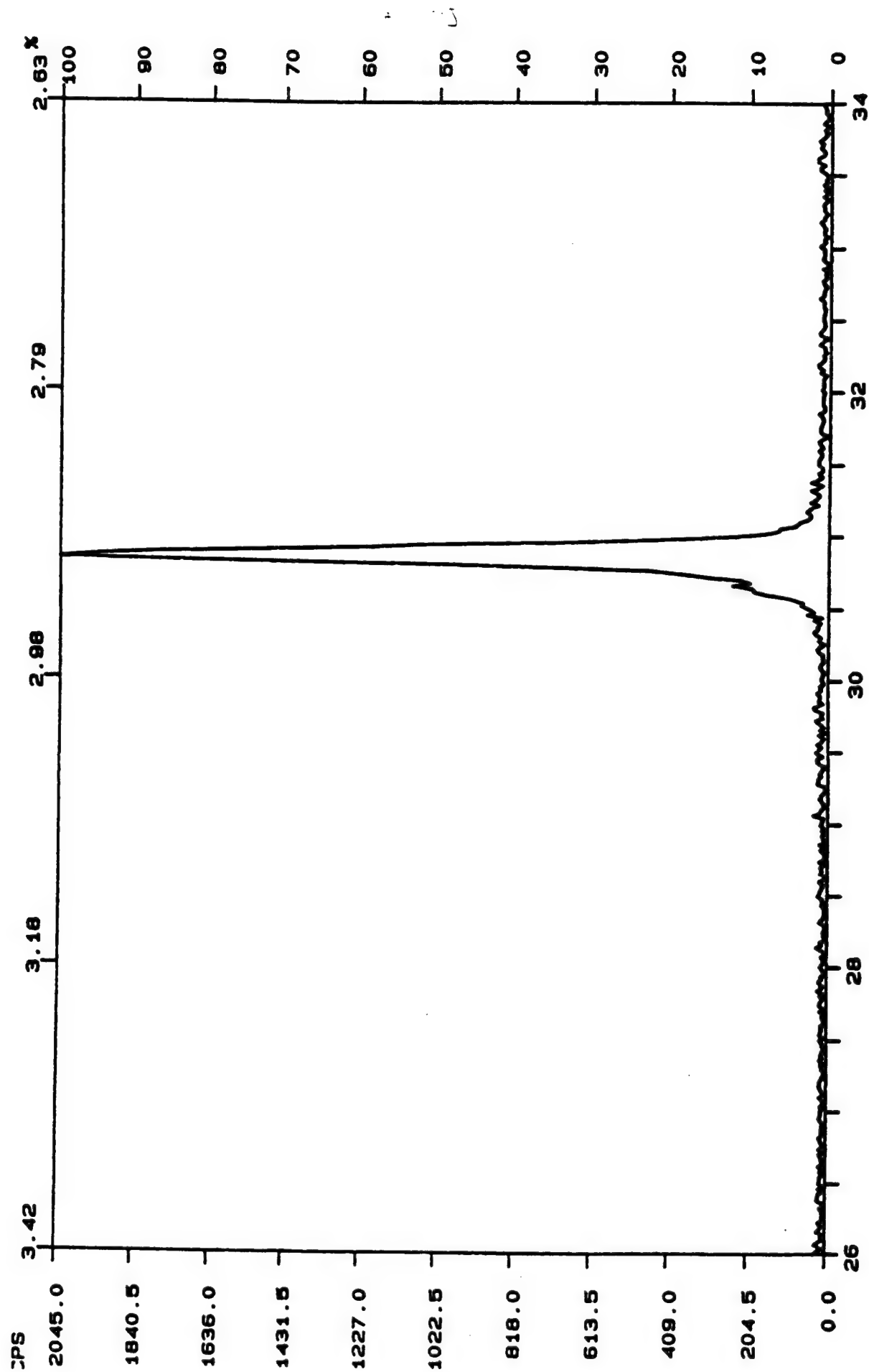
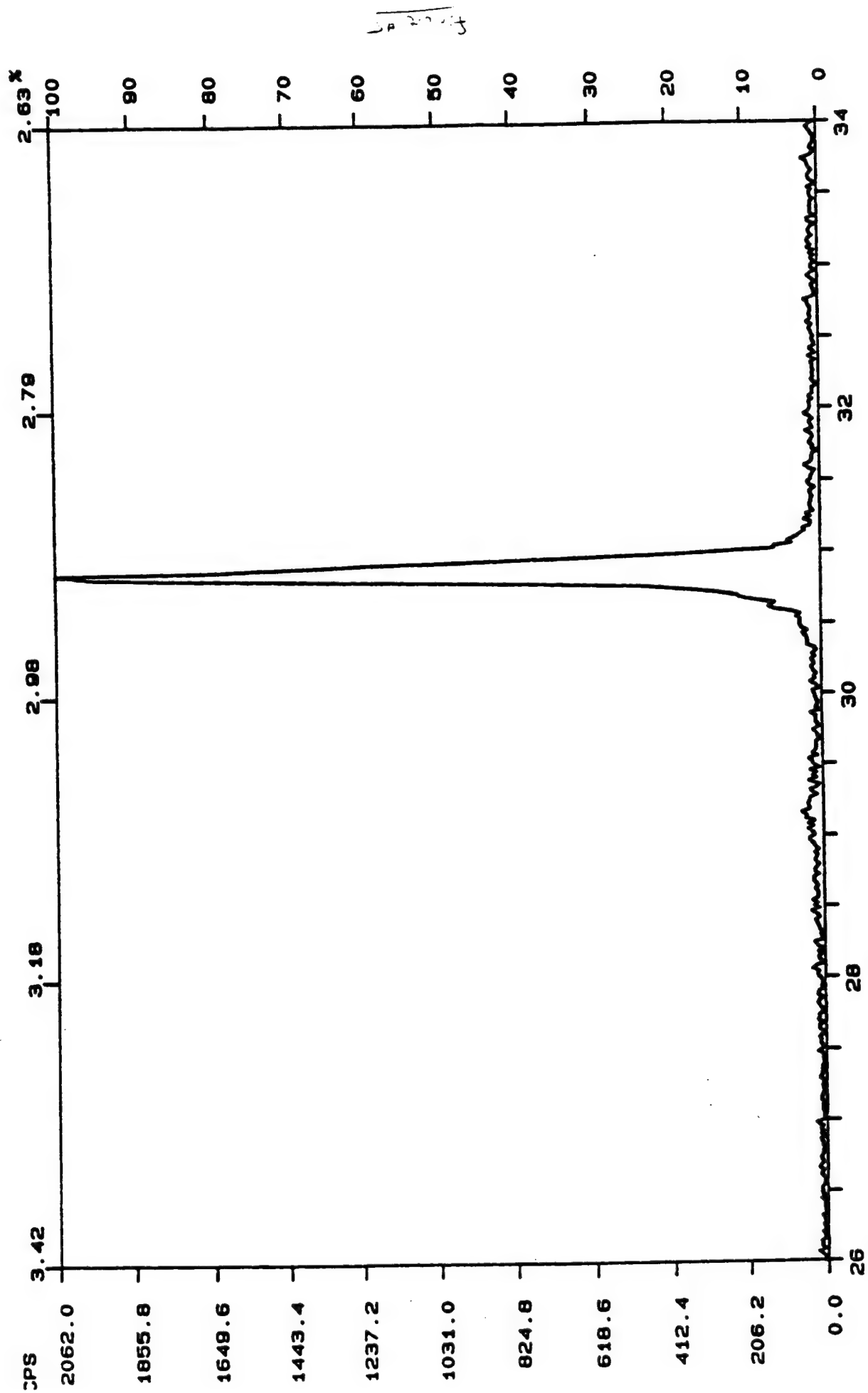


Figure 3





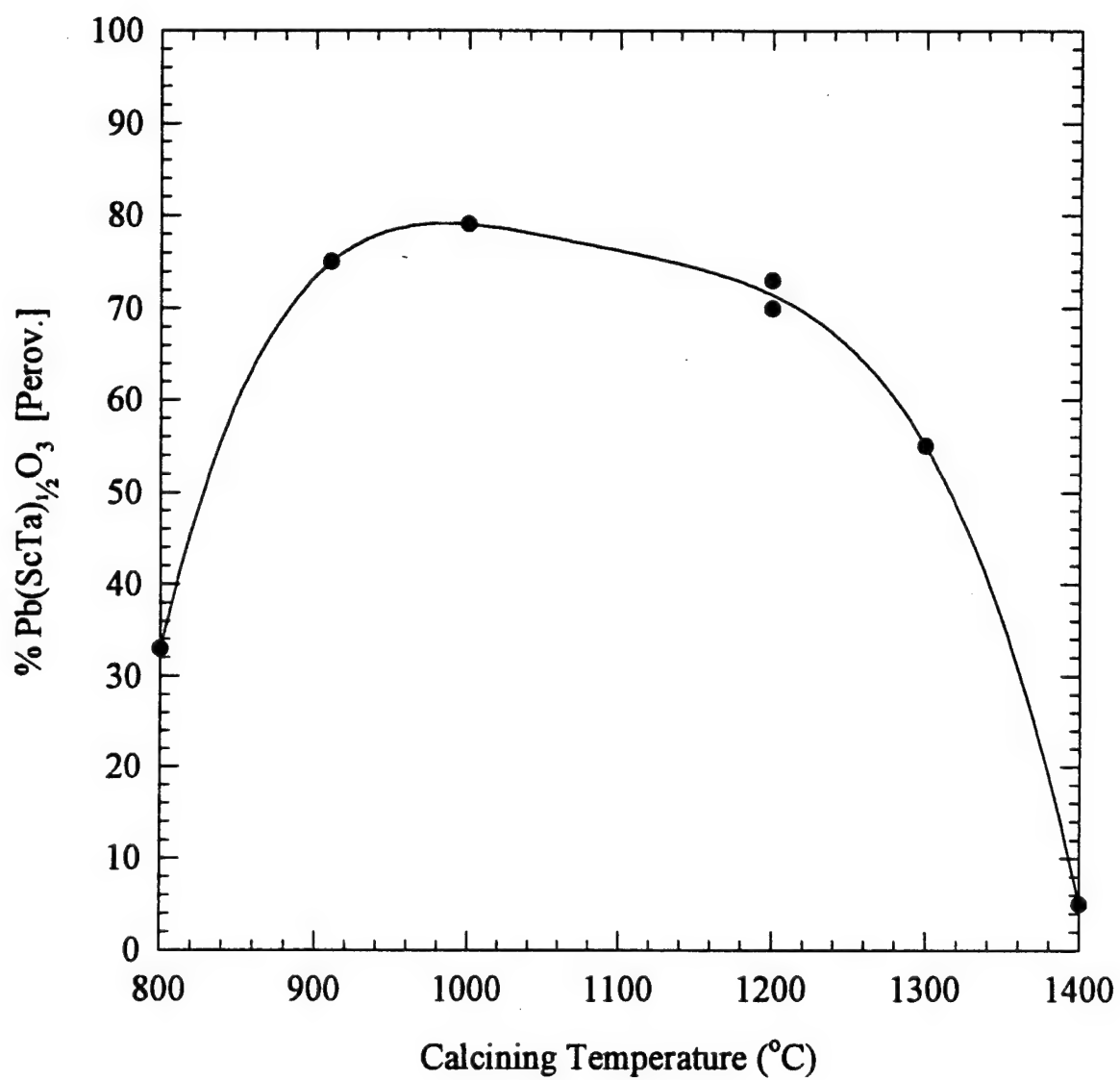


figure #6

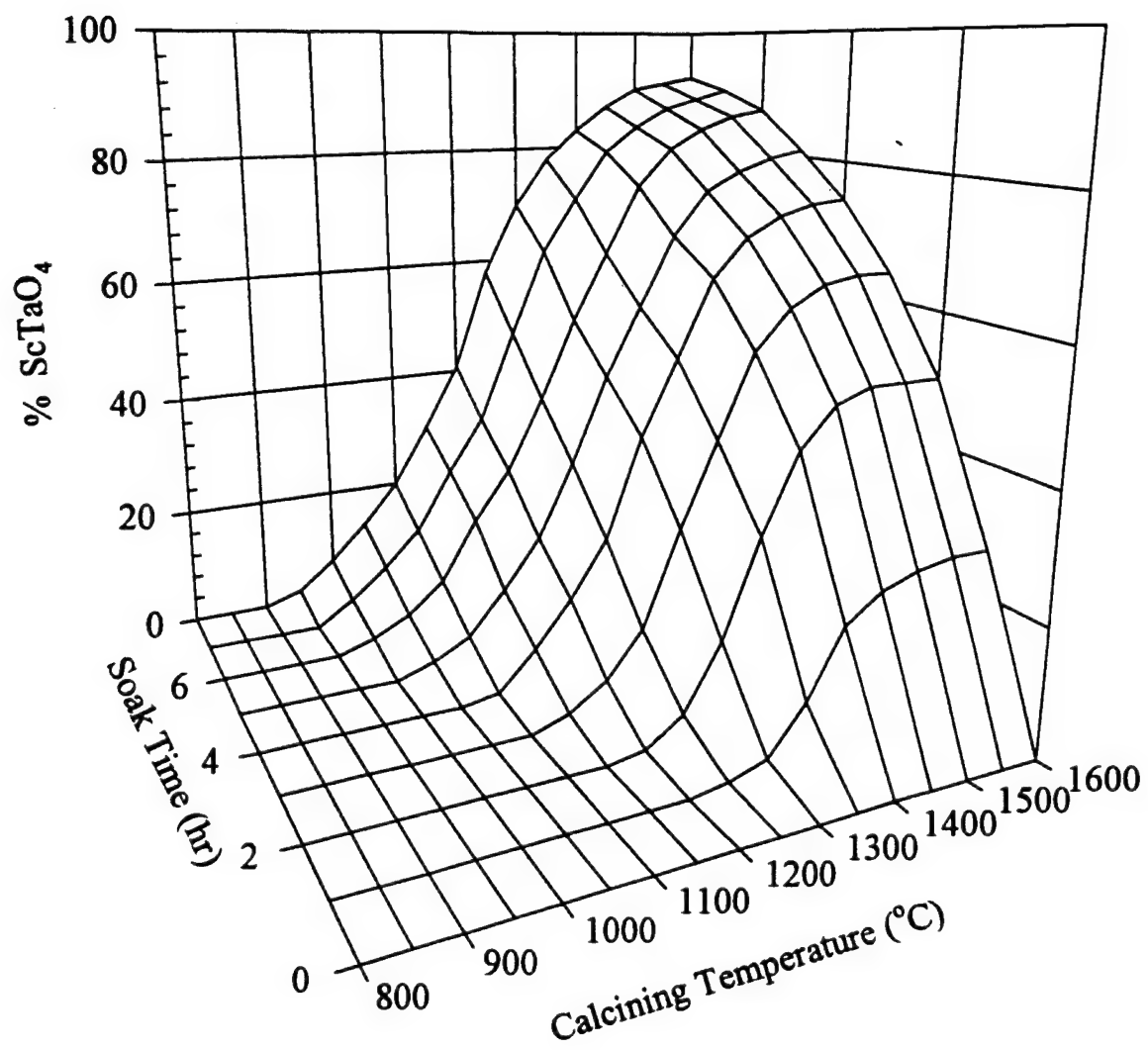


figure 11

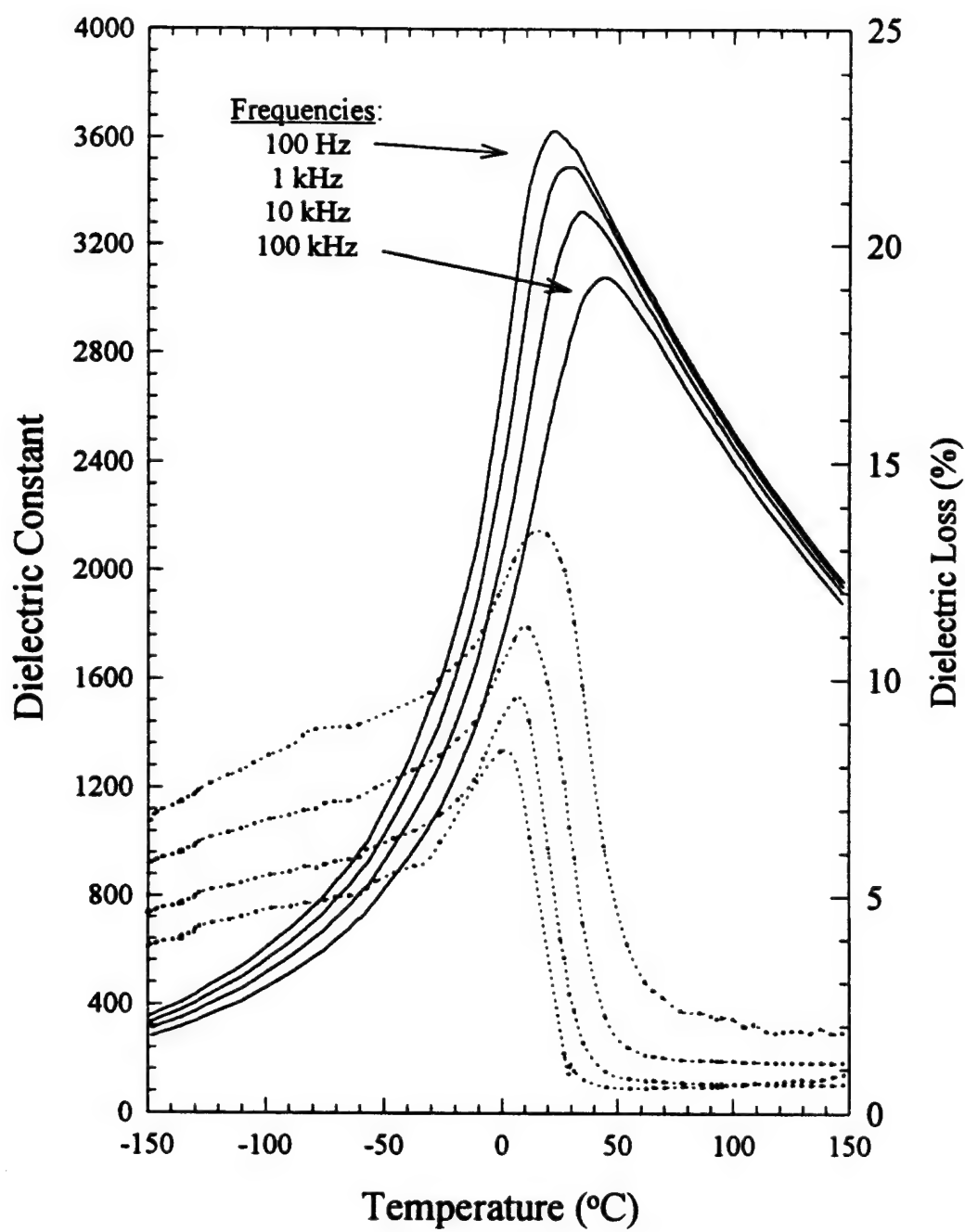
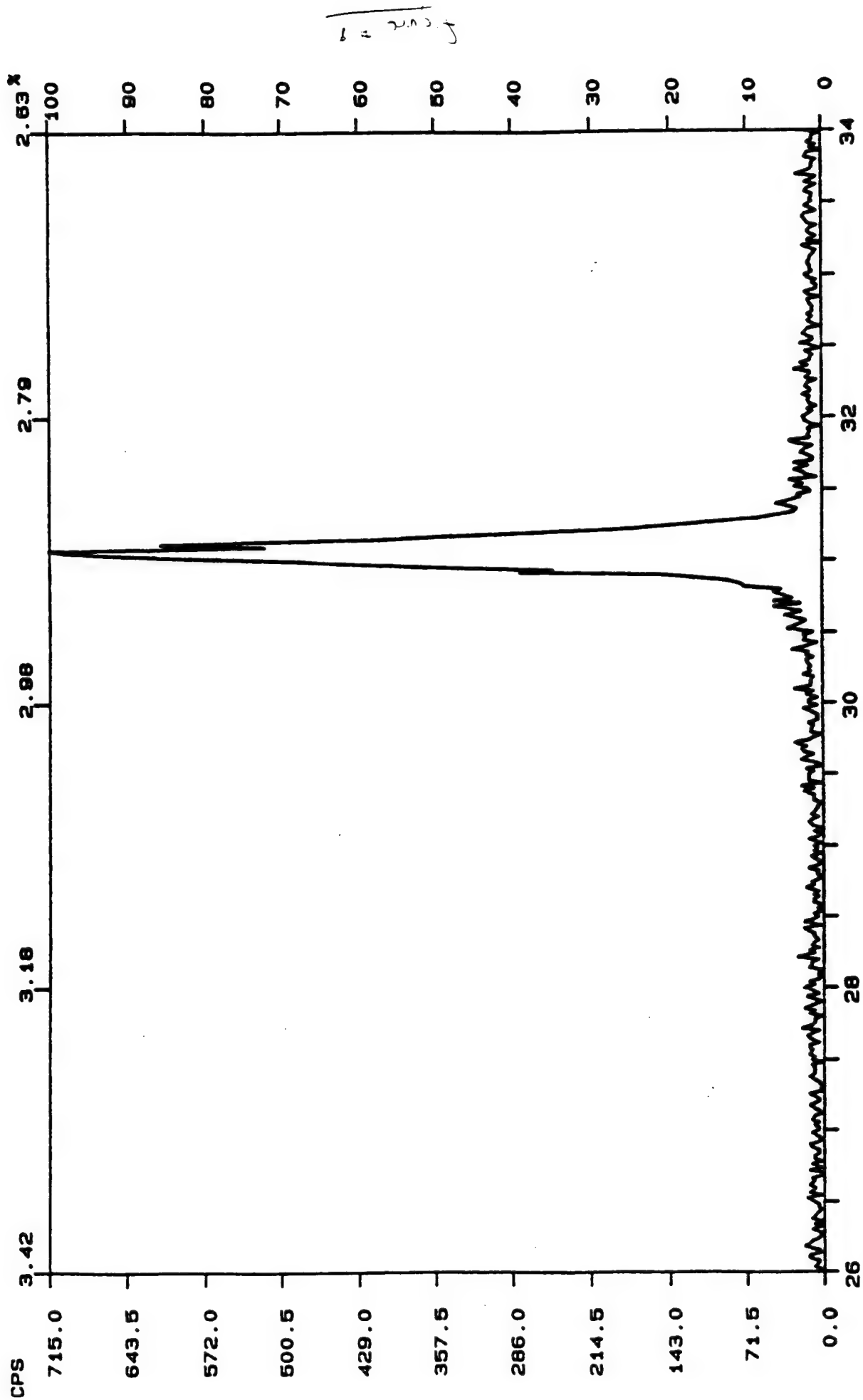


Figure #9(a)



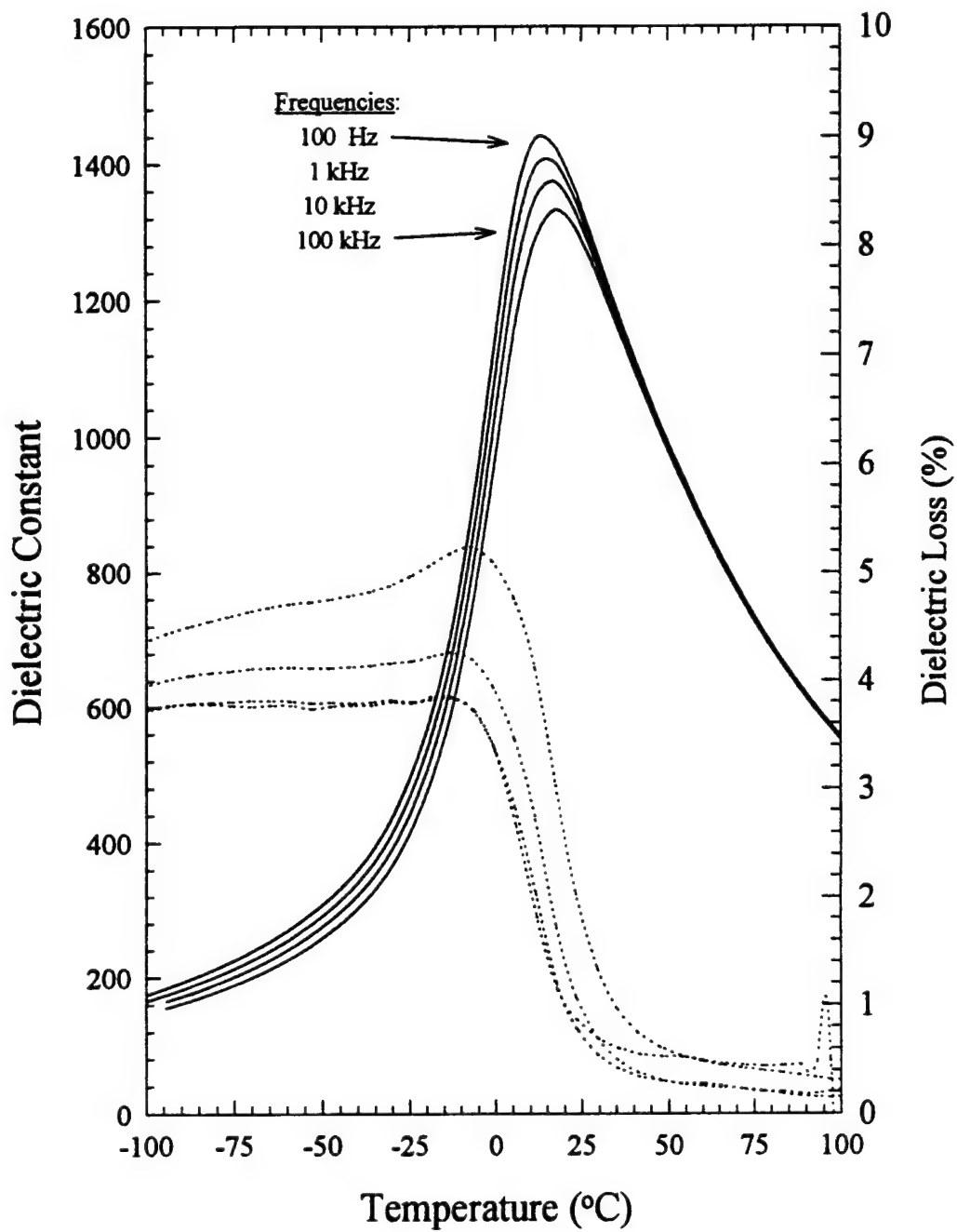


Figure #96

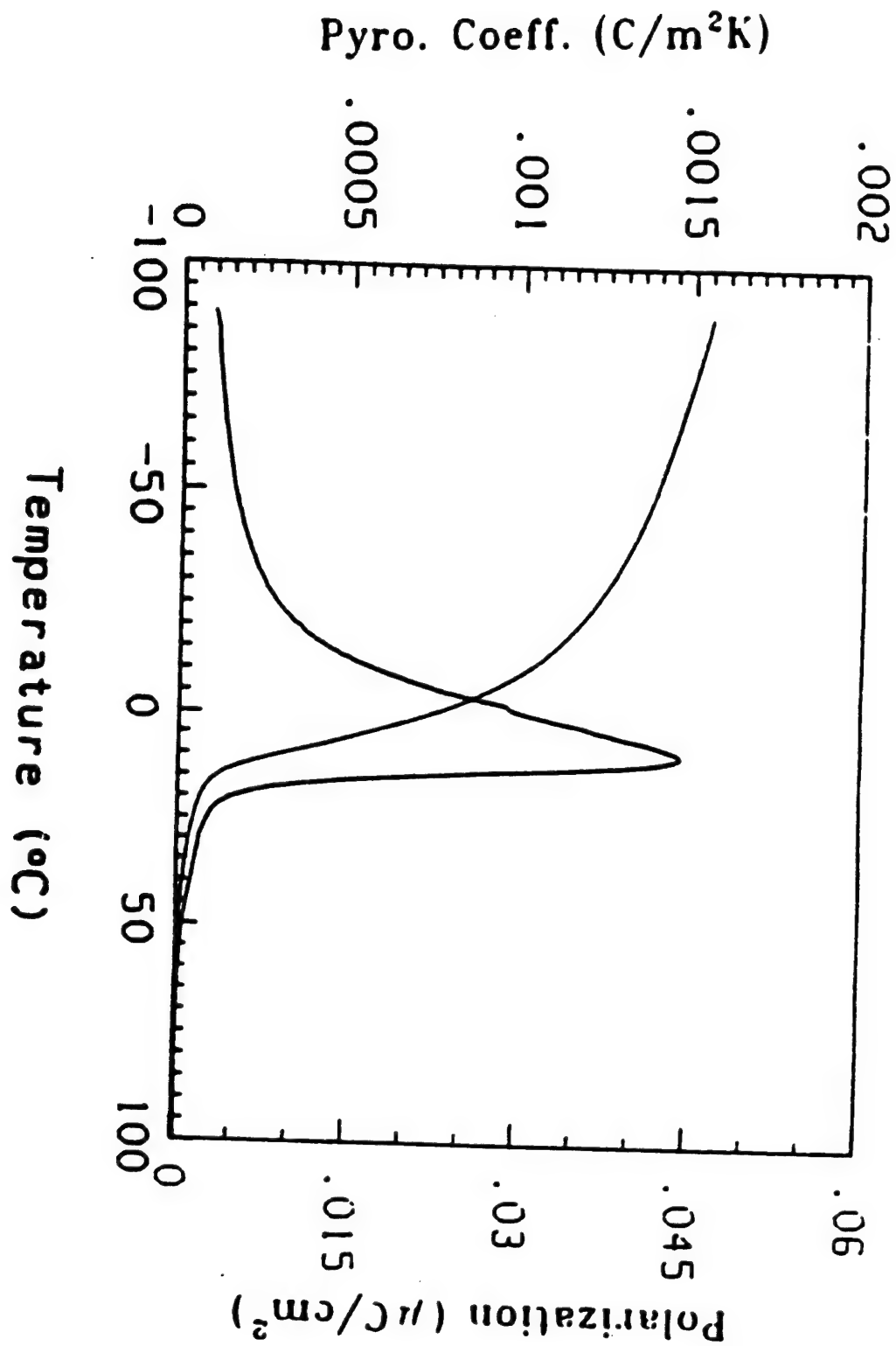


Figure 10c

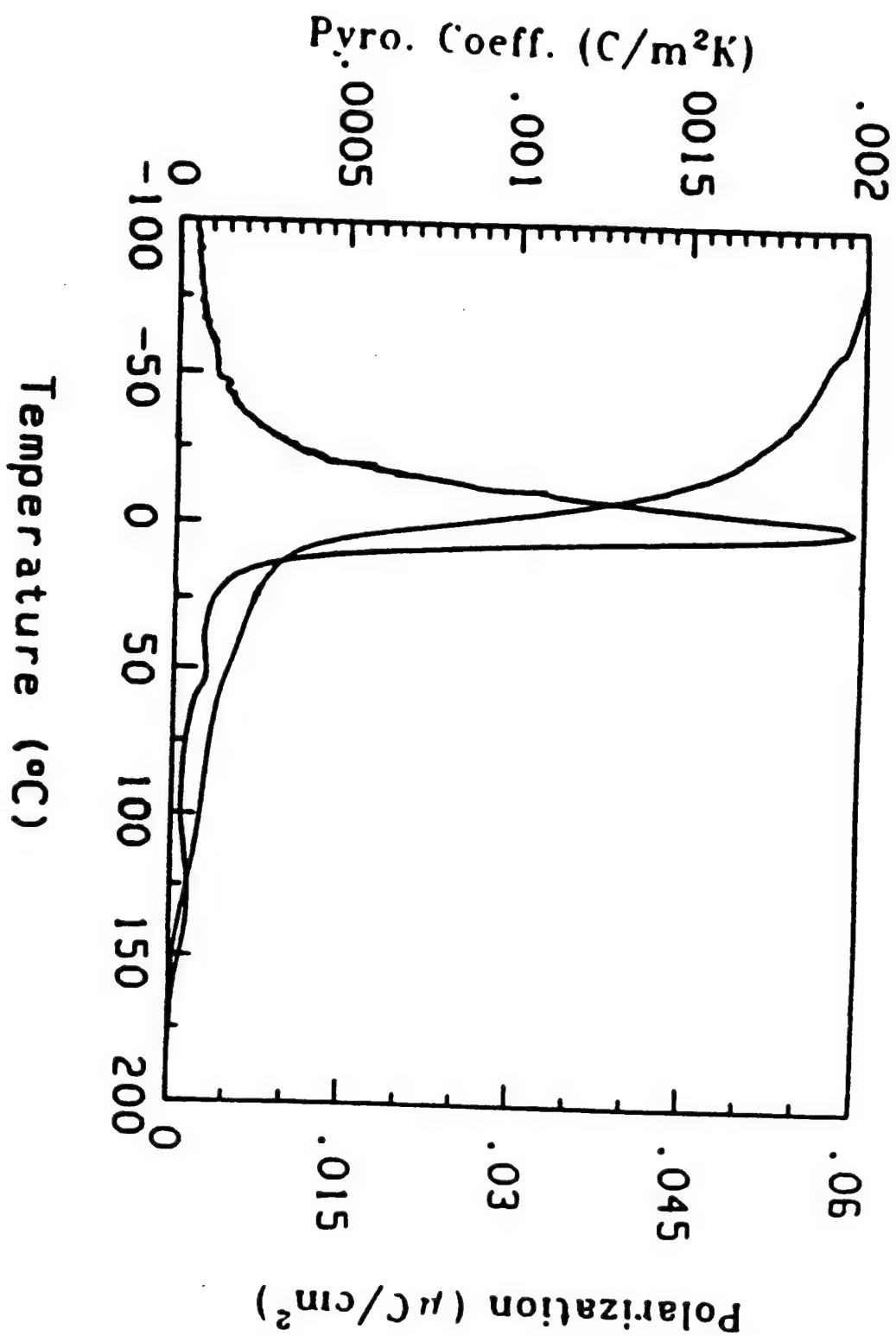


Figure 106

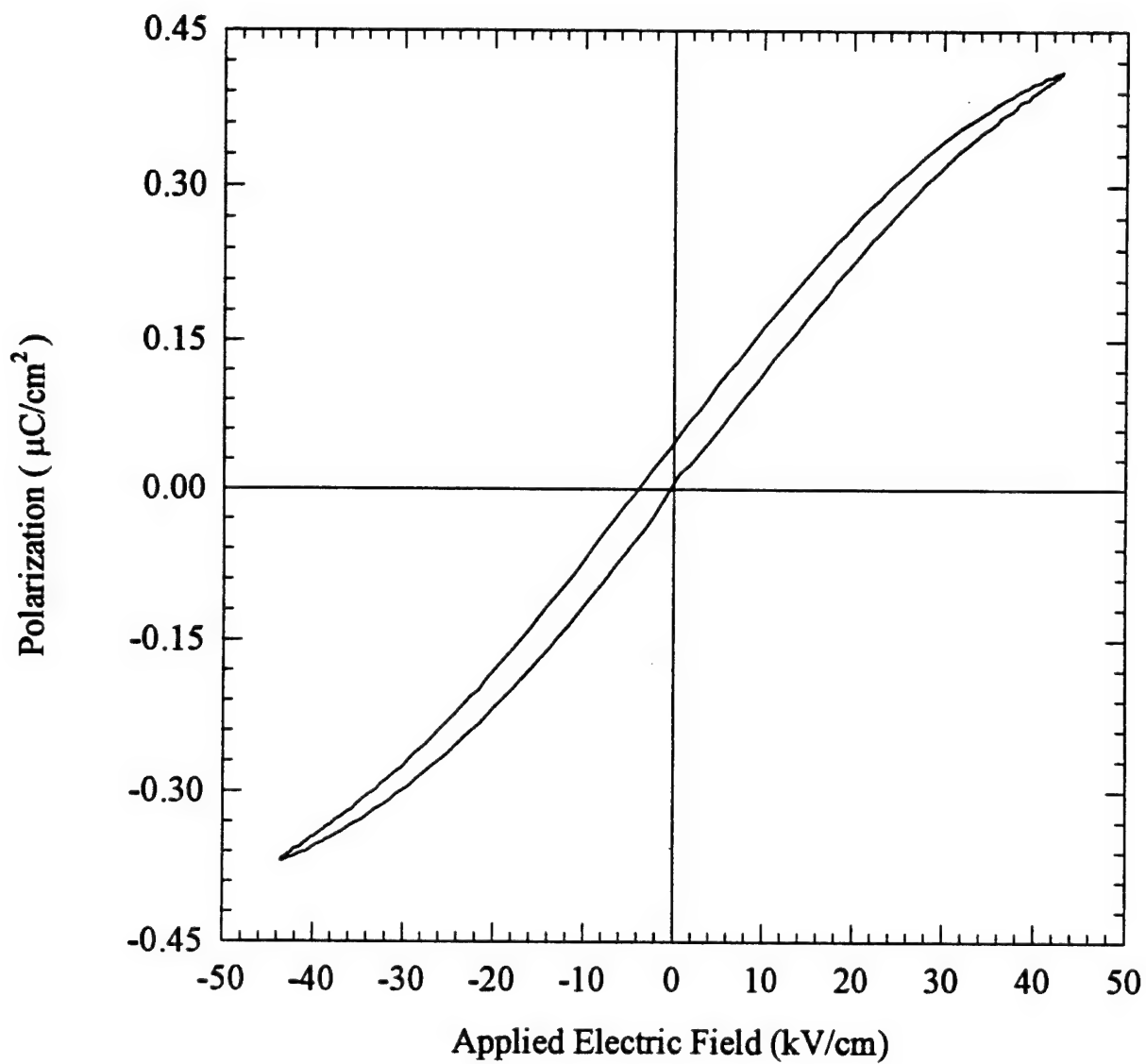


Figure #11a

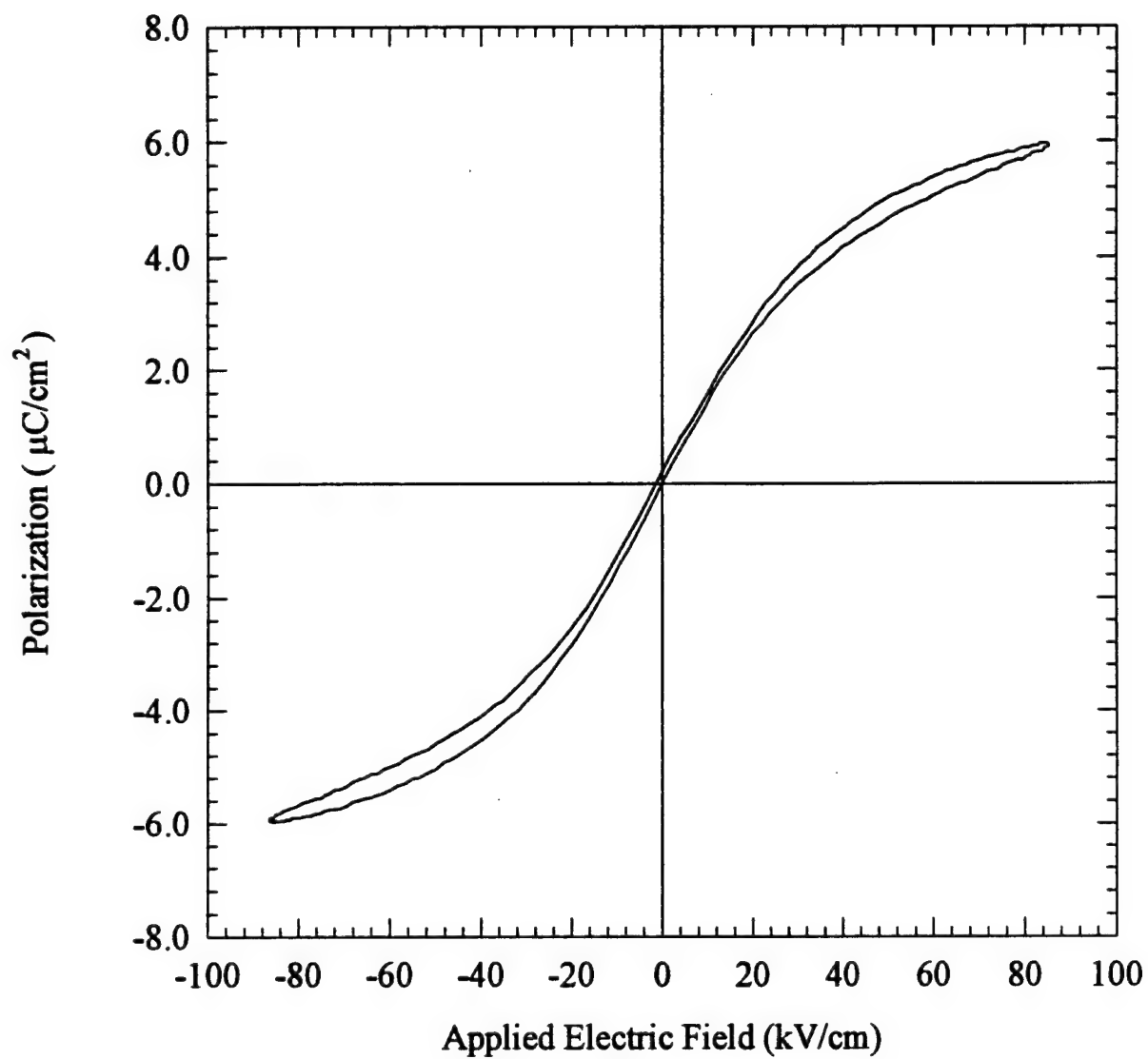


Figure #11b

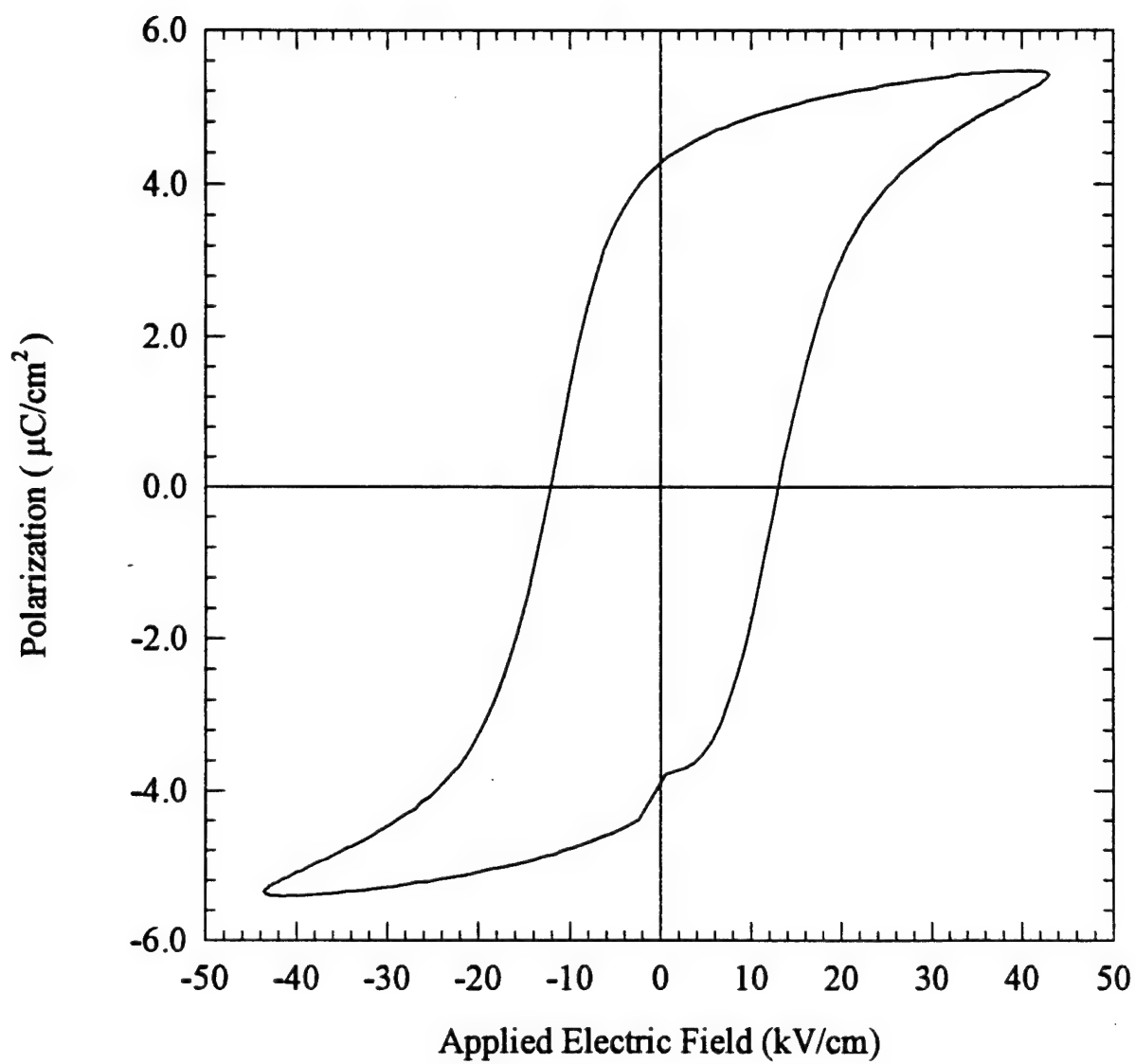


Figure 12

APPENDIX 10

0038–1098(95)00647-8

AN X-RAY DIFFRACTION STUDY OF SUPERLATTICE ORDERING IN LEAD MAGNESIUM NIOBATE

Q.M. Zhang

Materials Research Laboratory, The Penn State University, University Park, PA 16802, U.S.A.

Hoydoo You

Materials Science Division, Argonne National Laboratory, Argonne, IL 60439, U.S.A.

and

Maureen L. Mulvihill and S.J. Jang

Materials Research Laboratory, The Penn State University, University Park, PA 16802, U.S.A.

(Received 21 August 1995; accepted 12 September 1995 by S.G. Louie)

We report a direct observation of the superlattice diffraction peaks, indicating a doubling of unit cell, from lead magnesium niobate (PMN) single crystal using X-ray diffraction technique. The broad width of the superlattice diffraction peaks indicates that the superlattice ordering in PMN is of short range. In the temperature range studied (from 10 K to 355 K) the peak width shows no temperature dependence. The intensity distribution among the observed superlattice peaks suggests that the doubling of unit cell in the superlattice regions involves significant ionic displacements in addition to a chemical ordering.

Keywords: A. ferroelectrics, C. crystal structure and symmetry, C. X-ray scattering, D. order–disorder effects.

1. INTRODUCTION

LEAD MAGNESIUM niobate, $\text{PbMg}_{1/3}\text{Nb}_{2/3}\text{O}_3$ (PMN), belongs to a special class of ferroelectric materials known as relaxor ferroelectrics [1, 2]. This class of material is characterized by a broad maximum of weak field dielectric permittivity and its frequency dependent behavior. For a regular ferroelectric material, there is no significant frequency dispersion at the ferroelectric–paraelectric phase transition region at frequencies up to sub-GHz [3]. However, for a relaxor ferroelectric material, a strong frequency dispersion exists at the so-called diffused phase transition region which extends to frequencies down to near zero. Recently, it has been shown that this relaxation behavior can be described by the Vogel–Fulcher relation, reflecting the broad relaxation spectrum in the system and a non-zero freezing temperature into a disordered state [4], analogous to the critical slowing down observed in the random fields magnetic system and spin glass [5]. X-ray and neutron scattering data

also revealed that in the zero field cooled state, PMN remains in the pseudo-cubic phase with non-macroscopic polarization [6, 7]. However, with an applied electric field, a macroscopic ferroelectric phase can be induced, and once it is established, this phase is stable after the field is removed up to a temperature near the maximum of the dielectric permittivity [8, 9]. Due to their peculiar physical properties, relaxor materials, especially PMN, have been studied extensively for many decades [1, 2, 10–13].

Although in PMN, there is non-macroscopic polarization even at temperatures near 0 K, overwhelming experimental evidence from the thermal expansion, optical refractive index, and X-ray diffraction experiments has shown that local polarization domains exist in the microscopic scale [2, 6, 14]. The scale of the micro-polar regions, based on the information from the quasi-elastic neutron scattering experiment and from reasoning on the phenomenological basis, is estimated in the range from 100 Å to a few hundred Angstroms [2, 15]. The

existence of such micro-polar regions and the absence of a macroscopic polarization state indicate a competition in the material between the tendency of the system towards a macroscopically polar state and the frustration of the local random fields to break the global symmetry of the system.

To elucidate the relaxor behavior in PMN type materials, which have a perovskite ABO_3 structure, the role of compositional fluctuation on the B-site is often emphasized. For PMN, the two cations sharing the B-sites, namely Mg^{2+} and Nb^{5+} , have different valence and ionic size. As a result, the chemical fluctuation in the B-sites will produce a local electric field and stress field which breaks the local symmetry and prevents the formation of a macroscopic polar state, a situation analogous to the polar glass state in mixed crystals [16, 17]. From the extensive TEM studies [18, 19], it was found that there are superlattice diffraction peaks at reciprocal lattice points of $(h/2, k/2, l/2)$ where h, k, l are odd numbers. In addition, TEM data also showed that the size of the superlattice region is about 50 Å. These micro-regions exist over a wide temperature range and do not coarsen with high temperature annealing, which leads to the conclusion that the superlattice ordering is from a 1:1 nonstoichiometric ordering in the B site of Mg and Nb along $\langle 111 \rangle$ direction [18]. More recently, Egami and Rosenfeld investigated the short and intermediate range structural and chemical ordering in PMN using the pair-density function (PDF) analysis based on X-ray and neutron powder diffraction data. From the fit modeling results at the observed PDF, they proposed that in PMN there exist two different B sites. The cations in the B1 sites are at the ideal cubic lattice position and in the B2 sites are displaced along $\langle 111 \rangle$ direction. Their model showed the existence of two structurally different regions: one with a structural ordering of B1 and B2 sites along $\langle 111 \rangle$ directions, giving rise to the observed superlattice diffraction, and the other with B2 sites only [20, 21].

To understand the microstructure related to the superlattice diffractions, it is advantageous to investigate directly the superlattice diffractions. Although TEM provides a valuable tool for detecting the superlattice diffraction, a quantitative analysis and structure determination on the superlattice region in PMN is often difficult [22]. Since the TEM experiment is performed on thin specimens (typical sample thickness is in the order of a couple of hundred Angstroms), one should be cautious in interpreting the observed phenomena in TEM because of the possible surface effect and finite size effect. In addition, in spite of extensive structure investigations of powder samples using both

X-ray and neutron diffractions, the existence of the superlattice peaks, as reported in TEM studies, has not been confirmed. In this paper, we report a recent investigation of PMN single crystals using X-ray diffraction technique. With careful scans through the peak position of the superlattice diffraction, the superlattice diffraction peaks were indeed observed and the data suggest that the superlattice ordering involves significant ionic displacements.

2. EXPERIMENTAL

Single crystals of PMN were grown by the flux solution technique. They were light yellow in color with a cubic morphology. The crystal used in this experiment was oriented and cut into a rectangular plate with the large face parallel to the (100) plane. The size of the specimen was 2 mm \times 4 mm \times 4 mm. Prior to the X-ray experiment, the dielectric constant of the specimen was measured and the results are shown in Fig. 1. The data exhibit a well-defined diffused phase transition with the dielectric relaxation observed in typical PMN materials [2-4].

The X-ray experiment was carried out using a 12 kW rotating anode with $Cu K\alpha$ radiation and a four circle goniometer. A bent graphite monochromator was used to focus the X-ray beam to an area of $1 \times 2 \text{ mm}^2$ at the sample position. The temperature range for the experimental set-up was from 10 K to 355 K and temperature was regulated with a close cycle He refrigerator. Temperature stability was better than 0.1 K. The scattering measurements were performed in (HKL) units and throughout this paper, the scattering vector Q is expressed as

$$Q = H b_1 + K b_2 + L b_3,$$

where b_1, b_2 , and b_3 are the reciprocal vectors in the

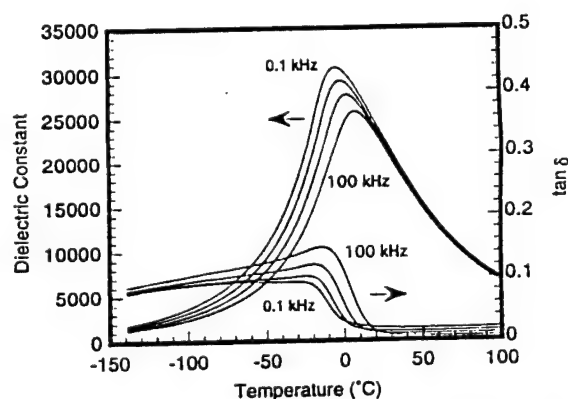


Fig. 1. Dielectric constant and loss of PMN single crystal used in the experiment. The dielectric constant was measured along $\langle 111 \rangle$ direction with frequencies of 0.1, 1, 10 and 100 kHz.

x -, y - and z -directions, respectively. For PMN which has a pseudo-cubic symmetry, $|b_1| = |b_2| = |b_3| = 2\pi/a$, where a is the lattice constant of the primitive cubic perovskite unit cell.

3. RESULTS AND DISCUSSIONS

Shown in Fig. 2 is the scattering profile for (001) and (113) diffraction peaks measured at 355 K. The scans were along the L -direction with H and K fixed. The solid lines in the figure are the fitting of the data using a Gaussian line shape. From the fitting of the peak positions, the lattice constant a for the primitive perovskite unit cell is determined to be $a = 4.040 \pm 0.001$ Å. A careful inspection of Fig. 2 reveals that there is a tail (diffuse scattering) at the basis of the peaks. As temperature is lowered, there is a slight broadening of the peak width and the diffuse scattering near the foot of the peaks also increases. However, there is very little change in the peak position with temperature. These features are consistent with the results from the earlier scattering experiment which were interpreted as evidence for the existence and growth of local polar regions as the temperature is lowered and which have a short correlation length [6].

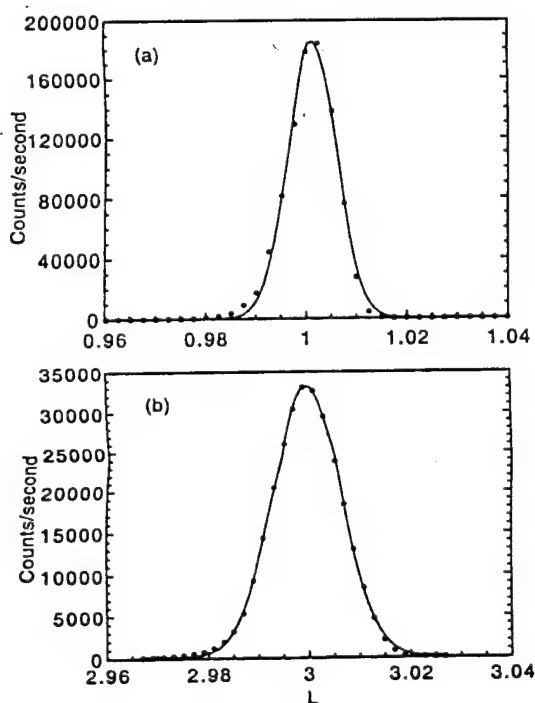


Fig. 2. Diffraction profiles for (001) and (113) peaks measured at 355 K [(a) and (b) respectively]. The scans were taken along the L -direction. Black dots are the data points and solid lines are the Gaussian line shape fitting.

Careful scans at the vicinity of the superlattice peak positions reported in TEM studies reveal the existence of very weak superlattice peaks in X-ray diffraction measurements. Shown in Fig. 3 are the superlattice diffraction peaks (1/2, 1/2, 1/2) and (3/2, 3/2, 3/2) measured at three different temperatures. The scans were taken along [111] direction (HKL scan) and the data are shown in the unit of H in Fig. 3. Within the counting statistics of the experiment, no superlattice diffraction was observed at (1/2, 0, 0) and (1/2, 1/2, 0) positions. Therefore, the results here confirm the existence of the regions in the specimen corresponding to an ordered structure which gives rise to doubling of the primitive unit cell. Scans were taken in the temperature range from 10 K to 355 K and in the temperature range studied, the width of these superlattice diffraction peaks remains constant while the peak intensity decreases gradually as the temperature is lowered.

In addition to the (1/2, 1/2, 1/2) and (3/2, 3/2, 3/2) diffraction peaks, scans were also made along the L -direction with H and K fixed at 1/2 where a series of superlattice peaks (1/2, 1/2, 1/2), (1/2, 1/2, 3/2),

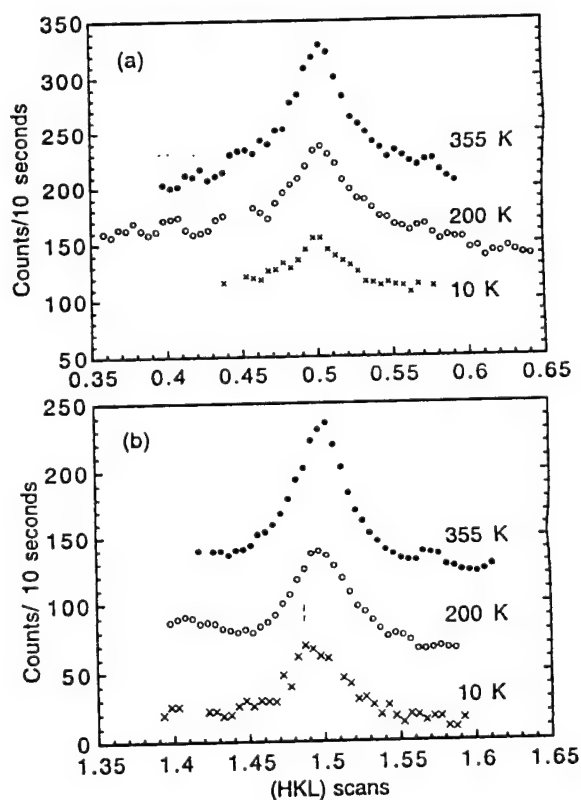


Fig. 3. Selected X-ray diffraction profiles for (1/2, 1/2, 1/2) and (3/2, 3/2, 3/2) superlattice diffraction peaks illustrating the temperature dependent behavior of these peaks.

$(1/2, 1/2, 5/2)$, and $(1/2, 1/2, 7/2)$ were observed. Again, scans were taken at temperatures from 10 K to 350 K. Shown in Fig. 4 are the data at 10 K, 200 K and 350 K. Similar to the data in Fig. 3, within the experiment resolution, the peak width does not change with temperature in the temperature range studied.

Hence, the X-ray data here confirm the existence of the superlattice diffractions in PMN and the unit cell doubling. However, as is evident from the data, compared with regular diffraction peaks, the intensity of the superlattice diffraction is extremely weak. For instance, the peak intensity of the regular diffraction peaks, such as (100) , is about 10 000 times of that of the superlattice peaks. This explains why the earlier X-ray and neutron scattering experiments with powder samples failed to detect these superlattice peaks.

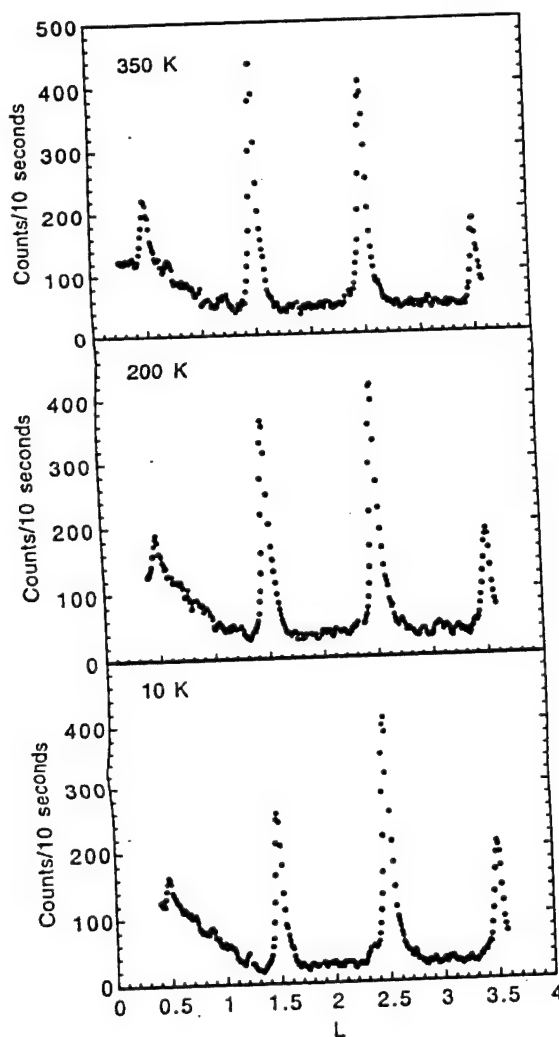


Fig. 4. Selected X-ray diffraction profiles for $(1/2, 1/2, 1/2)$, $(1/2, 1/2, 3/2)$, $(1/2, 1/2, 5/2)$ and $(1/2, 1/2, 7/2)$ superlattice diffraction peaks. The scans were taken along the L -direction with H and K fixed at $1/2$.

Clearly, the width of the superlattice diffraction peaks is much broader than that of the integer lattice peaks. In addition, the line shape of the superlattice peaks can be fitted quite well with a Lorentzian function, as shown in Fig. 5,

$$I(Q) = \frac{A}{\kappa^2 + (Q - Q_0)^2}, \quad (1)$$

where A is a constant, Q_0 is the center position of the peak, κ is inversely proportional to the peak width and is related to the size of the correlated region giving rise to the superlattice diffraction. A Lorentzian line shape for the superlattice peak is in sharp contrast to the Gaussian line shape of the integer diffraction peaks. Except for the $(1/2, 1/2, 1/2)$ peak, κ is nearly the same in all the superlattice diffraction peaks. Owing to a large background and data scattering, the line shape of the $(1/2, 1/2, 1/2)$ peak has not been analyzed. Shown in Fig. 6 is the temperature dependence of κ and clearly, within the uncertainty of the data, κ remains a constant in the temperature range studied. To provide a qualitative estimation of the size

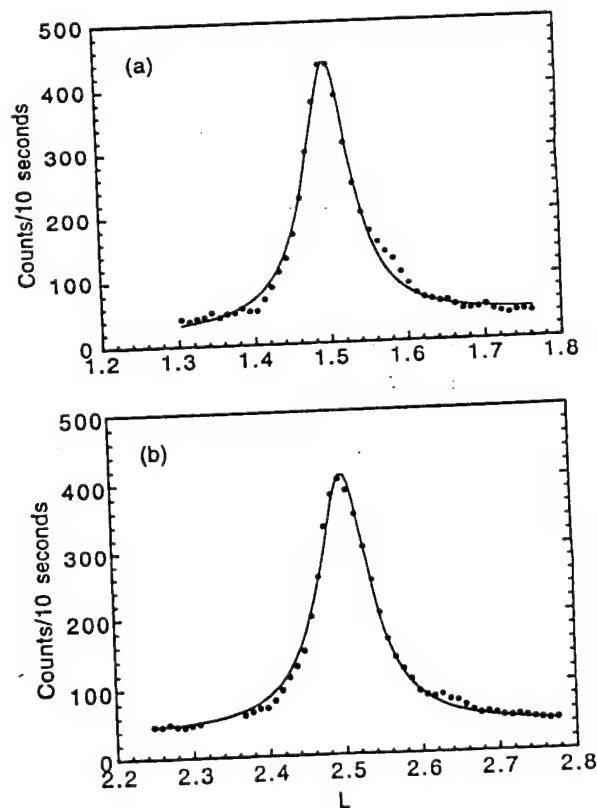


Fig. 5. Data illustrating that the peak shape for the superlattice diffraction is a Lorentzian function. Black dots are the data points at 350 K for $(1/2, 1/2, 3/2)$ and $(1/2, 1/2, 5/2)$ peaks and solid lines are the fitting to the data with a Lorentzian function.

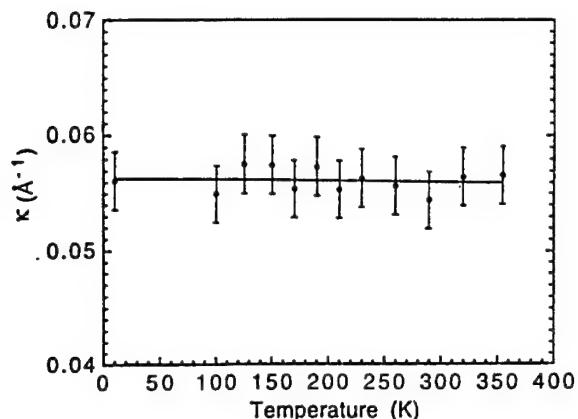


Fig. 6. κ as a function of temperature. The data show that in the temperature range studied, the peak width of the superlattice diffraction remains a constant, indicating that the size of the superlattice domain does not change with temperature.

of the superlattice domains, Scherrer particle size equation was employed which relates the particle size W with the full width at half maximum (FWHM) ΔQ of the diffraction peak [23]

$$W = 3.76\pi/\Delta Q.$$

This equation yields a W of 100 Å which does not change with temperature in the temperature range studied.

In order to understand what might be the structure responsible for the weak superlattice peaks, it is instructive to consider the difference in the structure factors of a chemical ordering and of a displacive ordering.

In PMN, the chemical ordering can occur in the B-sites either as stoichiometric or nonstoichiometric. To describe the degree of ordering, an order parameter δ is introduced here. For a stoichiometric ordering leading to the unit cell doubling, the chemical compositions in the two sublattices B1 and B2 are $\{(2/3)(1 + \delta/2) \text{ Nb} + (1/3)(1 - \delta) \text{ Mg}\}$ and $\{(2/3)(1 - \delta/2) \text{ Nb} + (1/3)(1 + \delta) \text{ Mg}\}$, respectively. For $\delta = 1$, B1 site will be totally occupied by Nb while B2 site has a Mg to Nb ratio of 2:1, as in the $(\text{NH}_4)_3\text{FeF}_6$ structure. Additionally $\delta = 0$ corresponds to a random distribution in the B-sites with a ratio of 1/2 of Mg/Nb. The structure factor for such a superstructure is $(8\delta/3) |f_{\text{Nb}} - f_{\text{Mg}}|$. For a nonstoichiometric ordering such as the one leading to a 1:1 Mg and Nb ordering, the chemical compositions of the B1 and B2 sites are $\{(2/3)(1 + \delta/2) \text{ Nb} + (1/3)(1 - \delta) \text{ Mg}\}$ and B2-site $\{(2/3)(1 - \delta) \text{ Nb} + (1/3)(1 + 2\delta) \text{ Mg}\}$, respectively. Again, a perfect 1:1 Mg and Nb ordering corresponds to $\delta = 1$. The structure factor for the superlattice diffraction from the

1:1 chemical ordering will be $4\delta |f_{\text{Nb}} - f_{\text{Mg}}|$. Hence, for chemical ordering, due to DWF and atomic scattering factor, the peak intensity should decrease monotonically as the scattering vector Q increases. Although this trend seems to be consistent with the data in Fig. 3, this is not the case for the peak intensity distribution shown in Fig. 4 where the peak intensity increases with Q at first and then drops.

For the ordering due to the atomic displacement, the change of the peak intensity with Q will have a quite different trend. If we assume the unit cell doubling is due to the cation displacement at B-sites along $[111]$ direction where cations in B1-site stay at the center of the unit cell and in B2-sites the cations move off-center by $(a\delta, a\delta, a\delta)$, the peak intensity for the superlattice diffraction will be proportional to $\{8f_{\text{B}}[\sin(\pi\delta(H + K + L))]\}^2$ times the DWF where f_{B} is the average atomic scattering factor in the B-site which equals $(2/3)f_{\text{Nb}} + (1/3)f_{\text{Mg}}$. δ generally is a small number and the term of $\sin[\pi\delta(H + K + L)]$ will increase as $H + K + L$ increases as long as $\delta(H + K + L)$ is less than 0.5. Combining this with the effect of DWF and atomic scattering factor on the diffraction intensity, the peak intensity for the superlattice diffraction will rise at first and then drop as the scattering vector Q increases, which are consistent with the data in Figs 3 and 4.

In general, the doubling of unit cell in PMN superlattice domains can be the result of the cation shifts, i.e. Mg/Nb in the B-sites and Pb in the A-sites, from their ideal lattice positions and/or the anti-parallel rotation of the oxygen octahedra. As an example, by assuming an anisotropic DWF and a shift of Mg/Nb in B2-sites and Pb in the corresponding cell along $\langle 111 \rangle$ direction, the data at 355 K can be described quite well with this simple structural ordering model.

It should be pointed out that although the structural ordering can provide a reasonable account for the observed peak intensity distribution with (HKL) , the fact that the peak width does not change with temperature even though there is a significant change in the local strain in the same temperature range suggests that some degree of chemical ordering exists in the superlattice region. A model with a structural ordering with some degree of weak chemical ordering can describe the observed data well. However, the number of constraints here is smaller than the number of undetermined parameters to fully account for the atomic shifts in both A and B sites, oxygen octahedra rotations, and the weak chemical ordering, responsible for the doubling of the primitive unit cell in the superlattice regions. We do not intend to pursue the structure determination further. A

detailed quantitative structure determination of the superlattice region will be reported in the future.

Based on these analyses, it is clear that in order to consistently account for the experimental results obtained, it is necessary to assume that there is a displacive ordering in the atomic position with some degree of 1:1 chemical ordering in the B-sites in PMN.

4. SUMMARY

We reported a direct observation of the superlattice diffraction peaks from PMN single crystals using X-ray diffraction technique. The size of the superlattice domain, estimated using Scherrer particle size equation, is about 100 Å. In the temperature range of this investigation, the superlattice peak width does not change with temperature. The intensity distribution among different superlattice peaks suggests that the doubling of the unit cell is mainly from a structural ordering.

Acknowledgements — The authors wish to thank Prof. L.E. Cross and Prof. R. Newnham for stimulating discussions. The work at the Materials Research Laboratory of Penn State was supported in full by the Office of Naval Research. The work at Argonne National Laboratory was supported by DOE under contract W-31-109-ENG-38.

REFERENCES

1. G.A. Smolenskii & A.I. Agranovskaya, *Sov. Phys. Solid State* **1**, 1429 (1959).
2. L.E. Cross, *Ferro* **76**, 241 (1987).
3. M.E. Lines & A.M. Glass, *Principles and Applications of Ferroelectrics and Related Materials*. Clarendon Press, Oxford (1977).
4. D. Viehland, S. Jang, L.E. Cross & M. Wuttig, *Phil. Mag.* **B64**, 335 (1991).
5. D.S. Fisher, G.M. Grinstein & A. Khurana, *Phys. Today* **56** (Dec. 1988).
6. N. de Mathan, E. Husson, G. Calvarin, J.R. Gavarri, A.W. Hewat & A. Morell, *J. Phys.: Condens Matter* **3**, 8159 (1991).
7. P. Bonneau, P. Garnier, G. Calvarin, E. Husson, J.R. Gavarri, A.W. Hewat & A. Morell, *J. Solid State Chem.* **91**, 350 (1991).
8. Z.G. Ye & Hans Schmid, *Ferro* **145**, 83 (1993).
9. G. Calvarin, E. Husson & Z.G. Ye, *Ferro* **165**, 83 (1995).
10. V. Westphal, W. Kleemann & M.D. Glinchuk, *Phys. Rev. Lett.* **68**, 847 (1992).
11. E.V. Colla, E.Yu. Koroleva, N.M. Okuneva & S.B. Vakhruşev, *Phys. Rev. Lett.* **74**, 1681 (1995).
12. R. Sommer, N.K. Yushin & J.J. van der Klink, *Phys. Rev.* **B48**, 13230 (1993).
13. G.J. Kavarnos, NUWC-NPT Technical Report 10, 797 (1995).
14. D. Viehland, Ph.D. Thesis, The Pennsylvania State University (1991).
15. S. Vakhruşev, B. Kryatkovsky, A. Naberezhov, N. Okuneva & B. Topervers, *Ferro* **90**, 173 (1989).
16. A. Loidl, *Ann. Rev. Phys. Chem.* **40**, 29 (1989).
17. A. Cheng, M.L. Klein & L.J. Lewis, *Phys. Rev. Lett.* (1991).
18. J. Chen, H.M. Chan & M. Harmer, *J. Am. Ceram. Soc.* **72**, 593 (1989).
19. C.A. Randal & A.S. Bhalla, *Jpn. J. Appl. Phys.* **29**, 327 (1990).
20. T. Egami, H.D. Rosenfeld & R. Hu, *Ferro* **136**, 15 (1992).
21. H.D. Rosenfeld & T. Egami, *Ferro* **158**, 351 (1994).
22. K. Park, L. Salamanca-Riba, M. Wuttig & D. Viehland, *J. Mater. Sci.* **29**, 1284 (1994).
23. B.E. Warren, *X-Ray Diffraction*. Dover Publications, New York (1969).

APPENDIX 11

Aging of the dielectric and piezoelectric properties of relaxor ferroelectric lead magnesium niobate–lead titanate in the electric field biased state

Q. M. Zhang, J. Zhao, and L. E. Cross

Materials Research Laboratory, The Pennsylvania State University, University Park, Pennsylvania 16802

(Received 2 October 1995; accepted for publication 4 December 1995)

The aging characteristics of the electrostrictive lead magnesium niobate–lead titanate $[(1-x)\text{PMN}-x\text{PT}]$ under dc bias field were investigated. It was observed that the amount of aging increases with the PT content for the compositions investigated ($x \leq 0.3$). For a fixed composition, the aging rate rises with temperature. It was shown that the aging follows a stretched exponential time law, which is typical for the time-dependent behavior in polar glass and random field systems. In PMN–PT, the dielectric constant shows a much weaker aging than the piezoelectric coefficient, reflecting the importance of the stress coupling of the defect field to the micropolar region during the aging since the polar vector of the microregions can have both 180° and non- 180° reorientations while only the non- 180° reorientation contributes to the observed piezoelectric effect. Experimental results also reveal that the defect field developed during the aging in these materials under dc bias field is quite different from those in normal ferroelectrics and in Mn-doped PMN and 0.9 PMN–0.1PT. The direction of the defect electric field is opposite to the direction of the original dc bias field, indicating that the defect field is the result of a direct coupling to the external bias field rather than induced by the polar domains. © 1996 American Institute of Physics. [S0021-8979(96)01806-0]

1. INTRODUCTION

The electrostrictive lead magnesium niobate (PMN) and its solid solution with lead titanate (PT) exhibit many unique features such as high dielectric permittivity, very little strain hysteresis, and large applied field induced piezoelectric activity which make them very attractive for a wide range of electromechanical transduction applications.^{1–4} In most of the transducer and actuator applications utilizing electrostrictive PMN or PMN–PT, the material is subjected to a dc bias electric field E_{dc} . The function of this dc bias field is to break the central symmetry of the material with a bias polarization P so the strain response ΔS of the material to an ac field E_{ac} , which is superimposed on the dc bias field, will be piezoelectriclike with an effective piezoelectric coefficient d ,

$$d = \Delta S / E_{ac}.$$

For a material under a dc bias field, changes in the induced properties of the material over time will inevitably result in a phenomenon called aging. In general, aging is a process for a system to evolve from a nonequilibrium state to an equilibrium state. For PMN and PMN–PT relaxor ferroelectrics, it has been shown that many of the properties resemble those of polar glass and random field systems.^{5–8} One of the most distinctive characteristics for these systems is the long relaxation time as the freezing temperature is approached.⁹ As a result, a metastable state may exist for a long time which manifests itself as an aging process when there is a change in external conditions.

In the past, several studies have been conducted on the aging phenomenon in electrostrictive PMN and $(1-x)\text{PMN}-x\text{PT}$ solid solution system at low PT content ($x < 0.1$).^{5,10,11} The focus of those earlier studies was primarily on the dielectric aging and on materials without external bias electric fields. It was found that for pure PMN and 0.9PMN–0.1PT,

there is no aging in the experimental time scale at temperatures near T_m , the temperature of dielectric permittivity maximum. The results, although relevant to the aging occurring in the dc field biased state, do not provide direct information on how the properties of a material (especially the effective piezoelectric response d) change with time under a dc bias field. It is the objective of this investigation to extend the earlier studies of aging in electrostrictive PMN and PMN–PT to the dc field biased state and to compositions with PT content higher than 10%. It is also intended to explore the time-dependent characteristics of the aging process in the material in some detail. As demonstrated in a recent investigation, the effective piezoelectric response in PMN–PT can be increased by using compositions with PT content higher than 10%.⁴ There exist many areas of applications requiring the use of electrostrictive PMN–PT with high PT compositions such as high temperature actuators for ink-jet applications.

To facilitate the discussion in the paper, we will briefly review some of the highlights from the earlier studies of aging in normal ferroelectrics and in a doped PMN relaxor.

Many works have been conducted to elucidate the aging phenomena in normal ferroelectrics such as lead zirconate–titanate (PZT) and barium titanate (BT). A comprehensive review of these works can be found in an article by Schälze and Ogino.¹²

In normal ferroelectrics, aging was manifested by the change in both the small signal and large signal parameters with time. It was observed that the dielectric aging follows a linear logarithmic time dependence and the aging rate increases with temperature.¹³ Hence, the aging can be characterized by a thermally activated process.¹⁴ In the paraelectric phase no aging was found. It has also been observed that the polarization hysteresis loop of aged specimens exhibits con-

stricted shapes, reflecting the buildup of an internal field due to the defect structure during the aging. The direction of the internal defect field is the same as that of the original poling field (or the local polarization direction).^{15,16}

Several mechanisms have been suggested to elucidate the origin of aging in a normal ferroelectric material. The relocation of charges, i.e., ions and electrons, and the reorientation of the defect dipoles in the host lattice will affect the domain wall mobility as well as the intrinsic dielectric response and result in aging. Under stress, the relaxation of the domain structure toward a more stable configuration can reduce the dielectric constant due to the reduction of the domain boundary contribution and the piezoelectric coupling to the intrinsic dielectric response of the material. Depending on the type of defect existing in the specimen, it has been shown that the internal bias field developed in the aging process can be either a volume effect (the field exists within grains and domains), or a boundary effect (it is located in the domain boundary or grain boundary).^{12,15-17}

In contrast, the aging in relaxor ferroelectrics exhibits quite different features. For this type of material, most of the aging studies were conducted in the temperatures near T_m . The experimental results obtained up-to-date clearly indicate the importance of the defect structure to the aging in this type of material. For example, for a carefully prepared pure PMN and 0.9PMN-0.1PT very little dielectric aging was observed.¹⁰ However, samples of PMN and 0.9PMN-0.1PT doped with Mn and other acceptor dopants, which create oxygen vacancies in the host lattice, show significant aging. It was observed that aging does not follow the linear logarithmic time law and is strongly frequency dependent with the low frequency dielectric constant aging faster than the high frequency dielectric constant. In addition, aging was also observed in the temperature region where the remanent polarization is near zero and is no longer a thermally activated process, i.e., the aging is the strongest at temperatures just below T_m . The defect bias field was shown to be originated from the reorientation of the defect dipoles formed from pairs of O^{2-} vacancy and positively charged dopant sites. The reorientation and alignment of the defect dipoles with the local polar domains provide a pinning field to the micropolar region, where the regions with larger micropolar volume will experience stronger pinning potential. As a consequence, the aging in the material exhibits a strong frequency dependence.^{5,10,11,18}

II. EXPERIMENT

To address the concerns of using PMN-PT based relaxor materials for electromechanical transduction applications, this study focuses on the aging characteristics of the effective piezoelectric coefficient, d , in the dc field biased state of electrostrictive PMN-PT. A detailed report on the dependence of the aging in a dc field biased state on the ceramic processing conditions is to be presented in another publication.¹⁹

Following the phase diagram of the solid solution PMN-PT as shown in Fig. 1, (1-x)PMN-xPT with compositions of PT less than 30% ($x=0.3$) was chosen for the investigation.²⁰ Both pure PMN-PT and PMN-PT doped

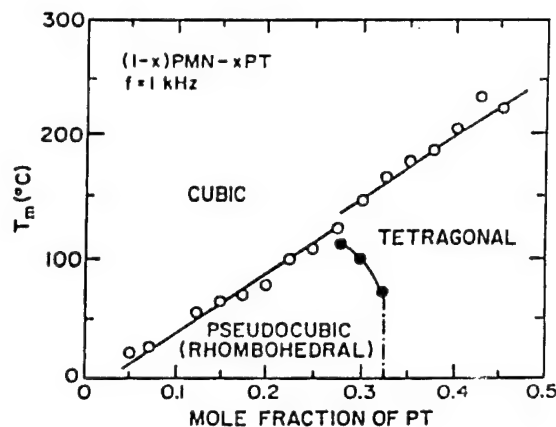


FIG. 1. Phase diagram of PMN-PT solid solution system (from Ref. 2).

with La were examined. For La-doped compositions, only those with $y=0.01$ in $(Pb_{(1-3y/2)}La_y)(Mg_{1/3}Nb_{2/3})_{(1-x)}Ti_xO_3$ are reported here. The x-ray powder diffraction data show the material is in the pseudocubic phase in this composition range; a typical one is presented in Fig. 2. The experimental temperature range for each composition was chosen near and above its T_m . In this temperature and composition range, PMN-PT exhibits the typical electrostrictive behavior, i.e., slim polarization and strain hysteresis loops with near zero remanent polarization and the strain is proportional to the square of the polarization.⁵

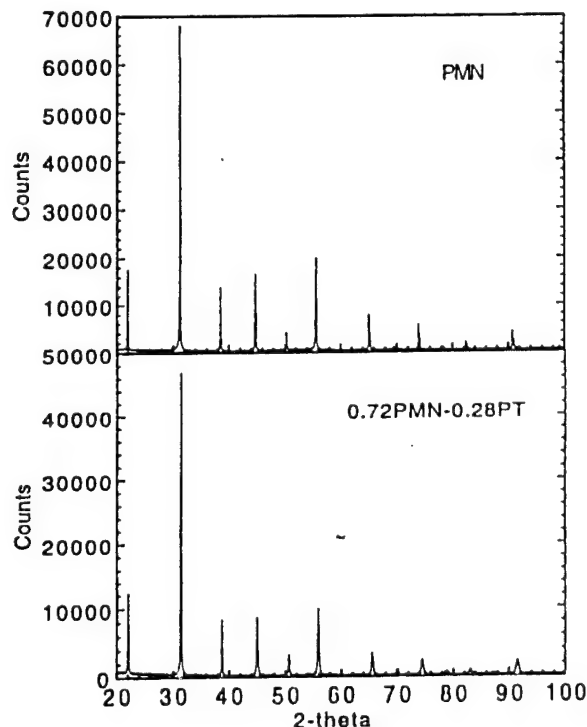


FIG. 2. Powder x-ray diffraction pattern of PMN and 0.72PMN-0.28PT at room temperature which show that in this composition range, the PMN-PT solid solution is in the pseudocubic phase.

The ceramic samples across the series were prepared using the columbite precursor method as described by Swartz and Shrout.²¹ In this processing, reagent grade MgO and Nb₂O₅ were first reacted to form the columbite structure MgNb₂O₆, which was then reacted with PbO and TiO₂ to form Pb(Mg_{1/3}Nb_{2/3})O₃:PbTiO₃ compositions. Completion of the reactions was verified using x-ray diffraction, which was also used to determine the appropriate structure. After milling, the various powders were cold pressed to form disks, followed by sintering at temperatures near 1250 °C for 4–6 h and then annealed in O₂ atmospheres at 900 °C for about 6 h. The final sample quality was checked using x-ray diffraction and dielectric constant measurement. The grain size of the specimens investigated also was measured with scanning electron microscopy and the average grain size is about 4 μm.

The effective piezoelectric coefficient d (either d_{33} or d_{31}) was measured using a laser dilatometer which is equipped with an optical temperature chamber.²² The temperature stability of the system is better than 0.2 °C. For electrostrictive materials such as PMN–PT, the strain S_1 or S_3 is proportional to the square of the polarization P ,

$$S_3 = Q_{11}P^2, \quad S_1 = Q_{12}P^2. \quad (1)$$

In the equations, S_1 and S_3 are the induced strains perpendicular to and parallel with the direction of polarization, and the proportional coefficients Q_{11} and Q_{12} are the so-called electrostrictive coefficients for the material. It has been shown that the effective piezoelectric coefficients in the dc field biased state can be expressed approximately as

$$d_{33} = 2Q_{11}\epsilon_{33}P, \quad d_{13} = 2Q_{12}\epsilon_{33}P, \quad (2)$$

where ϵ_{33} is the dielectric permittivity along the polarization direction and P is the polarization level induced by the dc bias field.²³ Equation (2) reveals that the aging in d_{33} and d_{31} can be the result of the change of Q_{ij} , ϵ_{33} , and P with time. Hence, the dielectric aging and the change of polarization under the bias condition were also measured concomitantly with the field induced strain by a modified Sayer–Tower circuit. As will be shown, the dielectric aging can add valuable information to the understanding of the aging mechanism in this type of material.

An important fact about aging in ferroelectric materials is that it will depend on the aging temperature. For the aging in a dc field biased state, it will also depend on the bias field level. For a relaxor ferroelectric aging is also frequency dependent. In this paper, we do not intend to address all the issues associated with aging in PMN–PT relaxor materials. Instead we will focus on the effect of temperature and composition on the aging process. The data presented provide information on how the aging will change with the other parameters. All data reported in this paper were acquired at 1 kHz, and the dc bias field in the aging process was fixed at 5 kV/cm.

For PMN–PT, the temperature of diffused phase transition T_m varies with composition (see Fig. 1). To compare the aging characterizations from different compositions, it is necessary to establish a reference temperature for each com-

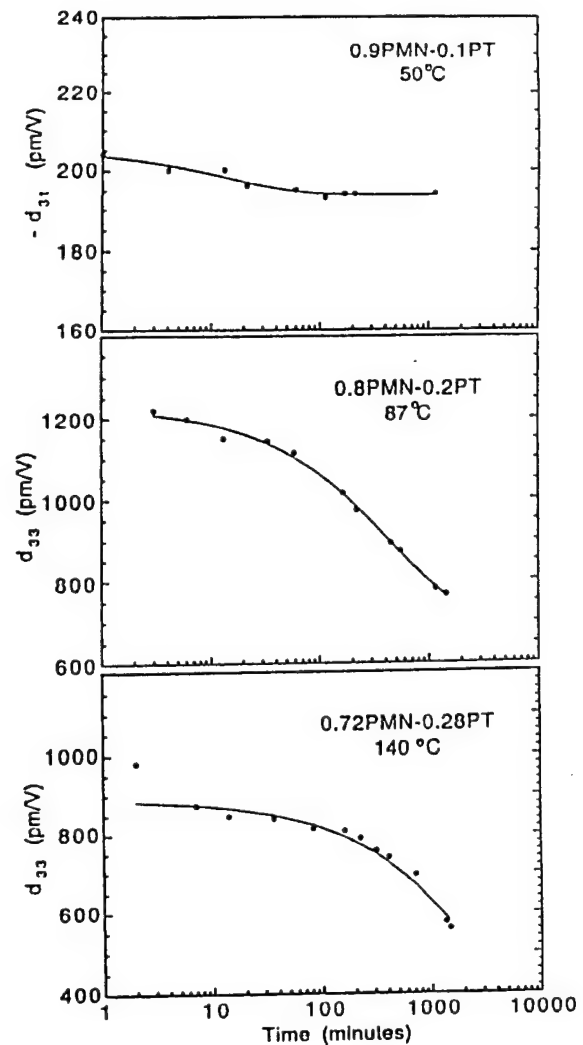


FIG. 3. The aging of the effective piezoelectric coefficient d_{31} for 0.9PMN–0.1PT, and d_{33} for 0.8PMN–0.2PT and 0.72PMN–0.28PT in the field induced piezoelectric state at a temperature near their respective T_m . The black dots are data points and solid curves are the fitting using Eq. (3). The dc bias field is 5 kV/cm. The data show that the relaxation time τ and the amount of aging in d coefficient increase with PT content.

position to account for this variation. In this paper, the respective T_m for each composition is chosen as the reference temperature for that composition.

III. RESULTS AND DISCUSSIONS

A. Dependence of the aging of the effective piezoelectric coefficient on PT content and on temperature

The aging of the effective piezoelectric coefficient d_{33} or d_{31} for three compositions: 0.9PMN–0.1PT, 0.8PMN–0.2PT, and 0.72PMN–0.28PT, at a temperature near their respective T_m is shown in Fig. 3. As shown in the figure, there is only very weak aging for 0.9PMN–0.1PT. In fact, very weak aging was observed at all the temperatures investigated (25, 50, and 100 °C) for 0.9PMN–0.1PT composition (only the data at 50 °C are shown here). This is consistent with the results

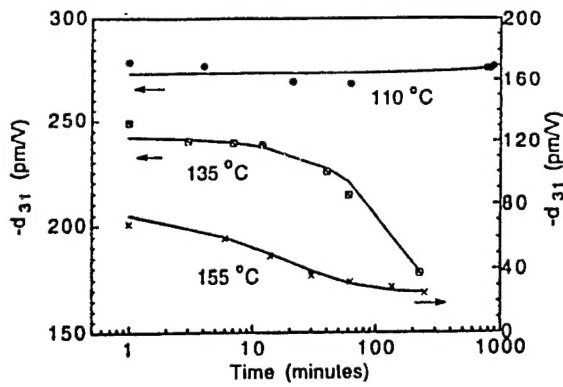


FIG. 4. The aging of d_{31} for 0.7PMN-0.3PT doped with 1% La as a function of temperature. The dc bias field is 5 kV/cm. The solid curves for 135 and 155 °C data are the fitting with Eq. (3) and for 110 °C is drawn to guide the eye. The data show that the relaxation time τ decreases with temperature.

of the earlier aging studies where no aging was observed for undoped 0.9PMN-0.1PT specimens without external bias field.¹⁰ From the data in Fig. 3, it is evident that the amount of aging in the effective piezoelectric coefficient increases as the PT content increases. It is also obvious that the aging observed in these compositions is not linear with logarithmic time.

From the measured aging data it was also observed that in the temperature range studied, the aging rate increases as the temperature difference $T - T_m$ increases. This is demonstrated in Fig. 4 for 0.7PMN-0.3PT with 1% La ($y=0.01$) (T_m is at 110 °C) and Fig. 5 for 0.8PMN-0.2PT (T_m is at 87 °C). The rise of the aging rate with temperature implies that the aging process is a thermally activated process. This behavior is obviously different from the aging observed in doped PMN (as mentioned in Sec. I), where the aging rate is the highest at temperatures near T_m .⁵

The linear logarithmic time law of the aging in normal ferroelectrics is related to the relaxation of the domain structure in the material toward an equilibrium configuration.¹² In a relaxor ferroelectric, deviation of the aging behavior from the linear logarithmic time behavior can be the result of the lack of this macrodomain structure. For a material exhibiting glass or random field behavior, it is well known that the time dependence may follow the stretched exponential law and for the small signal parameters investigated, it can be expressed as

$$d = d_{\infty} + d_1 \exp[-(t/\tau)^{\nu}], \quad (3)$$

where d_{∞} represents the part which is not time dependent and the second term on the right-hand side of the equation represents the part which is time dependent and as $t \rightarrow \infty$, the contribution of this term becomes zero, which represents the aging.^{9,24} The time constant τ reflects the aging rate. As is evident from the solid curves in Figs. 3-5, which are the fitting curves using Eq. (3), the stretched exponential function can describe the experimental data quite well. In fact, Eq. (3) can be used to fit almost all of the experimental data obtained. For the data at temperatures near T_m , ν in Eq. (3) is at about 0.62. As the temperature moves away from T_m , ν

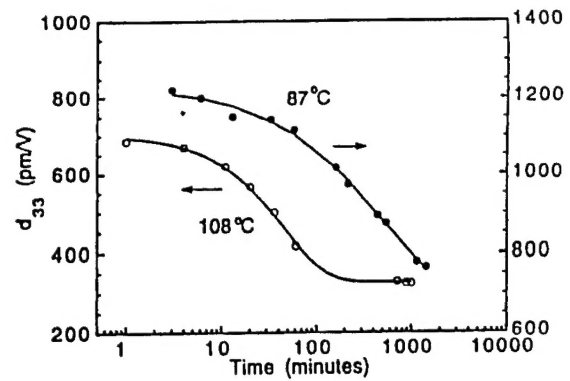


FIG. 5. The aging of d_{33} for 0.8PMN-0.2PT at 87 and 108 °C under 5 kV/cm dc bias field. The solid curves are the fitting of the data with Eq. (3). The data show that the relaxation time τ decreases with temperature.

varies in the range from 0.6 to 0.95. The fitting parameters for the data in Fig. 3 are listed in Table I. Evidently, as the PT content increases, the ratio of d_1/d_{∞} increases significantly, indicating that the metastable part of the contribution to the effective piezoelectric coefficient rises sharply with PT content. In addition, the relaxation time τ also increases sharply with PT content, reflecting an increase in the activation energy for the motion of the micropolar domains.

For a fixed composition, the fitting to Eq. (3) reveals that as the temperature is raised, the relaxation time τ is reduced while the ratio d_1/d_{∞} does not change very much in the experimental temperature range, as expected for a random field and polar glass systems.

In earlier studies on aging in acceptor-doped PMN and 0.9 PMN-0.1PT, it was observed that the aging rate increases as the measuring frequency is reduced. It was proposed that such a trend could be the result of the pinning of the polarization components which have low relaxation time or high activation energy by the defect field.⁵ In a relaxor ferroelectric, although the average lattice has the pseudocubic symmetry, local micropolar domains exist with the size of the domains distributing statistically over a broad range.⁵ The energy involved in reorienting a polar microdomain under an internal defect electric bias field E_{def} is proportional to $\nu P E_{\text{def}}$ where P is the polarization and ν is the volume of the micropolar domain, respectively. Hence, the micropolar regions with large ν which have longer relaxation times will be pinned more effectively by E_{def} than the micropolar domains of smaller size, which have shorter relaxation times. For the PMN-PT investigated here, it was observed that the rhombohedrality increases with PT content, indicating an increased elastic anisotropy and polarization P in the micropolar domains.^{5,20,25} It is also conceivable that at temperatures near T_m , the micropolar regions with large volume ν and

TABLE I. Fitting parameters of Eq. (3) to the data in Fig. 3.

Composition	d_{∞}	d_1	d_1/d_{∞}	τ (min)	ν
0.9 PMN-0.1PT	193.7	12.0	0.061	13.46	0.62
0.8PMN-0.2PT	696	534	0.767	448	0.64
0.72PMN-0.28PT	201	691	3.44	3.261	0.62

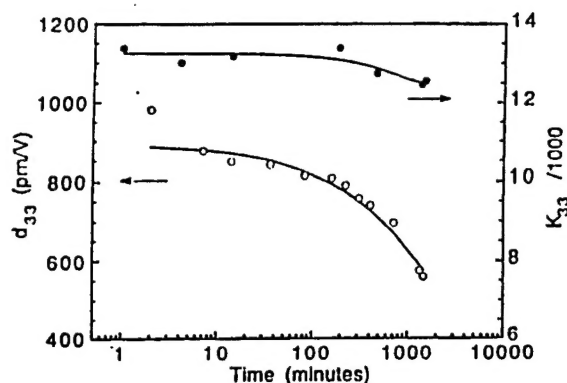


FIG. 6. Aging data of both the dielectric constant K_{33} (solid dots) and effective piezoelectric coefficient d_{33} (open circles) for 0.72PMN-0.28PT at 140 °C under 5 kV/cm dc bias field. The solid curves are the fitting using Eq. (3). Apparently, K_{33} shows a much weak aging than d_{33} .

large P also increase with the PT content. Hence, even a relatively weak internal defect field can manifest itself by producing a pronounced aging in material properties. Based on this observation, it is suggested that the increased aging in PMN-PT with the PT content is related to the increased local crystal anisotropy (in the microdomains) in the material. This is consistent with other experimental results, i.e., the aging rate can be reduced by doping with La. It is well known that adding La to PMN-PT will increase the relaxor behavior in PMN-PT, implying that it breaks the polar regions to smaller size and reduces the crystal anisotropy in these regions. These results will be discussed in detail in another publication.¹⁹

B. Dielectric aging in the dc field biased state

The experimental data also reveal that aging in the effective piezoelectric coefficient is not necessarily accompanied by aging in the dielectric constant. Shown in Fig. 6 are the aging results for both the dielectric constant and effective piezoelectric coefficient for 0.72PMN-0.28PT at 135 °C under 5 kV/cm bias field. Clearly for this composition at this temperature and bias field, there is very weak aging in the dielectric constant in spite of the severe aging in the effective piezoelectric coefficient. A similar phenomenon was observed for 0.8PMN-0.2PT at 87 °C. On the other hand, for samples of 0.7PMN-0.3PT with 1% La, aging in both the dielectric constant and effective piezoelectric coefficient was observed. The data in Fig. 7 are for the dielectric aging of this composition which are compared to the data in Fig. 4 for the aging in the effective piezoelectric coefficient of the same composition and show a much weaker dielectric aging.

At first glance, the results here seem to be quite puzzling. However, it should be remembered that Eqs. (1) and (2) are held only for a true electrostrictive response, i.e., the strain due to the unit cell deformation in a central symmetric single-domain crystal. For materials having a macroscopic central symmetry but with micro- or macropolar domain structures such as the relaxor and normal ferroelectrics, the strain polarization may or may not follow the relationships of Eqs. (1) and (2). For these materials, the change of polariza-

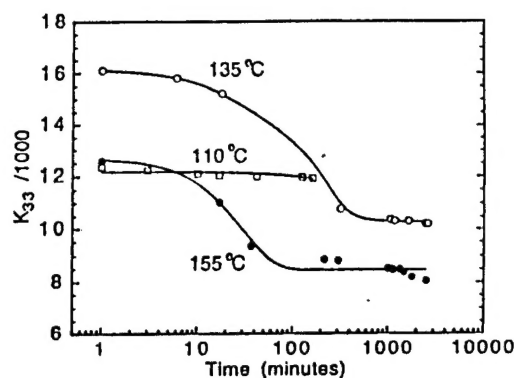


FIG. 7. The aging of K_{33} for 0.7PMN-0.3PT doped with 1% La as a function of temperature. The dc bias field is 5 kV/cm. The solid curves for 135 and 155 °C data are the fitting with Eq. (3) and for 110 °C is drawn to guide the eye. The data show that the relaxation time τ decreases with temperature.

tion involves the reorientation of the polar vector through either the 180° process or non-180° process, respectively.²⁶ While both the 180° and non-180° processes contribute to the dielectric activity, only the non-180° polarization reorientation produces the strain change in the material. If during the polarization switching process, the ratio between the 180° process and non-180° processes changes, Eq. (1) will not hold and Q_{ij} in Eq. (2) will depend on P , the bias polarization level. For this reason Q_{ij} in Eq. (2) may change during the aging process. Aging in the effective piezoelectric coefficient will be a direct result of the hindrance of the non-180° polarization reorientation process. However, the hindrance of the non-180° polarization reorientation process can have opposite effects on the dielectric aging. If the defect field does not pin the polarization vector but instead favors the 180° process over the non-180° process, the dielectric constant may not show much aging even though there is a strong piezoelectric aging. On the other hand, if the polarization vectors in the microdomains are pinned by the defect field, both the dielectric and piezoelectric aging will occur. Furthermore, the dielectric aging is related to the change in both the 180° and non-180° polarization reorientation processes. Hence, the aging in the dielectric constant may have very different relaxation time from that of the aging in the effective piezoelectric coefficient, which was observed in the experimental data presented here.

To relate these general principles to the details of the experimental results here requires more detailed investigation, including structure studies. However, some conclusions still can be drawn from the experimental data here. The strong aging in the effective piezoelectric coefficient in pure PMN-PT is a result of the hindrance of the non-180° polar vector reorientation which is due to the coupling of these polar regions to the stress component of the defect field developed during the aging process. The increased anisotropy in the micropolar domains with the PT content increases the coupling of the defect stress field to the polar region which may incur a higher potential barrier for the non-180° polarization reorientation and a large aging in the piezoelectric

TABLE II. Comparison of the amount of aging in d_{31} and K_{33} (Figs. 4 and 7) for 0.7PMN–0.3PT doped with 1% La.^a

Temp. (°C)	d_{31}			K_{33}		
	d_m	d_1	d_1/d_m	K_m	K_1	K_1/K_m
135	80	162.6	2.03	10 300	5900	0.57
155	25.5	54.4	2.13	8 500	4240	0.50

^aFor dielectric constant, Eq. (3) is written as $K = K_m + K_1 \exp[-(t/\tau)^n]$.

properties. However, in these materials, these polar regions may not be totally pinned by the defect field and some of the polar regions may still be able to follow the driving ac electric field through 180° flipping. As a consequence, the dielectric aging is much weaker and has a much longer relaxation time (weak driving field).

Doping with a suitable amount of La³⁺ in PMN–PT reduces the lattice anisotropy,²⁵ apparently reducing the amount of aging in the effective piezoelectric coefficient, and moves the material into a state with more relaxor behavior, also reducing both the dielectric and piezoelectric aging.¹¹ However, excessive La³⁺ doping will introduce more defect sites in the lattice which may cause strong aging in the material properties.¹¹ The result of these two competing effects will determine the aging in both the dielectric and effective piezoelectric coefficients in a material. For the compositions studied here, the aging rate is lower for La-doped materials compared with pure PMN–PT if the two compositions have the same T_m .

The fact that the dielectric aging is much weaker than the aging in the effective piezoelectric coefficient in both La-doped and undoped PMN–PT implies that the effect of the defect field on the aging in the material properties is mainly through the stress field rather than the electric field. The observation may shed some light on the understanding of the relaxor ferroelectrics and may indicate that the random field in the materials which breaks the long-range ferroelectric ordering and induces the relaxor behavior is more a stress field effect rather than an electric field effect.

In Table II, the amount of aging in both the effective piezoelectric coefficient and dielectric constant for 0.7PMN–0.3PT with 1% La is compared. The data explicitly show that in the field bias state, even for La-doped samples, the dielectric aging is still much weaker than the piezoelectric aging.

C. Internal defect field developed during the aging

The experimental results presented in the preceding sections show that there is a defect field developed during the aging process which couples to the micropolar regions mainly through the mechanical stress effect. In this section, we will show that this field also has an unusual electric component.

For all the aged samples investigated here, the piezoelectric d_{33} coefficient at room temperature was measured by a Berlincourt d_{33} meter after the bias field was removed and the samples were cooled under no external field. Surprisingly, all the samples exhibited negative d_{33} value which is against the direction of the original bias field. The d_{33} values

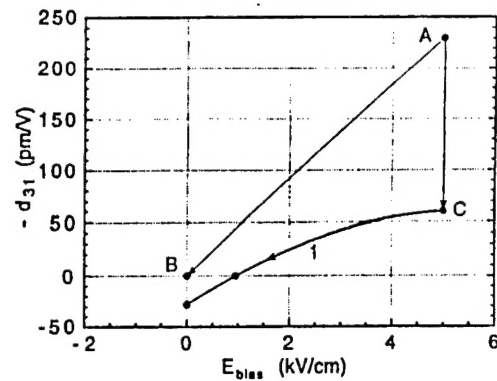


FIG. 8. The variation of d_{31} for 0.7PMN–0.3PT with 1% La at 140 °C under different dc bias conditions. The data point A was taken from a fresh sample immediately after the dc bias field was applied, point B was taken after the dc bias field was removed from the fresh sample and apparently, d_{31} is zero, point C was taken from the sample aged under the dc bias field for 32 h. The solid curve 1 indicates the change of d_{31} for the aged sample during the reduction of the dc bias field. The d_{31} became zero even at a finite dc bias field (about 1 kV/cm) indicating that the direction of the internal electric field from the defects is opposite to that of the aging field.

for these samples were in the range of 10–70 pm/V. For nonaged specimens, that is, a bias field was applied only briefly at high temperature and removed during the cooling, there was no measurable d_{33} value at room temperature within the uncertainty of the Berlincourt d_{33} meter. For specimens cooled under a dc bias field a normal positive d_{33} value was observed. It appears that aging does not have a significant effect on the room temperature d_{33} value thus obtained. The results indicate that the direction of the defect electric field here is different from that of the applied dc bias field under which it is developed.

An experiment was also conducted to evaluate the d_{33} and/or d_{31} values at the aging temperature for aged samples as the dc bias field was reduced. Shown in Fig. 8 is the result for 0.7PMN–0.3PT with 1% La where the data were acquired using the double beam laser dilatometer. The data show that for specimens without aging, the d_{31} value is near zero after removing the dc bias field. However, for aged specimens, the d_{31} value drops to zero at a finite dc bias field, indicating that the electric field from the defect field was opposing the applied bias field. When the external dc bias field was totally removed, the specimens exhibited a d_{31} value opposite to that induced by the original dc bias field.

The two experimental results presented indicate the defect field developed during the aging process is quite different from those in the normal ferroelectrics and those found in the aged specimens of Mn-doped PMN and 0.9PMN–0.1PT where the defect electric field direction is parallel to the applied field direction or the local polarization direction.^{14–18} It is likely that the defect field responsible for the internal bias electric field here is a result of the drifting defect changes under the external dc bias field which are accumulated at the grain boundaries and local pore regions and will be in opposite direction to the applied electric field.

It should be pointed out that although the stress field plays a dominant role in the aging process observed here, the

buildup of the defect field is still the direct result of the external dc electric bias field which can couple only to the charged defects. This was clearly demonstrated by the following experiment results. Specimens were held at a temperature T ($T > T_m$) without dc bias field for more than one day. Afterwards a dc bias field was applied and the effective piezoelectric coefficient was evaluated. No observable aging in the effective piezoelectric coefficient was observed for these specimens. A dc bias field can have two functions in the aging process; one is to cause the coalescing of the microdomains and the other is to cause the drifting of the defect charges (or reorientation of defect dipoles) in the host lattice which can be accumulated at the grain boundary or pore regions to produce a defect field. We believe that it is the combination of these two effects which causes aging observed here. A detailed mechanism of how the stress coupling is generated in the aging process from these electrically induced defect fields still needs to be determined. We do not intend to speculate further without more experimental evidence.

IV. SUMMARY

The aging characteristics of the electrostrictive PMN-PT under dc bias field were investigated. Very weak aging in both the effective piezoelectric coefficient and dielectric constant was found for 0.9PMN-0.1PT. As the PT content increases, the aging in these coefficients becomes increasingly severe. For a fixed composition, the aging rate rises with the temperature difference $T - T_m$. It was shown that the aging curve does not follow the linear logarithmic time law. Instead, the time dependent behavior can be described quite well by a stretched exponential function, which is typical for the time dependent behavior in polar glass and random field systems.

It was also observed that the effective piezoelectric coefficients exhibit stronger aging than the dielectric aging. It is believed that the aging in PMN-PT is caused mainly by the elastic coupling of the micropolar regions to the defect field instead of electric coupling which hinders the non-180° reorientation of the polar vectors and results in the observed phenomena. Hence, for PMN-PT with high PT content, the increased crystal anisotropy and the probability of having microregions with larger polar volume will incur a higher aging rate compared with specimens with low PT content. By doping with suitable amounts of La, the aging rate can be reduced.

Experimental results also reveal that the defect field developed during the aging in these materials under dc bias field is quite different from those in normal ferroelectrics and

in Mn-doped PMN and 0.9PMN-0.1PT. Here, the defect field is the result of the direct coupling to the external bias field rather than induced by the polar domains. Hence, the direction of the defect electric field is opposite to the direction of the original dc bias field.

The experimental results here show that even for a defect field developed under an external dc electric field, its effect on the aging in PMN-PT is mainly through the stress coupling, which may imply that a defect stress field is more effective in disrupting a macroscopic polarization and inducing relaxor behavior in the material.

ACKNOWLEDGMENTS

The authors wish to thank Dr. D. Huse for many stimulating discussions. This work was supported in part by a grant from Tektronix, Inc., and in part by the Office of Naval Research.

- ¹S. J. Jang, K. Uchino, S. Nomura, and L. E. Cross, *Ferroelectrics*, **27**, 31 (1980).
- ²K. Uchino, S. Nomura, L. E. Cross, S. J. Jang, and R. E. Newnham, *J. Appl. Phys.* **51**, 1142 (1981).
- ³K. Uchino, *Am. Ceram. Bull.* **65**, 647 (1986).
- ⁴J. Zhao, Q. M. Zhang, N. Kim, and T. Shrout, *Jpn. J. Appl. Phys.* (to be published).
- ⁵L. E. Cross, *Ferroelectrics* **76**, 241 (1987).
- ⁶V. Westphal, W. Kleeman, and M. D. Glinchuk, *Phys. Rev. Lett.* **68**, 847 (1992).
- ⁷E. V. Colla, E. Y. Koroleva, N. M. Okuneva, and S. B. Vakhruшев, *Phys. Rev. Lett.* **74**, 1681 (1995).
- ⁸D. Viehland, S. Jang, L. E. Cross, and M. Wuttig, *Philos. Mag. B* **64**, 335 (1991).
- ⁹K. Binder and A. P. Young, *Rev. Mod. Phys.* **58**, 801 (1986).
- ¹⁰W. Pan, E. Furman, G. O. Dayton, and L. E. Cross, *J. Mater. Sci. Lett.* **5**, 647 (1986).
- ¹¹T. R. Shrout, W. Huebner, C. A. Randall, and A. D. Hilton, *Ferroelectrics* **93**, 361 (1989).
- ¹²W. A. Schulze and K. Ogino, *Ferroelectrics* **87**, 361 (1988).
- ¹³K. W. Plessner, *Proc. Phys. Soc. London Ser. B*, **69**, 1261 (1956).
- ¹⁴R. C. Brandt and G. S. Ansell, *J. Am. Ceram. Soc.* **52**, 192 (1969).
- ¹⁵G. H. Jonker, *J. Am. Cer. Soc.* **55**, 57 (1972).
- ¹⁶W. Wersing, *Ferroelectrics* **12**, 143 (1976).
- ¹⁷M. E. Lines and A. M. Glass, *Principles and Applications of Ferroelectrics and Related Materials* (Clarendon, Oxford, 1977).
- ¹⁸W. Pan, Q. Zhuang, and L. E. Cross, *J. Am. Ceram. Soc.* **71**, C17 (1988).
- ¹⁹J. Zhao, Q. M. Zhang, and T. Shrout (unpublished).
- ²⁰S. W. Choi, T. R. Shrout, S. J. Jang, and A. S. Bhalla, *Ferroelectrics* **100**, 29 (1989).
- ²¹S. L. Swartz and T. R. Shrout, *Mater. Res. Bull.* **17**, 1245 (1982).
- ²²Q. M. Zhang, S. J. Jang, and L. E. Cross, *J. Appl. Phys.* **65**, 2807 (1989).
- ²³W. Y. Pan, W. Y. Gu, D. J. Taylor, and L. E. Cross, *Jpn. J. Appl. Phys.* **28**, 653 (1989).
- ²⁴D. Huse (private communication).
- ²⁵T. B. Wu, M. Shyu, C. Chung, and H. Lee, *J. Am. Ceram. Soc.* **78**, 2168 (1995).
- ²⁶G. Arlt, *Ferroelectrics* **104**, 217 (1990).